NANOPARTICLES OF METAL-ORGANIC FRAMEWORKS: A GENERAL SYNTHETIC METHOD AND SIZE-DEPENDENT PROPERTIES

by

CHECKERS MARSHALL

A DISSERTATION

Presented to the Department of Chemistry and Biochemistry
and the Division of Graduate Studies of the University of
Oregon in partial fulfillment of the requirements
for the degree of
Doctorate of Philosophy

March 2023

DISSERTATION APPROVAL PAGE

Student: Checkers Marshall

Title: Nanoparticles of Metal-Organic Frameworks: A General Synthetic Method and Size-Dependent Properties

This dissertation has been accepted and approved in partial fulfillment of the requirements for the Doctorate of Philosophy degree in the Department of Chemistry and Biochemistry by:

Victoria J. DeRose	Chair
Carl K. Brozek	Core Member
Jim E. Hutchison	Core Member
Matthew L. Polizzotto	Outside Member

and

Krista Chronister	Vice Provost for Graduate Studies

Original approval signatures are on file with the University of Oregon Division of Graduate Studies.

Degree awarded March 2023

DISSERTATION ABSTRACT

Checkers Marshall

Doctorate of Philosophy

Department of Chemistry and Biochemistry

March 2023

Title: Nanoparticles of Metal-Organic Frameworks: A General Synthetic Method and Size-Dependent Properties

Metal-organic framework nanoparticles exhibit both high internal surface area and good colloidal stability in a variety of solvents including biological media. These materials are sought after for a range of applications, mainly in drug delivery, catalysis, and separation membranes.[1] Considerable effort has been put into controlling the size and shape of MOF crystals to develop materials that, due to small particle size and good colloidal stability, may be solution-processable. In this thesis, a simple model to help predict size trends in MOF nanoparticle syntheses is developed, then the model is applied both to well-known and novel MOF nanoparticle systems. In Chapter 2, I first present a simple equilibrium model to further our understanding of how to control MOF nanoparticle size. MOF nanoparticles can be synthesized via several top-down and bottom-up approaches. One of the most prevalent bottom-up methods is to use "modulators," molecules added to the growth media to change the reaction conditions and therefore the crystals' growth. This chapter encompasses a literature-based perspective on how the presence and identity of a modulator will impact the final size of a MOF nanoparticle and introduces the "Seesaw model" to explain these effects. In Chapter 3, I then apply this model to the well-known nanoMOF systems $Zn(mIm)_2$

(ZIF-8) and Cu_3BTC_2 (HKUST-1). We show that, by using a mixture of an conjugate acid/base pair, that both modulator equivalents and proton activity play a role in determining final particle size. In Chapter 4, I first develop the synthesis for a novel nanoMOF system, a family of metal-triazolate MOFs, then explore the MOF Fe(1,2,3-triazolate)$_2$ in more depth for its size-dependent optical and electronic properties. Finally, in Chapter 5, the effects of ion identity, solvent identity, particle size, and film thickness on the redox activity of Fe(TA)$_2$ thin films is studied in depth.

This dissertation contains both published and unpublished co-authored material.

CURRICULUM VITAE

NAME OF AUTHOR: Checkers Marshall

GRADUATE AND UNDERGRADUATE SCHOOLS ATTENDED:

University of Oregon, Eugene, OR, USA
Fort Lewis College, CO, USA

DEGREES AWARDED:

Doctor of Philosophy, Inorganic Chemistry, 2023, University of Oregon
Master of Science, 2023, University of Oregon
Bachelor of Science, Chemistry, 2016, Fort Lewis College

AREAS OF SPECIAL INTEREST:

Sustainable Energy
Metal-Organic Frameworks

PROFESSIONAL EXPERIENCE:

Graduate Teaching Fellow, University of Oregon, 2017-2020
General & Organic Chemistry Lab TA, Fort Lewis College, 2014-2016

GRANTS, AWARDS AND HONORS:

Rosaria Haugland Fellowship, 2020
Deans First Year Merit Award, University of Oregon, 2017
James Mills Outstanding Performance in Physical Chemistry, 2016

PUBLICATIONS:

Marshall, C.R.; Dvorak, J.D.; Twight, L.P.; Kadota, K.; Chen, L.; Overland, A.E.; Ericson, T.; Cozzolino, A.F.; Brozek, C.K. "Size-Dependent Properties of Solution-Processable Conductive MOF Nanoparticles," *J. Am. Chem. Soc.*, **2022**

Marshall, C.R.; Timmel, E.T; Staudhammer, S.A.; Brozek, C.K. "Experimental Evidence for a General Model of Modulated MOF Nanoparticle Growth," *Chem. Sci.*, **2020**

Schaub, T. A.; Prantl, E.; Kohn, J.; Bursch, M.; **Marshall, C. R.**; Leonhardt, E. J.; Lovell, T. C.; Zakharov, L. N.; Brozek, C. K.; Waldvogel, S. R.; Grimme, S.; Jasti, R. "Exploration of the Solid-State Sorption Properties of Shape-Persistent Macrocyclic Nanocarbons as Bulk Materials and Small Aggregates," *J. Am. Chem. Soc.*, **2020**.

Van Raden, J.; Leonhardt, E.; Zakharov, L.; Pérez-Guardiola, A.; Pérez-Jiménez, Á.; Marshall, C.; Brozek, C.; Sancho-García, J.-C.; Jasti, R. "Precision Nanotube Mimics via Self-Assembly of Programmed Carbon Nanohoops," *Chem. Mater.*, **2020**, 32, 5802.

Marshall, C. R.; Staudhammer, S. A.; Brozek, C. K. "Size Control of Metal-Organic Framework Porous Nanocrystals," *Chem. Sci.*, **2019**

ACKNOWLEDGEMENTS

During my PhD, I faced challenges I thought I never would. I have made it through this experience with my own hard work, but it would not have been possible without the support of those around me. Most importantly, I am deeply grateful to my advisor, Dr. Carl Brozek, who taught me about the innerworkings of academia and pushed me to be the best scientist I could become. I would also like to thank my commitee members, Dr. Jim Hutchison, Dr. Vickie DeRose, and Dr. Matt Polizzotto, for their valuable advice. Special thanks to the Rosaria Haugland Foundation for granting me a generous Fellowship. I would like to thank the CAMCOR staff, in particular Valerie Brogden, Stephen Golledge, and Josh Razink, for their invaluable knowledge and skills that helped me collect beautiful data. Thank you to my mentors during my first year: Lisa Enman, Brandon Crockett, Meredith Sharps, and Dani Hamann. Many thanks to the front office staff in the Chemistry department, without whom this place would certainly fall apart.

My community made my success possible. To my partner, Alex Brunner, I give my heartfelt thanks for his constant pep talks, incredible cooking, and for taking me on weekend adventures even when I told him I should be in lab. To my closest friends, I am deeply indebted: Kai Pham, Courtney Ragle, Remington Koltes, Sam and Evan West, Jake Anderson, and Quinn Valentine. To those in my cohort who helped me through the program with study dates and lunches, particularly Jenna Mancuso and Marisa Choffel. To my parents, who have always encouraged my creative and scientific pursuits, even though some of them are rather dangerous. To my sister Laura, for endless LOTR memes, and her partner Dan, who I can always rely on to share my complaints about working in science. To

Henry Tregillus, who helped me format this giant document properly. And to Jess Lohrman, who read drafts of my documents and who let me borrow her backyard.

To my lab mates, who inspired me, challenged my thinking, and occasionally challenged my patience. To every one of my mentees, both rotation students and undergraduates: you taught me as much as I taught you. I would like to thank all of my incredible undergraduate researchers individually: Sara Staudhammer, Maria Anderson, Alexi Overland, Kelsie Heffernan, and Jeff Gombart. To the lovely and creative people I met through flow arts, blues dancing, and the Oregon Country Fair. To the staff at Staszak Physical Therapy, who somehow make injury management fun. To my undergraduate professors, who ignited my passion in chemistry. And finally to the discipline of chemistry itself, for as we all know, we stand on the shoulders of giants.

This thesis is dedicated to the potato, the most noble of Earth tubers.

TABLE OF CONTENTS

Chapter Page

LIST OF FIGURES

Figure Page

Figure Page

Figure Page

LIST OF TABLES

Table Page

Table Page

CHAPTER I

INTRODUCTION

Metal-organic framework nanoparticles exhibit both high internal surface area and colloidal stability in a variety of solvents, including biological media. These materials are sought after for a range of applications, mainly in drug delivery, catalysis, and separation membranes.[1] MOFs are materials that self-assemble from metal ions and multitopic organic ligands; because the particular metal ion and ligand can be chosen by the chemist, this class of materials is astonishingly diverse, with over 90,000 unique structures having been synthesized to-date.[3] Most often, MOFs are synthesized as "bulk powders," meaning that their crystal size and shape is not controlled, and typically the diameteres of the crystals are hundreds to thousands of nanometers. Hence, the materials are in a powdered form that can be difficult to process for use in practical applications. Considerable effort has been put towards controlling the size and shape of MOF crystals to develop materials that, due to small particle size and good colloidal stability, may be solution-processable.[4] Smaller crystals additionally boast a shorter diffusion pathlength for molecules of interest, meaning that catalytic efficiency and separation efficiency are often inversely related to particle size.[5] Due to the compositional and structural diversity of MOF materials, each new nanoparticle synthesis typically requires high-throughput testing methods; this type of development is time-intensive. In this thesis, an approachable model to help predict size trends in MOF nanoparticle syntheses is developed, then the model is applied both to well-known and novel MOF nanoparticle systems.

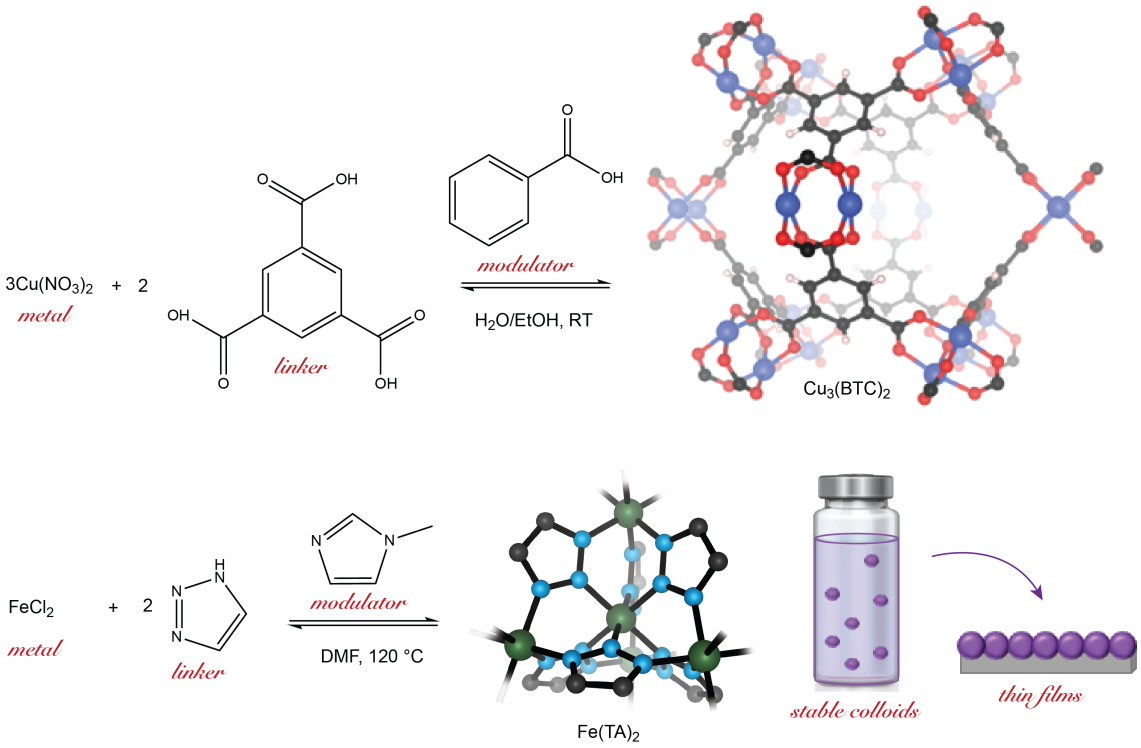

Figure 1.1. Summary of work presented in this thesis. Classic MOF nanoparticles (Cu_3BTC_2) and redox-active MOF nanocrystals ($Fe(TA)_2$) are synthesized by applying the Seesaw model. $Fe(TA)_2$ nanoparticles are processed into thin films and studied via electrochemical methods.

Chapter 2 encompasses a literature-based perspective on how the presence and identity of a modulator will impact the final size of a MOF nanoparticle. MOF nanoparticles can be synthesized via several top-down and bottom-up approaches. One of the most prevalent bottom-up methods is to use "modulators," molecules added to the growth medium to change the reaction conditions and therefore the crystals' growth. Most often, modulators are monotopic ligands and are employed as the acidic form of their conjugate acid/base pair.[4] The modulator method has facilitated the development of many carboxylate, imidazolate, and azolate

MOF nanocrystals.[6] While it is not often clear how modulators affect crystal growth, there are several in-situ reports that shed light on nanoMOF growth mechanisms for some species. Rather than relying on complex in-situ analysis for each individual synthesis, the "Seeesaw model" uses a system of coupled equilibria to help the chemist intuit whether adding a certain modulator to their reaction will result in an increase or a decrease in particle size.

In chapter 3, syntheses of prototypical MOF nanoparticles are explored to support the Seesaw model. One classic example of a modulated nanocrystal synthesis is that of of $Zn(2\text{-mIm})_2$ (ZIF-8), which simply uses excess of the MOF's linker (2-methylimidazole) to achieve smaller crystal sizes.[7] An equilibrium model was proposed by Cravillon et al in 2009 to explain the effect of excess ligand.[8] In-situ studies using SAXS found that small amorphous particles are formed prior to crystallization.[9] Ex-situ studies by ESI-MS and PDF analysis additionally show many small clusters in the reaction solutions.[10] The example of ZIF-8 nanoparticles shows that, whereas simple equilibrium models can aid in our understanding of synthetic conditions that yield nanoparticles, their growth mechanisms are complicated and individual, requiring advanced analysis to elucidate. The size control of ZIF-8 is used as an example in this chapter to show how the system of equilibria can be de-coupled in certain situations. In the case of the carboxylic acid MOF Cu_3BTC_2 (HKUST-1), there are a handful of existing modulated syntheses. Basic modulators such as sodium formate and trimethylamine have been shown to decrease particle size, while acidic modulators such as dodecanoic acid increase particle size.[11;12] By using a mixture of an conjugate acid/base pair, we show that not only can both of these seemingly conflicting trends can be observed by changing a single variable, but that both

modulator equivalents and proton activity play a role in determining final particle size (Fig. 1.1).

With evidence that the Seesaw model can be used to predict MOF particle size trends in modulated syntheses, chapter 4 moves forward to develop a novel class of nanoMOFs. In the realm of redox-active metal-organic frameworks, there are only limited synthetic studies in which crystal size is controlled. Despite this, evidence suggests that crystal size and shape influence the bulk electronic properties of MOF materials. For instance, the electronic conductivity of $Cu_3(HHTP)_2$ and $Ni_3(HITP)_2$ was first discussed as being dependent on crystal size and shape in 2019 (HHTP = 2,3,6,7,10,11-hexahydroxytriphenylene; HITP = 2,3,6,7,10,11-hexaiminotriphenylene).[13] A single rod-shaped crystal of $Ni_3(HITP)_2$ shows metallic behavior, while a polycrystalline pellet shows semiconducting behavior. This experiment confirmed computational results that implied the material is metallic.[14] A variety of defects, including grain boundaries, in the polycrystalline material create a band-gap that is not present in the single crystal. Additionally, measurements of rods and exfoliated flakes of $Cu_3(HHTP)_2$ show that both in-plane and out-of-plane conductivity are of a similar order of magnitude, indicating that charge carriers flow through the 2D sheets in addition to hopping between them. In a separate study, the conductivity of single crystals of $Ni_3(HHTP)_2$ show an increase of two orders of magnitude over polycrystalline $Ni_3(HHTP)_2$.[13] Only two other studies delve into the morphology control of conductive MOFs, in which $Cu_3(HHTP)_2$ is modulated with pyridine, ammonia, and DMF.[15;16] Most studies are limited to top-down methods, by which a variety of thin film materials have been made.[17;18] Generally, the perception of the utility of conductive MOFs has been dependent upon the difficulty of single

crystal synthesis. This roadblock, however, appeared as an opportunity to create a novel class of semiconductor nanocrystals that exhibit permanent porosity. The conductive MOF Fe(1,2,3-triazolate)$_2$ was first reported in 2012.[19] Since then, the bulk material has been studied for its redox-hopping conductivity that is dependent upon the mixed valency of $Fe^{2+/3+}$ centers, as well as its spin-crossover behavior.[20;21] This material was identified as a promising nanoMOF candidate since it is one of few 3-D connected conductive MOFs and the synthesis of the material is relatively simple and results in a phase-pure product (Fig. 1.1). Finally, in chapter 5, the redox chemistry of iron triazolate nanoparticles is studied in-depth, showing how particle size can be used as a tool to tune redox activity. This work shows that, to consider using conductive MOFs in real-world technological applications, processability, particle size, and thin film thickness are important practical considerations.

In this thesis, the development of the Seesaw model led to the synthesis of a novel family of nanoMOFs that show size-dependent optical and electronic properties. The materials Fe(1,2,3-triazolate)$_2$, Co(1,2,3-triazolate)$_2$, and Cd(1,2,3-triazolate)$_2$ were synthesized as nanoparticles of different sizes for the first time. It was found that Fe(TA)$_2$'s optical absorption, thin film conductivity and redox properties depend on particle size.

CHAPTER II

SIZE CONTROL OVER MOF NANOPARTICLES

This chapter includes an excerpt from previously published and co-authored material from Marshall, C.R.; Staudhammer, S.A.; Brozek, C.K. Size control over metal–organic framework porous nanocrystals. *Chem. Sci.* **2019**, 10, 9396-9408. This work was conceptualized and developed by Checkers R. Marshall and Carl K. Brozek. The perspective was written by Checkers Marshall, with data collection assistance from Sara Staudhammer and with editorial assistance from Professor Carl K. Brozek.

Nanocrystals are distinguished from their bulk counterparts by the extreme size-dependence of their functional properties. For example, catalytic activities of metal nanoparticles,[22] nanocrystal plasmon resonance energies,[23;24] and quantum dot absorption and emission profiles in photovoltaic, solar fuel, and luminescence technologies[25;26] reflect underlying electronic structures sensitive to sub-nanometer size variations. Tailoring nanocrystals to a given application therefore relies on generating particles with precise diameter values and uniform size distributions. Since the advent of reliable synthetic methods, inorganic nanocrystals of metals[27] and semiconductors[28;29;30] have found widespread use as advanced materials in diverse areas, whereas design principles for organic-inorganic hybrid nanomaterials are just emerging.

Recently, considerable efforts have focused on exploring the nanoscale synthesis of metal-organic frameworks (nano-MOFs) due to the promise of their heightened performance in drug delivery,[31;32;33] catalysis,[34] membrane design for gas storage and separation,[35;36;37] and analyte sensing.[38] As 3D porous coordination polymers comprised of inorganic clusters bridged by multi-topic

organic linkers, MOFs display immense modularity that has given rise to more than 20,000 unique bulk phases,[39] each with the potential to adopt enhanced functionalities when prepared as nanocrystals.[40] To advance this research frontier, we must identify synthetic targets and universal mechanistic principles. Building on the publication of recent reviews[41;42;43;44] and rigorous mechanistic studies,[9;45;46;47;48] we identified key open questions: Which MOFs have been prepared as nanocrystals? Which sizes are achievable? And Which mechanistic parameters govern nano-MOF sizes? Here, we address these outstanding questions by compiling experimental parameters and particle sizes from across the nano-MOF literature; statistically treating reported size data (see Methods section below); comparing nano-MOF sizes, size-measurement techniques, and synthetic conditions; and identifying underlying chemical principles from observed trends. Whereas recent reviews[49;1;41;50] have compared the impacts of varying synthetic techniques, such as microwave versus solvothermal, and conditions, such as time and temperature, we target the generalized chemical equilibria and kinetic pathways universal to nano-MOF syntheses.

NanoMOF Metadata

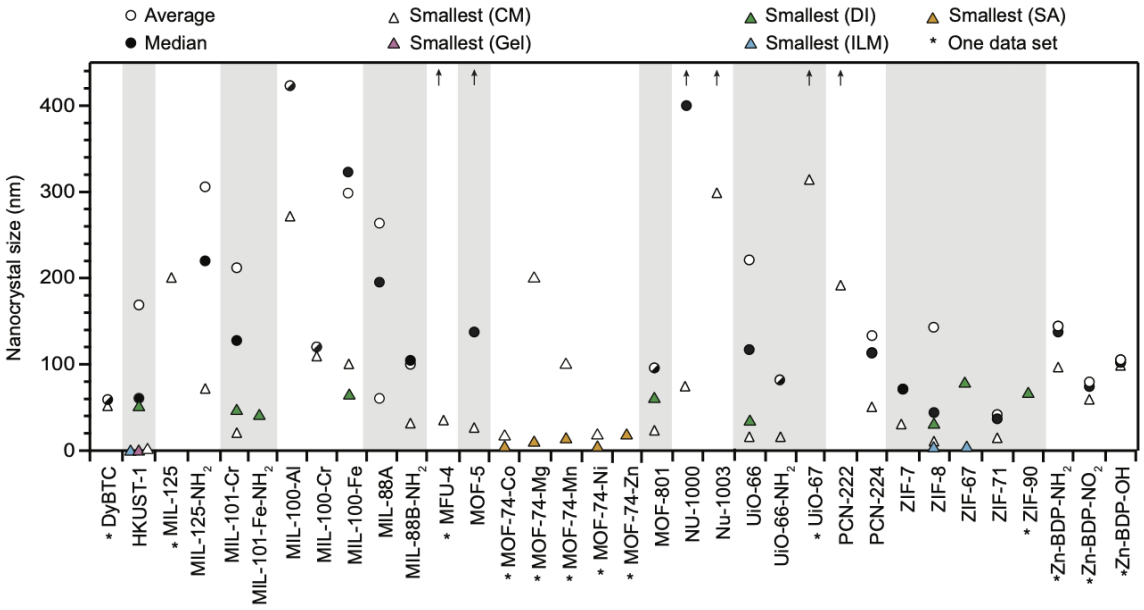

Figure 2.1. Summary of all MOF materials reported to-date as nanocrystals with precisely measured particle diameters. Average and median sizes are included using all reported literature values for each MOF material. Smallest known sizes for each MOF are labelled according to the corresponding synthetic method, i.e., coordination modulation (CM), metal-organic gel (gel), slow addition (SA), and ionic liquid microemulsions (ILM). See methods section for details of data treatment. All tabulated values are included in Table A.1.

Figure 2.1 summarizes all nano-MOFs we identified with quantifiable size diameters, plotted by average, median, and smallest sizes (listed in Table A.1), and in Table 2.1 with MOF compositions and experimental details. These data indicate that while many MOF materials have been accessed as nanocrystals, the vast majority have not. Furthermore, Fig. 2.1 suggests that typical nano-MOF sizes exist on the 100 nm scale, with few extending below 20 nm, in contrast to the 1–10 nm diameters achievable for inorganic nanocrystals.[28] For most MOF materials, select studies have achieved sub-100 nm diameters, but these cases are exceptions, as size averages and median values are far larger. For each class of MOF materials displayed in Fig. 2.1, the smallest size provides the current state-

of-the-art in minimizing nanocrystal sizes, median values indicate the most likely achievable sizes when using the coordination modulation synthetic method, and average values lend insight into the distribution of reported values for each given class of MOF nanocrystals.

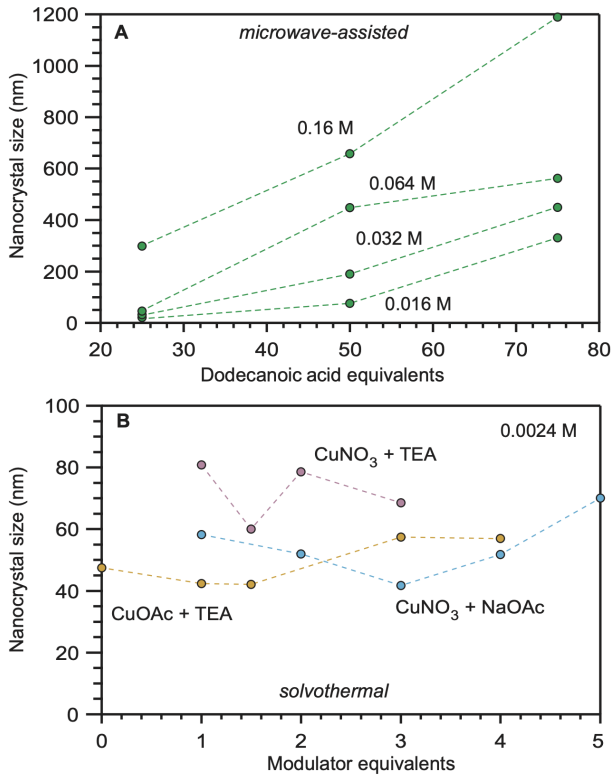

Figure 2.2. Size comparisons of HKUST-1 nanocrystals prepared by (A) microwave-assisted growth at varying reactant concentrations and added equivalents of dodecanoic acid and (B) by solvothermal synthesis at a fixed reactant concentration of 0.0024 M and varying equivalents of triethylamine (TEA) or acetate (OAc) modulators.[51;52;53] The nanocrystal sizes in these studies were determined by TEM (A) and PXRD (B).

Interestingly, compiling size data for a given MOF revealed that often the most impactful size determinants were those that changed between separate synthetic investigations, rather than the parameters systematically explored within isolated studies. For example, Figure 2.2 shows a portion of data compiled

for nanoscale HKUST-1 ($Cu_3(BTC)_2(H_2O)_3$). Clearly, the differing reaction conditions between the results in panel a versus panel b had a greater impact on the nanocrystal sizes compared to the minor impact of copper salt and added base identities shown in panel b. Either the differing reactant concentrations (2.34 mmol versus 0.17 mmol), solvent conditions (DMF/H_2O/EtOH versus butanol), or solvothermal versus microwave synthetic routes involved distinct processes that produced stark size differences. In response to such cases, we focus our mechanistic analysis on reports that employed "coordination modulators"—typically monotopic acid ligands—as these represent the bulk of literature examples, although small particles of MOFs have been generated by many other techniques, such as preparation via microemulsions,[54;55] dual injection,[52] and metal organic gels.[56]

Reliable preparation of small nano-MOF particles depends on a firm mechanistic understanding of nano-MOF initiation, growth, and termination. Typically, nano-MOF syntheses are discussed[43;45;57;50] in terms of the LaMer model of particle growth,[58] which separates crystal nucleation from growth, and describes both in terms of thermodynamic driving forces triggered by high precursor concentrations. In-situ data suggest that MOF-5 ($Zn_4O(BDC)_3$) may follow this model, as nucleation and growth appear to be effectively separated.[45] However, systems such as HKUST-1 and ZIF-8 ($Zn(Hmim)_2$) behave differently, exhibiting slow nucleation phases that overlap with growth.[59;60] A collection of in-situ XRD studies of MOF crystal formation revealed no significant difference in the time scales between nucleation and growth phases, implying that both processes can occur simultaneously.[61] Furthermore, the majority of nano-MOF syntheses occur under dilute conditions (Table A.2).

We argue, therefore, that while thermodynamics remain central to understanding MOF crystal nucleation and growth, nano-MOF sizes are kinetically controlled by chemical parameters that arrest particle growth. In particular, the critical conditions for ensuring small nano-MOF sizes involve depleting the local concentrations of reactant metal ions, thereby allowing linkers and monotopic modulators to trap nano-MOF particles. Analysis of the literature reveals that ideal conditions involve excess ligand (linker or modulator), dilute reactant concentrations, strong metal-ligand bonds, and low proton activities. In this perspective, we support this kinetic model with literature examples that illustrate the role performed by each parameter and apply this insight to rationalizing previously unexplained phenomena.

Table 2.1. A guide to MOF names, their component linkers and metals, and modulators that have been shown to access nanoscale particle size.

MOF Names	Linker	Metal Source	Effective Modulators
COMOC-4, MOF-253	2,2'-bipyrimidine-5,5'-dicarboxylic acid	$GaNO_3$ * H_2O	none [62]
DUT-23	4,4,4"-benzene-1,3,5-triyl-tribenzoic acid, 4-4'-bipyrimidine	$CuNO_3$ * H_2O	none [63]
DyBTC	1,3,5-benzenetricarboxylic acid	$DyNO_3$ * H_2O	acetic acid sodium acetate [64]
Fe-soc-MOF	3,3',5,5'-azobenzenetetra-carboxylic acid	$Fe(NO_3)_3$ * $9H_2O$	sorbitan trioleate (tween-85) [65]
HKUST-1, Cu-BTC	1,3,5-benzenetricarboxylic acid	$Cu(NO_3)_2$ or $Cu(Oac)_2$	dodecanoic acid [51] acetic acid sodium acetate [64] w/ triethylamine [53] 2-methylimidazole [66] PAA [67]
IR-MOF-3	2-aminoterepthalic acid	$Zn(NO_3)_2$	PVP [67] PVP + TMAB [68]
MFU-4	1H,5H-benzo(1,2-d:4,5-d')bistriazole	$ZnCl_2$	lutidene [69] NaOH, KOH [33]
MIL-88A	fumaric acid	$FeCl_3$ * $6H_2O$	NaOH [70] NaOH, acetic acid [71]
MIL-88-Fe	1,4-benzenedicarboxylic acid	$FeCl_3$ * $6H_2O$	acetic acid [72]
MIL-88B-NH_2	1,4-benzenedicarboxylic acid	$FeCl_3$ * $6H_2O$	acetic acid, F127 [73]

MOF Names	Linker	Metal Source	Effective Modulators
MIL-96	1,3,5-benzenetricarboxylic acid	$Al(NO_3)_3$	trimethyl-1,3,5-benzenetricarboxylate [74]
MIL-100-Al	1,3,5-benzenetricarboxylic acid	$Al(NO_3)_3$	benzoic acid, trimethyltrimesate [75]
MIL-100-Cr	1,3,5-benzenetricarboxylic acid	$Cr(NO_3)_3$	none [76;75]
MIL-100-Fe	1,3,5-benzenetricarboxylic acid	$FeCl_3$	none [75]
MIL-101	1,4-benzenedicarboxylic acid	$Cr(NO_3)_3$	none, stearic acid, 4-methoxybenzoic acid, benzoic acid, 4-nitrobenzoic acid, perfluorobenzoic acid [77] acetic acid [78] benzoic acid, HF, TMAOH, sodium hydroxide [79] benzoic acid [80] (Fe) 2-methylimidazole [81]
MIL-125	1,4-benzenedicarboxylic acid	$Ti(OCH(CH_3)_2)_4$	poly(ethylene glycol) diglycidyl ether [82]
MIL-125-NH_2	2-aminoterephthalic acid	$Ti(OCH(CH_3)_2)_4$	benzoic acid p-toluylic acid none [83]
MOF-5 / IR-MOF-1	1,4-benzenedicarboxylic acid	$Zn(NO_3)_2$	Acetate (counterion) [64] decylbenzoic acid [84] TEA [85] TEA+PVP [86] TEA+CTAB [87] p-perfluoromethyl-benzenecarboxylate [45]
MOF-74, CPO-27	1,4-benzenedicarboxylic acid	$Cu(NO_3)_2$, $Ni(NO_3)_2$	benzoic acid, acetic acid [88] 2-methylimidazole [81]
NU-1000	(1,3,6,8-tetrakis(p-benzoic acid)pyrene	$ZrOCl_2$	benzoic acid + trifluoroacetic acid [89] biphenyl-4-carboxylic acid [90] acetic acid [91]
NU-1003	1,3,6,8-Tetra(6-carboxynaphthalen-2-yl)pyrene	$ZrOCl_2$	benzoic acid + trifluoroacetic acid [83]
PCN-222, MOF-525	tetrakis(4-carboxyphenyl)porphyrin	$ZrOCl_2$	benzoic acid, [89] dichloroacetic acid [91]
PCN-224	tetrakis(4-carboxyphenyl)porphyrin	$ZrOCl_2$	benzoic acid [92;57]
UiO-66	1,4-benzenedicarboxylic acid	$ZrOCl_2$	trifluoroacetic acid, dichloroacetic acid, acetic acid, formic acid [93]
UiO-68	Biphenyl-4,40-dicarboxylic acid (BPDC)	$ZrOCl_2$	Benzoic acid, acetic acid [94]
ZIF-7	benzimidazole	$Zn(NO_3)_2 * 6H_2O$	Polyethyleneimine [95]
ZIF-71	4,5,-dichloroimidazole	$Zn(NO_3)_2 * 6H_2O$	n-butylamine + 1-mIm [96]
ZIF-8	2-methylimidazole	$Zn(NO_3)_2 * 6H_2O$	Excess linker [8] n-butylamine [59]

MOF Names	Linker	Metal Source	Effective Modulators
Zn-BDP	1,4-Bis(1H-pyrazol-4-yl)benzene	$Zn(OAc)_2$ * $2H_2O$	None [97]

Factors Controlling MOF Nanocrystal Sizes

We propose that the kinetic trapping of MOF nanocrystals of particular sizes depends on the competition between four chemical equilibria (Figure 2.3): 1) linker deprotonation; 2) modulator deprotonation; 3) linker complexation, and 4) termination. Equilibria with fast forward-direction rates and low reversibility dictate whether MOF particles steadily grow toward bulk phases or arrest quickly to form small nanocrystals. MOF linkers must deprotonate (Eq. 1) before forming metal-linker bonds. Modulators are usually acids, and so must also be deprotonated (Eq. 2). Complexation between metal ions and linkers facilitates particle growth (Eq. 3). Reports suggest that early in MOF growth, large collections of molecular complexes and oligomers develop in solution before coalescing into MOF particles.[10] Subsequent MOF growth is then dominated by the arrival of oligomer clusters or solvated reactant molecules.[98] During the final termination step (Eq. 4), linker and modulator ligands compete for metal ion coordination sites.

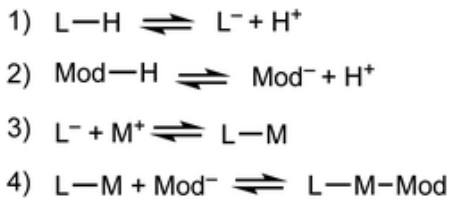

Figure 2.3. Key chemical equilibria controlling nano-MOF growth and termination.

According to our kinetic model, this process continues until the local concentration of ligands far exceeds the metal ions, thereby arresting particle growth. In addition to these four chemical processes, the assembly of cluster nodes

and solvent decomposition have also been invoked to discuss nano-MOF nucleation and growth,[99] but we focus on the most general processes that dominate particle trapping. Critical analysis of nano-MOF sizes and synthetic conditions reveal the existence of key parameters that may be programmed to deplete local concentrations of metal ions and generate small particle sizes: modulator identity and concentration, equivalents of linker or modulator, and metal–ligand bond strengths.

Modulators. Modulators are typically monotopic carboxylic acids and occasionally Brønsted bases added to nano-MOF syntheses. The intended purpose of modulators varies, but we propose that their function is to influence nano-MOF sizes by affecting linker deprotonation and arresting particle growth.[51] Modulators also act to prevent particle aggregation. Although modulators produce size trends that appear complex and contradictory, their role can be rationalized in terms of the four equilibria outlined above. When strong Brønsted bases are used as modulators, their primary role is to facilitate ligand deprotonation (Eq. 1) and enhance metal-linker complexation (Eq. 3) relative to metal-ion diffusion, thereby depleting local metal ion concentrations and forming small MOF nanocrystals. For example, nanocrystals of MFU-4 ($Zn_5Cl_4(BBTA)_3$) decrease in size with added lutidine or KOH.[69] Similarly, when nanocrystals of NU-1000 ($Zr_6(\mu3\text{–}OH)_8(OH)_8(TBAPy)_2$) are prepared with the addition of 4-biphenyl-carboxylic acid, particle sizes decrease further if NaOH is added to the precursor linker solution.[90] and IR-MOF-3 ($Zn_4O(TPDC)_3$) require triethylamine (TEA), which become more uniform with initial addition of cetyltrimethylammonium bromide (CTAB).[87] Similarly, including n-butylamine decreases nanocrystal sizes of ZIF-71 ($Zn(Hdcim)_2$).[10] Interestingly, nanoparticles of MIL-101(Cr)

($Cr_3(H_2O)_2O[(C_6H_3)(CO_2)_3]_2$) are synthesized without any modulator by simply decreasing the amount of HF, which is used as a mineralizing agent in the traditional bulk synthesis.[100;80;78] Adding a strong base to the reaction mixture, however, results in smaller particle sizes.[79]

When carboxylic acids serve as modulators, their presence can increase or decrease nano-MOF sizes depending on whether they impede linker deprotonation (Eq. 1) or act as surface capping ligands (Eq. 4). By interfering with deprotonation, they slow down metal-linker complexation (Eq. 3) relative to metal-ion diffusion, resulting in large nano-MOF sizes. On the other hand, they can terminate particle growth by acting as surface-capping ligands and produce small sizes. For example, Figure 2.4a shows that while adding 0.33 equivalents of perfluorobenzoic acid generates larger MIL-101 particles relative to using no HF or modulator, the addition of more weakly acidic 4-nitrobenzoic acid, benzoic acid, 4-methoxybenzoic acid, and stearic acid decreases particle sizes with increasing modulator pKa values.[101] The less acidic the modulator, the lower the H^+ activity in solution available to protonate linker molecules (Eq. 1).

Adding small quantities of acidic modulators decreases nano-MOF sizes until the H^+ activity in solution reaches a threshold value that begins to interfere with linker deprotonation (Eq. 1). Further addition of acid slows metal-ligand complexation relative to metal-ion diffusion, leading to large particle sizes. For example, Figure 2.4b serves as a useful comparison to the data in Figure 2.4a. Both studies were conducted at similar concentrations (0.076 M versus 0.033 M) and both involve similarly strong metal-ligand bond strengths (Zr^{4+}-carboxylate and Cr^{3+}-carboxylate) but whereas 0.33 modulator equivalents were employed in Figure 2.4a, much higher quantities were involved in Figure 2.4b. The data show

that UiO-66 ($Zr_6O_6(BDC)_6$) nanocrystal sizes increase with additional modulator. Interestingly, modulators with lower pKa values produce larger particle sizes at a given amount of added modulator. For instance, 15-20 equivalents of trifluoroacetic acid (TFA) or dichloroacetic acid (DCA) produce 200-nm UiO-66 nanocrystal sizes, whereas twice that amount of acetic and formic acid are needed. Acidic modulators hinder metal-ligand complexation (Eq. 3) relative to metal-ion diffusion so that particles continue to grow. Indeed, adding thousands of equivalents of formic acid to the synthesis of UiO-66 generates single crystals hundreds of microns in diameter.[102] This kinetic explanation fits many other studies in which particle sizes increase with additional acidic modulator,[51;103;94;104] including HKUST-1 modulated by dodecanoic acid,[51] PCN-224 (Zr-TCPP) with benzoic acid,[103] UiO-66 with benzoic acid[94] and MIL-88B-NH_2 ($[Fe_3O(BDC\text{-}NH_2)_3(H_2O)_2$) with acetic acid.[104]

Concentrated reaction conditions necessitate the addition of modulator; otherwise, rapid metal-ion diffusion due to short effective pathlengths outcompetes growth termination (Eq. 4). Indeed, most nanoscale MOF syntheses rely on dilute conditions (Table A.2). For example, synthesis of MIL-101-Cr involving high concentrations (0.2 M H_2BDC) produces small particle sizes only with addition of small quantities of benzoic acid (Fig 2.3c).[80] Benzoic acid has a greater effect than acetic acid on decreasing particle sizes at such high reactant concentrations, suggesting that under these reaction conditions, interfering with metal-ligand complexation is critical to kinetically trapping small MIL-101-Cr nanocrystals.

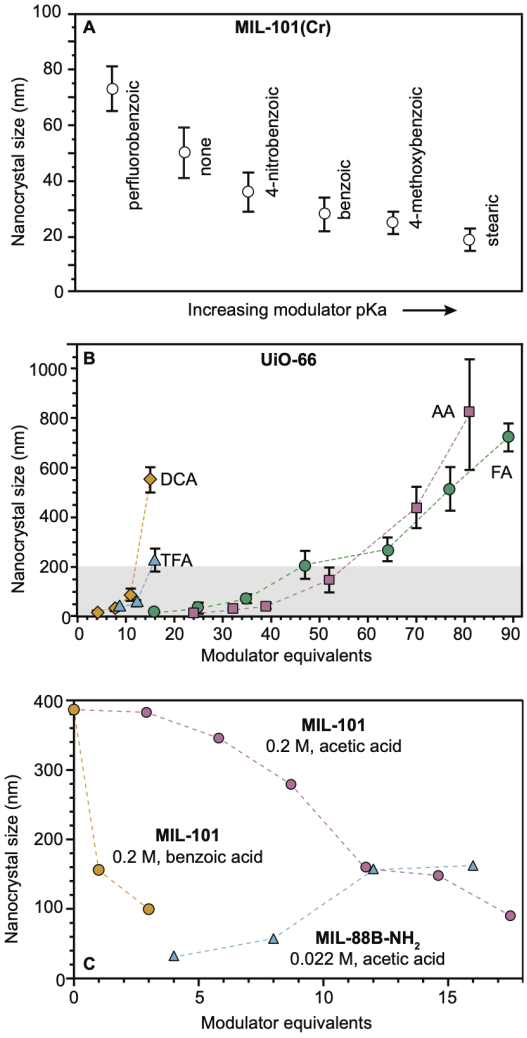

Figure 2.4. Nanoscale MOF sizes depend on the equivalents and pKa values of added modulator reagents. (A) MIL-101(Cr) nanocrystal sizes decrease with increasing modulator pKa values. Sizes were determined by TEM.[101] (B) As modulator equivalents increases, sizes of UiO-66 particles increase. (TFA: trifluoroacetic acid, DCA: dichloroacetic acid, FA: formic acid, and AA: acetic acid). Shaded box provided to emphasize sizes below 200 nm. Sizes were determined with STEM and DLS (DLS not shown).[105] (C) MIL-101-Cr nanocrystal sizes decrease with increased modulator equivalents, while MIL-88B-NH_2-Fe exhibits the opposite trend. Interestingly, MIL-88B microcrystals are formed as an impurity at and above 5 benzoic acid equivalents (orange). Sizes were determined with SEM (orange and pink) and TEM (blue).[80;78;106]

Phase purity must be considered when choosing modulator equivalents and reaction concentrations. For example, while adding few equivalents of either acetic or benzoic acid in the synthesis of MIL-101 at high concentrations results in phase-pure MIL-101 nanocrystals, greater equivalents induce the formation of mixed-phase products[107] because MIL-101 and MIL-88B occupy the same reaction space, with both arising from Fe^{3+} or Cr^{3+} and trimesic acid.[108] Therefore, at a benzoic acid : linker ratio of 10 : 1, only MIL-88B microcrystals form.[79] Concentration plays an important role in controlling nanocrystal phase purity as well. For example, MIL-101-Cr and MIL-88B-Fe nanocrystals have been obtained with similar equivalents of acetic acid, but the synthesis of MIL-88B-Fe was an order of magnitude more dilute (Fig. 2.4c). Such phase transformations with variable modulator equivalents indicate the importance of nonclassical growth mechanisms.[61] Similar phenomena have been observed for the phases spaces involving MIL-100-Al ($Al_3{\times}(H_2O)_{20}(BTC)_2$) / MIL-96-Al ($Al_{12}O$-$(OH)_{16}(H_2O)_5(BTC)_6$ MIL-110-Al ($Al_8(OH)_{12}(OH)_3(H_2O)_3(BTC)_3$) and NU-901 ($Zr_6(\mu 3\text{-}OH)_8(OH)_8(TBAPy)_2$) / NU-1000.[90;109;110]

Linker Equivalents. Excess linker equivalents shift equilibria toward enhanced metal-ligand complexation (Eq. 3), thereby depleting local metal ion concentrations[51] and arresting particle growth without added modulator (Eq. 4). In other words, excess linkers serve as surface-capping ligands. The excess linker method was first reported in 2009 for ZIF-8 and has since been used in further ZIF-8 and ZIF-71 nanocrystal syntheses (Fig. 2.4).[8;10;59] Nano-MOF particle sizes can be further reduced by adding Brønsted bases to enhance linker deprotonation (Eq. 1).[8] Irreversible ligand deprotonation may lead, however, to unchecked particle growth through rapid metal-ligand complexation, unless counterbalanced by excess

surface-capping ligands—illustrating the intricate kinetic balance of the four key underlying processes outlined in Eq. 1–4.

Although several chemical parameters may contribute to decreased nano-MOF sizes, the impact of certain factors may dominate over others. For example, linker excess was discovered to be the single strongest size determinant of ZIF-8 nanocrystals through systematic investigations into the role of Brønsted base, linker excess, and reactant concentrations (Fig. 2.5a,b).[8] Nanocrystals of ZIF-8 can be synthesized using an excess of the linker 2-methylimidazole (2-mIm),[8] whereas typical bulk syntheses of ZIF-8 combine the zinc salt and imidazole linker in a 1:1 - 1:2 ratio.[111] Simply increasing the metal-to-linker ratio to 1:5 results in nanocrystals sizes of 40 nm (Fig. 2.5a).[8] Reactant concentration was also studied as a size determinant, with the data in Figure 2.5a showing that more dilute systems lead to smaller ZIF-8 crystal sizes. In terms of our kinetic model, the role of dilution is to increase metal-ion diffusion pathlengths, allowing particles to be terminated in isolation from additional metal ions. The impact of added base was also investigated, but only the basic modulator n-butylamine resulted in reduced nanocrystal sizes, whereas less basic 1-methylimidazole and sodium formate resulted in micrometre-sized crystals.[59] Nevertheless, compared to the impact of dilution (Fig. 2.5a) and Brønsted base, the most significant decreases in ZIF-8 sizes were achieved by linker excess (Fig. 2.5b). These systematic comparisons suggest that growth termination is more important than linker deprotonation in controlling ZIF-8 nanocrystal sizes.

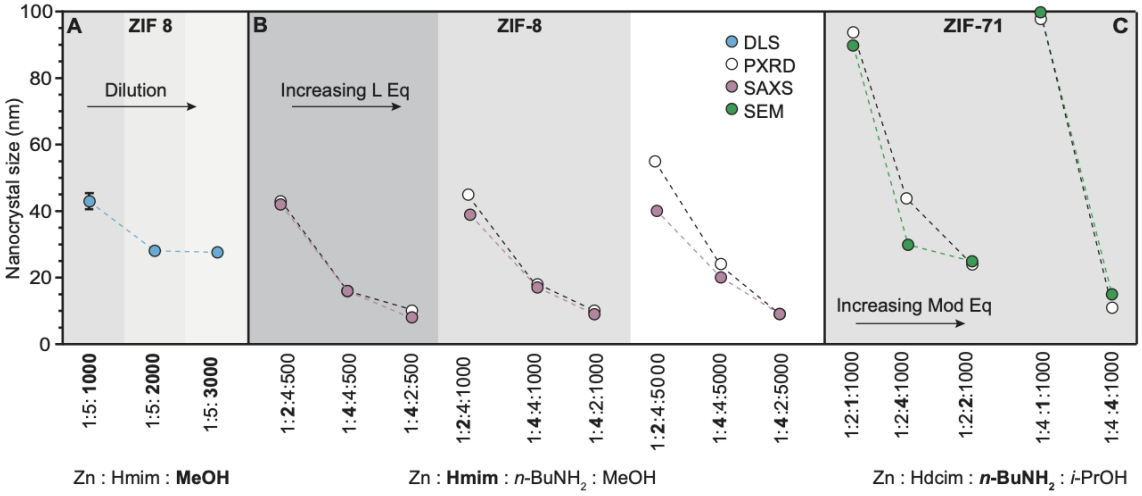

Figure 2.5. ZIF nanocrystal syntheses with varying relative ratios of metal, linker, modulator, and solvent. Synthetic variables are in bold. (Hmim: 2-methylimidazole, Hdcim: 4,5-dichloroimidazole). (A) Dilution results in a series of ZIF-8 nanocrystals sizes.[8] (B) Excess linker exerts a stronger influence than base on nanocrystal sizes.[59] (C) Addition of n-butylamine rather than linker excess exhibits biggest impact on ZIF-71 sizes.[10]

If linker deprotonation limits nanocrystal formation kinetics, however, addition of Brønsted base will produce a greater effect than the equivalents of excess linker. For example, systematic studies of ZIF-71 nanocrystal synthesis indicate that in contrast to ZIF-8, the most influential variable is n-butylamine equivalents (Fig. 2.5c).[10] When the linker-to-metal ratio is doubled from two to four with base and concentration held constant, particle sizes remain around 80-100 nm. Increasing the proportion of base, however, reduces particle sizes to approximately 20 nm. The sensitivity of ZIF-71 nanocrystal sizes to the equivalents of added base results from the less acidic 4,5-dichloroimidazole linker.

Interestingly, rather than follow this excess linker strategy, most reported nano-MOF syntheses rely on the same linker equivalents used in bulk syntheses (Table A.2). On the other hand, select studies have shown that excess linker was ineffective in generating nanoscale particles. Excess trimesic acid does not produce

HKUST-1 nanocrystals, for instance.[60] Although excess linker reduces the sizes of UiO-66 particles, higher water content exerted the greatest size control, perhaps due to its role in assembling the Zr^{4+}-oxo cluster nodes.[112]

Metal-Linker Binding Strength. Strong metal-ligand interactions favour small particle size because they enhance rates of both complexation (Eq. 3) and termination (Eq. 4) during nano-MOF growth, thereby depleting the local concentrations of metal ions relative to linkers or modulators. Systematic studies varying the metal identities of heterobimetallic materials illustrates the influence of metal-ligand interactions on nanocrystal size. For example, higher Co^{2+} contents in Zn^{2+}-based ZIF-8 nanocrystals results in larger nanocrystals (Fig. 2.6).[113] Using Cu^{2+} further accentuates this effect, with comparatively larger sizes produced at identical dopant metal concentrations.[114] Because linker-to-metal ratios remained

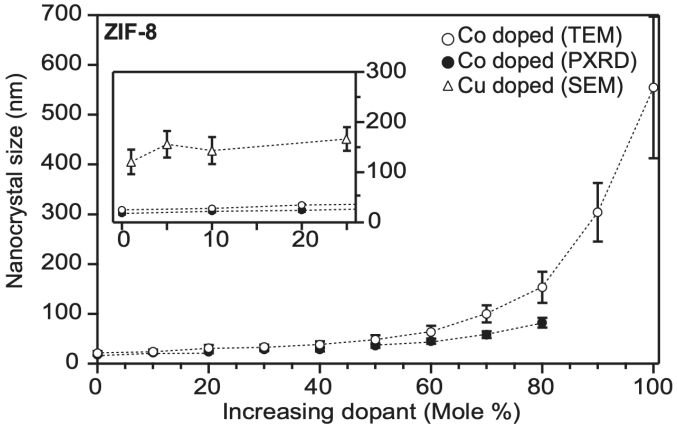

Figure 2.6. Heterobimetallic ZIF-8 nanocrystals increase in size as the Zn^{2+} atoms are substituted for Co^{2+} or Cu^{2+} atoms. Insert: highlighted data at low equivalents, where identical Co^{2+} and Cu^{2+} quantities produce different particle sizes. Particle sizes were determined by TEM (main) and SEM (inset).[113;114]

constant in these experiments, the increase in size with lower Zn^{2+} content can be attributed to the strong Zn^{2+}-imidazolate interactions, which quickly produce small particles unless harder ions such as Cu^{2+} interfere. Similarly, differences in

metal ion labilities were invoked to explain why MOF-74 (M_2(DOBDC)) crystals nucleate and grow faster with Zn^{2+} than with Co^{2+}.[98] Surprisingly, cobalt-doped UiO-66 nanoparticles are smaller in size than their zirconium-only counterparts when synthesized under otherwise identical conditions.[115] As the strength of the zirconium–carboxylate bond is expected to be stronger than cobalt-carboxylate bonds, metal-linker complexation rates may not be the only equilibrium to consider. For instance, weaker bonds might slow particle growth, allowing diffusing linkers trap the cobalt variants at smaller sizes. To date, there have been few studies regarding the effect of mixed metals on MOF nanocrystal size and this area warrants further exploration.

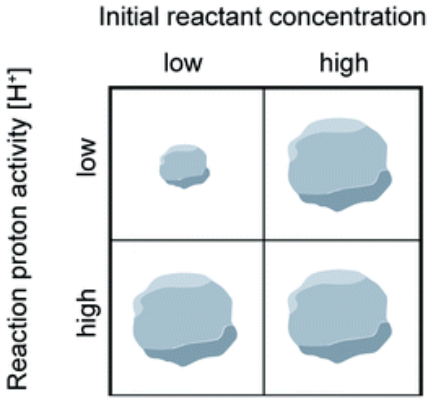

Figure 2.7. Reaction conditions that favor small or large MOF nanocrystal sizes when linker or acidic modulators are present in excess.

Summary. The metal-ligand chemistry outlined in Eq. 1–4 provides a framework for understanding trends in reported nano-MOF sizes. Based on these insights, Figure 2.6 offers a general guide for designing small MOF nanocrystals. Excess linker or acidic modulator generally reduce nanocrystal sizes unless either metal-linker complexation far exceeds termination kinetics or if acid addition inhibits linker deprotonation. Dilute reactant concentrations paired with low proton activities ensure small particle sizes by enhancing complexation (Eq. 3) and

termination (Eq. 4), while isolating particles from diffusing metal ions to prevent runaway growth.

The Seesaw Relationship

Seemingly incompatible trends reported for nano-MOF sizes can be reconciled by viewing nano-MOF growth as a balance between reactant concentration, linker and modulator deprotonation, metal-ligand interactions, and metal-ion diffusion. Figure 2.8a summarizes our model into two regimes. In regime I, small quantities of acidic ligands (either modulators or linkers) decrease particle sizes by supplying surface-capping ligands, overwhelming local metal ion concentrations. Higher quantities of acidic ligands further decrease nanocrystal sizes by increasing the rate of metal-ligand complexation relative to metal-ion diffusion. This trend continues until reaching minimum nanocrystal sizes α at threshold values of added acidic ligand ε (Fig. 2.8a). This critical point corresponds to a minimum of relative ratios between local metal ion-to-ligand concentrations β and ratios of relative rates of diffusion and metal-ligand complexation σ (Fig 2.8a). In Regime II, additional equivalents of acidic ligands raise solution proton activities such that they interfere with linker deprotonation. As a result, nanocrystal sizes increase with additional acidic ligand because metal-ion diffusion rates outcompete particle termination. This "Seesaw" relationship between nano-MOF sizes and relative termination versus diffusion rates strikes a balance precisely where particles sizes are at a minimum.

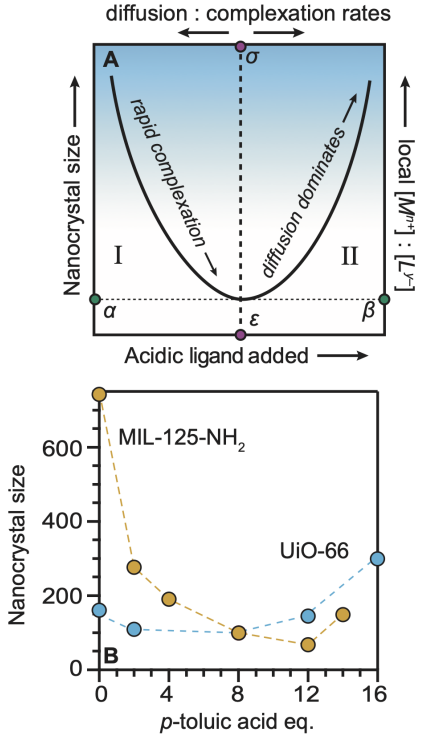

Figure 2.8. The "Seesaw" relationship between nanocrystal sizes and added equivalents of acidic ligands. Nanocrystal sizes increase with higher ratios of metal-to-linker local concentrations (A) particles reach a minimum size α at critical values of acidic ligand ε and minimum relative ratios local metal ion-to-ligand concentrations β and relative ratios diffusion and metal–ligand complexation ratios σ. (B) MIL-125-NH_2 and UiO-66 exhibit the full Seesaw relationship curve in trends between particle sizes and equivalents of p-toluic acid.[116]

Figure 2.8b summarizes data exhibiting a Seesaw curve for NH_2-MIL-125 and UiO-66 sizes with varying quantities of p-toluic acid.[116] For both materials, particle sizes at first decrease, bottom-out at minimum values, and then increase with higher quantities of modulator. Competition between complexation and metal-ion diffusion may explain Seesaw curves in related phenomena, such as the polymorphic balance between MIL-101 and MIL-88B phases achieved by tuning benzoic acid equivalents (Fig 2.4c).[80] Low benzoic acid equivalents produce decreasing sizes of MIL-101 until higher equivalents lead to large micron-sized particles of MIL-88B instead. We propose that most reported trends of nano-

MOF sizes capture just portions of the entire curve of the Seesaw relationship. Type-I behavior, where added acidic ligand decreases particle sizes, is observed for the MIL-101(Cr) and ZIF-8 syntheses discussed above (Fig. 2.4a, 2.5a).[117;78;8] Examples of regime II relationships behavior, where particle size increases with respect to increasing modulator equivalents, have been observed for many MOFs when monocarboxylic acids are added, including reports on UiO-66, HKUST-1, PCN-224, and MIL-88B-NH_2.[51;103;94;104] Based on numerous reports exhibiting regime II behavior, the curvature of the slope region II appears proportional to modulator acidity such that highly acidic ligands produce larger particle sizes at fixed equivalents. The impact of highly acidic modulators is so pronounced that they can halt particle growth entirely, whereas less acidic modulators added in large excess simply promote large particles.

Whether type-I or type-II behaviors emerge for a given MOF material depends on the similarities between the particular complexation, termination, and metal-ion diffusion rates. Although the Seesaw curve involves kinetic trapping, the extreme limit at the far right of the curve involves particles grow over much longer time periods due to sluggish metal–ligand complexation that places MOF crystal growth in an entirely different regime determined by thermodynamics. According to this model, defects incorporated in nano-MOFs must be kinetically trapped, whereas defects in macroscopic MOF single crystals arrive through thermodynamically driven processes. This model helps explains why addition of strong acid helps to produce large single crystals of MOFs.[118]

Best Practices and Outstanding Challenges

Elevating the rigor of MOF nanocrystal synthesis will require addressing critical challenges. Here, we offer recommendations on synthetic, characterization, and data-reporting methods to facilitate future MOF nanocrystal investigations.

Colloidal Stability. Applying MOF nanoparticles in applications such as drug delivery requires that the particles be colloidally stable. A re-dispersed nanoparticle solution may suffer from significant aggregation or coalescence without sufficient surfactant ligand coverage. Measurements of zeta potentials provide useful information on the charge at the nanoparticle surface, such that values far away from zero indicate that a dispersion is stable.[105] DLS (dynamic light scattering) measurements may be used to determine colloidal stability, as it is a solution-phase size measurement method. Aggregating particles observed by DLS display unusually high hydrodynamic radii. Additionally, further growth or aggregation causes the apparent sizes to increase over time.

Incorporation of Modulator. Identifying the presence and location of modulators in nano-MOFs is important in determining whether they serve as surface-capping ligands or form internal defects. Mirkin et al. found that while the colloidal stability of UiO-66 crystals correlated to the identity and amount of modulator, the exact role of modulators at the particles surfaces was unclear.[105] For example, while small equivalents of weakly acidic modulators resulted in aggregation, nanoparticles of UiO-66 have been synthesized without any monocarboxylic acid modulator.[112]

A common method to quantify ligand incorporation in MOFs is to perform acid digestion NMR studies. The linker-to-modulator ratio in the MOF can be elucidated through ^{1}H-NMR peak integration.[119] Defects may also be

identified as a weight percent by thermal gravimetric analysis (TGA).[87;120] The relative incorporation of a modulator depends on its function during synthesis. For instance, in the synthesis of ZIF-8 with n-butylamine, less than 1 percent incorporation is observed by ^{1}H NMR. The absence of incorporated modulator indicates its primary role is to deprotonate the linker, rather than cap particles during termination.[96] When the ratio of modulator is higher than would be expected for surface passivation, it must either be creating defects in the MOF particle, or be present as a guest. For example, a reported synthesis of UiO-66 modulated with benzoic acid revealed an 8:10 benzoic acid-to-linker ratio, even after extensive washing.[94] The amount of modulator incorporated can depend on pH, as one NMR digestion study of UiO-66 showed that acetic acid incorporation first decreased, then increased, with respect to the amount of triethylamine added.[119] The authors speculated that amount of deprotonated MOF linker BDC (benzenedicarboxylate) in the reaction was maximized at the minimum of the acetate incorporation curve. Interestingly, modulator incorporation observed in this study exhibits a U-shaped curve, indicating that modulator defect concentrations can be minimized at a critical amount of added modulator. This U-shape does not correspond to size, however; the size monotonically decreases, indicating the minimum size and minimum defect concentration occur with different quantities of added modulator. Due to the insight obtained from these studies, we recommend acid digestion NMR studies as a standard method to characterize MOF nanoparticles. We expect synthetic methods to advance toward finer levels of control as trends emerge from the impact modulators have on defect incorporation and nanocrystal size.

Measurement Methods. Size analysis of MOF nanocrystals relies on appropriate use of structural characterization methods, as has been discussed in a previous review.[46] Typical techniques include PXRD (powder X-ray diffraction), microscopy, DLS, and SAXS (small angle X-ray scattering). In general, we recommend reporting data from at least two complimentary methods, even when data contradict.

According to the Scherrer relation, the full-width-at-half-max of a given PXRD peak relates to the particle size. Although smaller particles will exhibit broader diffraction peaks in general, peak broadening may result from several factors, such as lattice stress or instrument effects.[121] Several peaks should be modelled to determine reliable size estimates. When considering polyhedral crystals, shape factors should be chosen to match the particle morphology and specific miller index of the peak under consideration.[121] Crystallographic domain, not particle, sizes, are estimated by this method. Aggregated particles comprise of multiple domains, which leads to conflicting data between PXRD and other sizing techniques.[122]

Dynamic light scattering (DLS) overestimates particle sizes because the method determines the hydrodynamic radii of particles. Authors often attribute size overestimates from DLS to aggregation. Recent reports have suggested that MOF porosity may induce unconventional diffusion behaviour, which would hamper analysis by DLS.[112] The interpretation of DLS relies on the assumption that particles are hard spheres that move in solution via Brownian motion.[123] Irregularly shaped particles or porous particles defy these simplified models.[124;125] Several advanced models exist that describe hollow nanoparticles, although these too may be inadequate for describing the complex microporosity of MOF

particles.[126] The key utility of DLS is in developing biological applications of large particles, where it can effectively identify the presence of microscopic aggregates in solution.[127]

Microscopy is the most common method to determine particle sizes. Both SEM (scanning electron microscopy) and TEM (transmission electron microscopy) are widely used, although they rely on high-energy electron beams that can compromise MOF structural integrity.[46] Microscopy finds its greatest advantage in probing particle morphology, although the 2D projections of 3D particle shapes should be considered carefully.[8] Furthermore, analysis must be applied to statistically relevant ensembles of particles. It is essential to report the size of the population used to estimate size and size distributions; these values are often missing in the literature.

SAXS is a less common technique, but it presents several advantages: SAXS measures solution-state samples without overestimating sizes and it examines statistically relevant populations.[59] Accurate analysis relies on choosing appropriate approximations and form factors.[128] Although size and porosity of hollow nanoparticles can be accurately determined by SAXS, nano-MOFs lack a generally accepted model due to their complex topology.[126] The model used, and any other relevant data analysis, should be rigorously reported. In general, critical treatment of particle size data is essential to rigorous investigations into the structure–property relationships of MOF nanocrystals.

Conclusions. MOF nanocrystal sizes and synthetic conditions were critically analysed from across the literature to develop a deeper mechanistic understanding of nanocrystal formation. A general model was presented that reconciles seemingly contradictory trends for MOF nanocrystal sizes versus

common synthetic parameters: excess ligand, additional acid or base, reactant concentrations, and metal ion identities. A universal "Seesaw" relationship is proposed that relates nano-MOF sizes to a competition between particle growth facilitated by diffusing metal ions and particle termination by depleting metal ion local concentrations through rapid ligand complexation. Therefore, conditions that favour high relative concentrations of ligands and that maximize metal-ion diffusion pathlengths produce the smallest nano-MOF sizes. This model also sheds light on the mechanism of MOF crystal growth, in general, and provides a framework for designing macroscopic single crystals. By compiling data for all known MOF nanocrystals, we define the goalposts for future nano-MOF synthetic targets and provide a mechanistic model rooted in chemical parameters that may be tuned to discover the full potential of this emerging class of nanomaterials.

CHAPTER III

EXPERIMENTAL EVIDENCE FOR THE SEESAW MODEL

This chapter includes an excerpt from previously published and co-authored material from Marshall, Timmel, E.T.; C.R.; Staudhammer, S.A.; Brozek, C.K. Experimental evidence for a general model of modulated MOF nanoparticle growth. *Chem. Sci.* **2020**, 11, 11539-11547. This work was conceptualized and developed by Checkers R. Marshall and Carl K. Brozek. The article was written by Checkers Marshall, with experimental and analytical assistance from Emma Timmel and Sara Staudhammer, and with editorial assistance from Professor Carl K. Brozek.

Precise size control can yield distinct functional behavior from materials with seemingly similar compositions. Achieving control at the nanoscale, in particular, has uncovered remarkable size-dependent properties, such as the luminescence of quantum dots and the distinct catalytic activities of metal nanoparticles.[26;22] Recent reports suggest that the rich structural and compositional diversity of bulk metal-organic frameworks (MOFs) produces enhanced functional properties when realized on the nanoscale.[44] For example, advanced MOF-based gas separation technologies use nanoparticulate MOFs (nanoMOFs) dispersed into mixed matrix membranes (MMMs) to achieve enhanced efficiencies over bulk phases. Remarkably, MMMs that employ nanoMOFs have been shown to surpass the Robeson limit—an intrinsic trade-off between selectivity and permeability in separation membranes.[129;130] While the gas separation performance of nanoMOFs has attracted industrial interest, their improved activities as atomically defined catalysts and drug delivery agents has opened emerging areas of research.[131;132;133] Despite advances in nanoMOF applications,

accurate models are still needed to probe fundamental mechanistic details and reliably control particle sizes.

Several models exist to describe nanocrystal nucleation and growth, including the classic LaMer model, the Watzky-Finke model, and various statistical models, yet recent evidence challenges their applicability to MOF growth.[134;135;136] Whereas the LaMer model describes distinct stages of a burst nucleation induced by supersaturated monomer concentrations, followed by diffusion-limited particle growth,[134] nanoMOFs form at dilute concentrations, and in-situ studies reveal continuous nucleation and growth of MOF particles.[59] Models based on monomer addition also do not apply to MOFs, as studies suggest MOF formation involves transiently metastable "primary" phases, aggregative growth, and other non-classical events.[61;9;137;138] Although these existing models can be modified to account for non-classical events, nanoMOF research requires a general model based on the acid-base and coordination chemistry of MOFs to reliably predict and control particle sizes.

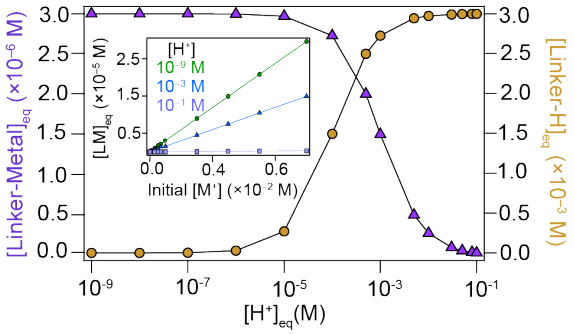

Figure 3.1. Equilibrium concentrations of MOF linker species determined from the coupled equilibria of the Seesaw model. Linker–metal ([LM]) and protonated linker ([LH]) concentrations calculated as a function of initial metal ion ($[M^+]$) and proton ($[H^+]$) concentrations. Inset: [LM] calculated as a function of initial $[M^+]$ for a range of $[H^+]$. Initial concentrations were chosen from typical experimental conditions reported here.

The Seesaw Model and pKa

Previously, we proposed a novel "Seesaw" model of nanoMOF growth based on a metadata analysis of existing literature.[6] This model specifically explained why the use of modulators—typically monotopic analogs of MOF linkers—causes particle sizes to increase in certain cases, but decrease in others. These trends could be explained by modulators functioning as capping ligands at low concentrations and as acids at high concentrations (Figure 3.2, regions I and II, respectively). More broadly, we proposed that MOF nanoparticles result from excess ligand depleting local concentrations of metal ions and kinetically trapping particle growth. Accordingly, the trapping process depends on the competition between coupled equilibria associated with ligand deprotonation and metal-ligand complexation. In the absence of aggregation, crystallite sizes, therefore, minimize when monomer ratios in solution are most "off-stoichiometric" relative to the MOF stoichiometry, which complements established models of bulk polymer and crystal growth that propose the largest particles are generated by solutions with monomer ratios that match the intended material stoichiometry (Figure 3.2a), as discussed below. The curious Seesaw-shaped relationship between particle size and modulator equivalents observed previously for MIL-125-NH_2 and UiO-66 nanoparticles[139] (Figure 3.2b) could be explained as exhibiting both region I and II behavior, where sizes first decrease with additional modulator acting as capping ligand and then increase as acidic modulators keep linkers protonated and unable to kinetically trap particles.

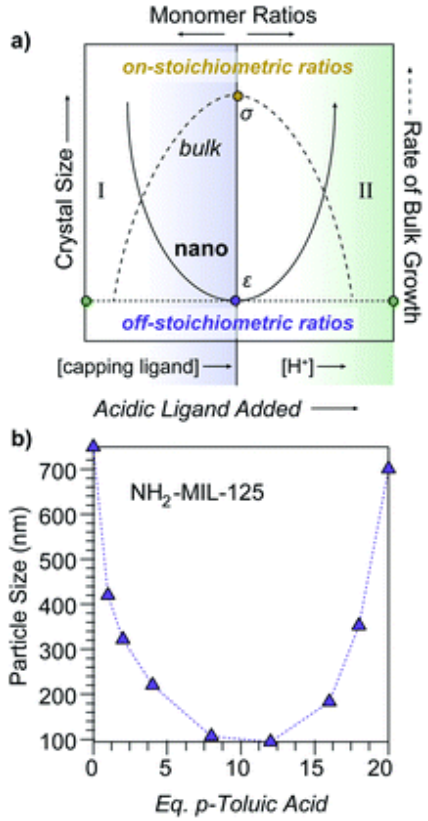

Figure 3.2. Scheme depicting the dependence of particle sizes on metal-to-linker solution stoichiometry. (a) In the proposed Seesaw model of MOF nanocrystal growth (solid line), particle sizes minimize at maximally imbalanced metal-to-linker ratios and at low proton concentrations (ε). The Seesaw arises from acidic ligands acting as capping agents in region I and as acids in region II. Conversely, rates of bulk ionic crystal growth (dashed line) maximizes at monomer solution stoichiometries that match the bulk crystal (σ). (b) Observation of the Seesaw relationship between NH_2-MIL-125 particle sizes and modulator equivalents, reproduced from ref. 115.

Although observed previously for just these materials, we posited that the Seesaw trend could be observed generally for all MOFs through deliberate control over the parameters outlined by the model. Herein, we provide experimental evidence for the Seesaw model by demonstrating that solution acidity, ligand excess, and concentration form independent parameters that can be used to achieve the first demonstration of a Seesaw relationship and reproducibly control

nanoparticle sizes of two iconic MOF materials, $Zn(mIm)_2$ (ZIF-8) and Cu_3BTC_2 (HKUST-1). With the results presented here, the Seesaw trend appears in at least four compositionally distinct MOF systems, suggesting that the mechanistic model outlined here is universal to all modulated MOF syntheses.

ZIF-8 and Cu_2BTC_3 Nanoparticle Syntheses

In chapter 2, the four key equilibria expressions that form the basis of the Seesaw model were presented (Fig. 2.3): linker deprotonation (Eq. 1), modulator deprotonation (Eq. 2), metal-linker complexation (Eq. 3), and metal-modulator complexation (Eq. 4). According to our model, the competition of these coupled reactions creates conditions that either produce bulk or nanocrystalline MOFs. For example, if these coupled equilibria maintain stoichiometric ratios of metal ions and linkers, then the reaction proceeds to form bulk MOF crystals. If, on the other hand, the coupled equilibria cause depletion of local metal ion concentrations, then excess ligand overwhelms particle surfaces, trapping MOFs as nanoparticles. Coupled equilibria can be studied by several mathematical formalisms.[140;141] Herein, we simplify the system of equations using assumptions similar to the well-known Initial-Change-Equilibrium (ICE) table method (Table B.19).

We propose that analysis of these coupled equilibria can be used to predict whether synthetic conditions produce nanoMOFs by 1) knowing equilibrium constants for the metal ions and carboxylic acids, 2) knowing the initial reactant concentrations, and 3) by assuming that nanoparticles arise from reaction conditions that develop excess concentrations of deprotonated linkers $[L^-]_{eq}$ relative to the concentration of uncoordinated metal ions $[M^+]_{eq}$. In other words, reactant concentrations and equilibrium constants could be chosen such that $[L^-]_{eq} + [Mod^-]_{eq} > [M^+]_{eq}$ in the distribution of chemical species at equilibrium.

For simplicity, we treat the MOF linkers as monotopic ligands and consider only individual metal–linker bonds rather than the entire coordination sphere. We also assume K_a of the modulator and MOF linker to be equal, and that the complexation equilibrium constants are equal.

For a fundamental justification of the Seesaw model, namely the U-shaped size trend arising from the dual roles of modulator acting as acid or capping ligand, we solved the system of coupled equilibria in Figure 2.3. Figure 3.1 shows the equilibrium concentration of linker-metal $[LM]_{eq}$ and protonated linker species $[LH]_{eq}$ as a function of $[H^+]$ donated by the linker and modulator under typical reaction concentrations (see Appendix B for full details). When initial concentrations of acid are low, $[LM]_{eq}$ is maximized and $[LH]_{eq}$ is minimized. In other words, reactions with low equivalents of acidic modulator favor linker deprotonation and metal-linker bond formation. Critical concentrations of acid, however, induce steep changes to $[LM]_{eq}$ and $[LH]_{eq}$. At higher $[H^+]$, $[LM]_{eq}$ is minimized and $[LH]_{eq}$ is maximized. The plateau of $[LM]_{eq}$ and $[LH]_{eq}$ spanning four orders of magnitude for low values of $[H^+]$ followed by a steep change supports our model that formation of linker-metal bonds can be favorable even with additional acid, until reaching a critical concentration threshold that causes linkers to remain protonated, thereby suppressing metal-linker bond formation and the trapping of MOF particles. These results therefore justify a key claim of the Seesaw model that acidic reaction conditions produce large particles by favoring linker protonation, which improve the equilibria reversibility and maintains solution stoichiometry required to grow MOF single crystals. Because we expect modulator to decrease metal ion concentrations by forming modulator-metal species (Eq. 4), we also investigated the relationship between $[LM]_{eq}$ and initial $[M^+]$. The

inset of Figure 3.1 shows that $[LM]_{eq}$ depends directly on the available $[M^+]$ in solution, suggesting that equivalents of modulator inhibits bulk MOF growth by modulators competing with linkers for metal ions. Interestingly, the formation of $[LM]_{eq}$ decreases for high initial $[H^+]$, providing further evidence that modulators in large excess function more as acids than as surface capping ligands. Taken together, these results provide a fundamental basis for the key claims of the Seesaw model.

Powerful predictions can be made about the outcome of MOF syntheses by analyzing the system of coupled equilibria in Figure 3.2. The results of the analysis suggest that, as long as the presence of excess deprotonated linker is a key determinant in kinetic trapping, nanoparticles should always result from cases that employ excess linker and no modulator, as well as cases that use deprotonated modulators as Brønsted bases or capping ligands. When modulators function solely as acids, they decrease the availability of L^-, which inhibits the kinetic trapping of nanoMOFs. The outcome depends on the particular equilibrium constants, initial reactant concentrations, and how the reactant concentrations change during MOF synthesis. The most complex scenario, which appears most frequently in the literature, involves modulators functioning as both acids and capping ligands.[4] Nevertheless, nanoMOF sizes should be tunable through careful manipulation of acid and ligand binding strengths if indeed nanoMOF growth depends on these two independent parameters.

With these predictions in hand, we sought experimental evidence for the Seesaw model and the independent tunability of nanoMOF sizes through acid and ligand addition. Figure 3.3a plots nanoparticle sizes of ZIF-8 ($Zn(mIm)_2$, mIm = 2-methylimidazolate) as a function of added HmIm ranging from 4 to 14 equivalents per Zn^{2+}, where conditions above 2 equivalents represent linker in excess. Based on

analysis of the coupled equilibria, addition of only HmIm without modulator should cause the depletion of [M^+], resulting in kinetic trapping of smaller nanoMOF sizes. Indeed, up to a reactant stoichiometry of 16-18 Hmim equivalents per metal, ZIF-8 particle sizes continue to decrease. Above this linker excess, product is simply not observed. These results resemble a previous report by Cravillon et al. that showed excess linker up to eight linker equivalents leads to progressively smaller ZIF-8 nanoparticles,[59] but the data presented here show that trend progresses further. We note that particle sizes isolated here are slightly smaller than those reported by Cravillon et al., which we attribute to the different characterization techniques: here, crystallite sizes are reported by Scherrer analysis whereas the previous account reported particle sizes from SEM imaging.

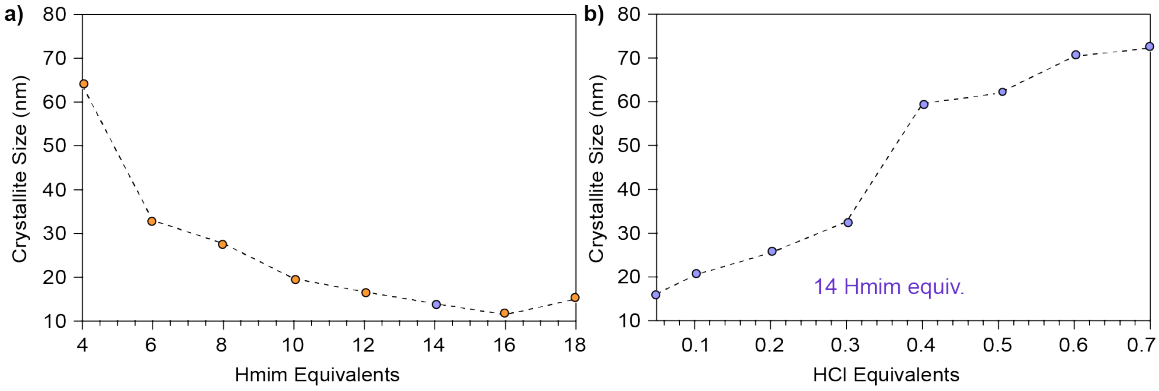

Figure 3.3. ZIF-8 nanoparticle sizes as a function of excess modulator equivalents. (a) Particle sizes versus excess linker equivalents of 2-methylimidazole (Hmim). Above 18–20 equivalents, formation of ZIF-8 was not observed. (b) Particle sizes resulting from increasing HCl equivalents with respect to zinc nitrate. Blue circles denote samples synthesized with 14 equivalents of Hmim compared to zinc nitrate. Details of the synthetic conditions can be found in the Experimental methods and Tables B.16–B.19.

Figure 3.3b plots the size of ZIF-8 particles versus number of HCl equivalents with respect to Zn^{2+} at a fixed linker excess of 14 equivalents. As a non-coordinating species, HCl acts only to increase proton activity. Therefore,

HCl addition allowed us to test the hypothesis that nanoMOF sizes increase with higher proportions of protonated linkers incapable of trapping nanoparticles, as indicated in Figure 3.1. The data show ZIF-8 nanoparticle sizes predictably increase with additions up to 0.7 HCl equivalents per Zn^{2+} ion. (Fig. 3.3b). These results corroborate previous studies showing that the addition of HCl can weaken metal-linker bonds in ZIF-8, implying there is a more dynamic equilibrium for metal-linker bond formation in acidic media.[142] Futher, the use of acids as modulators helps single-crystal growth for in several MOF systems.[143;94] These results demonstrate that protons and capping ligands form independent parameters that control nanoMOF sizes.

The dual role of modulators acting as acids and ligands complicates the synthetic control of nanoMOFs, but can nevertheless be separated and demonstrated to control the equilibria that govern particle sizes. Previously, we proposed that the dual role of modulators could give rise to a Seesaw relationship between particle sizes and modulator equivalents where sizes decrease with increasing equivalents and then increase as proton activities become sufficiently high to inhibit linker deprotonation. For proof of the Seesaw relationship, we targeted the iconic MOF Cu_3BTC_2 (BTC = 1,3,5-benzenetricarboxylate) because many modulated nanoMOF reports have focused on this material. These reports have shown that increasing equivalents of carboxylic acid modulators increases particle sizes, whereas Cu_3BTC_2 sizes decrease with increased amounts of deprotonated carboxylate, or other basic, modulators.[52;11;51;144] Hypothesizing that these trends reflect the dual role of modulators acting as acids versus ligands, we investigated the impact of adding benzoate versus benzoic acid to the synthesis of Cu_3BTC_2. Although literature reports often use SEM or light scattering methods

to determine sizes of MOF nanoparticles, sizes in this study are reported from Scherrer analysis because this method gives not particle size, but average size of coherently scattering domains. This metric is particularly useful for identifying the sizes of particles independent of aggregation. SEM images of Cu_3BTC_2 products in alkaline conditions (Figure B.9) revealed severe aggregation of particles, which is also prevalent in literature reports.[52;53;46] Because aggregation prevents accurate statistical analysis of particle sizes, all particle sizes reported here are derived using the Scherrer equation, with SEM images provided as supplements to discuss discrepancies in particle size determination techniques as well as the morphology of the products. Interestingly, MOF product could not be isolated from the synthesis with benzoic acid by mixing $Cu(NO_3)_2$ and trimesic acid at room temperature, whereas particle sizes strictly decreased by adding additional equivalents of sodium benzoate (Fig. B.2). Increasing sodium benzoate also leads to extra peaks in the PXRD patterns, likely arising from fast reaction kinetics causing benzoate ligands to trap within the MOF structure and cause defects. These results validate the prediction from the analysis of the coupled equilibria (Eq. 1-4) that deprotonated modulators acting as either ligands or bases lead to MOF nanoparticles, also consistent with previous studies.[11]

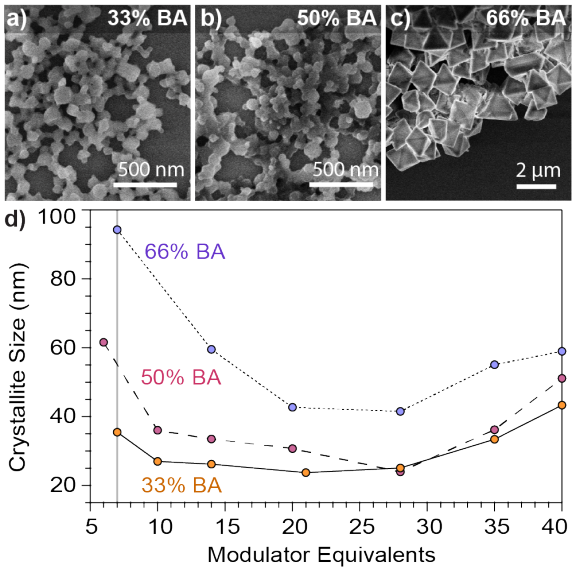

Figure 3.4. Dependence of Cu_3BTC_2 particle sizes on modulator equivalents. SEM images of particles synthesized with 7 modulator equivalents show globular morphology at (a) 33% and (b) 50% benzoic acid (BA), whereas (c) SEM shows octahedral particles when synthesized with 66% BA. Percentages indicate the mole fraction of BA, with the remainder added as sodium benzoate. (d) Dependence of size on modulator equivalents with varying benzoic acid content. Syntheses were performed with a linker:metal:modulator ratio of 3:1:X, where modulator corresponds to the sum of benzoic acid and sodium benzoate. The metal concentration was held constant (1 mM). The grey line at 7 equivalents shows the data used again in Fig. 3.5. Details of the synthetic conditions can be found in the Experimental methods and Tables B.5–B.7.

To observe a Seesaw dependence between Cu_3BTC_2 sizes and modulator equivalents, we employed a buffer mixture of sodium benzoate and benzoic acid to balance the opposing trends observed when adding only acid or ligand. Hypothesizing that particle stability depends on achieving ligand-rich surfaces, we employed excess linker stoichiometries (3 linkers to 1 metal). Figure 3.4 plots Cu_3BTC_2 nanoparticle sizes versus equivalents of modulator mixtures with benzoic acid (BA) molar contents of 33%, 50%, or 66%, with the remainder comprised of sodium benzoate. Indeed, Seesaw curves appear in all three cases with similar qualitative features: a decrease from 7 to 10 equivalents, a plateau, and a gradual

increase in sizes from 28 to 40 equivalents. When using 1 equivalent of modulator, SEM revealed particle sizes that exceeded 1 μm (Fig. 3.7, B.12), showing a steep decline in size at the beginning of the Seesaw trend. While the full data set is in the appendices (Fig. B.7a), we chose to include the data from 6 to 40 equivalents in the main text for clarity. Interestingly, the least acidic modulator mixture (33% BA) results in the steepest downward slope from 1 to 7 equivalents, which, according to the Seesaw model, reflects more favorable linker deprotonation or metal ion complexation (Fig. B.7a). Additionally, the most acidic modulator mixture produced sizes that were overall largest, whereas while the least acidic mixture gave the smallest sizes. Whereas Scherrer analysis provides insight into the impact of modulator on crystalline domain size, SEM provides information about the impact of modulator on morphology as well. Both techniques show a U-shaped size dependence at 33% benzoic acid (Fig. B.10), although sizes by SEM analysis were systematically larger, which is typical for the two instrumental techniques; there is reasonable agreement between the techniques when the Scherrer size is below 100 nm (Fig. B.10, Fig. B.11). Particles isolated with the 33% benzoic acid modulator show globular morphologies, except below 7 modulator equivalents where particles exhibit faceting (Fig. 3.7). Rather than exhibit minimum sizes around a narrow range of modulator equivalents, all data sets show a broad flat region that we attribute to the modulator mixture functioning as a buffer: the benzoic acid-benzoate pair accepts protons from the excess linkers so that sizes increase only when the proton activity exceeds the buffer capacity of the modulator mixture. Indeed, in conditions using copper acetate as a metal source and solely benzoic acid as a modulator, there is no long plateau and a minimum size occurs at 14 modulator equivalents (Fig. B.7b). Comparing the buffered systems, the most

dramatic size increase can be observed with the 66% BA set. In fact, SEM images of the product at 40 modulator equivalents show regions that resemble bulk crystal growth (Fig. B.9). While modulators have induced changes to MOF morphology, PXRD patterns exhibit peaks associated only with the Cu_3BTC_2 phase (Fig. B.3).[12] These results therefore validate the Seesaw model we had previously proposed: by using conjugate acid/base mixtures, nanoMOF sizes decrease with additional capping ligand until proton activities inhibit ligand from trapping metal ions, allowing for bulk MOF growth.[6]

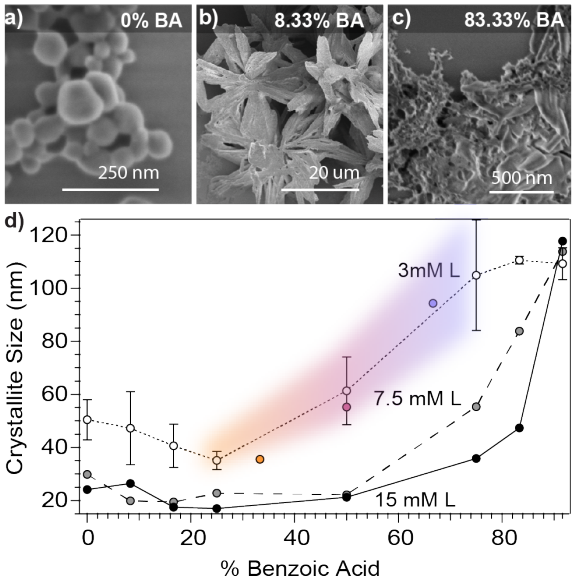

Figure 3.5. Dependence of Cu_3BTC_2 particle sizes on benzoic acid content (% BA). SEM images of samples from the 3 mM linker set show spherical morphology at 0% BA (a) large flower-like aggregates at 8.33% BA (b), but indistinct morphology for BA contents 83.33% and higher (c). (d) Cu_3BTC_2 grain sizes versus benzoic acid content of modulator mixtures at constant modulator equivalents. Two trials at low concentration were completed, and we present the data as the average of the two. Reactant concentrations are defined with respect to the linker (L). Details of the synthetic conditions can be found in the Experimental methods and Tables B.1–B.3.

To further decouple the independent roles of acidity and ligand complexation, we explored the size dependence of Cu_3BTC_2 nanoparticles as a

function of benzoic acid content in the modulator mixture at fixed modulator equivalents. Figure 3.5d plots Cu_3BTC_2 particle sizes versus benzoic acid content of modulator mixtures for three different reactant concentrations. According to the Seesaw model, larger crystallites should result from increased proton activities. Indeed, without adding additional modulator equivalents, Scherrer analysis shows increasing crystallite size in reactions where BA contents exceed 50%. Interestingly, higher reactant concentrations lead overall to smaller sizes except at BA contents near 100%, where sizes exceed the typical range of Scherrer analysis, showing that in all cases acidic conditions result in products that resemble bulk crystal growth. Within the context of the Seesaw model, the decreased sizes with higher reactant concentrations result from efficient metal ion depletion and kinetic trapping of particles. The experiments in Figures 3.4 and 3.5 thus explore a cross section of the same multi-dimensional reaction space. Datasets that intersect in this reaction space could be analyzed for reproducibility.

Figure 3.5d includes three data points from Figure 3.4d for comparison against the 3-mM dataset, which employs the same reaction conditions, showing good reproducibility. At low BA contents and low concentrations, average crystallite sizes increase slightly, whereas morphologies by SEM undergo dramatic changes. The particles isolated with only sodium benzoate appear spherical (Fig. 3.5a), but an increase in benzoic acid to 8.33% yields large star-like structures comprised of many aggregated crystallites (Fig. 3.5b). From 16.67% to 50%, BA contents, the particles show spherical morphologies and the 66% and 75% benzoic acid mixtures yield the octahedral particles typical of Cu_3BTC_2. For mixtures with BA contents as high as 83.33% and 91.67%, the particles no longer appear faceted, but instead become bulk-like aggregates (Fig. 3.5c). These results reveal that small

changes in proton activity can yield dramatic changes in particle morphology, which we will explore in ongoing studies. Although the Seesaw model at present does not offer predictions of particle morphologies, we expect that its foundation in acid-base and metal-ligand chemistry can help explain the dependence of morphology on solution acidity and modulator composition. Although previous reports have used modulators in combination with manipulation of pH,[11;145] this report is the first to systematically manipulate particle sizes with a buffer.

Concentration acts as a third key determinant of nanoMOF sizes because it controls the impact of the other two parameters, acidity and ligand excess. Building on the concentration dependence exhibited in Figure 3.5d for modulator acidity, we explored the impact of concentration in relation to modulator equivalents. Figure 3.6 plots the concentration dependence of Cu_3BTC_2 sizes using a 50% benzoic acid modulator mixture at three different equivalents of modulator. At both 0.7 and 7 equivalents of modulator, sizes decrease with increasing concentration. The effect of concentration on size is most pronounced at 7 modulator equivalents, spanning the size range of 20-80 nm, with the largest difference occurring between linker concentration of 3 and 5 mM (Fig. 4d), and little if any difference at 13.34 modulator equivalents (Fig. 3.6c).

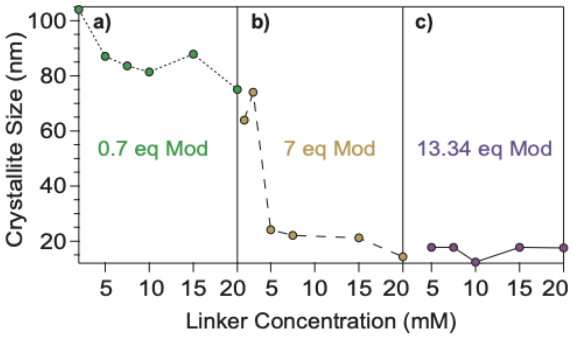

Figure 3.6. Cu_3BTC_2 particle sizes resulting from variable reactant concentrations and total modulator equivalents. Panels a, b, and c show dependence of particle sizes on concentration at three different modulator:linker ratios. Syntheses were performed with a linker:metal:modulator ratio of 3:1:X, with a 50% benzoic acid modulator mixture. Synthetic conditions can be found in Tables B.12–B.14.

Applying the Seesaw Model

These results demonstrate that MOF nanoparticle sizes can be tuned through independent control over solution acidity, ligand excess, and concentration, although certain parameters have greater impacts than others. For example, the data in Figure 3.6 show that while increased concentrations cause Cu_3BTC_2 particle sizes to decrease over a range of linker concentrations from 5 to 20 mM, increasing the modular equivalents produces a greater overall decrease in particle sizes. In terms of the Seesaw model, these results suggest that equilibria shift less in response to concentration changes compared to changes in stoichiometry. Furthermore, equilibria become so shifted by excess modulator that they become nearly insensitive to concentration changes, as indicated by Figure 3.6c. On the other hand, Figure 3.5d shows that changes to BA content have the greatest impact on crystallite size when the BA content exceeds 50%, which we propose corresponds to a critical decrease in the buffer capacity of the modulator mixture. Below the buffer capacity, concentration affects crystallite size to a lesser extent. Once the buffer mixture no longer absorbs excess protons, we expect that conditions

favor exchange of surface capping ligands for linkers that allow continued bulk growth, as has been observed in post-synthetic MOF linker exchange[146] and in reports on metal-linker stability in ZIF-8.[142] These results, taken to the extreme limit, explain why additional acid aids in the synthesis of large single crystals.[94] Interestingly, the cross-sectional data in Figure 3.5d indicate that modulator excess and BA content can produce similar absolute changes to crystallite sizes. These two variables have different effects on particle morphology, however. Whereas modulator equivalents have minimal impact on morphology, except in extreme cases of low or high equivalents (Fig. 3.7), minute changes to BA content can result in dramatic differences in particle morphology (Fig. B.8). These results suggest buffered systems may serve as a powerful synthetic tool for tailoring MOF particle shapes. The impact of changing any of these parameters appears strikingly nonlinear. Just as reducing BA content from 50% to 33% leads to small overall changes in sizes, doubling linker concentrations from 7.5 mM to 15 mM in Figure 3.5d has diminishing effects. Such nonlinearity complicates predictions about nanoparticle sizes, but its existence lends further proof for the Seesaw model, which relies on nonlinear relationships between coupled equilibria (Fig. 3.1).

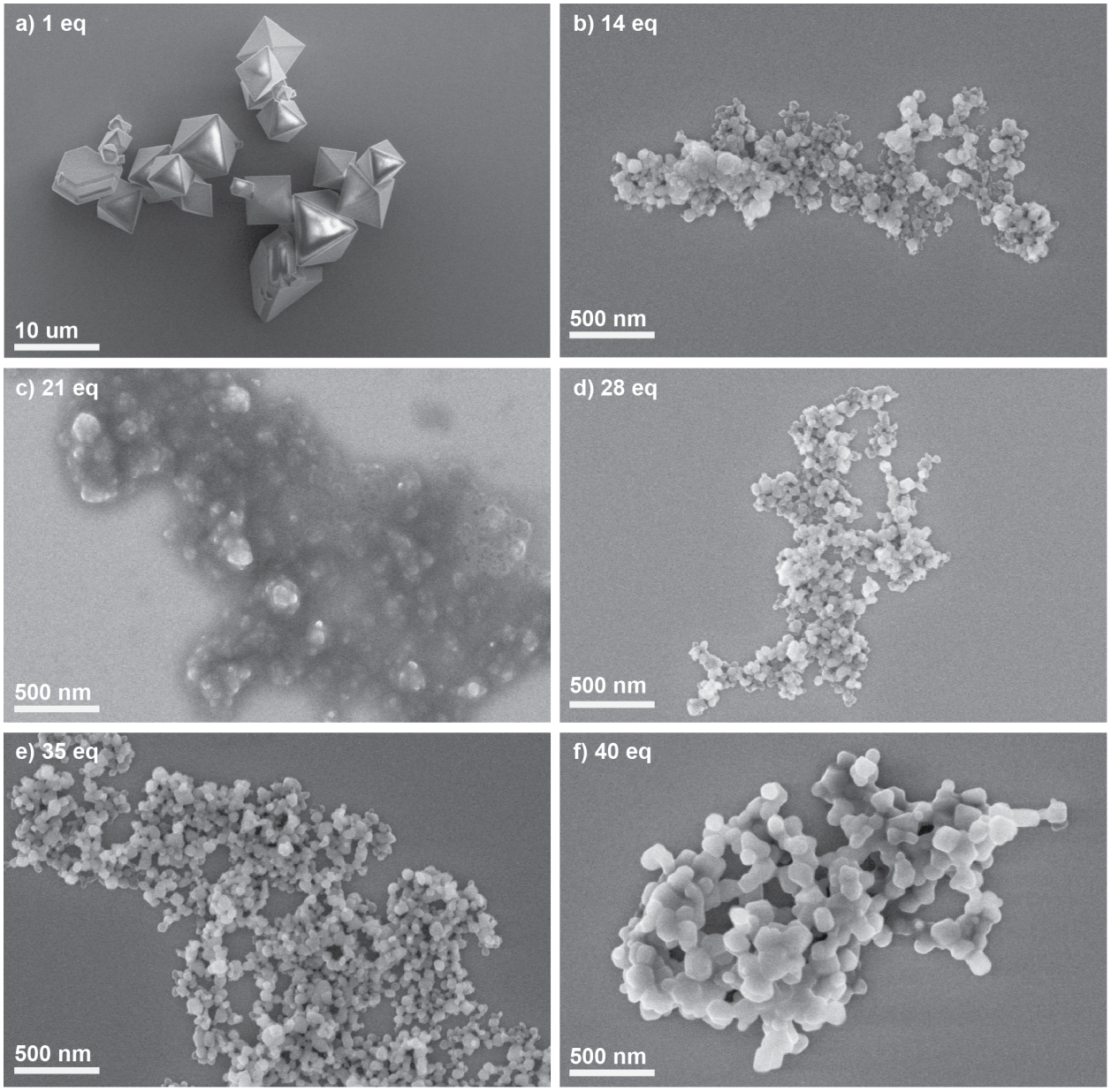

Figure 3.7. Dependence of Cu_3BTC_2 particle morphology on modulator equivalents for a 33% BA modulator mixture. Products isolated from syntheses with: a) 1 eq; b) 14 eq, c) 21 eq, d) 28 eq, e) 35 eq, and f) 40 eq. Details of the synthetic conditions can be found in the Experimental methods and Tables B.5–B.7.

Overall, these results suggest that ligand excess—of either linker or modulator—exerts the greatest impact on nanoMOF sizes. Whereas excess linker generates nanoparticles of ZIF-67, ZIF-7, and ZIF-71, cases for carboxylate MOFs

are rare.[147;148;149] While excess trimesic acid increases grain sizes of Cu_3BTC_2 particles, in NU-1000, another carboxylate MOF, particle sizes decrease as excess linker is used.[60;150] In the report of NU-1000 particles, a strong base is added as well, which likely counters any increase in $[H^+]$. We attribute this difference to the fact that imidazole linkers contain just single protic sites, whereas multi-topic carboxylates contain several, which, according to the Seesaw model, increase solution acidity and hinder the ability of ligands to trap metal ions. Additionally, the greater strength of zinc-imidazolate bonds should facilitate rapid trapping by excess linker, whereas metal-carboxylate bonds are more dynamic and, hence, less effective at terminating particle growth. The synthesis of carboxylate-based MOF nanoparticles therefore depends strongly on modulator excess. Although solution acidity and reactant concentration influence the kinetic trapping of MOF nanoparticles, achieving small nanoMOF sizes ultimately relies on the presence of excess ligands.

According to the Seesaw model, dilute local concentrations of metal ions overwhelmed by excess ligand leads to kinetic trapping of small particle sizes. This prediction helps explain previous reports that dilution yields smaller ZIF-8 nanoparticles,[8] which at first seems in conflict with the concentration studies presented here. Figures 3.4 and 3.5 both show Cu_3BTC_2 particle sizes decreasing with increased concentrations; we suggest two reasonable hypotheses to explain this apparent discrepancy. Firstly, imidazole and carboxylate MOFs exhibit rather different metal-linker bond strengths. Whereas ZIF-8 features strong metal-linker bonds that rapidly form bulk crystals under concentrated conditions, carboxylate-based MOFs exhibit slower growth kinetics that tend to form large single crystals through slow and dynamic exchange of ligands.[151]

Increasing the local concentration of linker therefore improves kinetic trapping of carboxylate MOF nanoparticles by shifting the weak metal-linker equilibrium towards complexation. The concentration dependence also depends on the stages of MOF growth. For example, it has been demonstrated in injection syntheses that including an excess of either linker or metal ions at the beginning of the reaction results in smaller particle sizes, which is attributed to the rapid formation of small MOF clusters and oligomers. On the other hand, slow addition of MOF components during the reaction results in the growth of larger particles.[152] In the context of the Seesaw model, this shows that with excess of either of the MOF components, rapid depletion can lead to the kinetic trapping of small particles. Increasing the total concentration during the reaction, however, will inevitably lead to larger particles because the metal ions and linkers will add onto existing particles.

These results also highlight the complex role played by ligands in trapping metal ions as molecular complexes, preventing their incorporation into growing MOF particles. For example, Figure 3.3 shows that extreme excess of linker equivalents suppresses ZIF-8 formation. Under these conditions, imidazolate molecules likely coordinatively saturate Zn^{2+} ions, shifting the metal-linker binding equilibrium far toward complexation and inhibiting the dynamic ligand dissociation needed for monomer attachment and growth. Indeed, a previously reported in-situ study of ZIF-8 growth under excess linker conditions suggested particle growth proceeds by linker dissociation from zinc-imidazolate oligomers under concentrated conditions.[153] Similarly, excess benzoate appears to inhibit Cu_3BTC_2 formation by trapping Cu^{2+} ions in benzoate complexes or small, saturated clusters. This hypothesis could explain why particle sizes at first decrease with added BA content

in Figure 3.5d at 3 mM linker concentration. By increasing the solution acidity, the modulator mixture becomes less competitive with the trimesate linker for Cu^{2+} coordination and Cu_3BTC_2 forms more readily, whereas benzoate-rich conditions make particle growth reliant on the slow release of Cu^{2+} ions, leading to larger particles. Another explanation for the larger sizes under benzoate-rich conditions is the tendency of deprotonated modulators to induce aggregation.[52;53] The extreme difference between the moderate crystallite size of the 8.33% BA sample and its large star-like morphology indicates that aggregative growth is operative (Fig. 3.5). Previous reports have shown that pH adjustment can manipulate the assembly and aggregation of MOF-525 particles[154;155] and that strongly acidic modulators improve the colloidal stability of UiO-66.[60]

More generally, the Seesaw model serves as a complement to well-established models of bulk crystal growth and polymer formation. Whereas successful growth of ionic crystals and condensation polymers depends on maintaining stoichiometric mixtures of reactants, the Seesaw model proposes that MOF nanoparticle sizes minimize from maximally imbalanced local concentrations of reactants: in modulated MOF syntheses, ligands always outnumber metal ions. For many classes of polymers, molecular weights decrease considerably under conditions of imbalanced monomer stoichiometries, producing oligomers instead of long polymer chains. Interestingly, molecular weights can also be controlled by terminating chain growth with the addition of monofunctional monomers, akin to MOF modulators.[156] For ionic solids, the rate of crystal growth maximizes when the relative ratios of monomers diffusing to crystal surfaces matches the stoichiometry of the bulk lattice.[157] Models of ionic crystal growth state that rates of monomer attachment relates directly to $n_{site} * \tau_m * J$, where n_{site} represents the density of

available binding surface sites, τ_m is the lifetime of monomer units, and J is the flux of the monomer to the growing crystal.[157] In terms of the Seesaw model, therefore, small nanoMOF sizes result from rapid depletion of metal ion concentrations and overwhelming particle surfaces with excess ligand. We note that the model assumes growth to depend solely on metal-linker bond formation, whereas interlayer stacking constitutes an important component of 2D MOF growth. We propose that the Seesaw model could be adjusted for such materials by including the formation constants for interlayer stacking.[13] Additionally, these models assume the absence of aggregation, which we expect to play a large role in determining size after crystallite formation. For MOFs, the relevant diffusing species may be metal ions, linkers, or even entire clusters, given in-situ studies that suggest Cu_3BTC_2 grows by increments of individual Cu_2BTC_4 paddlewheel units, or even the oriented attachment of small crystals.[158;159] Interestingly, typical representations of this model of ionic crystal growth plot growth rate versus solution stoichiometry, with maximum growth centered at balanced ratios in an "upside down Seesaw" curve.[160] Figure 3.2, therefore, illustrates the complementary relationship of the Seesaw model to common models of bulk crystal and polymer growth, where sizes minimize at maximally unbalanced stoichiometries, and vice versa.

Lastly, we propose that the steep downward slope observed in "region I" of the Seesaw curve can be interpreted in terms of classical collision theory. In collision theory, the probability of no collision taking place between particles as a function of time, P(t), equals $\exp(-t/\tau)$, where τ represents the average time between collisions.[161] Similarly, we propose that the probability of MOF nanoparticles not being kinetically trapped by excess ligand decreases exponentially as more modulator enters the reaction mixture. In other words, the probability of

particles colliding with capping ligand increases with higher available equivalents of excess ligand. This model helps explain why decreasing slopes in Figure B.7 become shallower from 1 to 7 equivalents with higher acidic content—the probability of successful particle trapping diminishes as the modulator becomes more acidified. Higher concentration leading to smaller particles is also discussed in classical nucleation theory (CNT), in which the energy barrier to nucleation is overcome only in supersaturated conditions. Here, MOFs grow in dilute conditions, but increasing concentration leads to smaller particles as there are more collisions in solution that lead to particle formation. We anticipate that temperature, concentration, and other factors expected to impact collision probability play decisive roles in the mechanism of MOF nanoparticle growth.

Conclusions

In conclusion, we offer experimental proof of the Seesaw model of nanoMOF growth by demonstrating for the first time the existence of a Seesaw relationship between nanoMOF sizes and modulator excess through deliberate manipulation of key parameters in the model. Specifically, we show that MOF nanoparticle sizes can be tuned through independent control over solution acidity, ligand excess, and reactant concentrations. Demonstrating that these three parameters control nanoMOF sizes supports the key claim of the model that nanoMOFs result from kinetic trapping of nanoparticles determined by competition between coupled equilibria involving metal-ligand complexation and ligand acid-base chemistry. The relative impact of these parameters on nanoparticle sizes was explored, with ligand excess showing the greatest overall impact. Sizes generally decease with lower acidity, greater ligand excess, and, for dynamic metal-linker bonds, higher concentrations. Importantly, particle sizes were reproducible when approaching

similar reaction conditions from different directions on the multi-dimensional reaction space defined by these three parameters. The Seesaw model represents a novel perspective for understanding MOF growth in general, and we further show that it complements well-established models of bulk polymer and crystal growth. Despite its clear relation to other models of crystal growth, the competing equilibria should be expanded to account for equilibrium constants associated with events such as oriented attachment, in which multiple metal-ligand bonds form at the same time. We further note that thus far the Seesaw curve has been observed by using aromatic carboxylate modulators with similar pKa values and expect that altering the size and acidity of modulators to have a large impact on the particle Seesaw dependence. Although the dependence of morphology on solution acidity was unexpected, buffer systems may prove powerful tools for deliberate control over tailoring particle architectures. Taken together, these results demonstrate that the Seesaw model offers a fundamental platform for advancing the synthesis and basic understanding of this emerging class of materials.

CHAPTER IV

SIZE-DEPENDENT PROPERTIES OF CONDUCTIVE MOF NANOCRYSTALS

This chapter includes an excerpt from previously published and co-authored material from Marshall, C.R.; Twight, L.P.; Dvorak, J.P.; Overland, A.E.; Brozek, C.K. Size-Dependent Properties of Solution-Processable Conductive MOF Nanocrystals. *J. Am. Chem. Soc.* **2022**, 144, 13, 5784-5794. The project in this chapter was conceptualized and developed by Checkers R. Marshall; the final manuscript was co-written by Checkers R. Marshall and Carl K. Brozek. The experimental work in this chapter was performed by Checkers R. Marshall, Josh. D. Dvorak, Lan Chen, and Alexi E. Overland. The Mössbauer data in this chapter was collected by Thomas Ericson.

The discovery of colloidal metal and semiconductor nanocrystals has led to a revolution in materials chemistry.[162] While the class of materials known as metal-organic frameworks (MOFs) attracts broad interest due to their high accessible surface areas and wide synthetic tunability, their preparation as stable, monodisperse nanoparticles remains an open frontier.[163] Nevertheless, recent research into the few examples of MOF nanoparticles has revealed enhanced properties compared to their bulk counterparts due to greater mass transport rates, higher ratios of exposed surface areas, and superior processability, leading to higher catalytic activities, improved gas permeability in separation membranes, more uniform integration into composite films, and utility as unique drug delivery agents.[31;164;165;166;167] The controlled synthesis of MOF nanoparticles with precise sizes will therefore facilitate their application in myriad applications, while enabling solution-state analysis to reveal size-dependent physical properties.[168] Currently, the few MOFs that can be prepared as colloidally stable nanoparticles with narrow

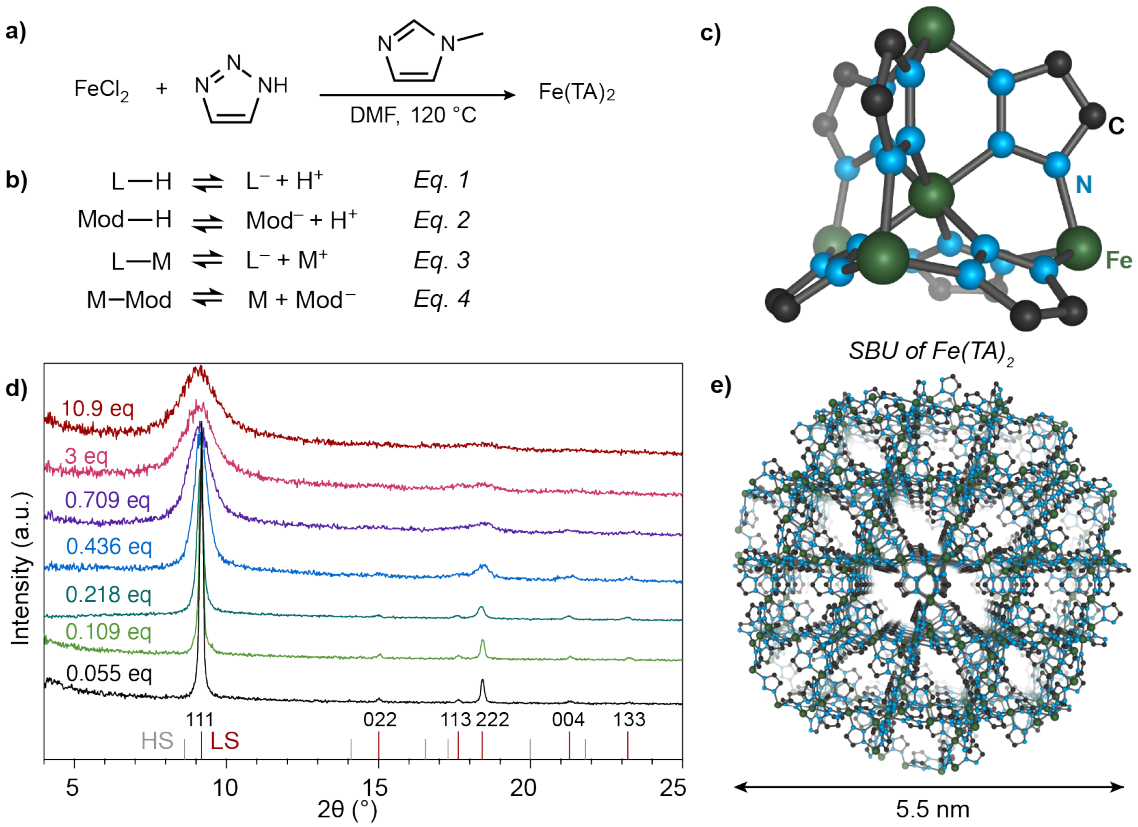

Figure 4.1. Overview of Fe(1,2,3,-triazolate)$_2$ (Fe(TA)$_2$) nanocrystal synthesis. a) General synthetic route to Fe(TA)$_2$ nanoparticles using 1-methylimidazole (1-mIm) as a modulator. b) Equilibrium between metal ions (M), linkers (L), and modulators (Mod) that control MOF nanoparticle formation. c) The secondary building unit (SBU) cluster of Fe(TA)$_2$. d) PXRD patterns of the Fe(TA)$_2$ nanoparticles synthesized with varying amounts of 1-mIm. Red and grey lines indicate expected reflections for the low-spin (LS) phase and high-spin (HS) phase, respectively. e) The SBU of Fe(TA)$_2$. e) An idealized representation of a 5.5-nm Fe(TA)$_2$ particle based on the bulk crystalline structure.

size dispersities are electrical insulators, whereas conductive MOF nanoparticles will enable electronic technologies that benefit from the microporosity and high surface areas of MOFs and the processability and size-control of nanoparticles.[169] Here, we address the long-standing challenge of making solution-processable conductive MOF nanoparticles (nanoMOFs) with controlled size and narrow dispersity. Solution processability also enables solution-state spectroscopy for

unprecedented analysis of electronic properties and thin film fabrication reveals unique insight into their redox chemistry and charge transport phenomena.

Size-tunable Synthesis of Iron Triazolate Nanoparticles

Nanoparticles of $Fe(TA)_2$ were prepared with tunable sizes by modifying the standard bulk synthesis11 through addition of 1-methylimidazole (1-mIm) as a "modulator" (Fig. 4.1). Although the use of "modulators," usually monotopic analogs of the native MOF linkers,[6] is common in MOF nanoparticle syntheses, their mechanistic role has been debated, especially because increasing modulator equivalents leads to smaller sizes in some systems, but larger sizes in others. Chapters 2 and 3 point to a "Seesaw" model where modulators impact particle sizes by interfering with linker deprotonation (Fig. 4.1, Eq. 1) and metal-linker complexation (Eq. 3). Based on a meta-data analysis of the literature,[6] this model contends that MOF particles result from kinetic trapping of metal ions by excess linker or modulator. Through deliberate control of the key parameters outlined by this model—proton activity, concentration, and ligand excess—excellent size reproducibility can be achieved for benchmark MOF materials. Using these insights, we can devise MOF syntheses previously inaccessible at the nanoscale. To access small and controllable particle sizes, we hypothesized that a monotopic imidazole linker, 1-methylimidazole, would work as a modulator that mimics the native MOF linker. Reversible bonds between Fe and 1-mIm (Eq. 4) would compete with metal-linker complexation (Eq. 3) to rapidly form the secondary building blocks (SBUs) of $Fe(TA)_2$, shown in Figure 4.1c. The presence of the monotopic linker at the surface of a growing particle also inhibits further growth until it dissociates. Additionally, previous work with other MOF

systems have shown promising nanosizing effects with the use of similar imidazole modulators.[170;171]

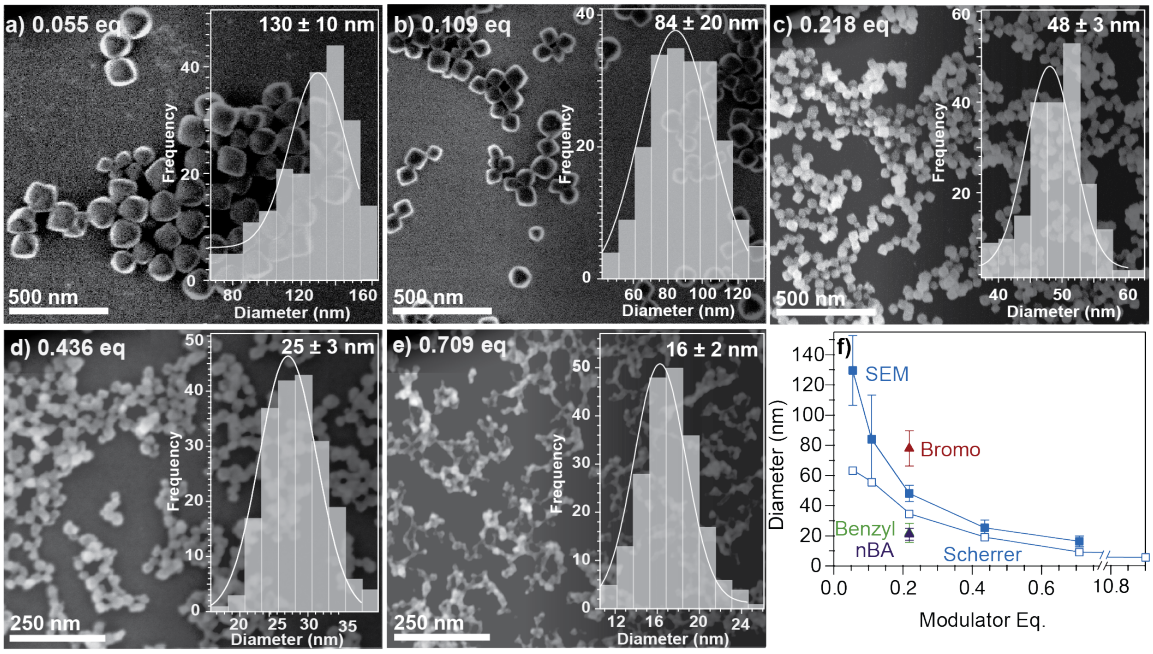

Figure 4.2. Particle sizes of $Fe(TA)_2$ resulting from modulated syntheses. (a) – (e) SEM images of $Fe(TA)_2$ nanoparticles synthesized with 1-methylimidazole equivalents (with respect to $FeCl_2$) ranging from 0.055 eq (a) to 0.709 eq (e). Images were set to greyscale using Adobe Illustrator. Insets: histograms of particle size distributions from >200 particles fitted to weighted gaussian distributions. f) Particle sizes using 1-mIm (blue squares), 1-benzyl-2-methylimidazole (Benzyl, green triangle) 5-bromo-1-methylimidazole (Bromo, red triangle), and n-butylamine (nBA, purple triangle). Filled data points were determined by SEM and open data points by Scherrer analysis.

In comparison to the bulk synthesis first reported by Yaghi et al in 2012,[19;20;21] the synthesis of nanoparticles was conducted under dilute conditions, with stirring, and varying modulator equivalents. After heating the reaction mixture under air-free conditions in DMF at 120 °C, the reaction was terminated after 1.5 h by removing from heat and immediate centrifugation and washing. These reactions are low yielding (6 – 23%), which is further evidence of arrested growth of kinetically trapped particles, as has been observed in other nanoMOF

systems (Fig. C.3). Indeed, Figure 4.1d shows the expected PXRD pattern of $Fe(TA)_2$ but with peaks that broaden with greater equivalents of modulator. Additionally, Figure 4.2 shows that particle sizes determined by Scherrer analysis of these data and by SEM imaging dramatically decrease with increasing equivalents of 1-mIm. At low equivalents of 1-mIm, the particle sizes decrease steeply: from 0.055 eq to 0.709 eq, the particle sizes reduce from 130 nm to 16 nm. Beyond 0.709 eq, the particle sizes level off abruptly, decreasing to 5.5 nm only with 10.9 equivalents of modulator (Fig. 4.2f). To the best of our knowledge, the 5.5-nm particles represent some of the smallest reported MOF particle sizes synthesized by a facile one-pot modulator method, whereas the synthesis of nanoMOFs below 10 nm typically requires multiphase systems, dropwise additions, or multiple modulator ligands.[172;173;174] Figure 1e depicts a simulated structure of 5.5-nm $Fe(TA)_2$, confirming that such a small size still includes many pores due to the unusually high density of this MOF. SEM analysis of the 16 and 25 nm particles reveals unimodal and symmetrical size distributions and essentially spherical morphologies (Fig. 4.2). Although the two smallest particle sizes synthesized were not well-resolved by SEM, the images clearly reveal small nanoscale particles (Fig. C.7). Instead, particle sizing was accomplished by Scherrer analysis. To confirm the domain sizes from PXRD, we additionally performed Le Bail refinements on patterns of the largest and smallest particles and found the domain sizes agree with SEM imaging for the 130 nm particles and Scherrer analysis for the 5.5 nm particles (Table C.1, Fig. C.2). Scherrer analysis, as expected, produces underestimated values, particularly as particle sizes increase. Microscopy of larger particles (0.055 eq 1-mIm, 130 nm) show octahedral faceting, akin to the bulk MOF product. Size distributions also skew towards larger sizes when the modulator

equivalents are low, indicating that particles may grow by non-classical mechanisms such as digestive ripening or interparticle coalescence.[175;176] The dispersity of the particle populations can be quantified by dividing the standard deviation given from a Gaussian fit by the mean size; these values vary between 0.09 and 0.18. These dispersity values are considerably lower than the typical dispersity values of nanoMOFs, which are often as high as 0.6, and rival the archetype of low-dispersity MOF particles, ZIF-8, which also exhibits values around 0.09.[177;8;32] Mössbauer spectra of the smallest particles before and after air exposure were collected to determine the efficacy of our air-free synthesis. In the air-free sample, Fe^{3+} is not observed (Fig. 4.3).

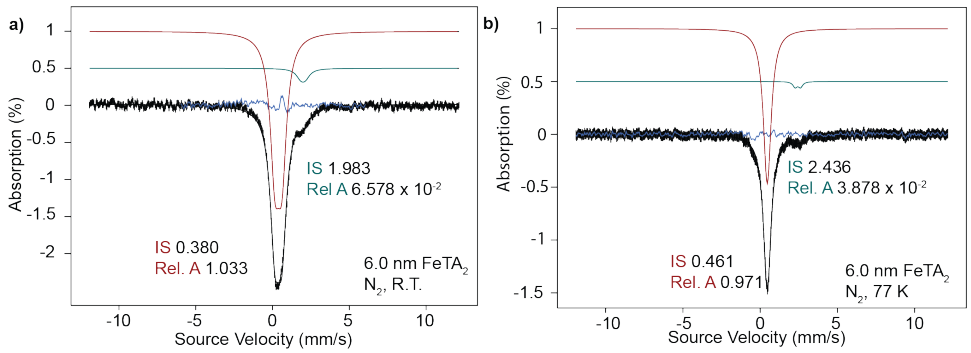

Figure 4.3. Mössbauer spectra of the smallest $FeTA_2$ samples under N_2. In addition to the main peak, indicative of low-spin Fe^{2+} in an octahedral environment, there is a shoulder at high isomer shift that may be related to undercoordinated iron sites at the surface.

As the smallest particles exhibit the highest external surface area and would therefore oxidize readily, these data suggest that all samples synthesized, stored, and measured air-free exist in the fully ferrous state. Whereas modulators may incorporate as internal defects or surface ligands in other MOF systems, ^{1}H acid digestion NMR indicates that 1-mIm does not incorporate in most cases (Fig. C.8). Remarkably, despite the lack of conventional capping ligands, particles of all sizes

exhibit colloidal stability in DMF under anaerobic conditions for at least three months, even at relatively high concentrations of 10-20 mg/mL. Dynamic light scattering measurements of 25-nm particles stored for three months gave a solvated diameter of 60 ± 10 nm, a reasonable increase from the SEM images of dried particles that did not exhibit aggregation (Fig. C.10). Therefore, these $Fe(TA)_2$ particles exhibit superior long-term stability compared to previously reported MOF systems, which, with the notable exception of ZIF-8 in methanol, are typically coated with polymers or surfactants to achieve colloidal stability.[178;179]

To explore the general application of this nanocrystal synthetic route, we investigated 5-bromo-1-methylimidazole, 1-benzyl-2-methylimidazole, and n-butylamine (nBA) as alternatives to 1-mIm. Due to their differences in Lewis and Brønsted-Lowry basicities, this series of modulators offers a platform for exploring the competing equilibria outlined in Figure 4.1b. Specifically, we expected that nBA, as the strongest ligand and proton accepter, would yield the smallest sizes. Figure 4.2f plots the resulting particle sizes using 0.218 equivalents of each modulator, indicating that each of these alternative modulators produces nanoparticles, with nBA giving the smallest sizes and the bromo-substituted variant, i.e., the weakest ligand, producing the largest sizes. This trend correlates with the strength of the N-Fe bond, as the weakly electron-donating benzyl group allows the imidazole nitrogen to increase its sigma-donating ability, whereas the electronegative bromine moiety withdraws electron density from the N-Fe bond. This size trend therefore provides further evidence that modulators compete with the triazole MOF linkers. SEM images confirms that the resulting particles are also uniform (Fig. 4.4)

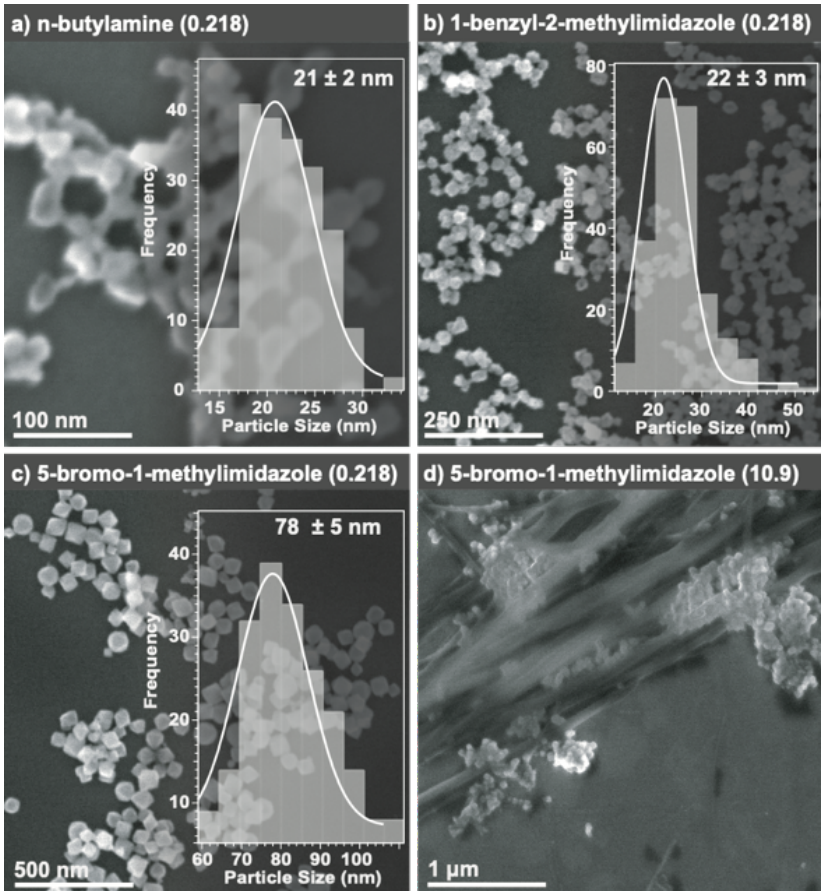

Figure 4.4. SEM images of particles synthesized with different modulators. a) $Fe(TA)_2$ synthesized with 0.218 eq of n-butylamine. b) $Fe(TA)_2$ synthesized with 0.218 eq of 1-benzyl-2-methylimdaizole. c) $Fe(TA)_2$ synthesized with 0.218 equivalents of 5-bromo-1-methylimidazole. d) $Fe(TA)_2$ product synthesized with 10.9 eq 5-bromo-1-methylimidazole showing small aggregated particles and long string-like structures.

High equivalents of n-butylamine (>1 eq) formed an amorphous precipitate at room temperature (Fig. C.1a). Interestingly, if heated and stirred, this gel-like reaction mixture still produced phase-pure $Fe(TA)_2$, although samples using this modulator suffered from poor colloidal stability. High equivalents of 5-bromo-1-methylimidazole resulted in significant particle aggregation as well as an unidentified phase impurity (Fig. 4.4d, C.1c,). With 10.9 equivalents of 5-bromo-1-methylimidazole, the PXRD peaks also appear to shift to slightly lower angles,

indicating a small increase in unit cell size. Additionally, particles synthesized with 5-bromo-1-methylimidazole often suffered from poor colloidal stability. The use of 1-benzylimidazole resulted in small Scherrer sizes, although a possible phase impurity is also observed (Fig. C.1b).

We therefore chose to move forward with 1-methylimidazole, as the products were consistently phase-pure and small particles were obtained at reasonably low equivalents. We also employed more dilute conditions compared to the previously reported bulk synthesis. To ensure that the results observed were due to the modulator and short reaction time, we performed our bulk synthesis under the same concentration (0.0575 M $FeCl_2$, Fig. C.6a). Encouraged by the results with $Fe(TA)_2$, we explored the synthesis of $Co(TA)_2$ and $Cd(TA)_2$ with the addition of 1-methylimidazole and observed a similar size trend by Scherrer analysis and SEM imaging (Fig. 4.5, 4.6). Indeed, this synthetic strategy yielded nanoparticles of both materials, showing that the addition of 1-mIm as a modulator may be a generally applicable method to synthesize nanoMOFs comprised of triazole linkers.

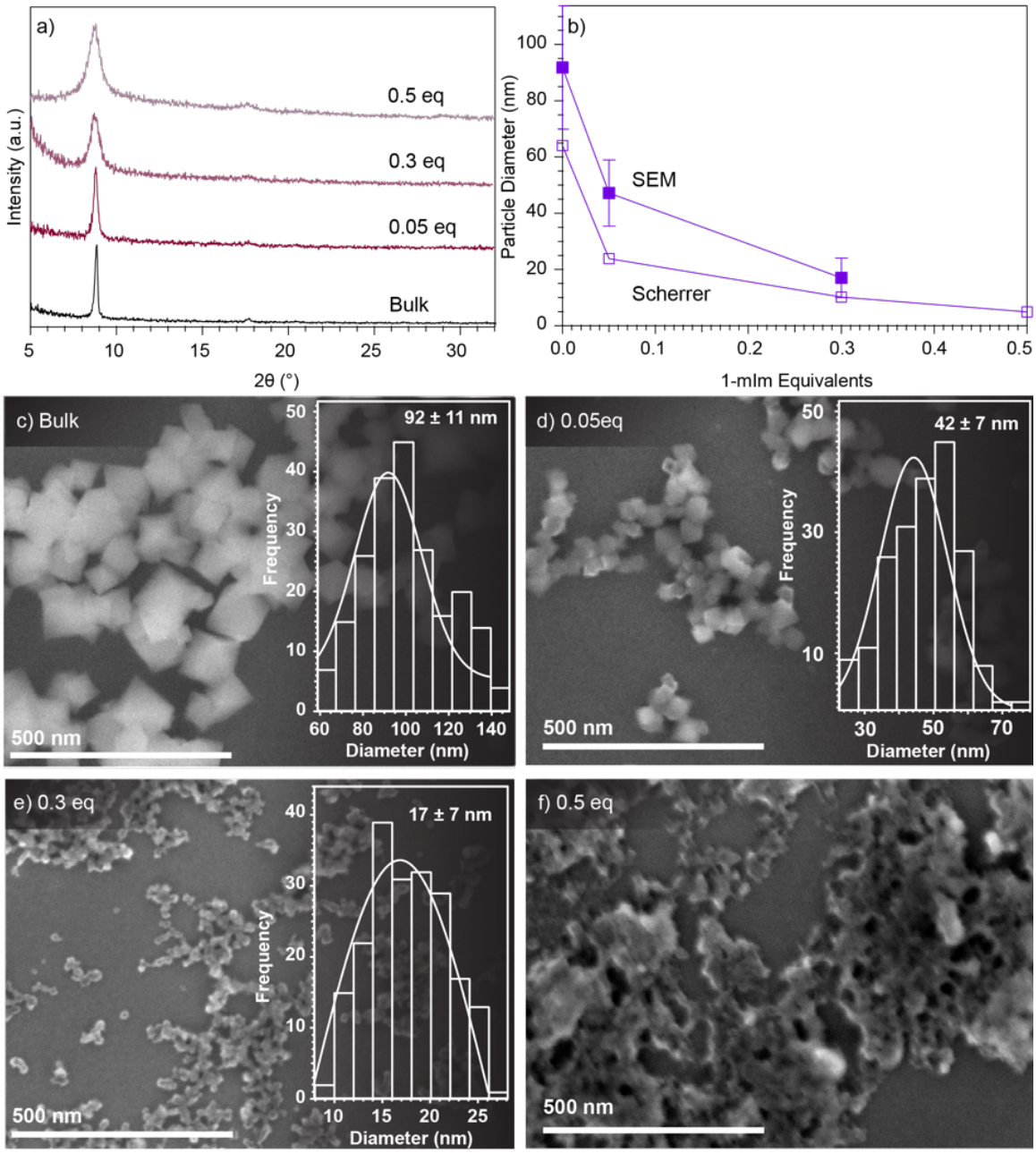

Figure 4.5. Synthesis of nanosized $Co(TA)_2$ using 1-mIm as a modulator. a) PXRD patterns of the bulk synthesis of $CoTA_2$ compared to the nanosized synthesis using varying equivalents of 1-methylimidazole. b) Particle diameter trend with respect to 1-methylimidazole equivalents. Filled squares are sizing from SEM, measuring >200 particles. Empty squares are Scherrer crystallite sizes. SEM images and size histograms for (c) the bulk synthesis with no modulator, (d) 0.05 equivalents of 1-mIm, and (e) 0.3 1-mIm equivalents. f) SEM image for 0.5 1-mIm equivalents; crystallite sizes from Scherrer analysis follow the expected trend but SEM shows poor morphology.

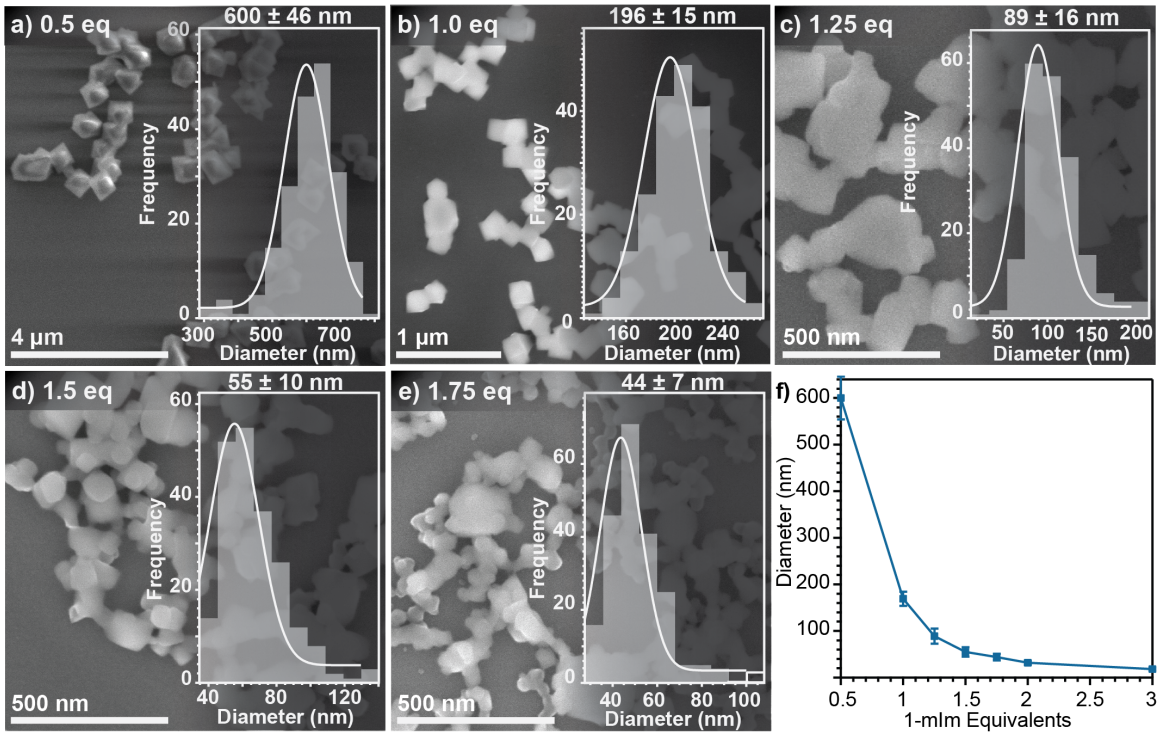

Figure 4.6. Size trends of new $Cd(TA)_2$ products modulated by 1-methylimidazole. Particles synthesized with a) 0.5 equivalents, b) 1.0 equivalents, c) 1.25 equivalents, d) 1.5 equivalents, and e) 1.75 equivalents with respect to Cd in the reaction. f) Particle sizes determined from SEM imaging vs 1-methylimidazole equivalents.

Size-Dependent Optical Properties of Colloidal $Fe(TA)_2$ Nanoparticles

The remarkable colloidal stability and small sizes of $Fe(TA)_2$ nanoparticles yielded suspensions with minimal light scattering, as seen in the inset photo of Fig. 4.7a. In fact, diluting colloidal suspensions of $Fe(TA)_2$ results in samples with sufficient transparency for solution-state UV-Vis absorption spectroscopy. In general, any spectroscopy of MOF materials involves analysis of solid-state samples, with UV-Vis analysis demanding diffuse reflectance methods. Figure 4.7a shows solution-state UV-Vis spectra for all $Fe(TA)_2$ particle sizes. These spectra comprise some of the only examples of solution-state spectroscopy of MOF materials, which include isolated reports of MOF-525, TMU-34, and Zn-MOF-74.[180;179;178;112] To the best of our knowledge, this report is the first to quantify fundamental optical properties from the absorbance spectra of MOF particles in solution. The spectra exhibit the same two MLCT bands (ca. 4.2 eV and 3.3 eV) as observed in the bulk material (Fig. 4.7a, shaded grey). Due to significant scattering observed in the spectra of larger particle sizes, the low-intensity d-d transition expected at 2.36 eV for the low-spin-state material from the bulk spectrum is obscured in all spectra. Notably, the spectra lack an inter-valence-charge-transfer (IVCT) band around 1.24 eV that arises from mixed $Fe^{2+/3+}$ valency, suggesting the particles exist in a fully ferrous state, in agreement with the Mössbauer spectra showing only Fe^{2+} (Fig. 4.3).[20]

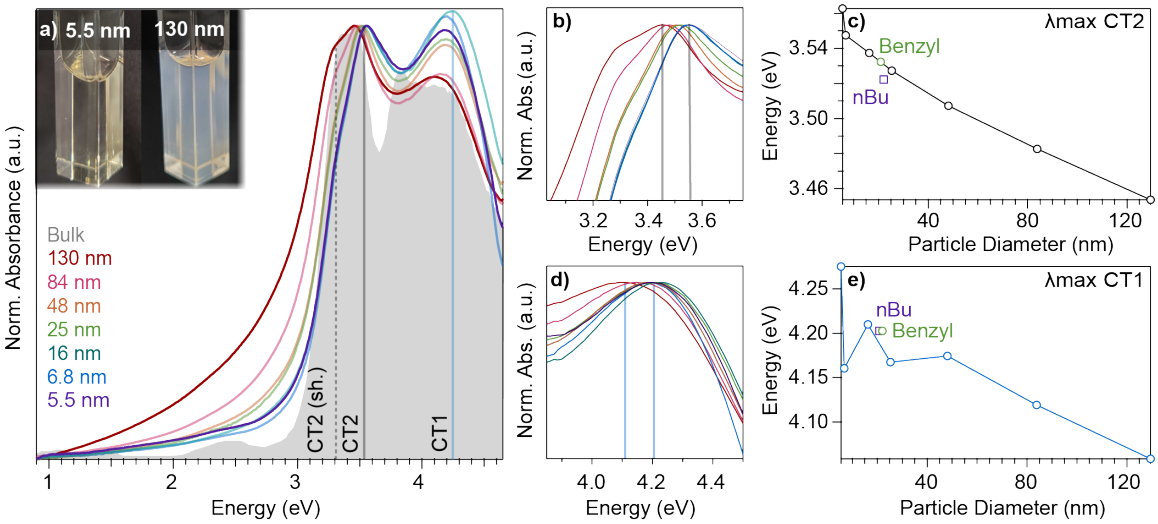

Figure 4.7. Solution-state UV-Vis absorption spectra of $Fe(TA)_2$ nanoparticles. a) Normalized spectra of colloidal $Fe(TA)_2$ nanoparticles of varying sizes suspended in DMF (colored traces) compared with the bulk MOF (filled grey area) as reported by diffuse reflectance.[20] Smallest and largest particles traces are emphasized. Inset contains a photo of the smallest and largest particles as solutions in cuvettes. b) Normalized CT2 band and c) corresponding peak maxima versus particles sizes. d) Normalized CT1 band and e) corresponding peak maxima versus particles sizes. Peak maxima are reported for syntheses modulated by 1-mIm except for data labeled for n-butylamine (nBA) and 1-benzyl-2-methylimidazole (Benzyl).

Close inspection of the solution-state spectra reveal that the peak maxima of the two charge transfer bands decrease in energy with increasing particle sizes, while a shoulder emerges at energies below the lower-energy band (Fig. 4.7). For the higher energy band (CT1), the maximum shifts a total of 0.22 eV, while the lower band (CT2) maximum shifts 0.11 eV. In the bulk material, the λ_{max} of CT1 appears at a lower energy of 3.99 eV, and CT2 appears at 3.47 eV, within range of the λ_{max} of the nanoparticles. Although the CT2 band is split in the bulk spectrum, the peak-to-peak separation appears more extreme in the nanoparticles, with the lower-energy shoulder appearing at much lower energies (Fig. C.15). These data represent the first examples of size-dependent shifts to optical properties of MOF materials. To determine whether the modulator plays a role in

the size dependence, UV-Vis spectra were collected of particles synthesized with n-butylamine and 1-benzyl-2-methylimidazole. Because modulated MOF syntheses often introduce defects, we anticipated the modulator identity to influence the extent of defect incorporation in $Fe(TA)_2$ nanoparticles.[112] Interestingly, the λ_{max} values for particles prepared with these alternative modulators are similar to $Fe(TA)_2$ particles prepared with 1-mIm. Therefore, the size-dependent optical behavior is unlikely due to modulator-induced defects and is reproducible (Fig. 4.7c, 4.7e).

The shift in the peak maxima suggest that the electronic structure of $Fe(TA)_2$ changes with particle size. Several physical scenarios might explain this observation. The first possibility is quantum confinement; particle sizes smaller than the excitonic Bohr radius of $Fe(TA)_2$ would exhibit blue-shifted absorption events. Previous electronic structure calculations of $Fe(TA)_2$, however, depict relatively shallow band curvatures and therefore low charge carrier mobilities, which would result in an insufficiently large excitonic radii for quantum confinement.[181] Additionally, band-gap transitions of quantum-confined materials linearly increase with $1/r^2$, based on the effective mass approximation, or as $1/r$ due to Coulombic electron-hole interactions.[182] However, a linear trend is not observed in this transition with respect to $1/r^2$ or $1/r$ (Fig. C.15). A second explanation may be that the observed optical shifts arise from a size-dependent magnetic transition. Previous studies of bulk $Fe(TA)_2$ indicate that low-spin Fe^{2+} centers undergo spin-crossover transitions at 290 °C,[21] but this transition temperature might occur at lower temperatures for smaller particles due to decreased cooperativity of smaller domain sizes. For example, the spin-crossover temperatures of related Fe-based 1-D coordination polymers decrease with decreasing particle sizes.[183]

The distinct electronic configurations of high- and low-spin states would produce different sets of spectra, as is well-documented for spin-crossover materials.[184;185] Preliminary PXRD analysis, however, suggests the nanoparticles exist in the denser low-spin crystallographic phase (Fig. 4.1d).[21] Additionally, we observe by differential scanning calorimetry (DSC) that the LS-HS phase transition still occurs far above room temperature for even the smallest $Fe(TA)_2$ particles (Fig. C.11). Partial oxidation of iron sites is another possibility, as a change in shape of the charge transfer bands has been reported for $Fe(TA)_2$ bulk powders after chemical oxidation.[20] This scenario is unlikely, however, as the colloids are stored and measured air-free, and the spectra lack an intervalence charge-transfer band and Mössbauer spectra of the smallest particles exhibit only a ferrous species (Fig. 4.3). Finally, structural distortions due to the high surface-to-volume ratios of small particles could be responsible for the size-dependent spectral shifts as optical shifts arising from surface restructuring has been reported in several metal-oxide nanoparticle systems.[186] Specifically, the localized orbitals of surface, sub-surface, and internal species in different geometries could contribute different absorption bands to UV-vis profile, with surface species playing the greatest role in the smallest particles. Delocalized wavefunctions, on the other hand, might respond coherently to structural distortions, contorting the shapes of valence band and conduction band orbitals and shifting their relative energies. The presence of surface defects is supported by N_2 sorption experiments, which show that the 48-nm particles display a lower accessible surface area than the bulk material despite their higher surface area to volume ratio (Fig. 4.8).

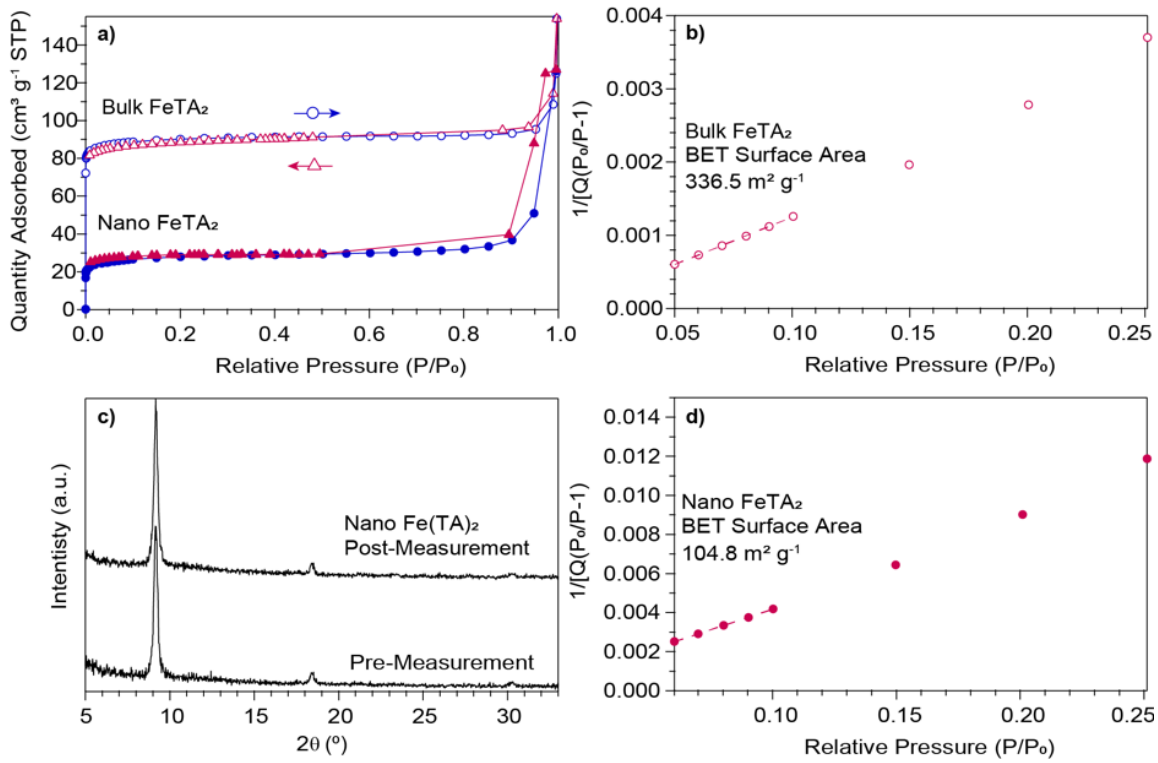

Figure 4.8. Nitrogen isotherms of bulk iron triazolate compared to 48-nm nanoparticles. The nanoparticles were synthesized with 0.218 equivalents 1-methylimidazole. Samples were washed with DMF (2), MeCN (2), and DCM (5) and evaporated to dryness. Samples were degassed at 120 °C for 24-48 hours, until the degas rate was below 2.5 μtorr/min. a) N_2 adsorption (blue circles) and desorption (red triangles) isotherms for bulk and nano $Fe(TA)_2$. b) BET plot for bulk $Fe(TA)_2$. c) PXRD of $Fe(TA)_2$ nanoparticles before and after measurement. d) BET plot for $Fe(TA)_2$ nanoparticles.

This strong size-dependence in the absorption energies has never before been observed for MOFs. Although the exact cause is yet unknown, we have ruled out several possibilities and are investigating the size-dependence further in on-going studies.

Conventional spectroscopy of bulk MOFs inhibits interpretation of absorption intensities, whereas solution state measurements allow for the determination of extinction coefficients (ε) for all $Fe(TA)_2$ particle sizes. Quantitative analysis of extinction coefficients has driven the quantum mechanical

understanding of semiconductor nanocrystal optical phenomena by relating optical oscillator strengths (f) to detailed information about electronic structure and by providing a practical estimation of particle concentrations from optical spectra.[187;188] Such analysis is currently limited for MOF materials; to date

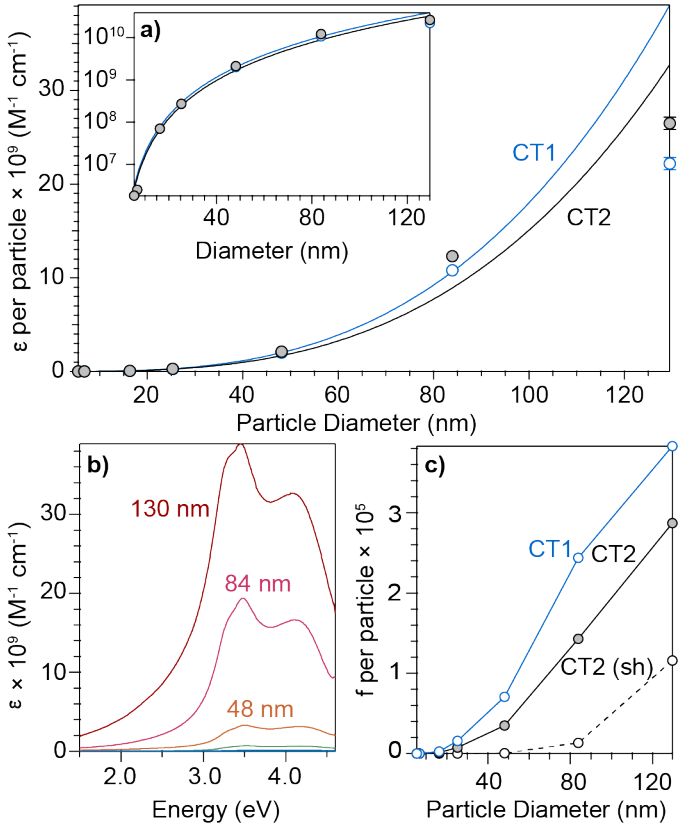

Figure 4.9. Extinction coefficients of $Fe(TA)_2$ nanoparticles. a) CT1 (blue) and CT2 (black) extinction coefficients plotted as ε per particle versus particle diameter. Solid curves are fits of ε to cubic functions of diameter. Pre-factors for CT1 and CT2 fits are 18013 and 15100, respectively. b) UV-Vis traces for all particle sizes plotted as extinction coefficient ε per particle. c) Oscillator strength determined per particle for the two charge transfer bands as well as the shoulder (sh) of CT2.

only one report discusses the dependence of optical properties—in this case fluorescence—on particle size and defectiveness.[112] Figure 4.9a plots the extinction coefficients of peak maxima versus particle diameters, which increase by four

orders of magnitude, from 10^6 (cm^{-1} M^{-1}) for 5.5 nm particles to 10^{10} (cm^{-1} M^{-1}) for 130 nm particles. Extinction coefficients were determined using a linear relationship between concentration and extinction at low concentration, with both absorption and scattering processes contributing to the overall extinction (Fig. C.14). It is evident from the spectra alone that the extinction coefficients depend strongly on particle sizes, with larger sizes absorbing more intensely than smaller particles, as expected from the increased number of absorber units (Fig 4.9b). To explain this dramatic increase in absorber strength, the extinction coefficient data were fitted to cubic functions of particle diameters, as has been demonstrated for lead chalcogenide semiconductor nanocrystals based on the hypothesis that absorber strength per particle arises from increased particle volumes.[189] A cubic relationship produces an excellent fit except for larger sizes, in which the experimental data appears depressed in relation to the expectic cubic trend, most likely due to light scattering (Fig. 4.9a). While greater extinction coefficients may be expected for larger particles, the absorption strength per $Fe(TA)_2$ formula unit depends on particle diameters as well, ranging from 3000 – 7000 cm^{-1} M^{-1}, which are typical values observed for molecular charge transfer bands (Fig. 4.10a).

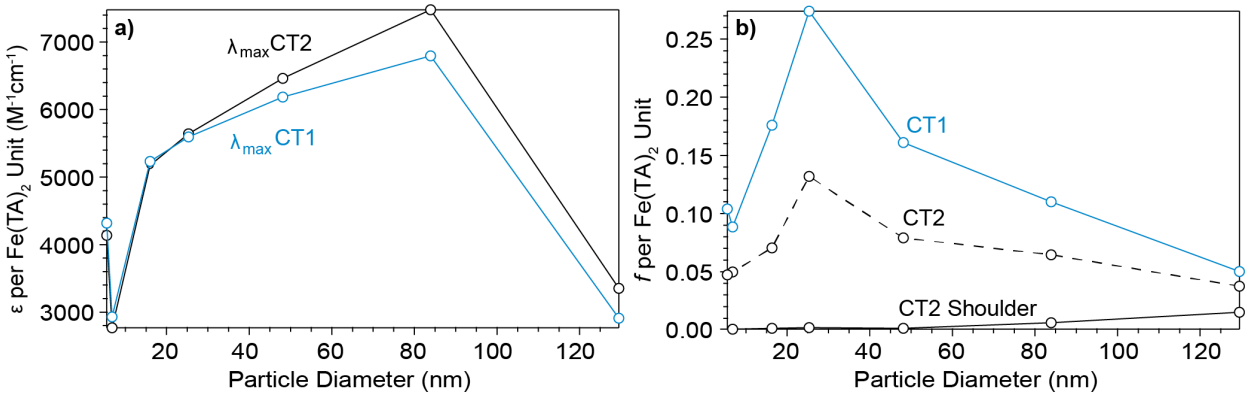

Figure 4.10. The extinction coefficient and oscillator strength of $Fe(TA)_2$ nanoparticles per formula unit. a) The extinction coefficient of $Fe(TA)_2$ nanoparticles per formula unit. Generally, the extinction coefficient per formula unit increases as size increases, although the 16 nm particles and 130 nm particles deviate from this trend. b) Oscillator strength determined per formula unit $Fe(TA)_2$. While the oscillator strength per particle clearly trends upwards with size, here the value appears to peak for the 25 nm particles. Values do not change significantly, however, and could be considered consistent across particle sizes.

For a deeper analysis of absorption intensities, oscillator strengths f can be determined for each of the absorption bands. When calculated per particle, f increases with particle sizes (Fig. 4.9c), as expected for an increased number of absorbing units. Determined per formula unit, the oscillator strength changes minimally with particle sizes, with f values ranging from 0.05 to 0.27 (Fig. 4.10b). In all cases, f per formula unit is on the order of 10^{-1}, as expected for a charge transfer that is both spin and parity allowed. Combined, these results show that colloidal stability enables powerful quantitative analysis of the optical properties of MOF nanocrystals. Although the analysis herein does not yet consider possible non-linear contributions of scattering to total extinction, this type of analysis represents a step forward for understanding the optical properties of MOF structures.[190;191]

Redox Chemistry and Charge Transport of $Fe(TA)_2$ Nanoparticles

Although solid-state techniques and additives such as polymer binders are required to study redox properties of bulk MOFs, the colloidal stability of $Fe(TA)_2$ nanoparticles enabled characterization by solution-state electrochemistry. Figure 4.12a shows cyclic voltammogram (CV) traces for several particle sizes using standard 3-electrode cell configurations. These four smallest-sized particles were stable in 0.1-M $TBAPF_6$ / DMF electrolyte mixtures under applied bias, while attempts to analyze 48-nm particles failed, likely due to aggregation, as the particles precipitated from the stored electrolyte solution over the course of a few days. Although we expected only a single redox event corresponding to $Fe^{2+/3+}$ oxidation, all samples exhibited qualitatively similar traces with three broad, quasi-reversible features appearing at similar applied potentials. The 16-nm colloidal suspension was further investigated due to the well-defined features of its CV trace. As summarized in Figure 4.11d, variable scan rate measurements showed a strong dependence of the peak-to-peak separation ΔE for the lowest-potential redox event at around -0.61 V (purple closed triangles), ranging from 9.2 mV at 100 mV/s to 56 mV at 130 mV/s, while the second event, centered at -0.29 V (purple open circles), showed less reversibility, with ΔE of 126 mV at 100 mV/s to 144 mV at 130 mV/s (Fig. 4.11d), while ΔE for the highest-potential feature, centered around 0.13 V, could not be resolved.

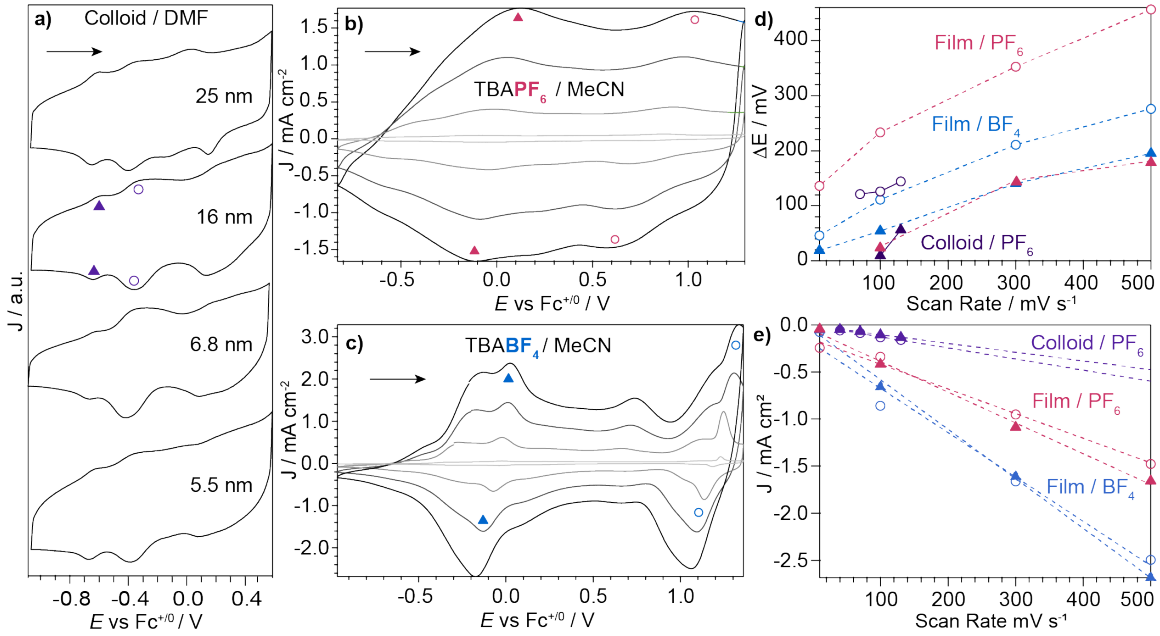

Figure 4.11. Cyclic voltammetry of $Fe(TA)_2$ nanoparticles analyzed as colloids or thin films. Initial scan directions are indicated by arrows. a) CV traces collected at a 130 mV/s scan rate for four particle sizes prepared as colloids in 0.1-M $TBAPF_6$ / DMF; current density is normalized to the second faradaic event. Scan rate dependence of 16-nm particles drop-casted onto glassy carbon in 0.1-M $TBAPF_6$ / MeCN (b) and $TBABF_4$/MeCN (c). Light to dark greyscale traces correspond to 10 mV/s – 500 mV/s. Relevant peaks are marked with filled triangles (first peak analyzed) or open circles (second peak analyzed) in all panels. d) Peak-to-peak separation with respect to scan rate. e) Peak current with respect to scan rate for two reduction peaks in each of the 16 nm particle CVs. Dashed lines correspond to linear fits.

To investigate the origin of these redox events and to demonstrate that the solution processability of colloidal $Fe(TA)_2$ nanoparticles will facilitate their use in MOF-based electrochemical devices, 16-nm $Fe(TA)_2$ were drop-casted onto the surface of glassy carbon electrodes. Figure 4.11b shows the variable-scan rate CVs of the particle films in 0.1 M $TBAPF_6$ / MeCN. Despite the difference in solvent, which was chosen to discourage particle delamination, the CV traces resemble those of the free-standing colloids in Figure 4.11a. Due to the small pore size of $Fe(TA)_2$, we hypothesized that the broad waves of the voltammetric response reflect the

hindered ability of the bulky PF_6^- anion to diffuse through the material. Therefore, these experiments were repeated on particle films using $TBABF_4$, as previous computational work has shown that the BF_4^- anion is just below the pore size of the MOF.[20] In contrast to voltammetry with $TBAPF_6$, the use of $TBABF_4$ causes all peaks to sharpen and induces new voltammetric responses, most notably a sharp, reversible feature at 1.2 V (Fig. 4.11c). For direct quantitative comparison, we investigated two well-defined features from each set of electrolyte experiments, as indicated by open circles and shaded triangles throughout Figure 4.11. Figure 4.11d shows that in both electrolyte media, ΔE is always smaller for the lower-potential event, supporting the assignment of this peak to a surface $Fe^{2+/3+}$ species, which benefits from both better ion-pairing and faster kinetics of ion diffusion. Additionally, the second event (pink circles) for a film in $TBAPF_6$ shows the largest ΔE among all conditions, including the colloidal suspension in $TBAPF_6$ / DMF (purple circles). Interestingly, as shown in Figure 4.11e, the peak current for the events in all experiments exhibit a linear dependence with respect to scan rate. Therefore, even if the particles are employed as colloids, the redox events are adsorption-controlled.[192]

To precisely quantify the role of ions in the redox chemistry of $Fe(TA)_2$ particles, we employed quartz crystal microbalance (QCM) electrodes. Spin-coating 16-nm particles onto the QCMs yielded uniform multi-layer nanoparticle films (Fig. C.21), which allowed us to measure their voltammetric responses and simultaneous mass changes in either $TBAPF_6$ or $TBABF_4$ environments. The frequency of the quartz crystal oscillation is sensitive to mass changes at the crystal surface, allowing monitoring of film loading and ion flux while the potential is scanned. Figures 4.12a and 4.12b show both the CV traces and the number of

moles of anion adsorbed to the particles based on the mass change of the QCM electrode, using the Sauerbrey equation[193] and assuming that all mass change is due to unsolvated PF_6 and BF_4 anions. Once again, the redox waves of the sample analyzed with $TBAPF_6$ exhibits broad features in comparison to the same size nanoparticles in $TBABF_4$ (Fig. 4.11, Fig. C.20). Additionally, substantially more current passes to the particles in the presence of $TBABF_4$. Charge integration shows nearly seven-fold enhancement, with stoichiometric oxidation of nearly all Fe sites, i.e., e^-:Fe = 0.9 when using $TBABF_4$, whereas $TBAPF_6$ yields only e^-:Fe = 0.3. This comparison suggests that more Fe sites are electrochemically accessible in the $TBABF_4$ experiment, which we attribute mainly to the ability of the smaller anions to diffuse through the porous MOF particles, while bulky PF_6 anions merely collect at the nanoparticle surface. This result contrasts with studies of ion diffusion in MOFs with large pores, wherein ion pairing hinders small ions to a greater degree than larger ions.[194] A further contribution may be differences in thin thickness and morphology, although films were homogenous for both cases (Fig. C.24, Table C.7). The mass of the particle films increases in both experiments with oxidizing potentials, as expected for incorporation of charge-balancing anions, but far more anions incorporate when using the smaller BF_4^- ions. Approximately four times as many moles of BF_4^- adsorb compared to PF_6^-, yielding PF_6:Fe = 0.1 and BF_4:Fe = 0.4 (Table C.7). We expect that surface ions provide additional charge-balancing anions needed for stoichiometric oxidation of all Fe sites. Comparing mass changes to redox waves at a given potential provides further insight into the nature of the redox chemistry. Most notably, the coincidence of a sharp increase in mass and current at ca. 1.2 V strongly suggest this redox event corresponds to ion-coupled charge transport to interior Fe sites enabled by the

smaller size of the BF_4^- anion in comparison to the gradual mass changes and broad redox waves of the $TBAPF_6$ experiments. None of the other features in the CV traces are obviously associated with an increase in mass; rather, in $TBAPF_6$ and at low potentials in $TBABF_4$, the mass increases gradually as the cell is scanned oxidatively. A gradual increase in mass therefore indicates that for these features, ions are collecting at the particle surface rather than diffusing through the pores. The observation of several voltammetric features spanning a wide potential window is surprising; however, it is expected that surface species would be oxidized at a lower potential than internal iron sites that require significant ion intercalation. These data stand in stark contrast to two prior reports of bulk $Fe(TA)_2$ cyclic voltammetry. In one study, scanning the bulk material in an air-free environment in $LiBF_4$ / propylene carbonate showed a single redox feature at high potential, assigned to $Fe^{2+/3+}$.[20] In the other report, the material was synthesized in aerobic conditions and scanned in 0.1-M KOH, showing several redox events assigned to varying Fe surface species.[195] Here, we assign the sharp reversible event at 1.2 V in $TBABF_4$ to $Fe^{2+/3+}$, while broad events at lower potential in either electrolyte are assigned to a combination of capacitive charging and surface $Fe^{2+/3+}$ species. Cyclic voltammetry of the 1,2,3-triazole linker in 0.1-M $TBAPF_6$ / DMF reveals a chemically irreversible event at 0.31 V vs $Fc^{+/0}$ (Fig. C.17), supporting the assignment of redox waves to $Fe^{2+/3+}$. Although ion intercalation and ion pairing are frequently invoked to understand MOF redox chemistry, charge storage and sensing, these data represent some of the only direct measurements of ion intercalation processes by employing quartz crystal microbalance electrodes.[194;196] They also show that nanosizing MOFs can improve the availability of redox-active

sites, thus lowering redox potentials through improved ion pairing, a key insight into designing electronic MOF devices.

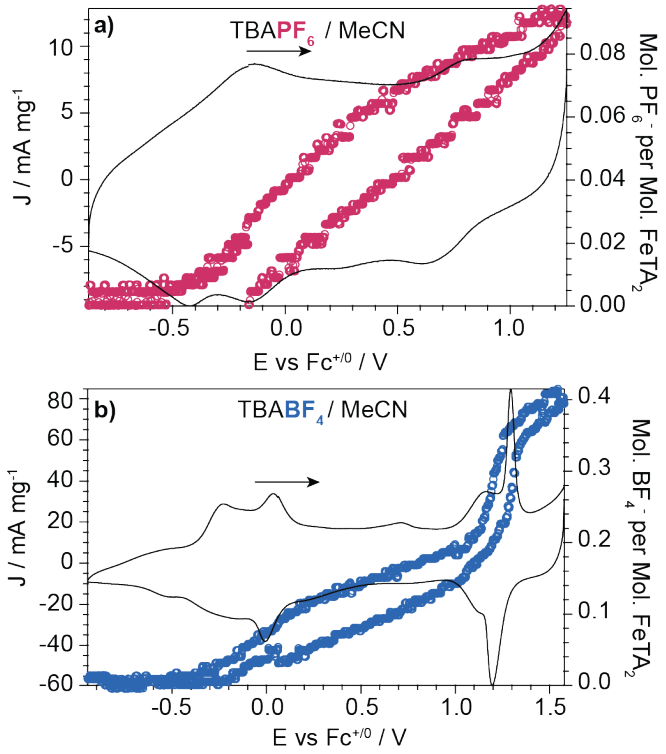

Figure 4.12. Cyclic voltammetry with superimposed QCM data of $Fe(TA)_2$ nanoparticles. Initial scan directions are indicated by arrows. CV traces collected at 100 mV/s with a Pt QCM electrode for 16-nm particles in $TBAPF_6$ / MeCN (a) and $TBABF_4$. (b) Colored open circles refer to the right axis, moles of anions with respect to moles $Fe(TA)_2$ on the QCMs.

Thin film fabrication and solid-state measurements are enabled by the long-term colloidal stability and solution-processability of $Fe(TA)_2$ nanoparticles. Doctor blading high-concentration suspensions onto glass slides afforded uniform films with smooth surfaces, as shown in the cross-sectional FIB-SEM images in Figure 4.13. Additional SEM images and photos of particle films can be found in Appendix C (Fig. C.22-C.25). Figure 4.13b shows conductivities of thin films under N_2 for the three particle sizes: the conductivity increases from 6.33 nS/cm

for the bulk sample to 50.6 nA/cm for 84 nm, and finally to 611 nS/cm for a film comprised of 25-nm particles. A previous report of bulk $Fe(TA)_2$ measured values of 0.1 nS/cm for a sample kept air-free.[20] Although the values herein are higher, the samples still lack oxidation, as even the smallest particles (5.5 nm) handled air-free do not show Fe^{3+} by Mössbauer spectroscopy (Fig. 4.3). After three days of air exposure, the conductivity of the samples increases to 1.21 μS/cm (Bulk), 8.25 μS/cm (84 nm), and 91.0 μS/cm (25 nm) (Fig. 4.13c). The values collected in air agree with the first reported value of 77 μS/cm; the bulk value herein is likely lower due to the air exposure time only lasting three days.[19] These measurements suggest a size-dependence in the charge transport behavior of $Fe(TA)_2$, with the conductivity increasing as the particle size decreases. While this trend may be unexpected due to smaller particles introducing more grain boundaries, the cross-sectional SEM images indicate that nanoparticles exhibit denser inter-particle packing in comparison to the bulk material (Fig. 4.13). Hence, despite the largest grain size, the overall conductivity of the bulk sample still suffers in comparison to well-packed nanoparticles. After air exposure, the conductivity of all samples increases 2 to 3 orders of magnitude, most likely due to oxidation and the creation of mixed valency. Mössbauer data shows that samples allowed to oxidize in air varying small amounts of Fe^{3+} but the degree of oxidation shows no trend with respect to particle size (Fig. C.12). Therefore, the main cause of size-dependence in the conductivity values arises from efficient particle packing. These results imply that grain boundaries in $Fe(TA)_2$ may present relatively shallow barriers to charge transport. Notably, in polycrystalline organic semiconductor films, smaller grain size does not always decrease conductivity; transport in such systems depends extensively on microstructure and grain boundary site energy.[197;198;199] Further

investigations are ongoing into the charge transport mechanisms of $Fe(TA)_2$ nanoparticles, including the dependence on size, redox-state, and guest-host interactions for technologies ranging from charge storage to electrochemical sensing.

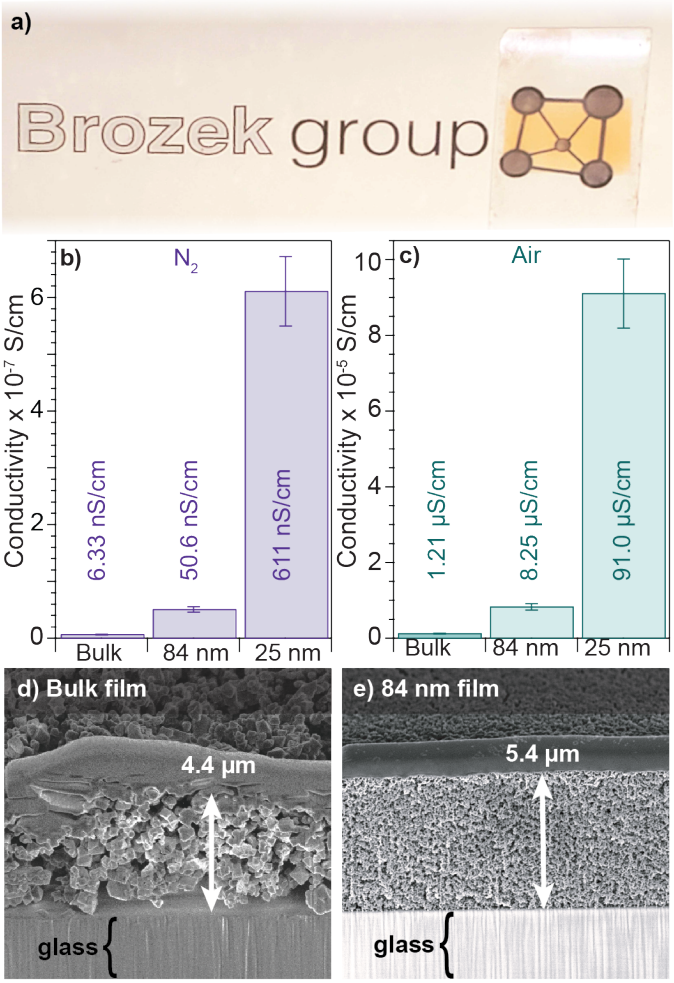

Figure 4.13. Charge transport measurements of $Fe(TA)_2$ nanoparticle thin films. a) Photograph of a thin film prepared under N_2 by doctor-blading 84-nm nanoparticles. b) Van der Pauw DC conductivity values of three $Fe(TA)_2$ thin films under N_2 and after three days of air exposure. Values for samples in air are in turquoise. Inset shows a zoomed-in view of conductivity values of the films under N_2. Error is derived from the ratio between the probe width and the sample width. d) FIB-SEM image of a cross-section of a representative bulk film. e) FIB-SEM cross-section of a representative 84-nm film, showing dense inter-particle packing.

Conclusions

In summary, conductive $Fe(TA)_2$ nanoparticles can be prepared reproducibly with excellent colloidal stability. The solution processability of this unprecedented class of semiconductor nanocrystals enables solution-state spectroscopy and electrochemistry, whereas MOF characterization typically requires solid-state techniques. These measurements reveal an unexpected size dependence to the optical transitions and enable the first analysis of MOF extinction coefficients, which scale with particle size. $Fe(TA)_2$ particles can be probed by colloidal and thin-film voltammetry, revealing show redox chemistry sensitive to ion pairing and intercalation effects within the porous materials. Finally, we demonstrated that the particles can be easily processed into thin films for charge transport measurements that reveal increased conductivity compared to the bulk material.

CHAPTER V

NANOCONFINEMENT EFFECT AND REDOX CHEMISTRY IN FE(TA)$_2$ NANOPARTICLE THIN FILMS

This chapter includes unpublished and co-authored material from the prospective manuscript Huang, J,; Marshall, C.R.; Ojha, K.; Shen, M.; Kadota, K.; McKenzie, J.; Fabrizio, K.; Brozek, C.K. Giant Redox Entropy in Intercalation Chemistry of Nanoconfined MOF Nanocrystals. The project in this chapter was conceptualized and developed by Checkers R. Marshall, Jiawei Huang, and Carl Brozek. The manuscript was written by Jiawei Huang, with editorial assistance from Checkers R. Marshall and Carl K. Brozek; the manuscript was edited by Checkers R. Marshall for this dissertation. The experimental work in this chapter was performed by Jiawei Huang, Kasinath Ojha, Checkers R. Marshall, Meikun Shen, and Jacob McKenzie.

Metal-organic frameworks (MOFs) have drawn tremendous scientific interest in the field of electrochemical energy storage and conversion. Their tunable porous structures allow facile transportation of electrolyte species, and the large surface area provides a high density of electroactive sites for driving electrochemical processes. Distinct from electrochemical reactions on the non-porous electrode surface, electrolyte species can intercalate into the MOF pores to drive redox events via ion-coupled charge transport at the interior electrochemical interface. Previous studies into porous carbon-based materials and two-dimensional layered transition metal oxides have reported that the nanoconfinement effect inside the pore environment alters the solvation and intercalation structures of electrolyte species, significantly impacting the electrochemical properties of porous materials.[200;201]

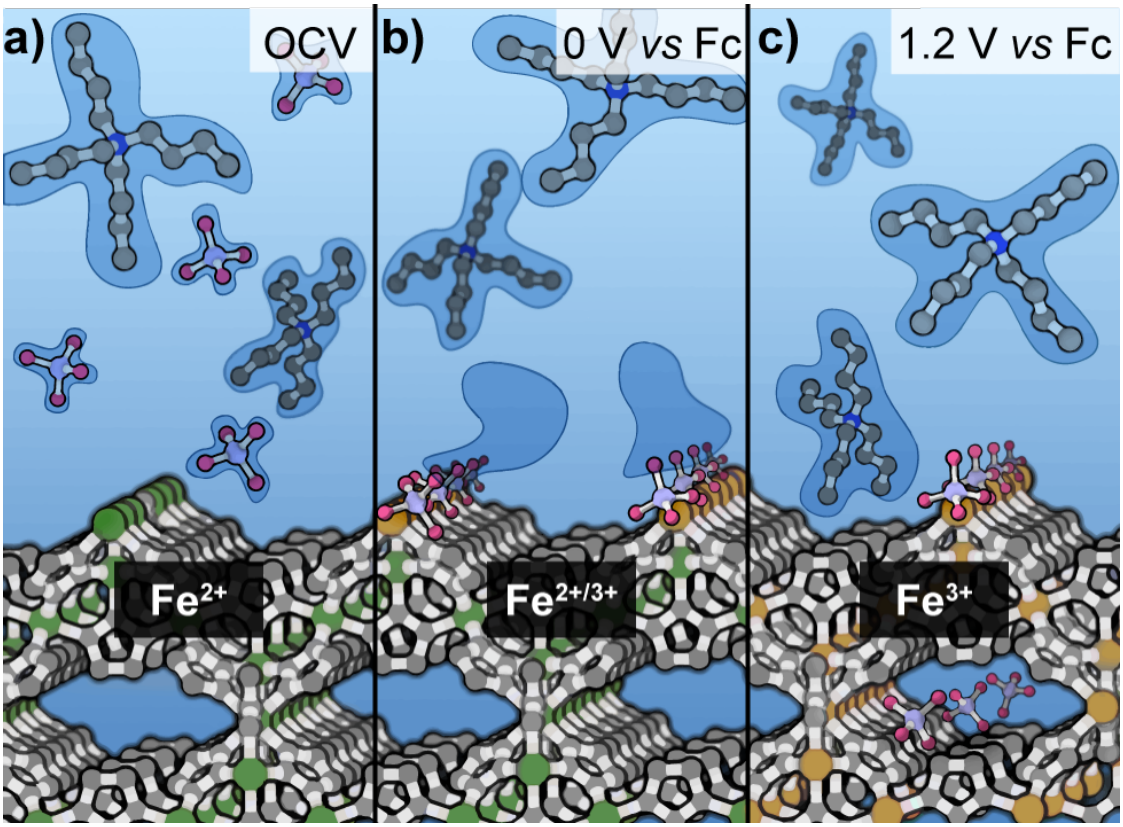

Figure 5.1. Scheme of ion intercalation and redox chemistry in $FeTA_2$ film. (a) $FeTA_2$ film in $TBABF_4$ electrolyte in acetonitrile under open circuit voltage (OCV). (b) BF_4^--induced Fe^{2+}/Fe^{3+} redox via the partial desolvation and adsorption of BF_4^- anions on the surface Fe sites. (c) BF_4^--induced Fe^{2+}/Fe^{3+} redox induced by the complete desolvation and intercalation of BF_4^- anions into the nanoconfined $FeTA_2$ pore. Note: green, orange, gray, red, blue, and purple dots represent Fe^{2+}, Fe^{3+}, C, F, N, and B atoms, respectively. Blue cloud-shaped area represents the solvation shell of electrolyte ions.

By comparison, a fundamental understanding of the ion intercalation redox chemistry inside the nanoconfined MOF pore and its implications for practical applications still remain elusive, mainly due to the difficulty of differentiating intercalation redox chemistry inside the pore from the reactions on the surface of the MOF electrode. Previous studies on the ferrocenecarboxylic acid-functionalized MOF-808/Nu-1000/NU-1003 series of MOFs, which are reticular structures with varying pore size, show clearly that ion diffusion increases with increasing pore

size, while electron transport shows the opposite trend.[202] Meanwhile, in the MOF Zn(dcph-Oh-NDI), ion diffusion was explored with different ion sizes and it was found that strong interactions between the ions and the reduced redox-active napthalenediimide linkers can hinder ion movement.[203] To date, the studies involving charge transport on MOFs are generally those with large pore size, with ample room for ion diffusion. Herein we explore a dense MOF, Fe(1,2,3-triazolate)$_2$, as we expect that a small pore size will lead to severe nanoconfinement effects. Solvated BF_4^- anions have a diameter of 10 Å in acetonitrile, and the Fe(TA)$_2$ pore is merely 4.54 Å. Desolvating the BF_4 anions entirely gives a radius of 3 Å, which would allow for ion intercalation, but the desolvaiton process requires energetic input. Therefore, in the previous chapter, we hypothesized that the voltammetric response of Fe(TA)$_2$ included both surface redox reactions at low oxidizing potentials, and intercalation redox chemistry at much higher potentials. Herein, we unravel how the nanoconfinement effect impacts the ion-intercalation redox chemistry inside Fe(TA)$_2$ (TA = 1,2,3-triazolate) nanoparticles and assign the redox features to surface and intercalation events (Fig. 5.1).

Fe(TA)$_2$ nanoparticles with tunable sizes were synthesized by following our recent work, where different amounts of 1-methylimidazole as a "modulator" were added into bulk synthesis procedures.[204] Scanning electron microscopy (SEM) analysis showed that nanoparticles of Fe(TA)$_2$ MOFs with sizes of 16 nm, 25 nm, and 46 nm were prepared (Fig. D.1). Powder X-ray diffraction (PXRD) patterns further confirmed the retention of the crystalline structure of obtained Fe(TA)$_2$ nanoparticles (Fig. D.1). Those nanoparticles were spin-coated into a Fe(TA)$_2$ film on the quartz crystal electrode for electrochemical investigations. Previous reports indicate that the Fe centers in Fe(TA)$_2$ are redox-active,[20;195] making this

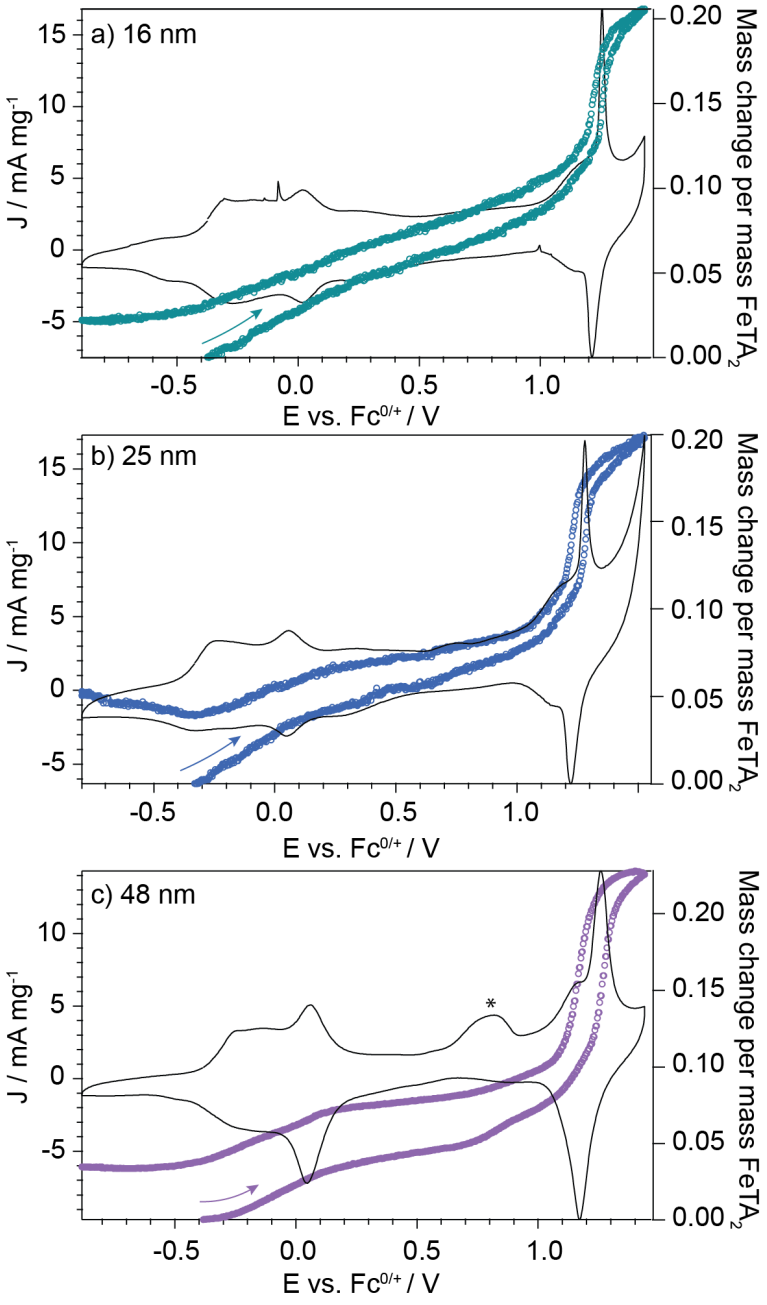

Figure 5.2. CV scans and corresponding mass change data from EQCM for three $Fe(TA)_2$ nanoparticle thin films: a) 16 nm particles (4.0 μg), b) 25 nm particles (4.0 μg) and c) 48 nm particles (5.7 μg). Asterisk indicates an irreverible event arising from the MOF linker. Arrows indicate the direction of the scan from open circuit potential; for clarity, the end of the QCM loop returning to open circuit has been removed.

small-pore MOF an ideal model to study ion intercalation in well-ordered porous materials.

Identifying Intercalation Chemistry in Fe(TA)$_2$ Films

THe CV scans of Fe(TA)$_2$ films, composed of particles of varying size, exhibit similar voltammetric features in the potential range from -0.4 V to 0.2 V vs. $Fc^{0/+}$ (Fig. 5.2). All films show several broad voltammetric features at low potential, and a sharp and reversible feature at ca. 1.2 V vs. $Fc^{0/+}$, which is independent of other voltammetric features in the CV trace (Fig. D.2). The difference in voltage between the various features suggests that the Fe sites within Fe(TA)$_2$ are fundamentally different in nature. Previous studies have shown that the position of $Fe^{2+/3+}$ redox can be tuned by manipulating the Fe coordination sphere.[205] In the case of the ideal Fe(TA)$_2$ material, all Fe sites are octahdral and coordinated by 6 N-donating triazole ligands. However, nanoparticles often exhibit significant surface defects, which may contribute to coordination site changes and a resulting shift in redox potential.

Even though coordination environment can shift redox potential, this is insufficient to explain the event at 1.2 V vs $Fc^{0/+}$, which unusally sharp and reversible. Such a sharp "butterfly" signature has previously been attributed to adsorbates on the surface of noble metal electrodes undergoing a disorder-order phase transition; notably, however, these events are not associated with any increase in mass as the adsorbates are already on the electrode surface.[206] Accordingly, we monitored the potential-dependent mass variation on Fe(TA)$_2$ film using in situ electrochemical quartz crystal microbalance (EQCM). A significant mass increase and decrease was observed at the 1.2 V feature in the anodic and cathodic direction of CV trace, respectively (Fig. 5.2), excluding the possibility

that the 1.2 V voltammetric feature was attributable to the phase change of absorbates on the $Fe(TA)_2$ film surface. The total mass change per formula unit $Fe(TA)_2$ only increases slightly as particle size increases. However, if normalized to particle volume, the mass change of the 1.2 V feature shows a linear trend, indicative that the feature originates from the intercalation of BF_4^- anions into the confined MOF pores (Fig. 5.3b). Reversibility also suffers in the case of the 48-nm particles; both the voltammetric features as well as the QCM loop are noticeably wider in this sample, most likley due to an intrinsically longer diffusion pathlegnth across the particles' diameter (Fig. 5.2c). Lower-energy redox events show a mass increase that is proportional to the surface area of the nanoparticles, further indicating that surface and intercalation redox events are distinct in this system (Fig. 5.3a).

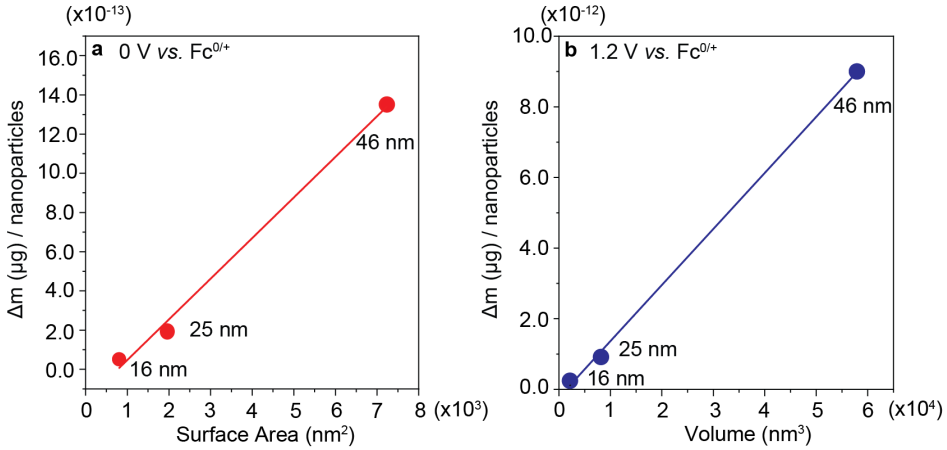

Figure 5.3. Plotting the change in mass on the QCM electrode over the voltage range of surface and intercalation features. a) The feature at 1.2 V vs $Fc^{0/+}$ for the three films of differently-sized particles vs the particle volume shows a linear relationship. b) The feature at 0.0 V instead shows a linear relationship with respect to paricle surface area.

To support the assignment of the 1.2 V feature to BF_4^- anion intercalation redox reaction, time-of-flight secondary ion mass spectrometry (ToF-SIMS) was

employed to map the depth distribution of both BF_4^- anions and TBA^+ cations via sputtering through the $Fe(TA)_2$ film. Given that bulky TBA^+ cations cannot intercalate into the pore of $Fe(TA)_2$ nanoparticles, the distribution of TBA^+ cations can be used as a reference to identify the surface region of $Fe(TA)_2$ film in ToF-SIMS results (denoted as the gray area throughout Fig. 5.4). After applying the reducing potential of -1.0 V vs. $Fc^{0/+}$ to $Fe(TA)_2$ film, the depth-dependent boron signal, originating from the bond cleavage of BF_4^- anions during the surface sputtering, was only detected within the surface region (Fig. 5.4a(i)). This is consistent with the spatial distribution of $TBABF_4$ electrolyte under a negative applied potential, where both BF_4^- anions and TBA^+ cations should remain on the surface of $Fe(TA)_2$ film. ToF-SIMS further showed that the boron signal remained on the surface region after applying 0.2 V vs. $Fc^{0/+}$ to $Fe(TA)_2$ film (Fig. 5.4a(ii)), illustrating that the voltammetric features in the potential range from -0.4 V to 0.2 V vs. $Fc^{0/+}$ originated from the adsorption (anodic current) or desorption (cathodic current) of BF_4^- anions on the surface Fe sites. By contrast, the boron signal is still observable even when sputtering into the $Fe(TA)_2$ nanoparticle film after applying the potential of 1.4 V vs. $Fc^{0/+}$ (Fig. 5.4a(iii)). These results clearly confirm the proposed mechanism depicted in Figure 5.1: at low voltage, surface redox occurs, then the intercalation of BF_4^- anions occurs at the 1.2 V voltammetric feature.

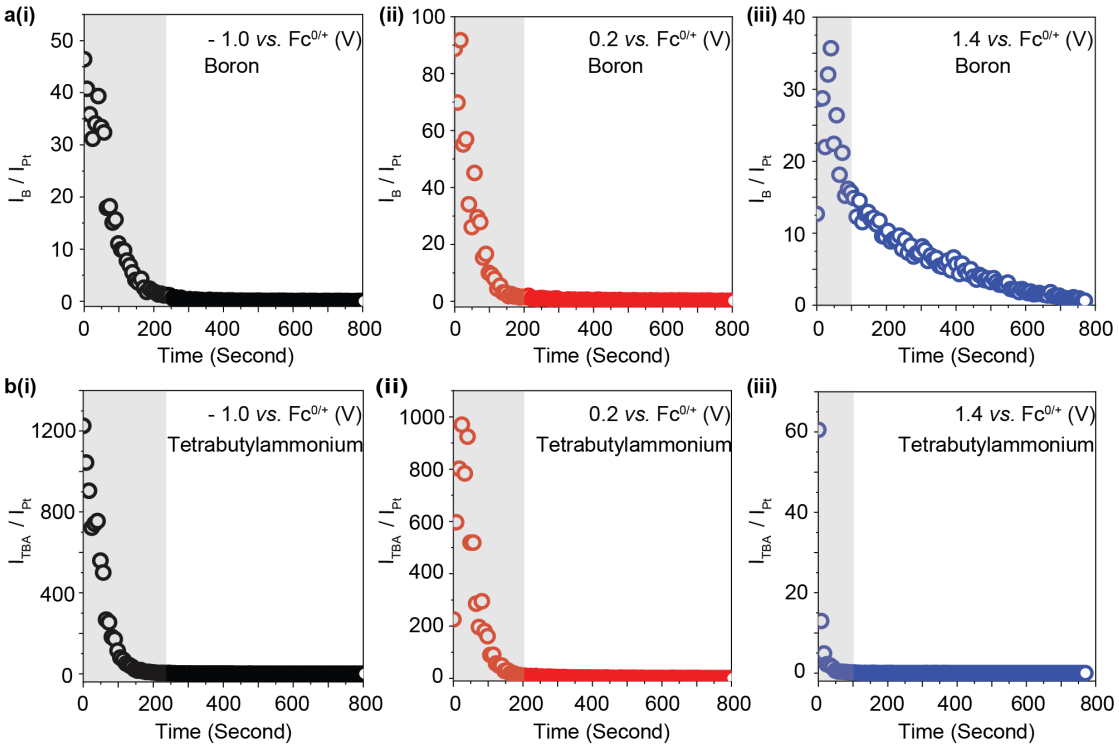

Figure 5.4. ToF-SIMS of spatial distribution of boron and tetrabutylammonium (TBA^+) in $Fe(TA)_2$ film after applying different voltages. (a) ToF-SIMS depth profile of boron within $Fe(TA)_2$ film after applying (i) -1.0 V vs. $Fc^{0/+}$, (ii) 0.2 V vs. $Fc^{0/+}$, and (iii) 1.4 V vs. $Fc^{0/+}$. (b) ToF-SIMS depth profile of TBA^+ within $Fe(TA)_2$ film after applying (i) -1.0 V vs. $Fc^{0/+}$, (ii) 0.2 V vs. $Fc^{0/+}$, and (iii) 1.4 V vs. $Fc^{0/+}$. Both boron and TBA^+ signals are referenced to the Pt signal from the QCM crystal surface. The gray area represents the surface region of $Fe(TA)_2$ film that is defined by the distribution of the TBA^+ siganl. The spin-coating amount of 16-nm $Fe(TA)_2$ nanoparticles to those three EQCM electrodes was controlled to be ca. 5.5 μg (i.e., ca. 60 nm in film thickness) in order to obtain depth-dependent data.

Investigations into the charge variation across the $Fe(TA)_2$ film in CV measurements found that the mass increase in the anodic CV direction also cooperated with the continuous accumulation of positive holes in the $Fe(TA)_2$ film (Fig. D.4). These mass and charge increases of the $Fe(TA)_2$ film suggest that voltammetric features both from the surface and inside the nanoconfined

pore of $Fe(TA)_2$ follow the ion-coupled charge transfer mechanism, where the oxidation of Fe^{2+} to Fe^{3+} requires the adsorption/intercalation of BF_4^- anions to Fe centers to maintain the charge neutrality of the $Fe(TA)_2$ film. Interestingly, distinct from the mass change (Fig. 5.2a), the charge increased more uniformly and did not exhibit a significant change at the redox feature of 1.2 V vs. $Fc^{0/+}$ (Fig. D.3). We propose that holes can be initially stored at C2p and N2p orbitals of triazolate linkers in $Fe(TA)_2$,[207;181] and the further intercalation of BF_4^- anions to the inner Fe sites induces the spatial redistribution of holes to Fe centers, leading to Fe^{2+}/Fe^{3+} redox reactions. The ratio of BF_4^-/integrated charge was ca. 0.42 rather than 1 in the CV trace of $Fe(TA)_2$ film; we note that the mass variation in EQCM is a net value including the mass decrease by the desorption of solvent and TBA^+ cations from the surface and nanopores, and the mass increase due to the adsorption/intercalation of BF_4^- anions to the $Fe(TA)_2$ film. This net effect might underestimate the number of BF_4^- anions that participate in Fe^{2+}/Fe^{3+} redox events inside the $Fe(TA)_2$ film.

To unravel the nature of ion intercalation, the apparent mass-to-charge ratio can be determined as follows in Equation 1:

$$M'_w = zF(\frac{\Delta m}{\Delta Q})$$

where z is the number of electrons and F is the Faraday's constant. The obtained M'_w can be further used to calculate the solvation number (n) of BF_4^- anions during the intercalation/de-intercalation process via Equation 2:

$$n = \frac{M'_w - M_w(BF_4^-)}{M_w(solvent)}$$

where $M_w(BF_4^-)$ is the molecular weight of BF_4^- anions and M_w (solvent) is the molecular weight of solvent (e.g., acetonitrile). For complete desolvation during

intercalation, a $\frac{\Delta m}{\Delta q}$ slope of 0.9 is expected, assuming that n = 0 and $M_w = M_w(BF_4^-)$. As shown in Figure 5.5, the slope of the intercalation feature (ca 0.8) matches well with this value, demonstrating that BF_4 anions undergo complete desolvation. By comparison, the slope of $\frac{\Delta m}{\Delta q}$ for BF_4^--adsorption-induced surface redox feature was found ca. 0.2, which is much smaller than the theoretical value (i.e., 0.9). This illustrates that the adsorption of BF_4^- anions must also induce desorption of other species from the film surface, such as solvent molecules and TBA^+ cations. In the cathodic scan direction, the de-intercalation gives a slope of 1.9, higher than the theoretical value of 0.9. From Equation 1 and 2, the corresponding solvation number n is ca. 2, suggesting that BF_4^- anions are partially solvated by acetonitrile once they de-intercalate from the nanopores and move to the surface. The surface events in the cathodic direction give a slope of 0.1, indicating that other species (solvent and cations) may replace BF_4 anions once they desorb from the film surface.

Taken together, potential-dependent mass and charge variations and ToF-SIMS analysis clearly demonstrat that the voltammetric features in the range of -0.4 to 0.2 V vs $Fc^{0/+}$ can be assigned to surface $Fe^{2+/3+}$ reactions, coupled with partial desolvation of the BF_4 anions, whereas the feature at 1.2 V originates from BF_4^- intercalation induced $Fe^{2+/3+}$ redox chemistry in the nanoconfined pores of $Fe(TA)_2$ particles (Fig. 5.1). Given that the solvated BF_4^- anions (diameter of ca. 10 Å in acetonitrile) are larger than the $Fe(TA)_2$ cavity (diameter of ca. 4.54 Å), a high potential of 1.2 V vs. $Fc^{0/+}$ is required as a driving force to achieve the complete desolvation of BF_4^- anions into the nanoconfined pores.

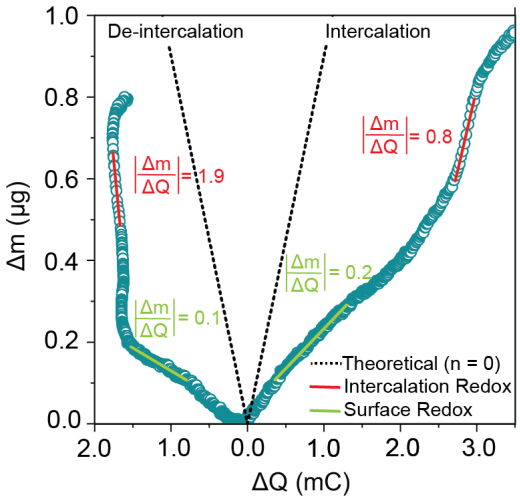

Figure 5.5. Mass change vs. charge change in $Fe(TA)_2$ film. The theoretical result with the slope of ca. 0.9 is shown in the black dashed line. The experimental data is shown as the blue dots, where the red line stands for the potential region for BF_4^--intercalation/de-intercalation-induced Fe^{2+}/Fe^{3+} redox feature at 1.2 V vs. $Fc^{0/+}$ and the green line stands for the potential region for BF_4^--adsorption/desorption-induced Fe^{2+}/Fe^{3+} redox feature from -0.4 V to 0.2 V vs. $Fc^{0/+}$. The mass and charge changes of $Fe(TA)_2$ film collected at a 10 mV/s scan rate using 0.1 M $TBABF_4$ / MeCN.

Factors Controlling Ion Intercalation Redox Chemistry in $Fe(TA)_2$

Investigating how different experimental factors will impact redox behaviors inside the pore and on the surface of $Fe(TA)_2$ nanoparticles help establish the fundamental picture of ion intercalation redox chemistry within the nanoconfinement environment of MOF nanoparticles. The role of film thickness in governing redox properties is usually not considered in MOF electrochemistry. Film-thickness-dependent studies were conducted by first spin-coating ca. 4.0 μg of 16-nm $Fe(TA)_2$ nanoparticles onto the quartz crystal electrode. Atomic force microscope (AFM) showed that those 16-nm $Fe(TA)_2$ nanoparticles self-assembled into a film with the thickness of ca. 21 $\pm$ 5 nm (Fig. 5.6a, suggesting the formation of single-particle-thickness $Fe(TA)_2$ film. CV measurements of this $Fe(TA)_2$ film were collected in a narrow potential window to isolate surface and

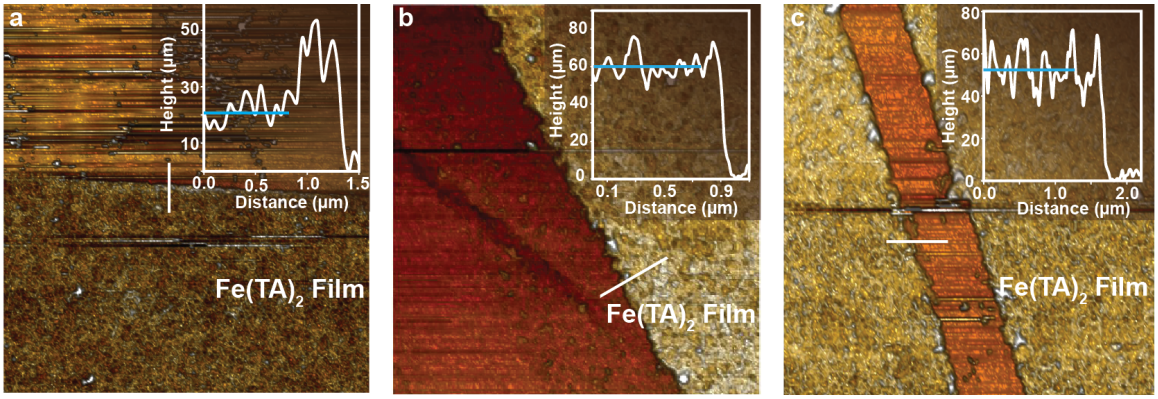

Figure 5.6. AFM images of films of $Fe(TA)_2$ particles on QCM electrodes to determine film thickness. a) A film comprised of 16-nm particles with a thickness of 21 ± 5 nm. A film comprised of 16-nm particles with a thickness of 60 ± 6 nm. c) A film comprised of 25-nm particles with a thickness of 53 ± 8 nm.

ion-intercalation redox features. It was found that ΔE of both surface and ion-intercalation redox features did not vary in different CV traces (Fig. 5.7a(ii) and (iii)). This demonstrates that both surface and intercalation redox reactions on 21-nm-thickness $Fe(TA)_2$ film are kinetically reversible. Further increasing the spin-coating amount of 16-nm $Fe(TA)_2$ nanoparticles to 5.5 μg led to a $Fe(TA)_2$ film with a thickness of 60 ± 6 nm (i.e., ca. four layers of particles as shown in Fig. 5.6b). In the thicker film, surface-isolated events remain kinetically reversible (Fig. 5.7b(ii)), whereas the intercalation chemistry at 1.2 V vs. $Fc^{0/+}$ gradually became kinetically irreversible as evidenced by the increase of ΔE in subsequent CV scans (Fig. 5.7b(iii) and 5.7b(iv)). Such ΔE increase together with the decrease of the current density (Fig. 3b(iii)) of the 1.2 V redox feature illustrates that increasing film thickness hinders the intercalation dynamics of BF_4^- anions and suppresses the ion intercalation redox chemistry inside the nanoconfined pore environment.

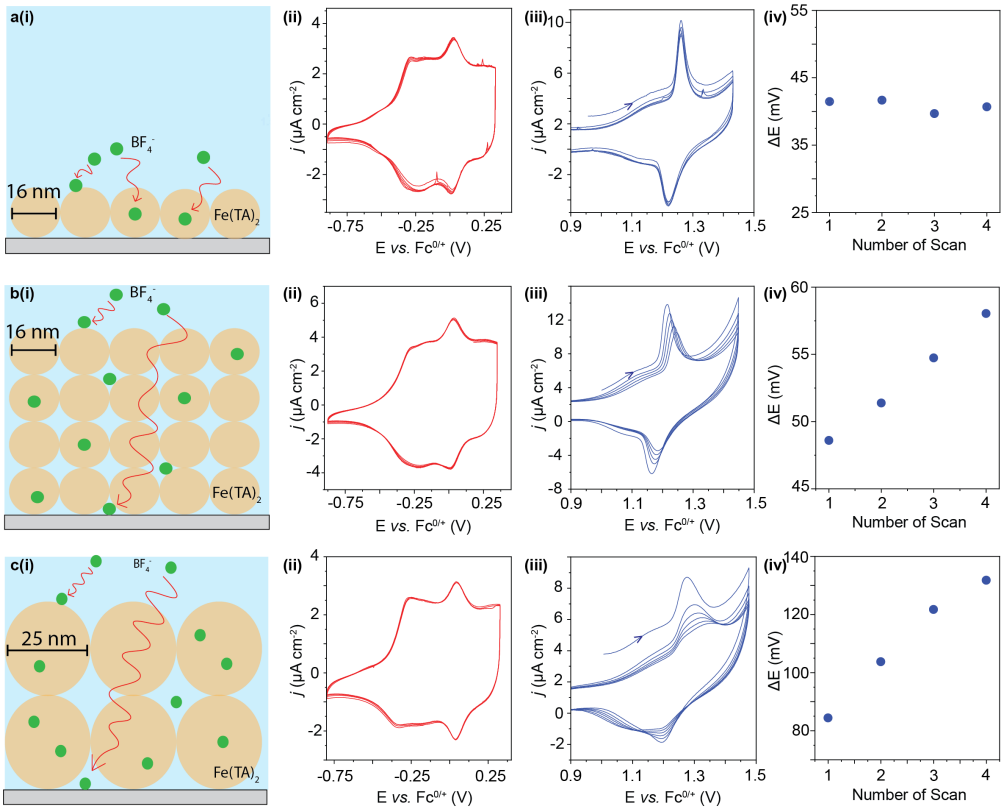

Figure 5.7. Film thickness, particle size, and redox reversibility. a) A thin 16-nm film with thickness of 21 ± 5 nm shows reversible features at both a low oxidizing potential (a(ii)) and a high oxidizing potential (a(iii, iv)). b) A thicker film, 60 ± 6 nm, also comprised of 16-nm particles, shows good reversibility only at lower potentials (b(ii)) and suffers at higher potential (b(iii, iv). c) A film made with larger 25-nm particles, measuring 53 ± 8 nm in thickness, also shows good reversibility in the lower range of potential (c(ii) and suffers from poor reversibility at high potential c(iii, iv)

Further, a 53 ± 8 nm-thickness $Fe(TA)_2$ film (i.e., ca. two particle layers) was prepared by loading ca. 4.0 μ g of 25-nm $Fe(TA)_2$ nanoparticles onto the electrode (Fig. 5.6c). As shown in Fig. 5.7c(ii) and Fig. D.5, the use of larger 25-nm nanoparticles did not affect the thermodynamic (i.e., E1/2) and kinetic properties (i.e., ΔE variation) of surface redox reaction. In contrast, a more significant ΔE increase (Fig. 5.7c(iv)) and the current density decrease (Fig.

5.7c(iii)) were detected in CV scans as compared to those on the similar thickness film made by 16-nm $Fe(TA)_2$ nanoparticles (Fig. 5.7b(iii) and 4b(iv)). It is possible that for BF_4^- anions, the distance of inner-particle intercalation inside the film prepared by 25-nm nanoparticles is longer than that inside the similar thickness film formed by more assembled layers of 16-nm $Fe(TA)_2$ nanoparticles, where more inter-particle space exists to provide possible ion pathways. A longer inner-particle intercalation pathway leads to the more sluggish intercalation dynamics of BF_4^- anions and severely hinders the intercalation redox reaction inside the pore of 25-nm $Fe(TA)_2$ nanoparticles. Taken together, film-thickness-dependent studies show that the intercalation of BF_4^- anions to $Fe(TA)_2$ has a more significant impact on the intercalation redox feature at 1.2 V vs. $Fc^{0/+}$ rather than the surface redox reaction since BF_4^- anions are still accessible to surface Fe sites regardless of the film thickness. The stark difference in peak position, shown in Figure 5.8, further indicates that thicker films and larger particles cause intercalation redox chemistry to require more energy with each subsequent scan. Practically, these results suggest that film thickness and particle size are both critical variables to consider in MOF-based charge storage devices.

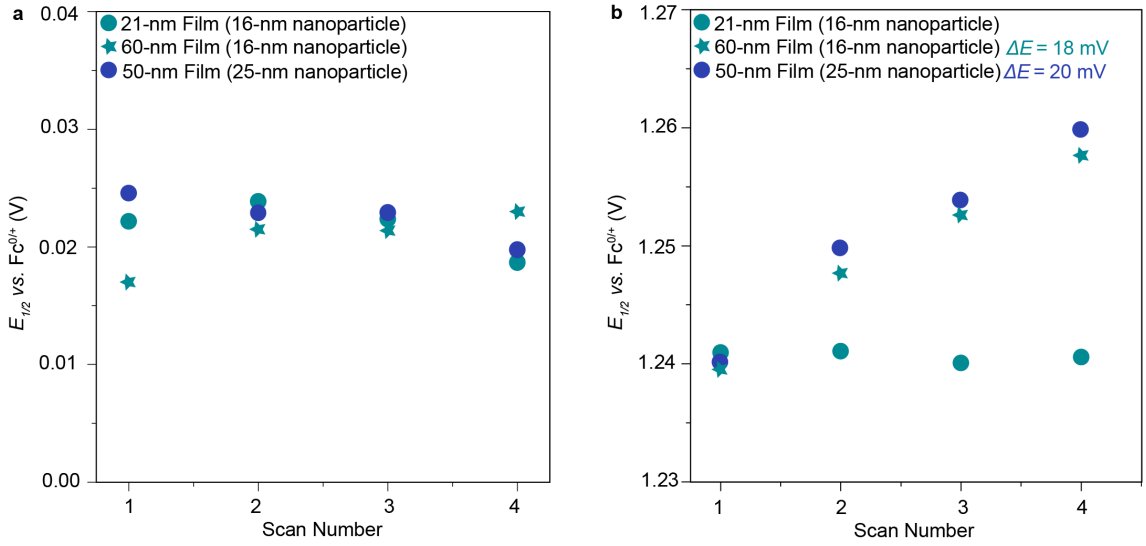

Figure 5.8. Tracking the changes in $E_{1/2}$ and ΔE in three different $Fe(TA)_2$ thin films. (a) $E_{1/2}$ of redox feature at 0 V vs. $Fc^{0/+}$ for $Fe(TA)_2$ film with different film thicknesses. (b) $E_{1/2}$ of redox feature at 1.2 V vs. $Fc^{0/+}$ for $Fe(TA)_2$ film with different film thicknesses. Green dots represent $E_{1/2}$ of 21-nm-thickness $Fe(TA)_2$ film (4.0 μg of 16-nm nanoparticles). Green stars represent $E_{1/2}$ of 60-nm-thickness $Fe(TA)_2$ film (5.5 μg of 16-nm nanoparticles). Blue dots stand for $E_{1/2}$ of 50-nm-thickness $Fe(TA)_2$ film (4.0 μg of 25-nm nanoparticles.)

Ion-pairing strength has also been reported to affect the intercalation of counter ions into the pore of MOF nanocrystals.[203] By keeping the BF_4^- anions constant, but changing the TBA^+ cations to the smaller trimethylamine cations (TMA^+), it is expected that the increase of ion-pairing strength will suppress the BF_4^- intercalation and the corresponding redox reactions within the $Fe(TA)_2$ pore. Indeed, as shown in Fig. 5.9a, $E_{1/2}$ of the intercalation redox feature shifted positivily by 40 mV from ca. 1.23 V vs. $Fc^{0/+}$ in $TBABF_4$ electrolyte to ca. 1.27 V vs. $Fc^{0/+}$ in $TMABF_4$ electrolyte. A positive shift of $E_{1/2}$ was also detected for surface redox features (e.g., from ca. 0.02 V vs. $Fc^{0/+}$ in $TBABF_4$ to ca. 0.04 V vs. $Fc^{0/+}$ in $TMABF_4$). Further use of $LiBF_4$ as the electrolyte greatly reduced the current density of both intercalation and surface redox features (Fig. 5.9a),

suggesting that the strongest ion-pairing strength induced by the smallest Li^+ cations severely prevented BF_4^- anions from neither adsorbing on the surface nor intercalating into the pore of $Fe(TA)_2$ nanoparticles. These cation-dependent electrochemical studies discover that the ion-pairing strength plays an essential role in determining both surface and intercalation redox properties of $Fe(TA)_2$ film.

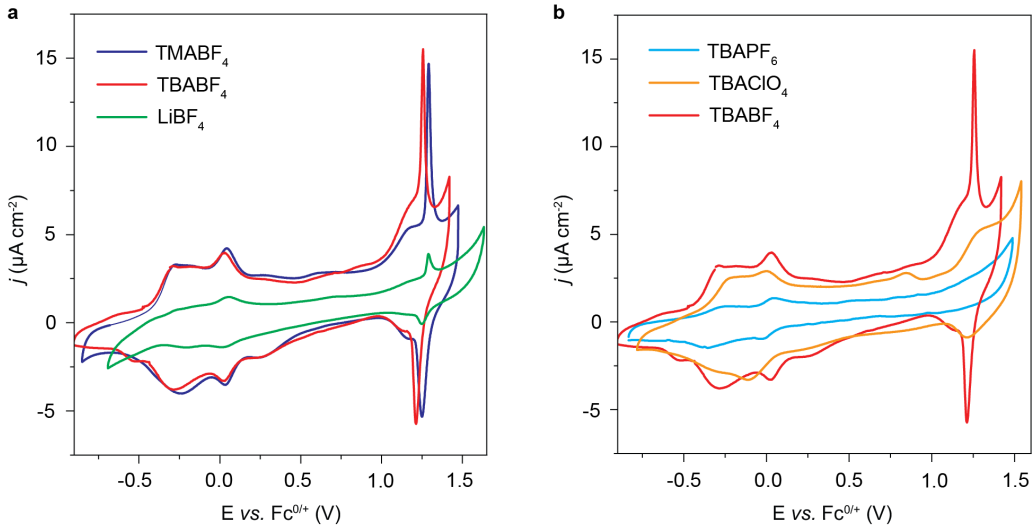

Figure 5.9. Electrolyte-dependent redox properties in $Fe(TA)_2$ nanoparticle film. (a) Cation-dependent CV measurements of 16-nm $Fe(TA)_2$ nanoparticle film. (b) Anion-dependent CV measurements of 16-nm $Fe(TA)_2$ nanoparticle film.

The impact of anion size relative to the pore size of $Fe(TA)_2$ nanoparticles on controlling the intercalation redox chemistry should also be considered. Given the similar size between BF_4^- anions (i.e., ca. 3 Å in diameter) and the cavity of $Fe(TA)_2$ nanoparticles (i.e., ca. 4.5 Å in diameter), BF_4^- anions enable to intercalate into the nanoconfined pore under the sufficient electrochemical potential at ca. 1.2 V vs. $Fc^{0/+}$. Instead, the use of ClO_4- anions (ca. 4.8 Å in diameter) greatly suppressed the ion-intercalation redox feature as compared to the surface redox features (Fig. 5.9b), suggesting that the intercalation was blocked if electrolyte ions are larger than the cavity of $Fe(TA)_2$ nanoparticles. Indeed, this

ion-intercalation redox feature from the nanoconfined $Fe(TA)_2$ pore completely disappeared by using even larger PF_6^- anions as electrolytes (i.e., ca. 5.0 Å in diameter) (Fig. 5.9b).

Further titration of small amounts of $TBAPF_6$ (i.e., in the mM scale) into 0.1 M $TBABF_4$ electrolyte was found to have a more pronounced impact on hindering the BF_4^- intercalation chemistry inside the $Fe(TA)_2$ pore as compared to the surface redox reaction as evidenced by the faster decrease of current density at 1.2 V vs. $Fc^{0/+}$ (Fig. 5.10). In addition, the ΔE of BF_4^- intercalation redox feature also increased more significant than that of surface redox features, showing the sluggish BF_4^- intercalation dynamics in the presence of the larger PF_6^- anions (Fig. D.4). Similar redox behaviors of $Fe(TA)_2$ film were also observed when titrating small amounts of $TBAClO_4$ into $TBABF_4$ electrolyte (Fig. D.5). These titration experiments suggest that larger PF_6^- and ClO_4^- anions block the intercalation of BF_4^- anions into the nanoconfined pore of $Fe(TA)_2$ nanoparticles and therefore suppress the intercalation redox chemistry. Indeed, EQCM detected a more severe mass decrease at the intercalation redox feature at 1.2 V vs. $Fc^{0/+}$ as compared to the mass decrease at one of the surface redox features at 0 V vs. $Fc^{0/+}$ (Fig. 5.10b). The blocking effect of larger PF_6^- anions on the BF_4^- intercalation further prevents the charge (i.e., hole) transfer to oxidize interior Fe^{2+} centers to Fe^{3+} (Fig, 5.10b). Taken together, the titration experiments along with anion-size-dependent and film-thickness-dependent investigations together illustrate that the rate-determining step of Fe^{2+}/Fe^{3+} redox reaction inside nanoconfined $Fe(TA)_2$ pore is the BF_4^- intercalation process.

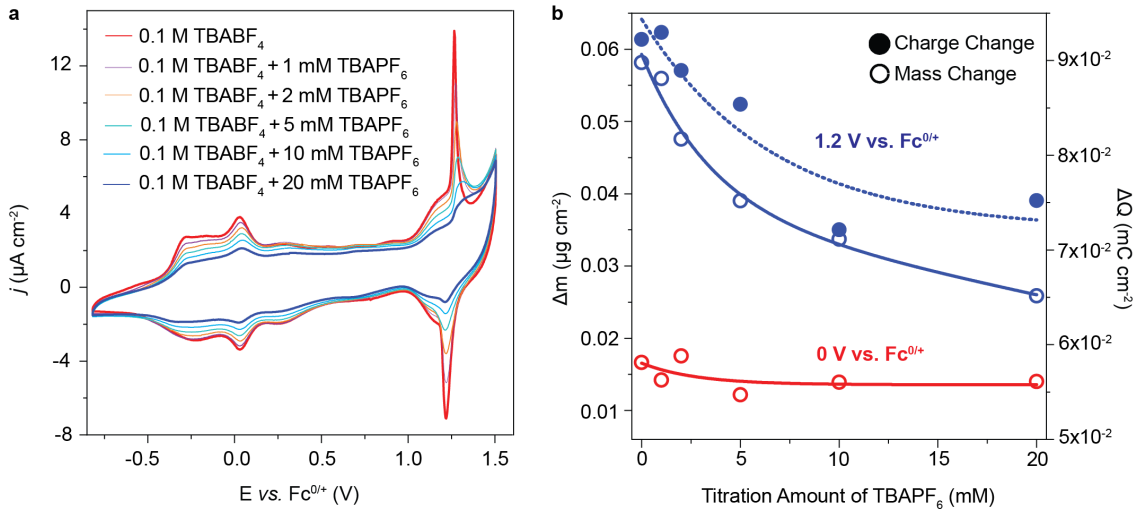

Figure 5.10. Electrolyte titrations show redox properties in $Fe(TA)_2$ nanoparticle film. (a) CV measurements of 16-nm $Fe(TA)_2$ nanoparticle film during titrating $TBAPF_6$ into 0.1 M $TBABF_4$ acetonitrile electrolyte. (b) Mass (hollow circle) and charge (solid circle) change of 16-nm $Fe(TA)_2$ nanoparticle film during titrating $TBAPF_6$ into 0.1 M $TBABF_4$ acetonitrile electrolyte. Note: CV scan is collected at a 10 mV/s scan rate. The loading amount of 16-nm $Fe(TA)_2$ nanoparticle is controlled to be ca. 4.0 μg on QCM crystal.

Given that the desolvation step occurs in both BF_4^- intercalation-induced redox chemistry and BF_4^- adsorption-induced surface reactions, it is necessary to investigate the importance of solvent effect in determining redox properties of $Fe(TA)_2$ film. In addition to acetonitrile, the CV of $Fe(TA)_2$ film was collected in 1,2-difluorobenzene. Since 1,2-difluorobenzene is known as a chemically inert and non-coordinating solvent, it is expected that a less positive voltage is already able to drive the desolvation and intercalation of BF_4^- anions into the $Fe(TA)_2$ pore as compared to that in acetonitrile. Fig. D.6 indeed detected ca. 150-mV cathodic shift of $E_{1/2}$ of BF_4^- intercalation redox reaction inside the $Fe(TA)_2$ pore when switching the solvent from acetonitrile to 1,2-difluorobenzene. Given that the potential of ca. 1.2 V vs. $Fc^{0/+}$ is already beyond the potential window of many commonly used organic electrolytes, we further studied the solvent effect on

governing surface redox properties of $Fe(TA)_2$ film. Similar to solvent-dependent intercalation redox reaction, $E_{1/2}$ of BF_4^- adsorption-induced Fe^{2+}/Fe^{3+} redox feature also shifted cathodically by switching acetonitrile to 1,2-difluorobenzene (Fig. D.6). Interestingly, it was found that those surface redox features were highly dependent on solvents as evidenced by different $E_{1/2}$ and current densities in distinct solvents (e.g., acetonitrile, dichloromethane, tetrahydrofuran, and 1,2-difluorobenzene in Fig. D.7). We hypothesize that those solvent-dependent surface redox features are due to the different re-organization structures of solvent and electrolyte on the $Fe(TA)_2$ film surface induced by the partial desolvation and adsorption of BF_4^- anions. Overall, our studies confirm that the solvent effect must be considered as an essential factor in the microscopic picture of both surface reactions and the ion intercalation redox chemistry inside nanoconfined MOF pores.

Conclusions

In summary, our studies unravel how the nanoconfinement effect governs the ion-intercalation redox chemistry inside the pore of $Fe(TA)_2$ nanoparticles. The nanoconfinement effect inside the $Fe(TA)_2$ pore requires a higher electrochemical potential to drive the complete desolvation and intercalation of BF_4^- anions into the pore as compared to the partial desolvation and adsorption of BF_4^- anions on the $Fe(TA)_2$ surface. The further manipulation of experimental factors (e.g., film thickness, electrolyte species, and solvents) discovers that the redox properties of ion intercalation into the nanoconfinement environment of $Fe(TA)_2$ pore behave significantly different from the surface redox. It is found that Fe^{2+}/Fe^{3+} redox chemistry inside the $Fe(TA)_2$ pore is determined by the BF_4^- intercalation step, while the surface Fe^{2+}/Fe^{3+} redox is more impacted by solvents. These fundamental studies establish a microscopic-level description of ion intercalation

redox chemistry inside the nanoconfined pore of conductive MOF nanoparticles, providing the guideline for designing efficient energy storage under confinement in porous materials.

Additional studies would be required to provide insights into the electrolyte and solvent ordering on the $Fe(TA)_2$ surface to further understand the solvent-dependent surface redox features. Meanwhile, the nanoconfinement-induced complete desolvation in the process of BF_4^- intercalation process shortens the distance (d) between $BF_4^-$and the interior $Fe(TA)_2$ surface inside the pore, suggesting $Fe(TA)_2$ nanoparticles as a promising material for pseudo-capacitance applications.

CHAPTER VI

CONCLUDING REMARKS

This dissertation presents the Seesaw model of Metal-Organic Framework (MOF) particle growth, verifies the model by applying it to known MOF systems, then implements it to develop the new nanoMOFs $Co(TA)_2$, $Cd(TA)_2$, and $Fe(TA)_2$. The research in this thesis shows that controlling particle size of 1,2,3-triazole MOFs can be done using the modulator method, and that the resulting particles are stable as colloids and can be processed into thin films. For these three MOFs, the modulator 1-methylimidazole can be added in increasing quantities in order to decrease particle size. Additionally, the development of this new class of MOF nanoparticles shows that the Seesaw model can guide synthetic chemists as we target new nanoMOF materials and reduce the amount of high-throughput testing needed.

This work demonstrates that solution-stable MOF nanoparticles can be analyzed via methods typically exclusive to smaller clusters and inorganic nanoparticles. Controlling particle concentration for UV-Vis absorption spectroscopy allowed for the first determination of a MOF material's extinction coefficient. It was found that the extinction coefficients of the charge transfer bands of $Fe(TA)_2$, per particle, scale with particle volume. In the future, these types of analyses may allow for a) the rapid determination of particle size and concentration through UV-Vis and b) the quantitative comparison of MOFs' optical properties. Unexpectedly, the charge transfer bands of $Fe(TA)_2$ also show size-dependence, blueshifting as particle size decreases. This is the first report of size-dependent optical properties in the absorbance spectra of MOF particles. This dependence is hypothesized to be due to the variations in coordination environment of Fe centers

in the particles as the surface area to volume ratio changes. Although the cause is not yet certain, this study opens the door to utilizing particle size as another useful handle to tune the optical properties of MOF materials. As crystal engineering emerges in the forefront of the MOF field, and the materials are increasingly sought out for selective sensing and other applications, quantitative UV-Vis will likely emerge as a standard characterization technique.

Synthesizing porous semiconductors with control over size will be a crucial step in developing conductive and redox-active MOF materials for technological applications. While there are no commercial uses of conductive MOFs in devices to-date, several studies show promise for their use as electrode and transducer materials.[208;209] By making conductive MOFs as solution-processable particles with low size dispersity, greater control over the materials' processing can be attained. The material $Fe(TA)_2$ shows size-dependent electronic behavior not previously observed: the redox behavior of the nanoparticles shows superior reversibility to its bulk counterpart. Additionally, an extremely sharp and reversible feature is observed which was unambiguously assigned to the complete desolvation and intercalation of BF_4^- anions into the MOF particles coupled with $Fe^{2+/3+}$ redox events. The reversibility of the intercalation chemistry suffers when film thickness is too high, particles are too large, or electrolyte anions are too large. The ion and solvent dependence of MOF redox chemistry is essential to their future development in devices. Further, it was found that the bulk conductivity of $Fe(TA)_2$ thin films increases as particle size decreases from bulk to 25 nm. This intriguing development suggests that nanoparticle thin films may be a more practical option for device applications over single crystals, as grain boundary sites may not impede bulk conductivity significantly. The advantage of solution processibility, in combination

with improving the efficiency of redox processes, will place conducting nanoMOF materials at the forefront of charge storage research and device implementaiton.

APPENDIX A

SUPPLEMENTARY INFORMATION FOR CHAPTER 2

Table A.2. Typical M:L ratios and L concentrations for MOF nanocrystals discussed in this perspective. These values are compared to 1-2 representative examples for bulk syntheses. Bold values indicate nanoscale syntheses where either excess linker or a more dilute system was used compared to bulk syntheses.

MOF Name	Bulk L : 1M	Bulk L Conc. (M)	Nano L : 1M	Nano L Conc. (M)	Nano Ref	Bulk Ref
[(2-PTZ)$_2$ $Cd(H_2O)_2$]	0.125 – 6,	0.66 – 1	2, 3	0.2, 0.3	(221)	(222)
	0.5 – 4 (M = Zn)	(M = Zn)				
COMOC-4	Not available		1.14	0.05	(223)	
DUT-23 (Cu)	0.4	0.0076	**2, 4**	**0.00052, 0.0010**	(224)	(225)
Dy-BTC	1	0.01	**1.5**	0.0125	(64)	(226)
Fe-soc-MOF	2		0.49	0.013	(227;228)	
HKUST-1	0.67	0.020	0.53	0.04	(64)	(229)
	0.53	0.012	0.67	0.042	(230)	(231)
			0.67	0.04	(81)	
			0.56	variable	(232)	
			0.56	0.099	(233)	
			1	0.041	(67)	
IR-MOF-3	0.34	0.04	0.34	**0.043**	(68)	(234)
			0.37	**0.02**	(67)	
MFU-4	0.25	0.0625	0.24	**0.03**	(69)	(235)
MFU-4l	0.048	0.0036	0.05	**0.0019**	(33)	(236)
MIL-100 (Al)	0.67	0.11	0.66	0.241	(75)	(237)
MIL-96 (Al)	0.81	0.14	0.081	**0.01**	(74)	(238)

MIL-100 (Cr)	0.67 (M = Cr(0))	0.14	0.67	0.1333	(75)	(239)
MIL-100 (Fe)	0.66 (M = Fe(0))	0.13	0.67	0.1333	(75)	(240)
			0.67	0.201	(76)	
MIL-101 (Cr)	1	0.21	1	0.2	(78)	(241)
			1	0.2	(79)	
			1	0.033	(77)	
			1	0.2	(242)	
MIL-101-NH_2 (Fe)	0.75	0.017	0.51	0.083	(81)	(68)
MIL-88A	1	0.2	1	0.2	(214)	(243)
MIL-88B (Cr)	1	0.08	1	0.2	(80)	(244)
MIL-88B (Fe)	1	0.046	0.65	0.1	(72)	(245)
MIL-88B-NH2 (Fe)	1	0.046	0.5	**0.022**	(73)	(245)
MIL-125	0.67	0.3	**1.3**	Not available	(82)	
			0.55	**1.44×10^{-7}**	(216)	(246)
MIL-125-NH_2	2	0.12	1.5	0.277	(83)	(246)
			1.55	**0.0775**	(139)	
MIL-53 (Al)	0.5	0.347	0.5	0.347	(247)	(248)
MOF-5	0.48	0.024	**0.4 – 1**	0.053 – 0.13	(64)	(249)
	0.337	0.0367	0.2	**0.0067**	(81)	(250)
			0.33	**0.01**	(251)	
			0.5	**0.0005**	(224)	
			1	**0.00166**	(84)	
			3	**0.005**		
			0.43	**0.000125 - 0.0028**	(86)	
			0.33	0.04	(252)	
			0.5	0.05	(253)	
			0.33	0.04	(45)	

MOF-74 (Co)	0.25	0.01	0.28	Not available	(81)	(81)
MOF-74 (Ni)	Not available		0.29	0.012	(81)	
			0.5	0.0417	(88)	
MOF-801	Not available		2	0.18	(213)	
NU-1000	0.2	0.0074	0.088	**0.0014**	(91)	(254)
			0.061	**0.0056**	(90)	
			0.1	**0.0018**	(89)	
			0.0054	**0.0036**	(255)	
PCN-222	0.12	0.0038	0.068	**0.00053**	(91)	(256)
			0.1	**0.0018**	(89)	
PCN-224	0.14	0.0065	0.14	**0.0013**	(92)	
			0.17	**0.002**	(57)	
UiO-66			1	0.0257	(257)	(258)
	1		**1.5**	0.0386		
			2	0.0515		
		0.0086	**3.34**	0.075	(155)	
			1	**0.0043**	(259)	
			1	varies	(260)	
			1	0.0172	(218)	
			1	0.0454	(261)	
			1	0.0454	(139)	
			0.74	0.02	(255)	
UiO-66 w/ Co			1	0.078	(262)	
UiO-66-NH_2	1 (X = NH_2)	0.0356				
UiO-67	Not available		0.74	0.02	(255)	
UMCM-150	0.49	0.0070	0.33	**0.00051**	(224)	(263)
ZIF 8 w/ Co	Not available		0.34	0.1	(264)	
			16	**0.000099**	(265)	
ZIF-65-Zn	0.5	0.067	2	0.1	(266)	(267)
ZIF-7	0.81	0.027	2	0.05	(266)	(268)

			2	**0.015**	20	
ZIF-71	4	0.053	2	0.2	(266)	(269)
ZIF-8	0.91	0.041	1.9-2	0.05	(264)	
			8	0.20, 0.089	(270)	(271)
Zn-BPD-X (X = NH_2, NO_2, OH)	1	0.05	1	0.013	(97)	(272)
Zn-BPD-OH			1	0.027	(97)	

Table A.1. Values for the smallest, median, and average nanocrystal sizes (all in nm) reported in Figure 1 of the main text. The smallest MOF nanocrystals made by other methods are reported along with the method used: metal organic gel (Gel,) ionic liquid microemulsion (ILM), dual injection (Inject), and slow addition (SA)

MOF	Smallest	Median	Average	Smallest by Other Methods	Smallest Ref
DyBTC	50	60	59.2		(64)
HKUST-1	2.6	60	164.71	2.6 – Gel 1.6 – ILM 24 – Inject	(173;210;174;211)
IR-MOF-3	30				(68)
MFU-4	33.66	1200	750.2		(69)
MOF-74	17 (Co)			16.6 (Zn, SA) 13.6 (Mn, SA), 9.4 (Mg) 5.1 (Co, SA) 2.8 (Ni, SA)	(172;212)
MOF-801	23	95.5	95.5		(213)
MIL-88-A	60 195	263.64			(214)
MIL-88B-NH_2	30	105	100		(73)
MIL-96	930	2100	2795.7		(74)
MIL-100-Al	272	423.5	423.5		(215)
MIL-100-Cr	109.33	119.79	119.79		(75)
MIL-100-Fe	100	323	298.81		(71)
MIL-101-Cr	19	127.5	211.8		(77)
MIL-101-Fe				47 – Inject	(211)
MIL-125	85	550	583.8		(216)
MIL-125-NH_2	70	220	305.6		(83)
MOF-5	25	137.5	709.8		
NU-1000	75	400	1965.5		(89)
NU-1003	300				(217)
PCN-222	190	550	535.8		(91)
PCN-224	49	1141	133.1		(92)
UiO-66	14	117	221.2	35 – Inject	(211;218)
UiO-66-NH_2	16	82	82		(218)
UiO-67	308	515.5	481		(218)
ZIF-7	30.7	71.4	71.4		(95)
ZIF-8	9	42.3	141.3	32 – Inject 2.2 - ILM	(174;211;219)
ZIF-67				80 - Inject 2.3 - ILM	(211;174)
ZIF-71	13	37	41.6		(220)
ZIF-90				65 – Inject	(211)
Zn-BPD-H	75.5	100	105.1		(97)
Zn-BPD-NH_2	95	137.5	144.4		(97)
Zn-BPD-NO_2	57.5	79.5	74.6		(97)
Zn-BPD-OH	97	102.5	105.1		(97)

Table A.3. Nanocrystal sizes used to create Fig 1 in the main text. Size distributions given in nanometers are shown in parentheses. Dispersity measurements reported as PDI (Polydispersity Index), standard deviation, relative standard deviation, or a range of nanometers are reported in Disp. (Other) with the type of data in parentheses (PDI, SD, RSD, or Range). In cases where anisotropic particles were presented with both length and width, they are differentiated here as (L) and (W). N/A stands for Not Available.

MOF	Size (nm)	Disp. (Other)	Method	Size	Method	Size	Method	Method Average	Citation
$[(2\text{-PTZ})_2Cd(H_2O)_2]$	Not available								(221)
BUT-12	Not available					(273)			
COMOC-4 (w/ Eu)	N/A								(223)
DUT-23 Cu	N/A								(224)
Dy-BTC	70(15)		SEM						
	50(30)		SEM						
	50(25)		SEM						
	65(25)		SEM						
	60(20)		SEM						
	60(20)		SEM						
Fe-soc-MOF	310(10)		SEM						
HKUST-1	100		DLS						(67)
	47		DLS						
	48		DLS						
	60		DLS						
	54		DLS						
	20000		SEM						(274)
	300		SEM						
	85		SEM						
	100		SEM						
	115		SEM						
	600		SEM						
	2500		SEM						
	2500		SEM						
	2500		SEM						
	Not available		SEM						(64)
	10		SEM						(81)
	21	19.90% (RSD)	TEM						(232)

	32	30% (RSD)	TEM						
	46	22.20% (RSD)	TEM						
	299	15.60% (RSD)	TEM						
	76	10.80% (RSD)	TEM						
	190	19.20% (RSD)	TEM						
	448	16.70% (RSD)	TEM						
	658	25.40% (RSD)	TEM						
	331	20.50% (RSD)	TEM						
	449	16.10% (RSD)	TEM						
	563	17.40% (RSD)	TEM						
	1190	12.40% (RSD)	TEM						
	58.3		PXRD						(233)
	51.9		PXRD						
	41.7		PXRD						
	51.8		PXRD						
	70		PXRD						
	80.9		PXRD						
	60		PXRD						
	78.6		PXRD						
	68.5		PXRD						
	42.4		PXRD						
	42.1		PXRD						
	57.4		PXRD						
	57		PXRD						
	N/A		TEM	2.2	PXRD	3	PXRD	2.6	(173)
	1.5		TEM	3.3	PXRD	4.7	PXRD	3.17	
	2		TEM	4.3	PXRD	6.1	PXRD	4.13	
	2.5		TEM	6.2	PXRD	8.7	PXRD	5.8	
IR-MOF-3	30		DLS						(68)
	32		DLS						
	33		DLS						
	47.5		DLS						
	46		DLS						
	N/A								(252)
Hf-BUT-12	N/A								(273)
Hf-UiO-66-NH_2	N/A								(273)

Hf-UiO-66-2,6-NDC	N/A							(273)
MFU-4	>1200	DLS						(69)
	>1200	DLS						
	>1200	DLS						
	>1200	DLS						
	>1200	DLS						
	>1200	DLS						
	>1200	DLS						
	119	DLS						
	46(2)	DLS	37(3)	PXRD	32(11)	TEM	38.33	
	42(1)	DLS	34(2)	PXRD	25(6)	TEM	33.67	
	48(1)	DLS	36(2)	PXRD	36(8)	TEM	40	
	43(3)	DLS	35(1)	PXRD	29(8)	TEM	35.67	
MIL-53	350(100)							(71)
MIL-53 Al	N/A							(247)
MIL-88B-Cr	N/A							(80)
MIL-88B-Fe	N/A							(72)
MIL-88B-Fe-NH_2	30	TEM						(73)
	55	TEM						
	155	TEM						
	160	TEM						
MIL-88A	100(25)	DLS						(71)
	N/A							(275)
	255(25)							(214)
	390(30)							
	360(35)							
	550(55)							
	110(25)	DLS						
	195(15)	DLS						
	230(25)	DLS						
	150(30)	DLS						
	270(20)	DLS						
	290(20)	DLS						
	210(25)	DLS						
	380(35)	DLS						
	360(50)	DLS						

275(65)	DLS
885(90)	DLS
1050(210)	DLS
720(75)	DLS
¿1200	DLS
380(35)	DLS
480(45)	DLS
¿1200	DLS
180(15)	DLS
240(15)	DLS
390(25)	DLS
95(15)	DLS
75(10)	DLS
190(20)	DLS
60(10)	DLS
70(10)	DLS
180(15)	DLS
115(15)	DLS
70(10)	DLS
75(10)	DLS
60(5)	DLS
80(5)	DLS
85(8)	DLS
110(10)	DLS
160(10)	DLS
270(23)	DLS
350(55)	DLS
87(15)	DLS
110(10)	DLS
280(45)	DLS
575(85)	DLS
110(10)	DLS
280(45)	DLS
575(85)	DLS
110(10)	DLS
185(25)	DLS

	275(25)	DLS						
MIL-89	75(25)	DLS						(71)
MIL-96 Al	8500	Length	1000	Width				(74)
	2900	SEM (L)	450	SEM (W)				
	1600	SEM (L)	410	SEM (W)				
	980	SEM (L)	510	SEM (W)				
	2100	SEM (L)	570	SEM (W)				
	2200	SEM (L)	810	SEM (W)				
	1290	SEM (L)	610	SEM (W)				
MIL-100 Al	585(150)	DLS (H_2O)	565(75)	DLS (EtOH)			575	(75)
	249(28)	DLS (H_2O)	237(41)	DLS (EtOH)	311(41)	DLS (DMEM)	272	(215)
	291(24)	DLS (MEM)						
MIL-100 Fe	100(50)	DLS						(71)
	452	DLS (Tris)	256	DLS (H_2O)			354	(76)
	646	DLS (Tris)					323	
	458	DLS (Tris)	215	DLS (H_2O)			336.5	
	698	DLS (Tris)					698	
	596	DLS (Tris)					596	
	592	DLS (Tris)	238	DLS (H_2O)			415	
	139(25)	DLS (H_2O)	168(10)	DLS (EtOH)			153.5	(75)
	110(25)	DLS (H_2O)	119(11)	DLS (EtOH)			114.5	
	141(43)	DLS (H_2O)	155(61)	DLS (PBS)	162(60)	DLS (PBS + Alb)	150.75	(276)
	145(38)	DLS (RMPI)						
	139(25)	DLS(H_2O)	168(10)	DLS (EtOH)	252(32)	DLS (DMEM)	203.5	(215)
	255(21)	DLS (MEM)						
MIL-100 Cr	143(63)	DLS (H2O)	80(41)	DLS (EtOH)	106(47)	DLS (MeOH)	109.33	(75)
	142(63)	DLS (H_2O)	80(41)	DLS (EtOH)	146(32)	DLS (DMEM)	130.25	(215)
	153(49)	DLS (MEM)						
MIL-101 Cr	50(9)	TEM						(77)
	19(4)	TEM						
	25(6)	TEM						
	28(6)	TEM						
	36(7)	TEM						
	73(8)	TEM						
	387(28)	TEM						(78)
	383(25)	TEM						

	346(19)	TEM		
	279(21)	TEM		
	160(16)	TEM		
	148(14)	TEM		
	90(10)	TEM		
	114(13)	SEM		(79)
	1336(174)	SEM		
	141(16)	SEM		
	87(9)	SEM		
	101(11)	SEM		
	214(25)	SEM		
	387(28)			(80)
	156(17)			
	100(12)			
MIL-101-Fe-NH_2	Not available			(81)
MIL-125	Not available			(82)
	200(50)			(216)
MIL-125-NH_2	240(70)	DLS (DMF)	313.33	(83)
	660(250)	DLS (H_2O)		
	320(100)	DLS (MeOH)		
	220(60)	DLS (EtOH)		
	230(60)	DLS (PBS)		
	210(100)	DLS (PBS FBS)		
	750	SEM		(139)
	280	SEM		
	192	SEM		
	100	SEM		
	70	SEM		
	150	SEM		
	190	SEM		
	750	SEM		
	420	SEM		
	320	SEM		
	220	SEM		
	100	SEM		
	90	SEM		

	180		SEM	
	350		SEM	
	720		SEM	
MOF-5	N/A			(64)
	N/A			(81)
	70(10)		TEM	(84)
	624(39)			(86)
	399(23)			
	220	140-420		(252)
	125(25)			(253)
	37.5(7.5)			(45)
	150			
MOF-74	N/A			(81)
	17(3) (Co)			(212)
	100(20) (Mn)			
	200(50) (Mg)			
	18(5) (Ni)			
MOF-801	168(24)		SEM	(213)
	23(11)		SEM	
NU-1000	180	140-220 (Range)		(91)
	N/A			(90)
	75			(89)
	150			
	500			
	1200			
	15000			
	150(50)			(255)
	300(50)			
	600(100)			
	1500(500)			
NU-1003	300		SEM	(217)
	1000		SEM	
	2000		SEM	
	7000		SEM	
	10000		SEM	
PCN-222	190	150-250 (Range)		(91)

	350(50)						(74)
	475(25)						
	625(125)						
	650(50)						
	925(75)						
	Not available						(273)
PCN-224	33(4)		TEM	65(3)	DLS	49	(92)
	91(5)		TEM	114(3)	DLS	86.5	
	91(8)		TEM	137(2)	DLS	114	
	144(7)		TEM	197(1)	DLS	170.5	
	189(11)		TEM	255(2)	DLS	222	
	100	50-120 (Range)					(57)
	190	150-150 (Range)					(91)
UiO-66	106.5(11.9)		SEM	547.1(25.1)	DLS	326.8	(257)
	118.2(18.1)		SEM	1327(57.6)	DLS	722.6	
	90.2(10.9)		SEM	472.7(182.3)	DLS	281.45	
	66.9(10.2)		SEM	288.1(31.4)	DLS	177.5	
	71.4(10.2)		SEM	167.7	DLS	119.55	
	82.5(12.2)		SEM	526.2(24.1)	DLS	304.35	
	87.9(15.3)		SEM	872.5(9.2)	DLS	480.2	
	66.4(12.3)		SEM	374.2(33.9)	DLS	220.3	
	23.7(5.0)		SEM	244.7(4.1)	DLS	134.2	
	23.1(3.5)		SEM	139.9(8.7)	DLS	81.5	
	91.9(21.0)		SEM	443.3(54.7)	DLS	267.6	
	53(9.7)		SEM	709.2(40.7)	DLS	381.1	
	29.2(6.8)		SEM	388.1(99)	DLS	208.65	
	26.5(5.9)		SEM	209.2(33)	DLS	117.85	
	20.0(4.0)		SEM	132.2(6.2)	DLS	76.2	
	26.5(5.5)		SEM	294.8	DLS	160.65	
	82.5(12.2)		SEM	526.2(24.1)	DLS	304.35	
	23.3(3.1)		SEM	575	DLS	299.15	
	17(2)		STEM	Not available	DLS	17	(155)
	34(22)		STEM	Not available	DLS	34	
	72(18)		STEM	158(19)	DLS	115	
	208(56)		STEM	173(40)	DLS	190.5	
	270(48)		STEM	319(67)	DLS	294.5	

514(88)		STEM	677(204)	DLS	595.5	
721(56)		STEM	826(135)	DLS	773.5	
17(4)		STEM	83(38)	DLS	50	
31(5)		STEM	89(25)	DLS	60	
44(12)		STEM	94(19)	DLS	69	
147(50)		STEM	175(31)	DLS	161	
439(83)		STEM	559(110)	DLS	499	
813(223)		STEM	919(144)	DLS	866	
1174(258)		STEM	1208(275)	DLS	1191	
19(5)		STEM	132(72)	DLS	75.5	
29(8)		STEM	74(18)	DLS	51.5	
88(25)		STEM	95(24)	DLS	91.5	
550(51)		STEM	784(70)	DLS	667	
38(7)		STEM	100(29)	DLS	69	
53(12)		STEM	140(30)	DLS	96.5	
227(46)		STEM	277(80)	DLS	252	
1949	154 (SD)	SEM				(259)
1060	65 (SD)	SEM				
783	32 (SD)	SEM				
583	19 (SD)	SEM				
522	24 (SD)	SEM				
502	26 (SD)	SEM				
220	122-615 (Range)	DLS				(260)
255	105-396 (Range)	DLS				
164	142-459 (Range)	DLS				
164	105-396 (Range)	DLS				
105	79-255 (Range)	DLS				
164	122-342 (Range)	DLS				
190	164-458 (Range)	DLS				
85		XRD				
83		XRD				
81		XRD				
78		XRD				
74		XRD				
71		XRD				
46		XRD				

	23	XRD	
	14	XRD	
	265	SEM	(261)
	96	SEM	
	48	SEM	
	155	SEM	
	75	SEM	
	40	SEM	
	190	SEM	
	153	SEM	
	144	SEM	
	117	SEM	
	224	SEM	
	150	SEM	
	167	SEM	
	177	SEM	
	150	SEM	
	100	SEM	
	97	SEM	
	102	SEM	
	265	SEM	
	91	SEM	
	78	SEM	
	61	SEM	
	41	SEM	
	230	SEM	(262)
	N/A		(273)
UiO-66-NH_2	115	PXRD	(218)
	90	PXRD	
	85	PXRD	
	82	PXRD	
	80	PXRD	
	54	PXRD	
	21	PXRD	
	16	PXRD	
	200	TEM	(273)

UiO-66-OH	N/A						(273)
UiO-66-2,6-NDC	N/A						(273)
UiO-67	641	365-995 (Range)	DLS				(218)
	553	356-859 (Range)	DLS				
	553	356-859 (Range)	DLS				
	413	308-641 (Range)	DLS				
	308	229-478 (Range)	DLS				
	478	356-742 (Range)	DLS				
	Not availble						(273)
ZIF-7	112		DLS				(266)
	30.7(5.9)		TEM				(95)
	40(10)		SEM				(277)
	70(10)		SEM				
ZIF-8	18		PXRD	17	SLS	17.5	(219)
	45		PXRD	39	SLS	42	
	10		PXRD	9	SLS	9.5	
	24		PXRD	20	SLS	22	
	55		PXRD	40	SLS	47.5	
	9		PXRD	9	SLS	9	
	16		PXRD	16	SLS	16	
	43		PXRD	42	SLS	42.5	
	10		PXRD	8	SLS	9	
	50(20)						(278)
	44(17)						
	34	15-65 (Range)					
	60(25)						
	21(4)		TEM				(265)
	744		TEM				(264)
	601		TEM				
	490		TEM				
	271		TEM				
	93		TEM				
	43		TEM				
	27		TEM				
	40.6	0.09 (PDI)	SLS				(270)
	45.4		SLS				

	28	SLS						
	31.2	SLS						
	25	SLS						
	25	SLS						
ZIF-65-Zn	125	DLS						(266)
	125	DLS						
ZIF-71	55	DLS						(266)
	83	DLS						
	83	DLS						
	98	PXRD	100	SEM			99	(279)
	11	PXRD	15	SEM			13	
	94	PXRD	90	SEM			92	
	44	PXRD	30	SEM			37	
	24	PXRD	25	SEM			24.5	
Zn-BPD-H	105(15)	DLS	46	PXRD			75.5	(97)
	150(20)	DLS	47	PXRD			98.5	
	145(15)	DLS	50	PXRD			97.5	
	155(30)	DLS	51	PXRD			103	
	140(20)	DLS	60	PXRD			100	
	170(25)	DLS	50	PXRD			110	
	180(25)	DLS	52	PXRD			151	
Zn-BDP-NH_2	190(35)	DLS	Not available				95	(97)
	210(30)	DLS	58	PXRD			134	
	193(40)	DLS	71	PXRD			132	
	220(35)	DLS	67	PXRD			143.5	
	210(35)	DLS	65	PXRD			137.5	
	210(35)	DLS	71	PXRD			140.5	
	275(35)	DLS	61	PXRD	120(40) (L), 45(20) (W)	SEM	228	
Zn-BPD-NO_2	125(35)	DLS	45				85	(97)
	100(30)	DLS	43	PXRD			71.5	
	120(25)	DLS	42	PXRD			81	
	120(30)	DLS	39	PXRD			79.5	
	115(30)	DLS	Not available				57.5	
	100(30)	DLS	37	PXRD			68.5	
	120(35)	DLS	39	PXRD	65(30)	SEM	79.5	
Zn-BPD-OH	145(35)	DLS	52	PXRD			98.5	(97)

145(35)	DLS	50	PXRD		97.5
160(30)	DLS	45	PXRD		102.5
165(35)	DLS	45	PXRD		105
165(35)	DLS	40	PXRD		102.5
160(35)	DLS	34	PXRD		97
155(40)	DLS	50	PXRD	60(20)	132.5

APPENDIX B

SUPPLEMENTARY INFORMATION FOR CHAPTER 3

Synthetic Details and Analytical Methods

Materials & Methods. Zinc nitrate hexahydrate was purchased from Sigma-Aldrich, 2-methylimidazole was purchased from Aldrich, and ACS grade methanol was purchased from Fisher Scientific. Copper (II) nitrate trihydrate was purchased from Acros organics, 1,3,5-benzenetricarbosylic acid from TCI America, and 200 proof dry ethanol from Fisher Scientific. Sodium benzoate was purchased from MCB and benzoic acid was purchased from JT Baker. All chemicals were used without further purification.

Cu_3BTC_2 (HKUST-1) Expanded Synthetic Methods. Initial syntheses to explore the use of sodium benzoate as a modulator for Cu_3BTC_2 were performed on a larger scale. Both ligands, 1,3,5-benzenetricarboxylic acid (0.1 mmol) and sodium benzoate (0.1-2.0 mmol) were dissolved in 10 mL 1:1 H_2O:EtOH. A solution of copper nitrate (0.005 M, 4 mL) was poured in, resulting in the immediate formation of a blue precipitate. If only the linker and metal are combined in these conditions, no product forms. If benzoic acid is added without any sodium benzoate, no product forms. For scale-up syntheses, four key conditions were selected (refer to table B.14). The stock solutions of 1,3,5-benzenetricarboxylic acid, benzoic acid, and sodium benzoate in 1:1 H_2O:EtOH were combined in 100 mL Schott bottles. The solutions were diluted to 90 mL. Copper nitrate stock solution was added under stirring. Schott bottles were removed from the stir plate as soon as the solution was homogenously blue in color—less than 1 second. Samples were left to sit 25 hours, then washed twice with 1:1 H_2O:EtOH.

Scherrer Size Estimations. ZIF-8 and Cu_3BTC_2 particles were characterized using PXRD and approximate sizes were determined using Scherrer equation:

$$\tau = \frac{K\lambda}{\beta cos\theta} \tag{B.1}$$

In this equation, β is the full width at half max of a peak, in radians, θ is the scattering angle, in radians, and λ is the wavelength in nm. The shape factor K was taken to be 1, a typical value for spherical particles.

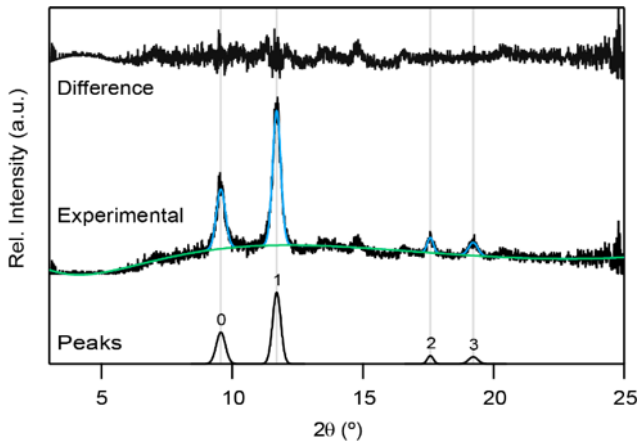

Figure B.1. An example of peak fitting in Igor 6.32. The sample being fit is denoted in table B.9.

Diffraction peaks were fit in Igor Pro 6.37 with Multipeak fit 2.0. A gaussian function with a constant baseline was used in cases where the peaks were thin and well-defined. The baseline function was changed to a log cubic function in cases where the constant background function did not produce representative fits. Particle size was estimated using compiled Full Width at Half Max (FWHM) and peak location data. For ZIF-8, the peaks [100], [111], and [102] were used and the size values were averaged. For Cu_3BTC_2, the peaks [200], [222], and [400] were used

and the size values were averaged. If not all these peaks were present or could be adequately fit, they were not included.

Tables Detailing Synthetic Conditions and Particle Size. The tables below detail the synthetic conditions and the resulting particle sizes. The amount of each component is given by their final concentration in mol L^{-1}, where M is the metal, L is the linker, and Mod is the total modulator. Refer to sections 1.2 and 1.3 for the general synthetic methods. Representative PXRD patterns for some of these sets can be found in section 1.7.

Table B.1. Cu_3BTC_2 synthesis using varying benzoic acid to sodium benzoate ratios with excess linker and a metal concentration of 0.001 M. M, L, and Mod refer to the concentrations of the metal salt, linker, and modulator in M. Sizes are calculated from the Scherrer equation. These data are depicted in Figure 3.4 of the main text and Figure B.8.

M	L	Mod	Abs. Eq. M : L : Mod	Mod BA : B-	Size (nm)	Morphology
0.001	0.003	0.021	1 : 3 : 21	11 : 1	115.3	Indistinct
0.001	0.003	0.021	1 : 3 : 21	5 : 1	112.1	Indistinct
0.001	0.003	0.021	1 : 3 : 21	3 : 1	125.7	Octahedral
0.001	0.003	0.021	1 : 3 : 21	2 : 1	94.3	Octahedral
0.001	0.003	0.021	1 : 3 : 21	1 : 1	74.0	Globular
0.001	0.003	0.021	1 : 3 : 21	1 : 2	35.5	Globular
0.001	0.003	0.021	1 : 3 : 21	1 : 3	38.6	Globular
0.001	0.003	0.021	1 : 3 : 21	1 : 5	48.9	Globular
0.001	0.003	0.021	1 : 3 : 21	1 : 11	61.0	Aggregates
0.001	0.003	0.021	1 : 3 : 21	All B-	58.0	Spherical

Table B.2. Cu_3BTC_2 synthesis using varying benzoic acid to sodium benzoate ratios with excess linker and a metal concentration of 0.025 M. M, L, and Mod refer to the concentrations of the metal salt, linker, and modulator in M.These data are depicted in Figure 3.4 of the main text.

M	L	Mod	Abs. Eq. M : L : Mod	Mod BA : B-	Scherrer Size (nm)
0.0025	0.0075	0.0525	1 : 3 : 21	11 : 1	113.8
0.0025	0.0075	0.0525	1 : 3 : 21	5 : 1	83.8
0.0025	0.0075	0.0525	1 : 3 : 21	3 : 1	55.3
0.0025	0.0075	0.0525	1 : 3 : 21	1 : 1	22.1
0.0025	0.0075	0.0525	1 : 3 : 21	1 : 3	22.8
0.0025	0.0075	0.0525	1 : 3 : 21	1 : 5	19.5
0.0025	0.0075	0.0525	1 : 3 : 21	1 : 11	19.9
0.0025	0.0075	0.0525	1 : 3 : 21	100% B-	29.8

Table B.3. Cu_3BTC_2 synthesis using varying benzoic acid to sodium benzoate ratios with excess linker and a metal concentration of 0.005 M. M, L, and Mod refer to the concentrations of the metal salt, linker, and modulator in M. These data are depicted in Figure 3.4 of the main text.

M	L	Mod	Abs. Eq. M : L : Mod	Mod BA : B-	Size (nm)
0.005	0.015	0.105	1 : 3 : 21	11 : 1	117.7
0.005	0.015	0.105	1 : 3 : 21	5 : 1	47.3
0.005	0.015	0.105	1 : 3 : 21	3 : 1	35.8
0.005	0.015	0.105	1 : 3 : 21	1 : 1	21.2
0.005	0.015	0.105	1 : 3 : 21	1 : 3	35.8
0.005	0.015	0.105	1 : 3 : 21	1 : 5	17.0
0.005	0.015	0.105	1 : 3 : 21	1 : 11	26.4
0.005	0.015	0.105	1 : 3 : 21	100% B-	24.1

Table B.4. Cu_3BTC_2 synthesis using varying benzoic acid to sodium benzoate ratios with a stoichiometric amount of linker and a metal concentration of 0.027 M. M, L, and Mod refer to the concentrations of the metal salt, linker, and modulator in M.

M	L	Mod	Abs. Eq. M : L : Mod	Mod BA : B-	Size (nm)
0.0027	0.0018	0.0126	3 : 2 : 14	11 : 1	99.7
0.0027	0.0018	0.0126	3 : 2 : 14	5 : 1	90.2
0.0027	0.0018	0.0126	3 : 2 : 14	3 : 1	83.5
0.0027	0.0018	0.0126	3 : 2 : 14	1 : 1	70.1
0.0027	0.0018	0.0126	3 : 2 : 14	1 : 3	52.2
0.0027	0.0018	0.0126	3 : 2 : 14	1 : 5	56.2
0.0027	0.0018	0.0126	3 : 2 : 14	1 : 11	42.8
0.0027	0.0018	0.0126	3 : 2 : 14	100% B-	54.1

Table B.5. Cu_3BTC_2 synthesis using varying equivalents of a 33% benzoic acid modulator, with excess linker and a metal concentration of 0.001 M. M, L, and Mod refer to the concentrations of the metal salt, linker, and modulator in M. These data are depicted in Figure 3.3 of the main text. SEM images of these samples are shown in figure 3.?, and the Scherrer crystallite sizes and apparent particle size from SEM images are compared in figure B.10.

M	L	Mod	Abs. Eq. M : L : Mod	Mod BA : B-	Size (nm)	Morphology
0.001	0.003	0.003	1 : 3 : 3	1 : 2	112.4	octahedral
0.001	0.003	0.021	1 : 3 : 21	1 : 2	35.5	globular
0.001	0.003	0.030	1 : 3 : 30	1 : 2	27.0	globular
0.001	0.003	0.042	1 : 3 : 42	1 : 2	26.2	globular
0.001	0.003	0.060	1 : 3 : 60	1 : 2	52.6	globular
0.001	0.003	0.063	1 : 3 : 63	1 : 2	23.7	globular
0.001	0.003	0.084	1 : 3 : 84	1 : 2	25.1	globular
0.001	0.003	0.105	1 : 3 : 105	1 : 2	33.4	globular
0.001	0.003	0.120	1 : 3 : 120	1 : 2	43.3	globular

Table B.6. Cu_3BTC_2 synthesis using varying equivalents of a 50% benzoic acid modulator, with excess linker and a metal concentration of 0.001 M.M, L, and Mod refer to the concentrations of the metal salt, linker, and modulator in M. These data are depicted in Figure 3.3 of the main text.

M	L	Mod	Abs. Eq. M : L : Mod	Mod BA : B-	Size (nm)	Morphology
0.001	0.003	0.006	1 : 3 : 3	1 : 1	104.6	
0.001	0.003	0.018	1 : 3 : 18	1 : 1	61.6	globular
0.001	0.003	0.030	1 : 3 : 30	1 : 1	36.0	
0.001	0.003	0.042	1 : 3 : 42	1 : 1	33.5	
0.001	0.003	0.060	1 : 3 : 60	1 : 1	30.7	
0.001	0.003	0.084	1 : 3 : 63	1 : 1	24.0	
0.001	0.003	0.105	1 : 3 : 105	1 : 1	36.2	
0.001	0.003	0.120	1 : 3 : 120	1 : 1	51.1	

Table B.7. Cu_3BTC_2 synthesis using varying equivalents of a 66% benzoic acid modulator, with excess linker and a metal concentration of 0.001 M. M, L, and Mod refer to the concentrations of the metal salt, linker, and modulator in M. These data are depicted in Figure 3.3 of the main text and SEM images are in figure B.10.

M	L	Mod	Abs. Eq. M : L : Mod	Mod BA : B-	Size (nm)	Morphology
0.001	0.003	0.003	1 : 3 : 3	2 : 1	111.2	
0.001	0.003	0.021	1 : 3 : 21	2 : 1	94.3	Octahedral
0.001	0.003	0.030	1 : 3 : 30	2 : 1	51.2	Globular
0.001	0.003	0.042	1 : 3 : 42	2 : 1	59.5	
0.001	0.003	0.060	1 : 3 : 63	2 : 1	42.7	
0.001	0.003	0.084	1 : 3 : 84	2 : 1	41.5	
0.001	0.003	0.105	1 : 3 : 105	2 : 1	55.1	
0.001	0.003	0.120	1 : 3 : 120	2 : 1	59.0	Octahedral

Table B.8. Cu_3BTC_2 synthesis using varying equivalents of a 33% benzoic acid modulator, with a stoichiometric amount of linker and a metal concentration of 0.0027 M. M, L, and Mod refer to the concentrations of the metal salt, linker, and modulator in M.

M	L	Mod	Abs. Eq. M : L : Mod	Mod BA : B-	Size (nm)
0.0027	0.0018	0.0018	1 : 3 : 1	1 : 2	85.6
0.0027	0.0018	0.0126	1 : 3 : 4.67	1 : 2	46.0
0.0027	0.0018	0.0252	1 : 3 : 9.33	1 : 2	32.0
0.0027	0.0018	0.0378	1 : 3 : 14	1 : 2	31.0
0.0027	0.0018	0.0504	1 : 3 : 18.67	1 : 2	32.0
0.0027	0.0018	0.0630	1 : 3 : 23.33	1 : 2	20.6
0.0027	0.0018	0.0720	1 : 3 : 26.67	1 : 2	23.0
0.0027	0.0018	0.1080	1 : 3 : 40	1 : 2	26.9

Table B.9. Cu_3BTC_2 synthesis using varying equivalents of a 50% benzoic acid modulator, with a stoichiometric amount of linker and a metal concentration of 0.0027 M. M, L, and Mod refer to the concentrations of the metal salt, linker, and modulator in M.

M	L	Mod	Abs. Eq. M : L : Mod	Mod BA : B-	Size (nm)
0.0027	0.0018	0.0018	1 : 3 : 1	1 : 1	126.0
0.0027	0.0018	0.0126	1 : 3 : 4.67	1 : 1	70.1
0.0027	0.0018	0.0252	1 : 3 : 9.33	1 : 1	74.5
0.0027	0.0018	0.0378	1 : 3 : 14	1 : 1	28.0
0.0027	0.0018	0.0504	1 : 3 : 18.67	1 : 1	20.0
0.0027	0.0018	0.0630	1 : 3 : 23.33	1 : 1	22.6*
0.0027	0.0018	0.0720	1 : 3 : 26.67	1 : 1	23.3
0.0027	0.0018	0.1080	1 : 3 : 40	1 : 1	27.7

*This sample was used to show the peak fitting process in Figure S1.

Table B.10. Cu_3BTC_2 synthesis using varying equivalents of a 66% benzoic acid modulator, with a stoichiometric amount of linker and a metal concentration of 0.0027 M. M, L, and Mod refer to the concentrations of the metal salt, linker, and modulator in M.

M	L	Mod	Abs. Eq. M : L : Mod	Mod BA : B-	Size (nm)
0.0027	0.0018	0.0018	1 : 3 : 1	2 : 1	99.9
0.0027	0.0018	0.0126	1 : 3 : 4.67	2 : 1	92.4
0.0027	0.0018	0.0252	1 : 3 : 9.33	2 : 1	44.4
0.0027	0.0018	0.0378	1 : 3 : 14	2 : 1	46.8
0.0027	0.0018	0.0504	1 : 3 : 18.67	2 : 1	36.4
0.0027	0.0018	0.063	1 : 3 : 23.33	2 : 1	32.5
0.0027	0.0018	0.072	1 : 3 : 26.67	2 : 1	31.6
0.0027	0.0018	0.108	1 : 3 : 40	2 : 1	31.5

Table B.11. Cu_3BTC_2 synthesis using varying equivalents of a 50% benzoic acid modulator, with a stoichiometric amount of linker and a metal concentration of 0.001 M. M, L, and Mod refer to the concentrations of the metal salt, linker, and modulator in M.

M	L	Mod	Abs. Eq. M : L : Mod	Mod BA : B-	Size (nm)
0.001	0.00067	0.00067	1 : 3 : 1	1 : 1	74.2
0.001	0.00067	0.00467	1 : 3 : 4.67	1 : 1	73.4
0.001	0.00067	0.00933	1 : 3 : 9.33	1 : 1	49.1
0.001	0.00067	0.01407	1 : 3 : 14	1 : 1	32.6†
0.001	0.00067	0.01867	1 : 3 : 18.67	1 : 1	55.8
0.001	0.00067	0.02345	1 : 3 : 23.33	1 : 1	43.8

†Note that a phase impurity was observed in this sample. These peaks were excluded from Scherrer analysis.

Table B.12. Cu_3BTC_2 synthesis with varying total concentration, employing 7 equivalents of modulator with respect to the linker. M, L, and Mod refer to the concentrations of the metal salt, linker, and modulator in M. The ratios of the reagents and the total volume were kept constant. These data are depicted in Figure 4 of the main text.

M	L	Mod	Abs. Eq. M : L : Mod	Mod BA : B-	Size (nm)
0.00067	0.002	0.0140	1 : 3 : 21	1 : 1	63.9
0.001	0.003	0.0210	1 : 3 : 21	1 : 1	74.0
0.00167	0.005	0.0350	1 : 3 : 21	1 : 1	24.1
0.00250	0.0075	0.0525	1 : 3 : 21	1 : 1	22.1
0.00500	0.015	0.1050	1 : 3 : 21	1 : 1	21.2
0.00667	0.02	0.1400	1 : 3 : 21	1 : 1	14.3

Table B.13. Cu_3BTC_2 synthesis with varying total concentration, employing 0.7 equivalents of modulator with respect to the linker. The ratios of the reagents and the total volume were kept constant. M, L, and Mod refer to the concentrations of the metal salt, linker, and modulator in M. These data are depicted in Figure 4 of the main text.

M	L	Mod	Abs. Eq. M : L : Mod	Mod BA : B-	Size (nm)
0.00067	0.002	0.0140	1 : 3 : 2.1	1 : 1	104.0
0.00167	0.005	0.0350	1 : 3 : 2.1	1 : 1	87.0
0.00250	0.0075	0.0525	1 : 3 : 2.1	1 : 1	83.6
0.00333	0.01	0.0700	1 : 3 : 2.1	1 : 1	81.4
0.00500	0.015	0.1050	1 : 3 : 2.1	1 : 1	87.8
0.00667	0.02	0.1400	1 : 3 : 2.1	1 : 1	75.0

Table B.14. Cu_3BTC_2 synthesis with varying total concentration, employing 13.34 equivalents of modulator with respect to the linker. The ratios of the reagents and the total volume were kept constant. These data are depicted in Figure 4 of the main text.

M Conc	L Conc	Mod Conc	Abs. Eq. M : L : Mod	Mod BA : B-	Size (nm)
0.00067	0.002	0.0140	1 : 3 : 40.02	1 : 1	‡
0.00167	0.005	0.0350	1 : 3 : 40.02	1 : 1	17.8
0.00250	0.0075	0.0525	1 : 3 : 40.02	1 : 1	17.8
0.00333	0.01	0.0700	1 : 3 : 40.02	1 : 1	12.4
0.00500	0.015	0.1050	1 : 3 : 40.02	1 : 1	17.8
0.00667	0.02	0.1400	1 : 3 : 40.02	1 : 1	17.6

‡This reaction mixture, although blue in color, never centrifuged down. If any particles were present, they could not be isolated.

Table B.15. Cu_3BTC_2 synthesis scale up of representative samples. The total volume was kept constant.

M	L	Mod	Abs. Eq. M : L : Mod	Mod BA : B	Size (nm)
0.001	0.003	0.021	1 : 3 : 21	2 : 1	82.8
0.001	0.003	0.021	1 : 3 : 21	1 : 1	61.0
0.001	0.003	0.021	1 : 3 : 21	1 : 2	50.7
0.001	0.003	0.063	1 : 3 : 63	1 : 1	46.4

Table B.16. Cu_3BTC_2 synthesis utilizing copper acetate as a metal source and benzoic acid as the modulator.

M	L	Mod	Abs. Eq. M : L : Mod	Scherrer Size (nm)
0.001	0.003	0.003	1 : 3 : 3	72.7
0.001	0.003	0.021	1 : 3 : 21	59.0
0.001	0.003	0.042	1 : 3 : 42	45.7
0.001	0.003	0.060	1 : 3 : 63	47.5
0.001	0.003	0.084	1 : 3 : 84	49.2
0.001	0.003	0.120	1 : 3 : 120	56.3

Table B.17. ZIF-8 synthesis with increasing linker equivalents: In this experiment, a modified literature method was used.1 The total volume changes, allowing linker concentration (0.1901 M) to remain constant.

Linker Eq	M Conc	L Conc	M : L	Total Volume (mL)	Scherrer Size (nm)
4	0.04752	0.1901	1:4	5	63.8
6	0.0317	0.1901	1:6	7.5	38.0
8	0.0238	0.1901	1:8	10	27.7
10	0.0190	0.1901	1:10	12.5	19.7
12	0.0158	0.1901	1:12	15	16.7
14	0.0136	0.1901	1:14	17.5	14.0
16	0.0119	0.1901	1:16	20	11.5
18	0.0106	0.1901	1:18	22.5	15.0

Table B.18. ZIF-8 synthesis with increasing linker equivalents: In this experiment, a modified literature method was used.1 The total volume changes, allowing linker concentration (0.0988 M) to remain constant.

Linker Eq	M Conc	L Conc	M : L	Total Volume (mL)	Scherrer Size (nm)
6	0.0165	0.0988	1 : 5.85	15	19.8
8	0.0123	0.0988	1 : 7.76	20	16.3
10	0.0099	0.0988	1 : 9.79	25	13.1
12	0.0082	0.0988	1 : 11.6	30	11.2
14	0.0071	0.0988	1 : 13.9	35	7.8
16	0.0062	0.0988	1 : 15.4	40	13.6

Table B.19. ZIF-8 synthesis with HCl: This experiment used the conditions for 14 Hmim equivalents. A 1 M solution of HCl was made from concentrated HCl mixed into methanol.

HCl Eq	M Conc	L Conc	M : L : HCl	Total Volume (mL)	Scherrer Size (nm)
0.05	0.0136	0.1901	1:14.0:0.05	17.5	16.1
0.1	0.0136	0.1901	1:14:0.1	17.5	20.4
0.2	0.0136	0.1901	1:14:0.2	17.5	25.5
0.3	0.0136	0.1901	1:14:0.3	17.5	32.6
0.4	0.0136	0.1901	1:14:0.4	17.5	59.6
0.5	0.0136	0.1901	1:14:0.5	17.5	61.9
0.6	0.0136	0.1901	1:14:0.6	17.5	70.4
0.7	0.0136	0.1901	1:14:0.7	17.5	72.3

PXRD Patterns of Cu_3BTC_2 and ZIF-8 Products.

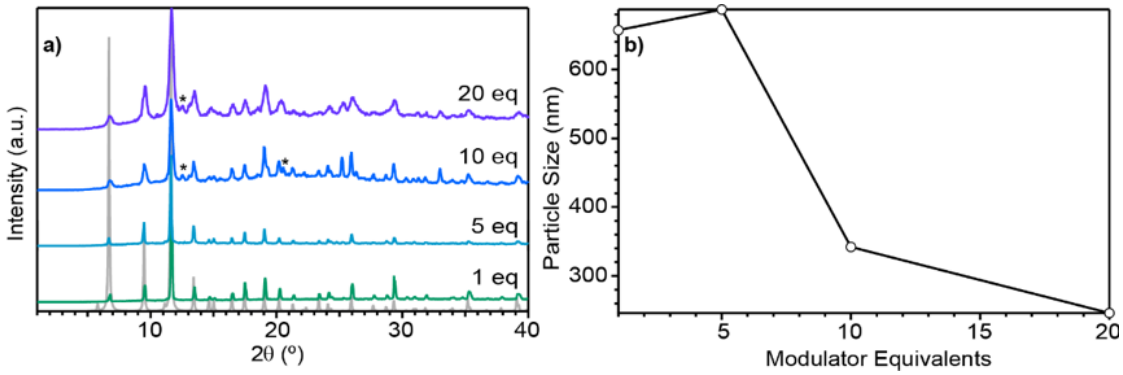

Figure B.2. Initial experiments were performed to explore the use of sodium benzoate in Cu_3BTC_2 synthesis. a) PXRD patterns of Cu_3BTC_2 synthesized using only sodium benzoate as the modulator. The simulated PXD pattern is shown in grey. Asterisks indicate peaks that are do not appear in the simulated pattern. b) Particle size decreases as the amount of sodium benzoate increases. Particle size was determined by Scherrer analysis.

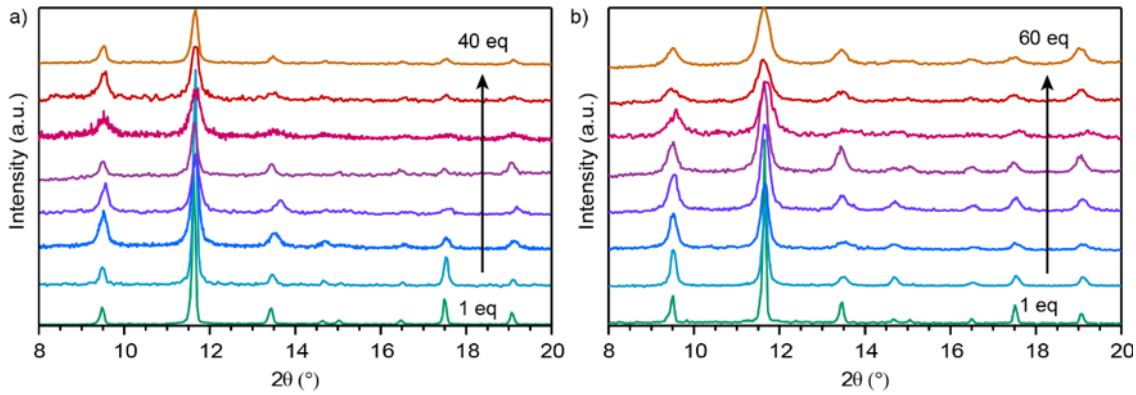

Figure B.3. Representative PXRD patterns of Cu_3BTC_2 synthesized with increasing modulator equivalents (50% benzoic acid) a) With linker in excess (L:M 3:1), the PXRD peaks first broaden with respect to added modulator up to 28 equivalents, after which the peaks begin to narrow. Synthetic parameters for these products can be found in table S6. b) With linker in a stoichiometric ratio (L:M 2:3), the PXRD peaks broaden with respect to added modulator up to 40 equivalents. At 60 equivalents, there is a slight narrowing of the peaks. Synthetic parameters for these products can be found in Table B.9.

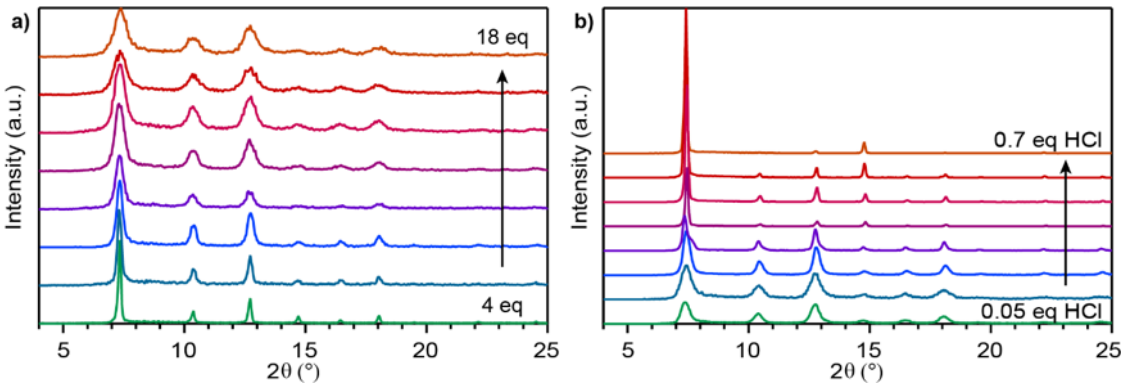

Figure B.4. Representative PXRD patterns of ZIF-8. a) ZIF-8 synthesized with increasing Hmim equivalents. Synthetic parameters for these products can be found in table B.16. b) ZIF-8 synthesized with 14 Hmim equivalents and increasing HCl. Synthetic parameters for these products can be found in table B.18.

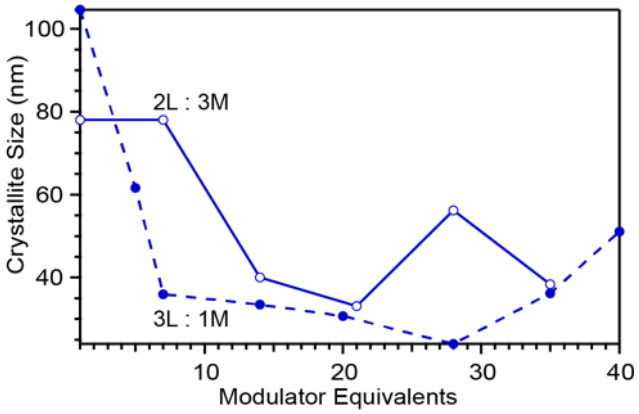

Figure B.5. The two ratios 3L : 1M and 2L : 3M are compared at the same metal concentration of 0.001 M with a 50% benzoic acid modulator. From 10 to 30 equivalents, the excess linker samples exhibit smaller sizes. Synthetic parameters for these samples can be found in Tables B.6 and B.11. Generally, we found conditions without excess linker to be less reproducible and chose to focus on 3L : 1M reaction conditions.

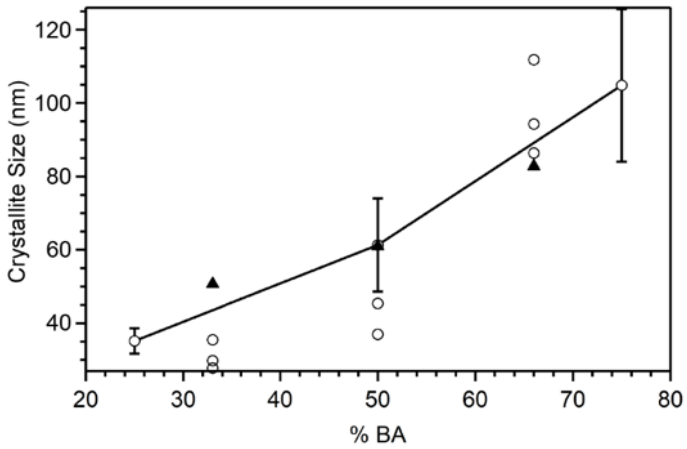

Figure B.6. Data from several samples is compared to show reproducibility. The trendline shown is the same data as in Figure 3 (Table B.1). Open circles are repeated trials. Black triangles are scale-up syntheses, the synthetic conditions for which can be found in Table B.14.

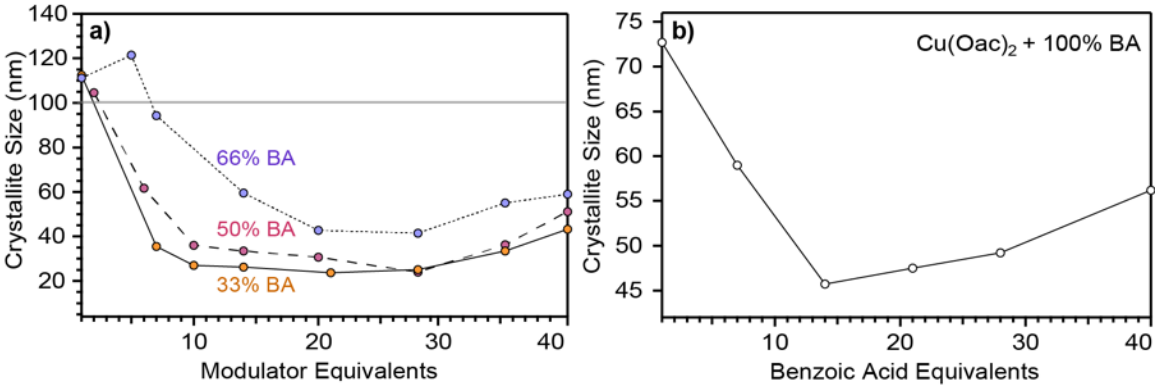

Figure B.7. Additional crystallite size data for Cu_3BTC_2 with respect to modulator equivalents. a) Full data set for modulator equivalents shown in Fig 3.4 in the main text. At 1 equivalent of modulator, all the crystallites are above 1 micron. b) Copper acetate can be used as a metal source without an external source of base, as acetate can deprotonate the MOF linkers. Increasing equivalents of benzoic acid results in a seesaw trend without the long plateau observed in the buffered systems.

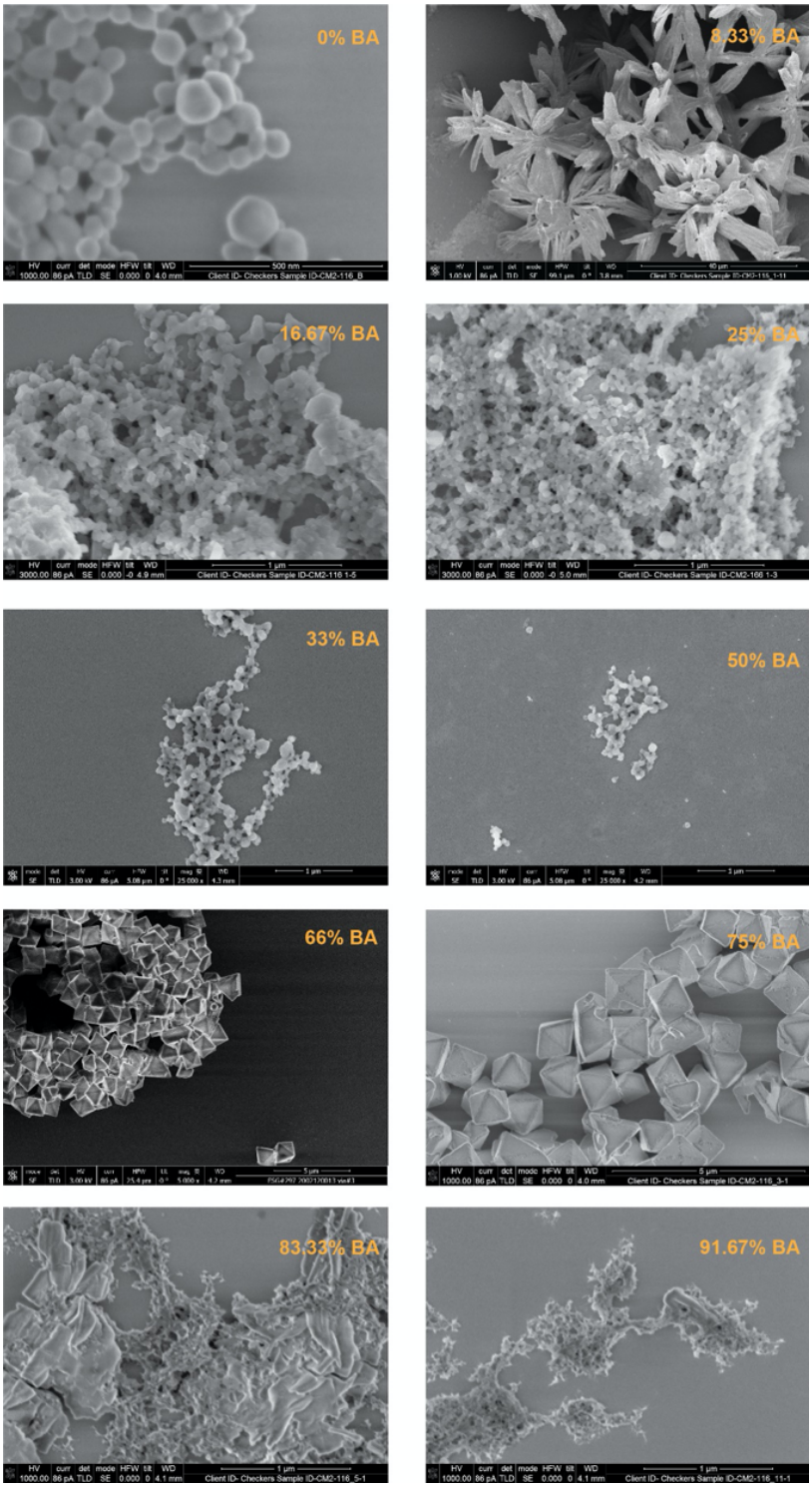

Figure B.8. SEM images of Cu_3BTC_2 particles as a function of benzoic acid content at constant modulator equivalents. Reaction conditions for these samples can be found in Table B.1.

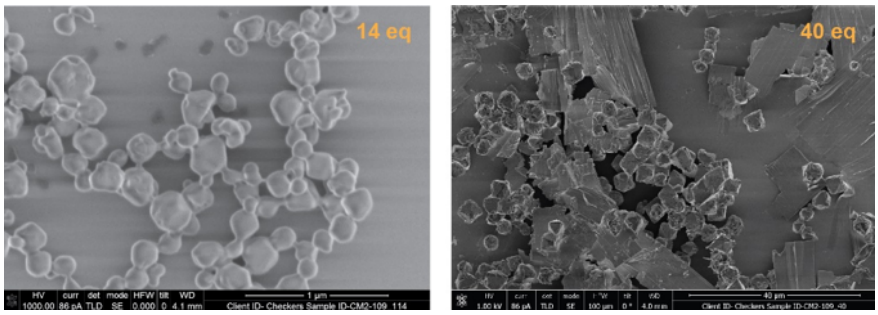

Figure B.9. SEM images of Cu_3BTC_2 particles as a function of modulator equivalents for a 66% benzoic acid modulator mixture. Reactant concentrations for these samples can be found in Table B.7.

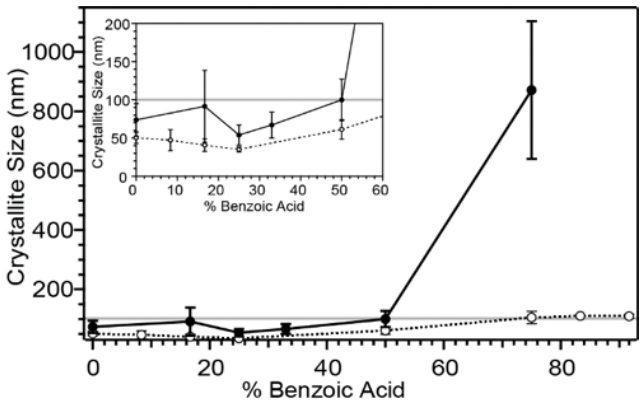

Figure B.10. Particle size from SEM compared to Scherrer crystallite size, as a function of benzoic acid content. Some samples were excluded from SEM sizing due to ambiguity when particles overlap or when the edges of particles are not clear (Fig. S9). SEM sizes are generally above Scherrer sizes. The two methods are in reasonable agreement until the Scherrer size exceeds 100 nm; grey lines show the 100 nm limit. Error bars on Scherrer sizes are from two batches, while error bars from SEM sizes are the size dispersity from at least 20 particles. SEM particle size was determined by using the circle tool and measure function in ImageJ.

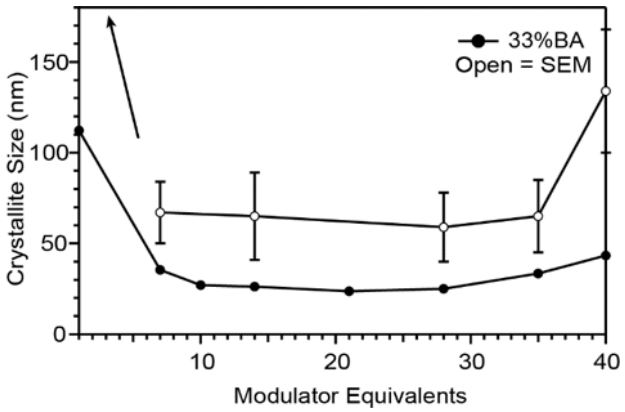

Figure B.11. Particle size from SEM compared to Scherrer crystallite size as a function of modulator equivalents for a 33% benzoic acid modulator mixture. SEM sizes are above Scherrer sizes in all cases, which is typical of the two instrumental techniques. SEM sizes for the crystals isolated with 1 eq. of modulator were over 1 m, indicated here by an arrow. Error bars from SEM sizes are the size dispersity from at least 20 particles using the circle and measure tools in ImageJ.() Sizes could not be determined for the sample at 21 equivalents. SEM images are in Figure B.7, and reaction conditions can be found in Table B.5.

APPENDIX C

SUPPLEMENTARY INFORMATION FOR CHAPTER 4

General Methods

Materials

All commercial chemicals were used as received and handled in inert conditions unless stated otherwise. All solvents were collected from a solvent purification system and stored over 4Å molecular sieves, and all liquid reagents were freeze-pump-thawed four cycles prior to use. N,N-dimethylformamide (DMF, ACS grade, Fisher Scientific), acetonitrile (MeCN, HPLC grade, Fisher Scientific), dichloromethane (DCM, ACS grade, Fisher Scientific), iron (II) chloride (98%, anhydrous, Strem), 1-methylimidazole (99%, Sigma-Aldrich), 1,2,3-triazole (98%, TCI), tetrabutylammonium hexafluorophosphate (98%, TCI, recrystallized 3 times from ethanol), tetrabutylammonium tetrafluoroborate (98%, ACROS, recrystallized once from ethanol and once from ethyl acetate).

All manipulations were performed under N2 unless stated otherwise. Solution-state UV-Vis spectra were collected using either a Shimazdu Biospec-1601 for visible range measurements, and a Perkin Elmer Lambda-1050 UV/Vis/NIR spectrophotometer for extended range measurements. For acid-digestion ^{1}H-NMR, samples were dried under vacuum, digested in 10% DCl / D_2O in DMSO-D_6 in air, then filtered through cotton plugs prior to analysis with a Bruker Advance III-HD 600 NMR Spectrometer. IR spectra were recorded on a Bruker Alpha II compact IR with an ATR attachment in a N_2-filled glovebox.

Dynamic Light Scattering (DLS) experiments. DLS data was collected using a Wyatt Mobius instrument with a custom-made airfree quartz cuvette with a pathlength of 1 mm. Samples suspended in DMF were filtered through 0.45-μm

PTFE filters, and the solvent itself was prepared by filtration through a 0.10-m PTFE filter. A normal 50-mW laser mode was used, and the samples were diluted such that the measured counts were between 1 and 8 million, and the correlation function was reproducible over the course of 6 measurements 1 minute apart.

N_2 sorption measurements. For gas sorption measurements, the samples were further washed with MeCN twice, and DCM five times. A typical washing process proceeded over the course of 1 week. Samples were dried under vacuum in tared ASAP tubes. Samples were degassed under high vacuum and 120 °C heat on an ASAP 2020 instrument; degassing was considered complete when the pressure in the closed manifold rose less than 2.5 μtorr/min. BET analysis was based on a linear fit in the BET plot to N_2 isotherm data at relative pressures between 10^{-5} – 10^{-1} P/P_0. Data for these experiments can be found in Figure C.10.

Crystallite size analysis by Le Bail fitting. Crystallite size of 130 nm particles and 5.5 nm particles was characterized by Le Bail fitting on the PXRD patterns in GSAS-II[(280)] according to the literature.[(281)] The analysis allows to deconvolute the sample (Lorentzian) and the instrumental (Gaussian) broadening parameters. Aluminum oxide (Al_2O_3, 300 nm) was used to determine the instrumental broadening parameters (U, V, W, the Gaussian component). The sample broadening parameters, crystallite size (X from the Lorentzian component) and crystalline strain (Y from the Lorentzian component) were refined while the obtained instrumental broadening parameters were fixed. X and Y parameters were utilized to estimate the crystallite size and crystalline strain with the following formulas.

Crystallite size:

$$p = \frac{18000K\lambda}{X\pi} \tag{C.1}$$

Crystalline strain:

$$S = Y\frac{\pi}{18000}100\% \tag{C.2}$$

where K is the Scherrer constant (0.90), λ is the wavelength (0.15418 nm), X and Y are the Lorentzian components of the peak profile, and = 3.14. The obtained parameters are summarized in Table C.1.

Synthesis of Fe(TA)$_2$ under Different Conditions

In the syntheses of iron triazolate particles, several variables were used to control particle size and dispersity: reaction time, concentration, and the identity of an added modulator. We found that the calculated Scherrer size of the particles decreased upon dilution, and upon the addition of sodium formate, n-butylamine, 1-methylimidazole, 5-bromo-1-methylimidazole, and 1-benzyl-2-methylimidazole. Additionally, particle size decreased upon using further excess 1,2,3-triazole: the typical synthesis gave 44 $\pm$ 7 nm but having 4 equivalents of triazolate rather than 3 further decreased the size to 10 $\pm$ 1 nm (Fig, D.2e).

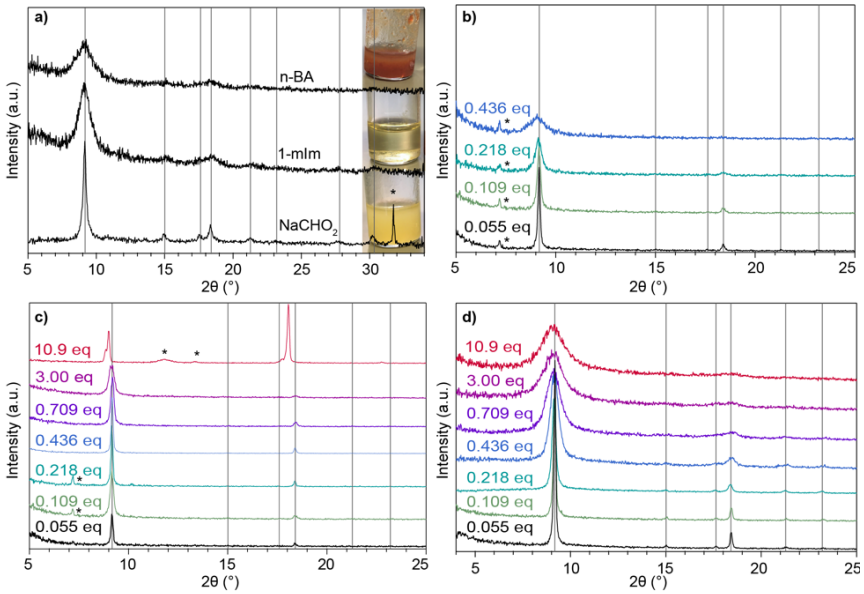

Figure C.1. PXRD patterns of $Fe(TA)_2$ products synthesized with modulators. Expected reflections are shown as grey lines, and possible phase impurities are denoted by asterisks. a) Syntheses using 1.0 eq of n-butylamine, sodium formate, and 1-methylimidazole. Photos of reaction solutions prior to heating are inset next to each trace. b) $Fe(TA)_2$ products created using varying equivalents of 1-benzyl-2-methlimidazole. c) $Fe(TA)_2$ products obtained from syntheses with varying amounts of 5-bromo-1-methylimidazole. d) $Fe(TA)_2$ products obtained from syntheses with varying amounts of 1-methylimidazole.

We noticed a dependence of particle size on the batch of iron (II) chloride stock. Purposeful oxidation of iron (II) chloride by brief oxygen exposure led to particles of decreased size: the control sample with rigorous air-free conditions gave 44 ± 7 nm and with air-exposed $FeCl_2$ the particle size was 12 ± 1 (Fig. C.2f) Tables C.1-C.4 contain reaction conditions and particle sizes for all $Fe(TA)_2$ particles discussed herein. Sodium formate (1 eq) did not have a significant impact on crystallite size, and the PXRD pattern exhibited a phase impurity peak (Fig. C.1a).

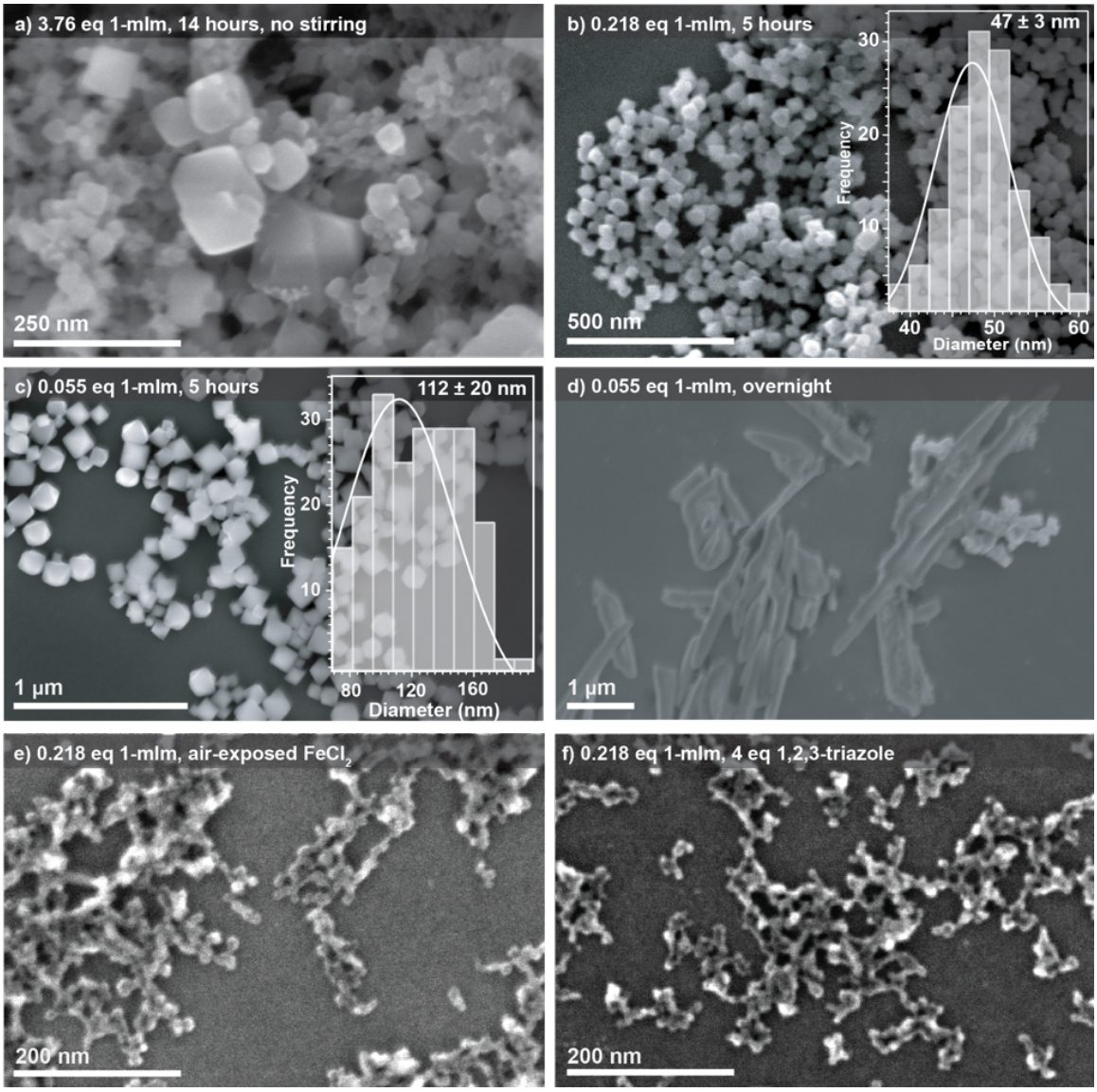

Figure C.2. SEM images of $Fe(TA)_2$ products synthesized with different reaction times and conditions. a) Polydisperse particles are created when a reaction with 3.763 eq 1-mIm was left overnight. b) Particles increase only slightly in polydispersity for 0.218 equivalents when allowed to react for 5 hours instead of 1.5. c) With 0.055 eq 1-mIm and a 5-hour reaction time, the resulting particles are more polydisperse. d) When allowed to react overnight, the 0.055 eq 1-mIm reaction will grow long rods in addition to smaller pseudo-octahedral particles.

Initially, reactions were performed without stirring and with a 18-21 hour reaction time, which resulted in extremely high polydispersity (Fig. C.2a). We

found that, at 0.055 equivalents of 1-mIm the particles would grow into bulk-like structures if allowed to react overnight, while a 5 hour reaction time did not significantly change the particle size, but did increase the polydispersity (130 ± 10 nm vs 112 ± 20 nm with a 5 hour reaction). A five-hour reaction time for 0.218 eq 1-mIm gave the same size and polydispersity as the 1.5 hour reaction (Fig. C.2b, Fig 4.2). The particles characterized throughout the main manuscript were all synthesized with a 1.5 hour reaction time. Exploratory syntheses were performed on a 2-mL scale; when suitable conditions were found, the reactions were scaled up to 14 mL, and no changes in the crystallite sizes or SEM sizes were observed. The particles synthesized with the lowest equivalents were less replicable than others, possibly due to the larger error in micropipettors at small volumes (Table C.2).

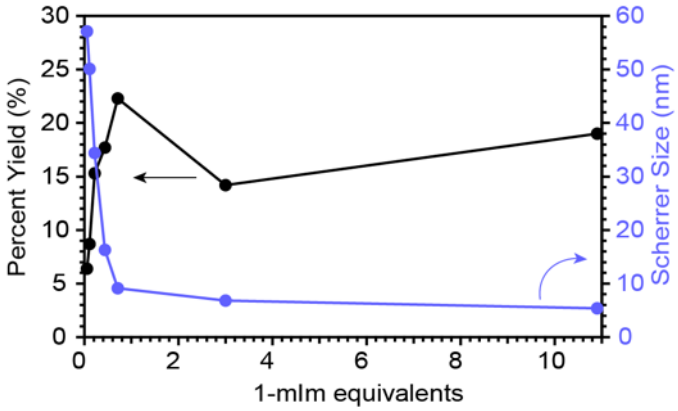

Figure C.3. Reaction yield of $Fe(TA)_2$ as a function of 1-methylimidazole equivalents. All nanoparticle reactions were halted at 1.5 hours. Low yield is typical in nanomof synthesis. Trials with 5 hours resulted in a higher polydispersity and a marginally improved yield.

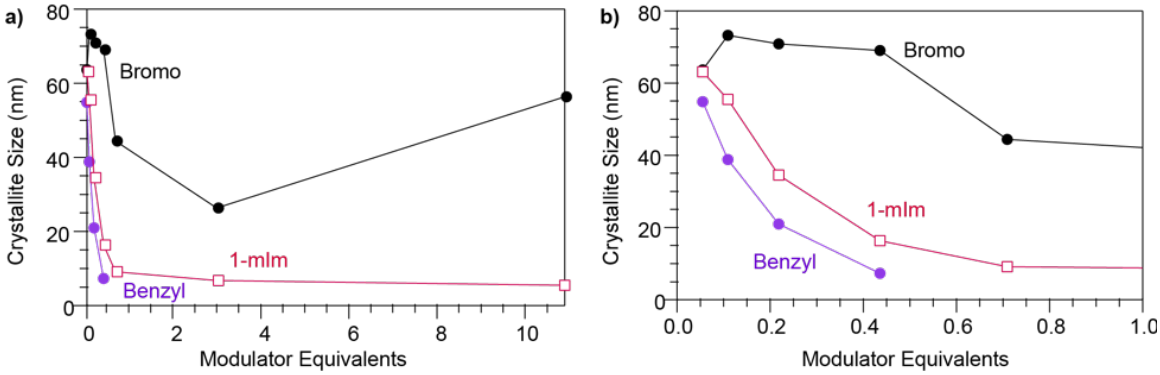

Figure C.4. Iron triazolate crystallize size trends with respect to modulator equivalents. Sizes were determined by Scherrer analysis. a) Trend of particle size from Scherrer analysis for three different modulators. Bromo = 5-bromo-1-methylimidazole; Benzyl = 1-benzyl-2-methylimidazole; 1-mIm = 1-methylimidazole. b) A zoom-in showing the trend at low equivalents for the three modulators.

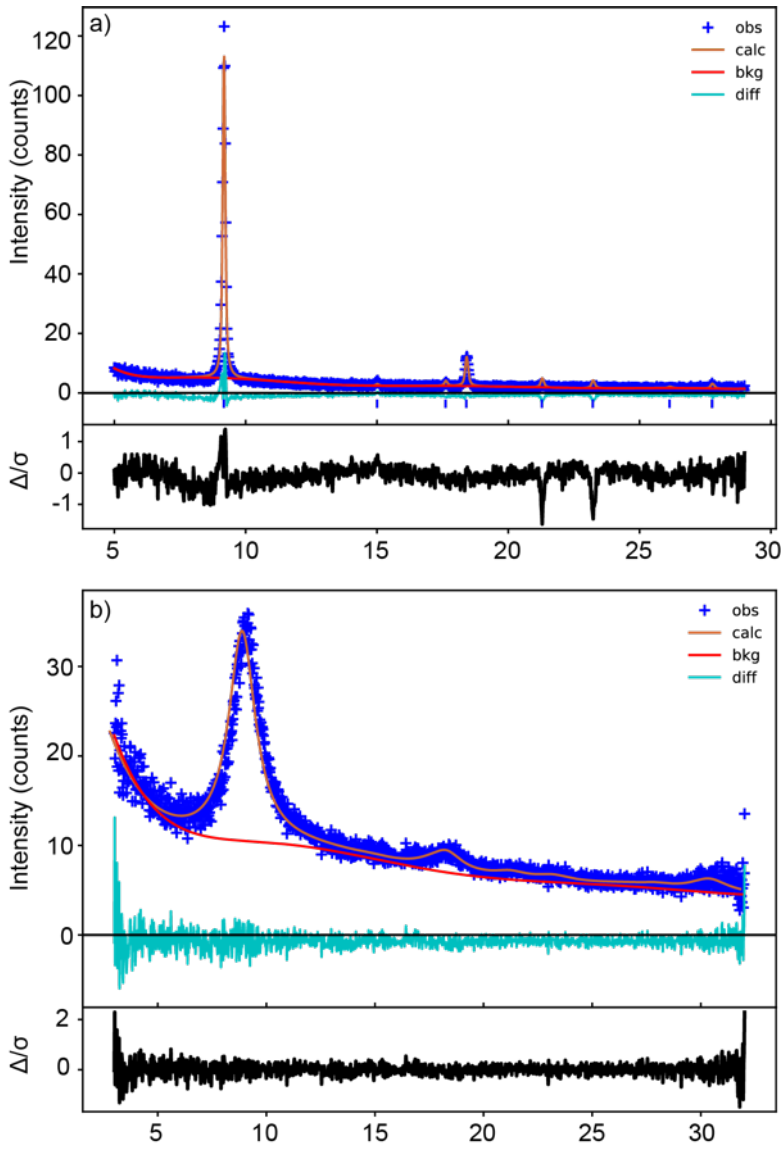

Figure C.5. Le Bail fits for largest and smallest $Fe(TA)_2$ nanoparticles. Fitting conditions and parameters can be found in Section C.1 and Table C.1. a) Le Bail fitting for 130 nm $Fe(TA)_2$ particles gives a domain size of 128.53 nm. b) Le Bail fitting for 5.5 nm particles gives a domain size of 6.40 nm.

Table C.1. Crystallite sizes and strain of 130 nm (0.05 eq 1-mIm) and 5.5 nm (10.9 eq 1-mIm) particles from Le Bail fitting

Sample	p /nm	S / %	Rwp / %
5.5-nm	6.40	4.76	8.01
130-nm	128.53	0.21	11.69

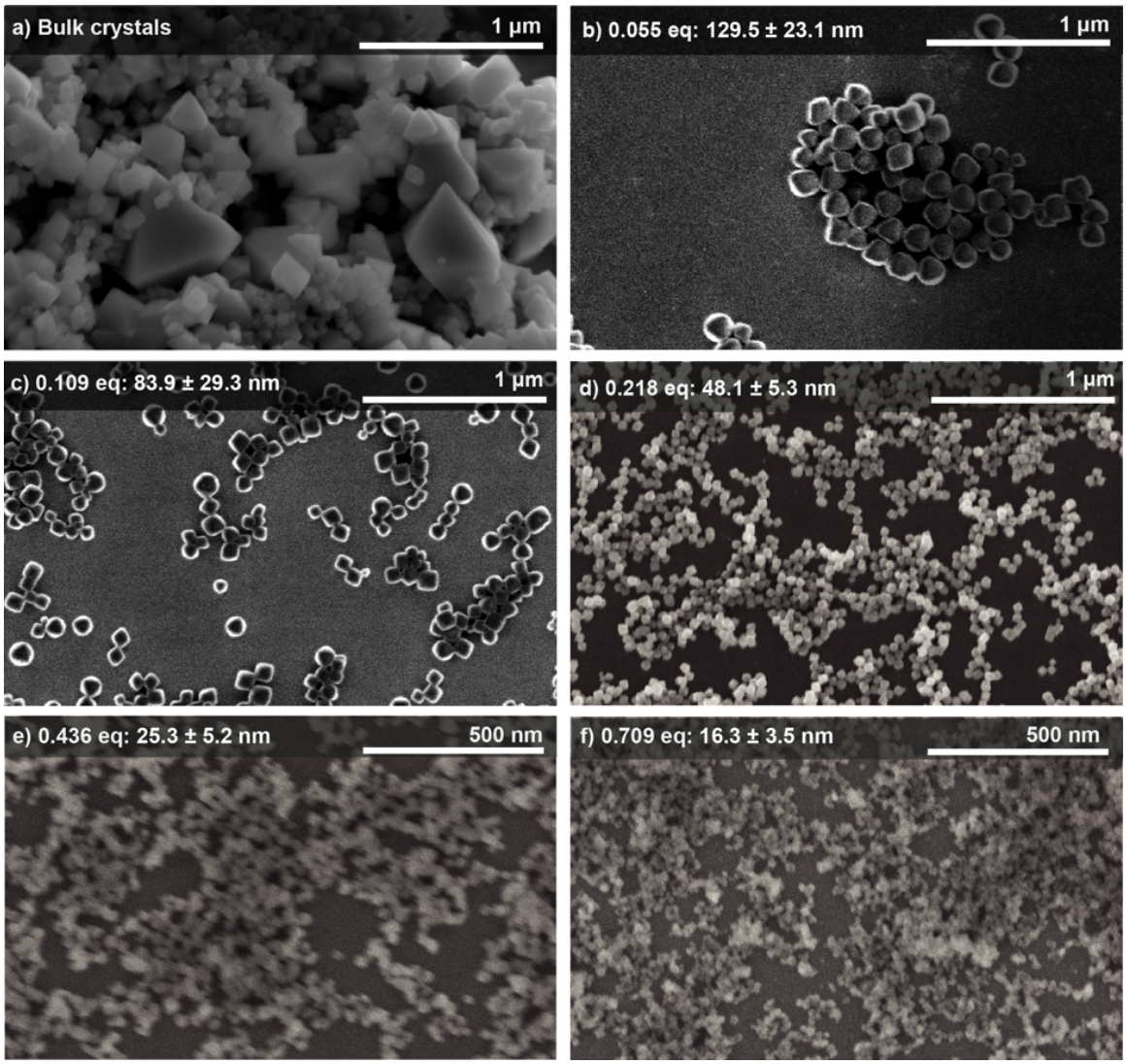

Figure C.6. Larger SEM images of iron triazolate products. a) the morphology resulting from a typical synthesis of bulk iron triazolate, b) – d) nanoparticles of iron triazolate synthesized with varying equivalents of 1-methylimidazole.

Table C.2. Iron triazolate particle sizes from syntheses with varying amounts of 1-methylimizadole (modulator eq is with respect to $FeCl_2$). We include Scherrer sizes for two separate batches, followed by the statistical particle distribution as determined by sizing particles from SEM image data with the line tool in ImageJ.[2] The particle size distribution was fit to a weighted gaussian, and the values presented are the mode ± standard deviation (σ).

Mod. Eq.	Batch 1 Size (nm)	Batch 2 Size (nm)	Batch 2 SEM Size (nm)	Dispersity
0.055	57	63	130 ± 10	0.09
0.109	50	56	84 ± 20	0.18
0.218	34	35	48 ± 3	0.06
0.436	16	19	25 ± 3	0.10
0.709	9.1	9.1	16 ± 2	0.11
3.00	6.8	6.8	—	—
10.9	5.4	5.5	—	—

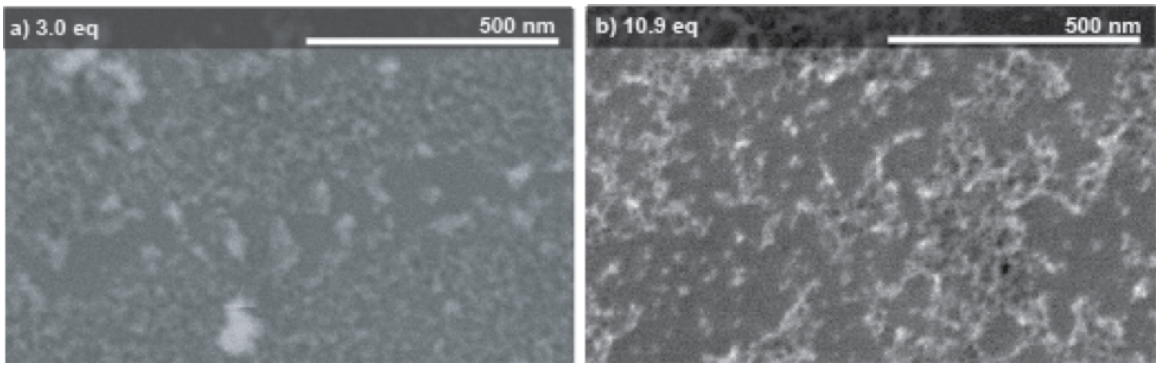

Figure C.7. SEM images of the two smallest $Fe(TA)_2$ particle sizes. a) With 3.0 1-mIm equivalents, the Scherrer size is 6.8 nm and although small nanosized features are observed in the SEM, they cannot be fully resolved. b) With 10.9 1-mIm equivalents, the Scherrer size is 5.5 nm and the SEM image shows small nanosized features that cannot be resolved.

Table C.3. Iron triazolate particle sizes from syntheses with varying amounts of 5-bromo-1-methylimidazole. We include Scherrer sizes, and a select SEM size for these exploratory modulator syntheses. The particle size distribution was fit to a weighted Gaussian curve, and the values presented are the mode ± standard deviation (σ). The asterisk denotes a significant phase impurity observed in the sample.

Mod. Eq. (to $FeCl_2$)	Scherrer Size (nm)	SEM Size (nm)	Dispersity
0.055	64	—	—
0.109	73	—	—
0.218	71	78 ± 6	0.08
0.436	69	—	—
0.709	45	—	—
3.00	26	—	—
10.9	56*	N/A	—

Table C.4. Iron triazolate particle sizes from syntheses with varying amounts of 1-benzyl-2-methylimidazole. We include Scherrer sizes, and a select SEM size for these exploratory modulator syntheses. The particle size distribution was fit to a weighted gaussian, and the values presented are the mode ± standard deviation (σ).

Mod. Eq. (to $FeCl_2$)	Scherrer Size (nm)	SEM Size (nm)	Dispersity
0.055	55	—	—
0.109	39	—	—
0.218	21	22 ± 3	0.14
0.436	7.3	—	—

Table C.5. Iron triazolate particle sizes from six identical syntheses. To ensure the synthesis was replicable, seven small scale syntheses were repeated. Phase purity was confirmed by PXRD and Scherrer analysis was performed to obtain particle sizes.

Equivalents	Scherrer Size (nm)
0.709	9.1
0.709	9.0
0.709	8.8
0.709	10
0.709	8.1
0.709	8.1
0.709	8.3

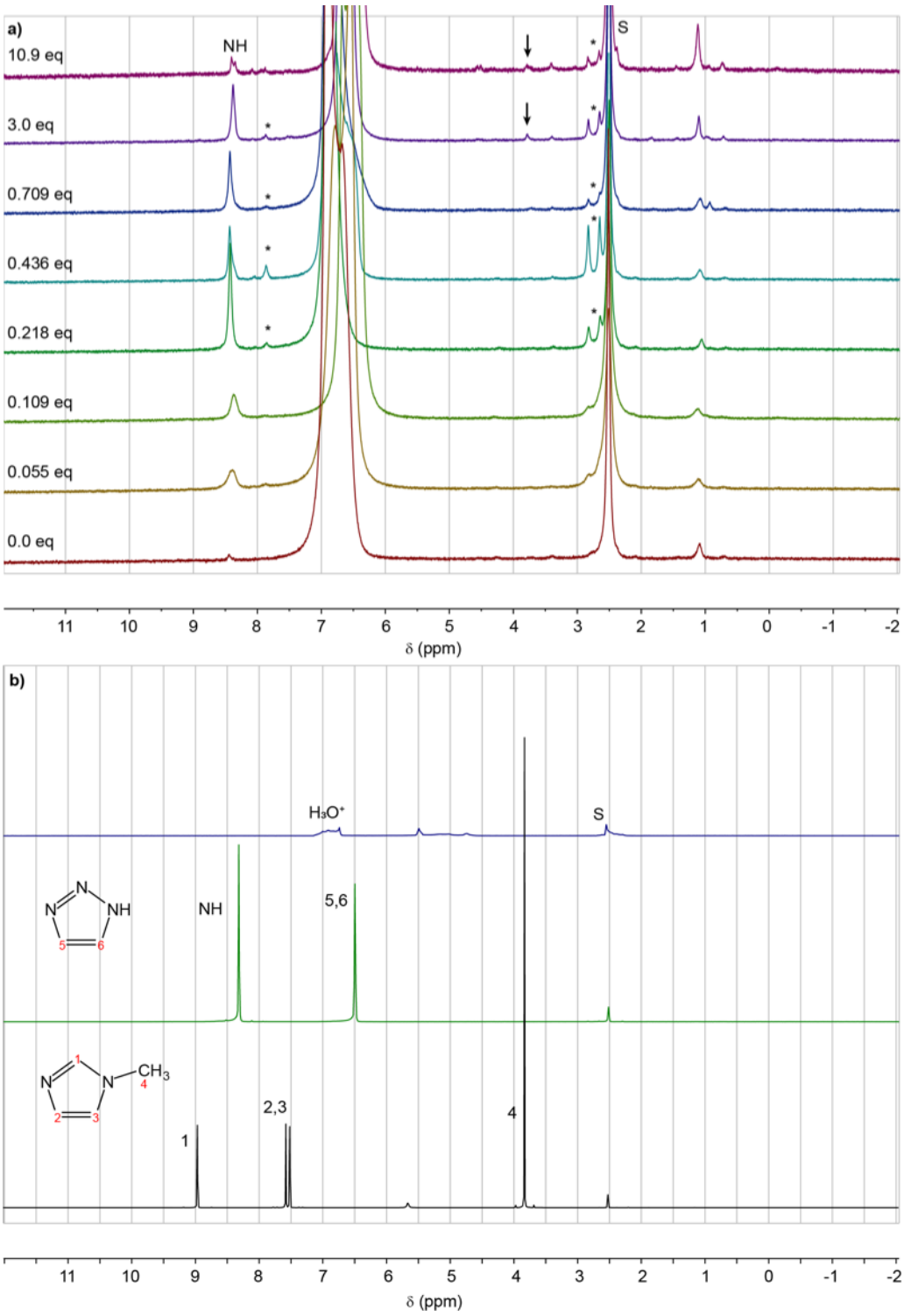

Figure C.8. Acid digestion ^{1}H NMR spectra of iron triazolate nanoparticles compared to the constituent ligands and the bulk MOF product. MOF samples were digested in 1.5 : 7 DCl : DMSO. Asterisks indicate peaks from DMF. An arrow indicates a peak coincident with the methyl group of 1-methylimidazole; no other peaks from the modulator appear.[153]

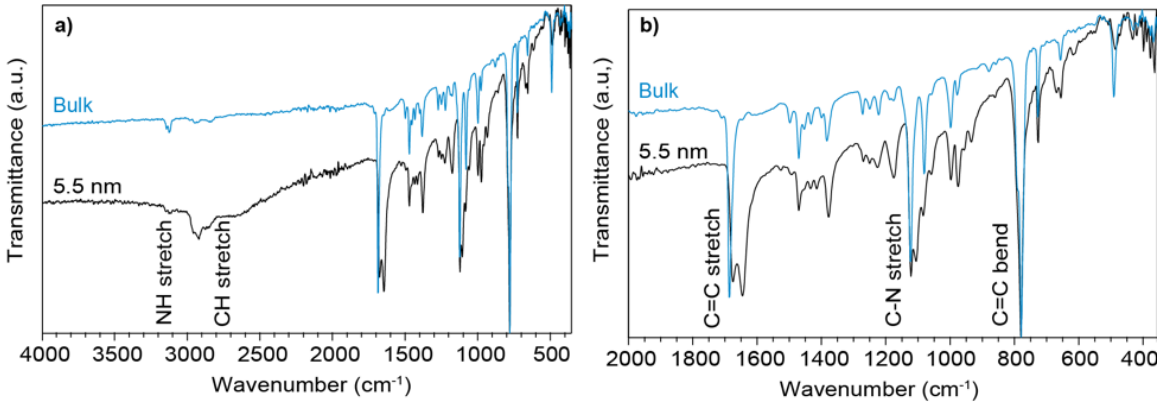

Figure C.9. IR spectra of the bulk material and the smallest $Fe(TA)_2$ nanoparticles. The expected stretches for the triazole ligand appear in both traces. For the nanoparticles, there are several additional stretched attributed to trapped DMF solvent.

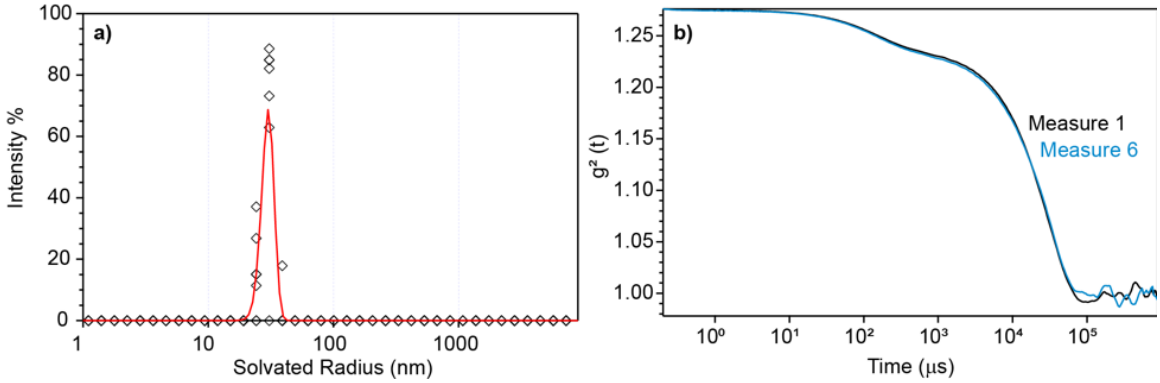

Figure C.10. DLS data collected for $Fe(TA)_2$ particles synthesized with 0.436 eq 1-methylimidazole. a) Solvated radius, in DMF, of the colloidal particles was measured six times and the collected data is plotted, then fit to a Gaussian curve, resulting in a solvated radius of 30 ± 5 nm. The x axis is presented in logarithmic scale. b) Representative correlation functions from the first and sixth measurement, showing a reproducible curve.

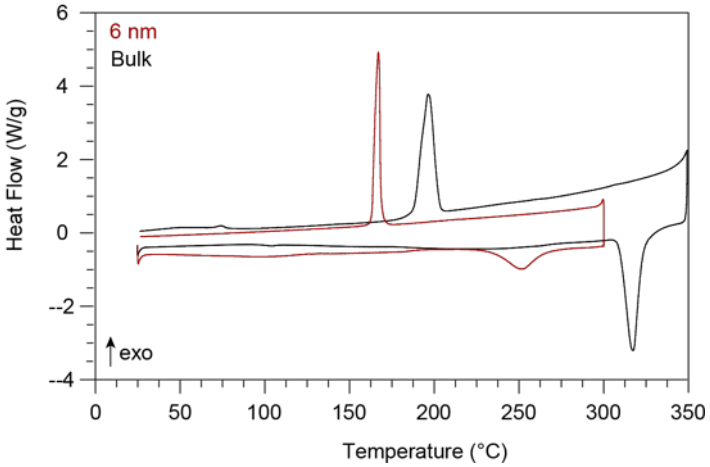

Figure C.11. Differential Scanning Calorimetry of $FeTA_2$ nanoparticles synthesized with 3.63 eq 1-mIm compared to previously published data of the bulk material.[()]3 Cycles were collected at a scan rate of 10 °C min⁻1.

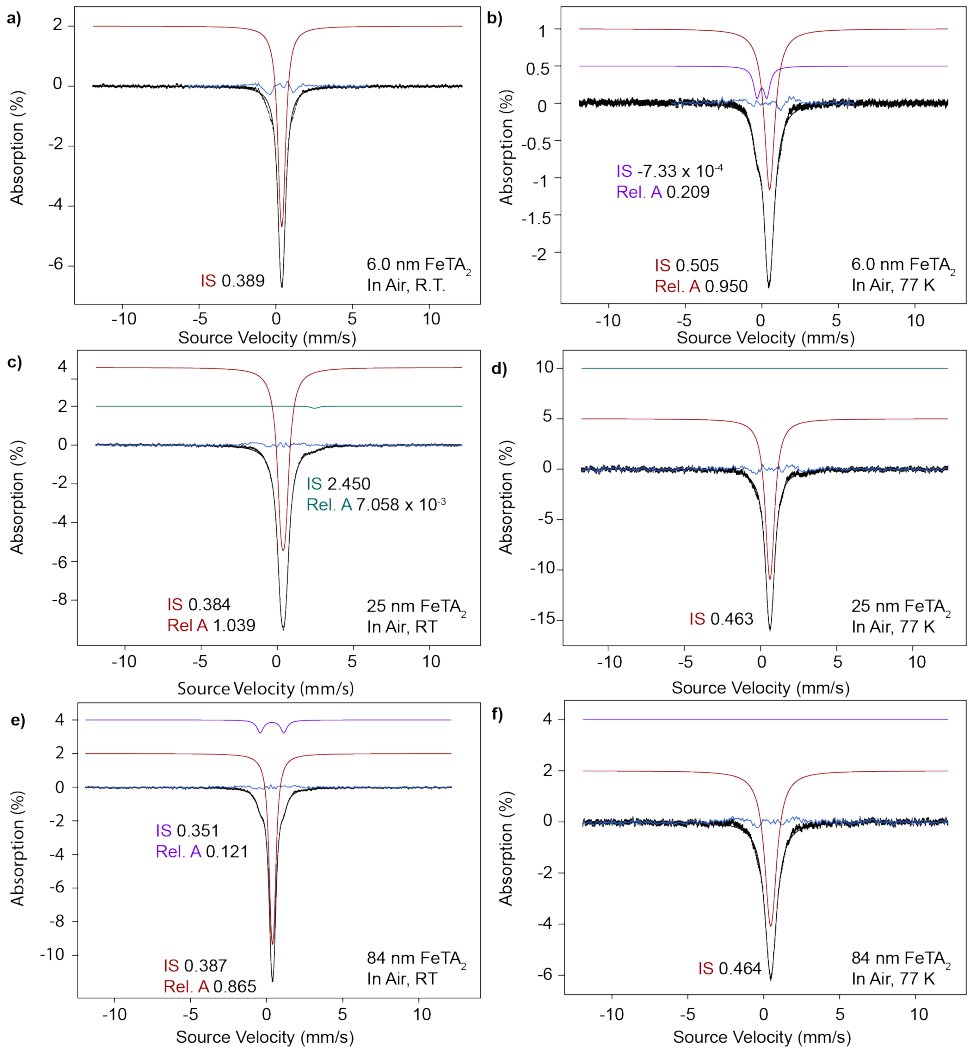

Figure C.12. Mössbauer spectra of several sizes of $Fe(TA)_2$ in air. Spectra of the smallest nanoparticles shows a slight shoulder at room temperature (RT) (a) and clear quadropole splitting at 77 K (b). Spectra of medium sized particles (25 nm) exhibit a second feature similar to that observed for the smallest particles under N_2 in Fig 4.3 (c,d). Spectra of large 84-nm particles show clear oxidation (e,f).

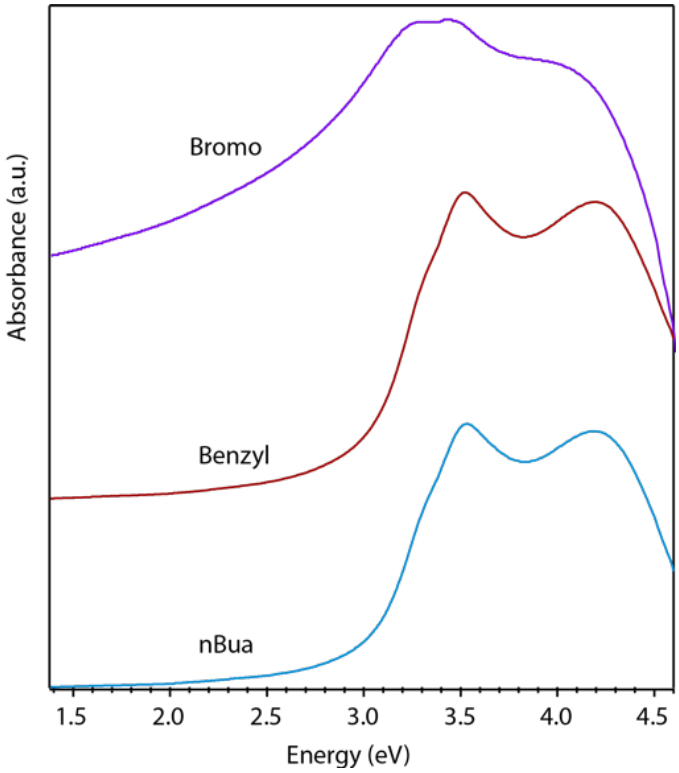

Figure C.13. UV-Vis traces for syntheses employing other modulators. Absorption is normalized. All samples were synthesized with 0.218 equivalents of the modulators: 5-bromo-1-methylimidazole (Bromo), 1-benzyl-2-methylimidazole (Benzyl), and n-butylamine (nBua). Broadening in the spectra of the Bromo sample is likely due to poor colloidal stability.

Additional UV-Vis Data.

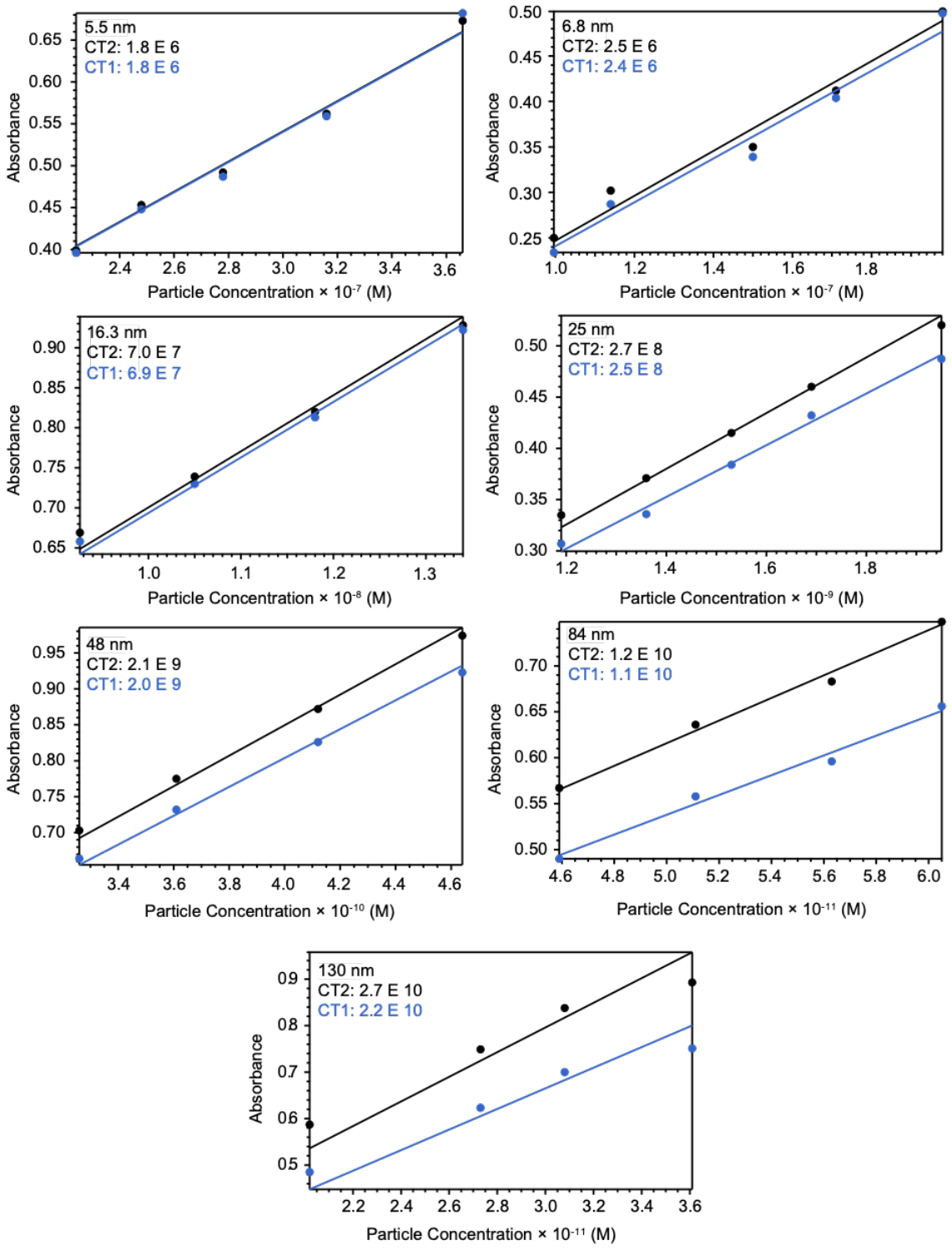

Figure C.14. Beer's Law plots used to determine Fe(TA)−2 extinction coefficients. At each concentration, two spectra were collected a few minutes apart to ensure there were no transient effects. Linear fits were conducted in Igor with the y-intercept held at 0.0 Abs.

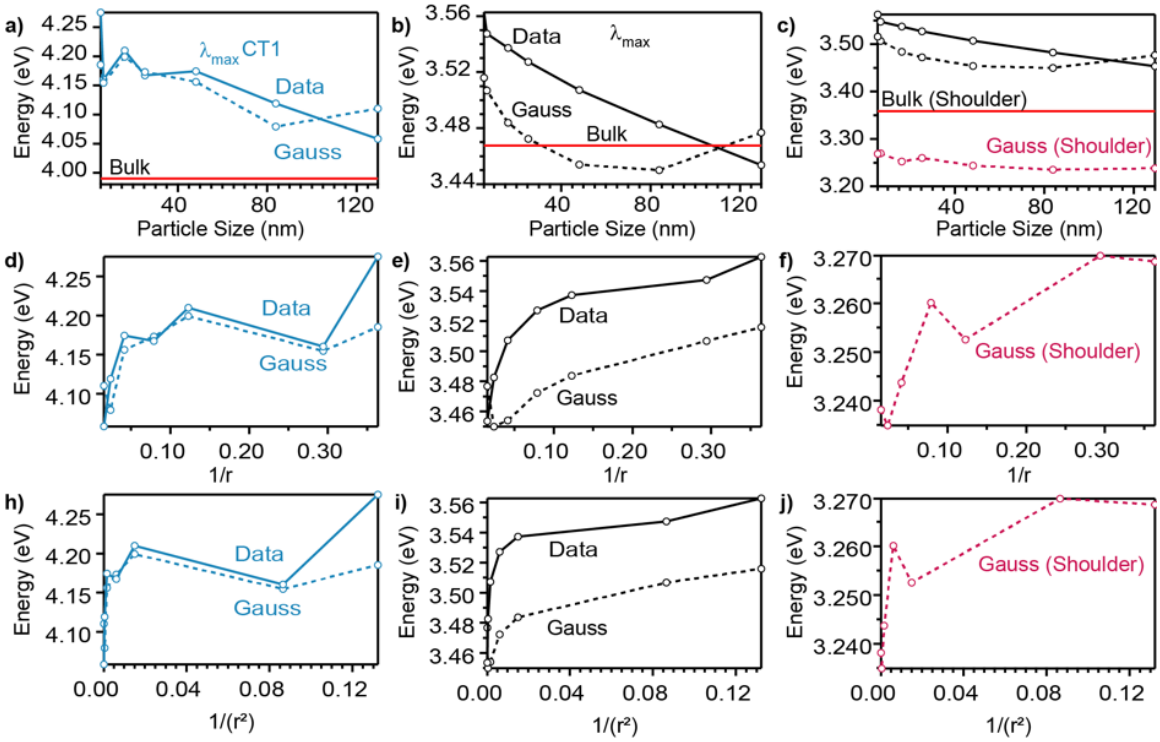

Figure C.15. Energetic transitions determined from UV-Vis spectra, from the raw data and from gaussian fits, plotted against particle diameter, 1/r, and $1/(r^2)$. The absolute maximum of the two peaks CT1 and CT2 were used to determine extinction coefficients (solid line). The peaks were additionally fitted to gaussian curves using the Multipeak 2.0 package in Igor 6.3 (dashed line).

Additional Electrochemical Data. Although the particle dispersions are colloidally stable for months, our CV analysis of the colloids was carefully conducted 3 days after the particle batch was synthesized to avoid any possible aggregation effects from long-term storage. All the relevant CV data was collected within four hours. Even so, there is a noticeable shift to lower potential in the first (70 mV/s) scan compared to the subsequent scans in the 6.8 nm particle batch (Fig D.15b).

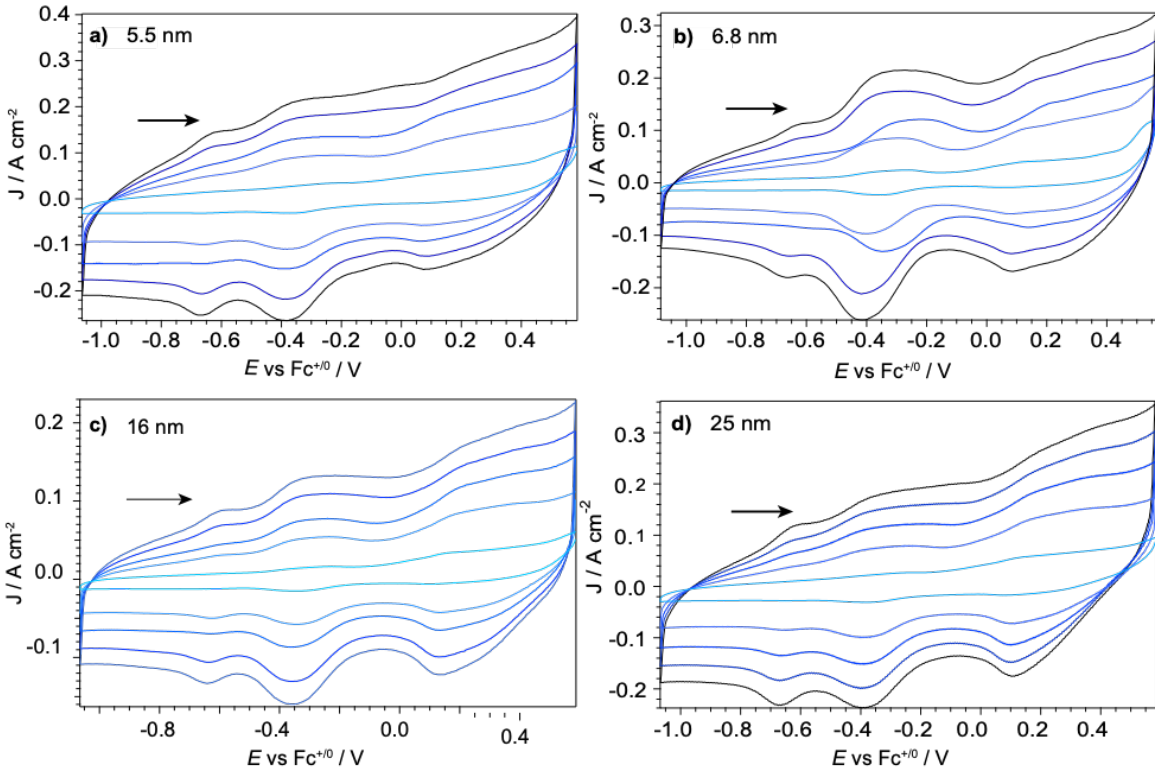

Figure C.16. CV scans of $Fe(TA)_2$ particles of varying size as colloids in 0.1 M $TBAPF_6$ / DMF. Scans were collected with rates of 10 mV/s (lightest blue), 40 mV/s, 70 mV/s, 100 mV/s, and 130 mV/s (black). The particle sizes are 5.5 nm (a), 6.8 nm (b), 15 nm (c) and 25 nm (d). The colloids have uncertain concentration due to the low stability of the particles under bias and in electrolyte solution; the current is therefore normalized to the area of the GC working electrode.

Table C.6. Peak positions of redox features in colloidal $Fe(TA)_2$ in 0.1 M $TBAPF_6$ / DMF. Peaks in the colloids are wide and they overlap one another, such that determining peak positions was not always possible to do accurately.

Particle Size nm	Scan Rate mV/s	Peak Pos R1 (V)	Peak Pos R2 (V)	Peak Pos O1 (V)
	130	-0.669	-0.382	
5.5	100	-0.667	-0.386	
	70		-0.390	
6.8	130	-0.661	-0.416	
	100		-0.417	
16.3	130	-0.641	-0.360	-0.585
	100	-0.631	-0.359	-0.622
	130	-0.675	-0.395	
25.3	100		-0.400	
	70		-0.353	

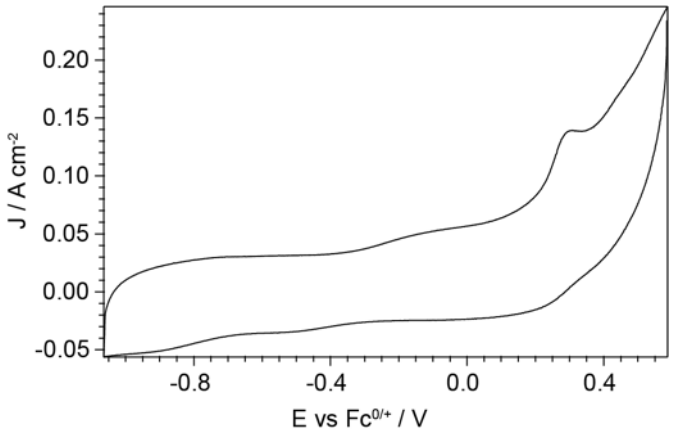

Figure C.17. Control CV collected of the triazole ligand in 0.1 M $TBAPF_6$ / DMF. Only a simple irreversible oxidation is observed. Current is normalized to the area of the glassy carbon working electrode.

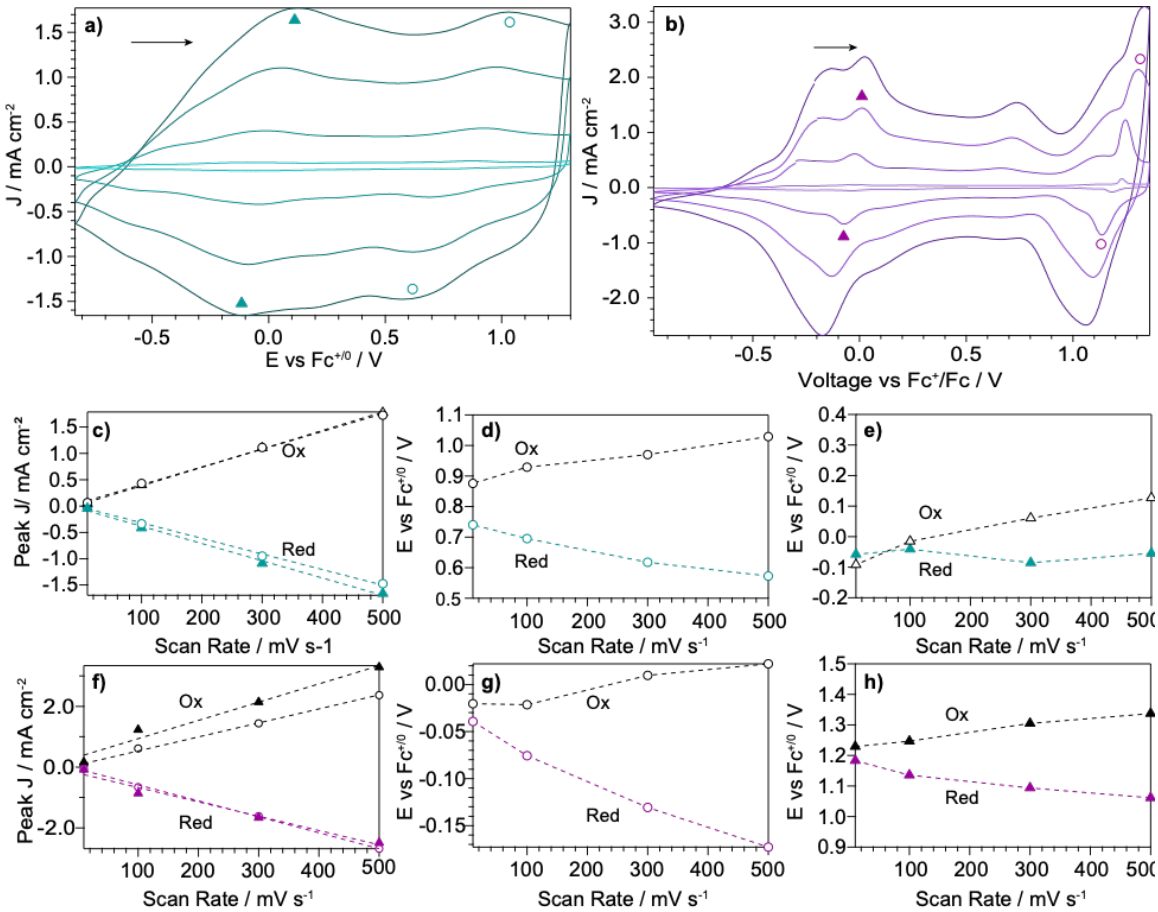

Figure C.18. CV scans of 16-nm $Fe(TA)_2$ particles drop-casted onto the glassy carbon working electrode in 0.1 M $TBAPF_6$ / MeCN. a) Scans were collected with rates of 10 mV/s (lightest green), 100 mV/s, 300 mV/s, and 500 mV/s (darkest green). Data is normalized with respect to the area of the bare GC electrode. b) Peak-to-peak separation of the two main faradaic events, denoted by a circle and a triangle in the CV. c) Peak current with respect to scan rate with a linear fit. Black and blue symbols correspond to oxidation and reduction events, respectively. d) Position of the peak ($E_{\frac{1}{2}}$) for the second faradaic event (circles). e) Position of the peak for the first faradaic event (triangles).

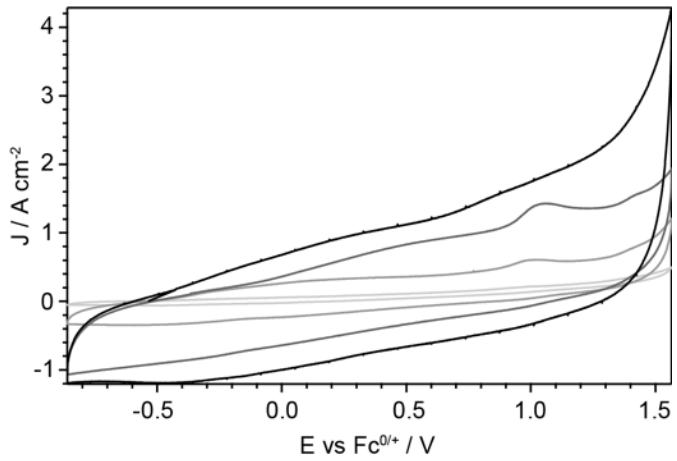

Figure C.19. CV scans of the bulk $Fe(TA)_2$ material. The bulk material was dispersed in DMF, sonicated, then dropcast onto a glassy carbon electrode. Data was collected in 0.1 M $TBAPF_6$ / MeCN. Scans were collected with rates of 10 mV/s (lightest grey), 100 mV/s, 300 mV/s, and 500 mV/s (black). Data is normalized with respect to the area of the bare GC electrode.

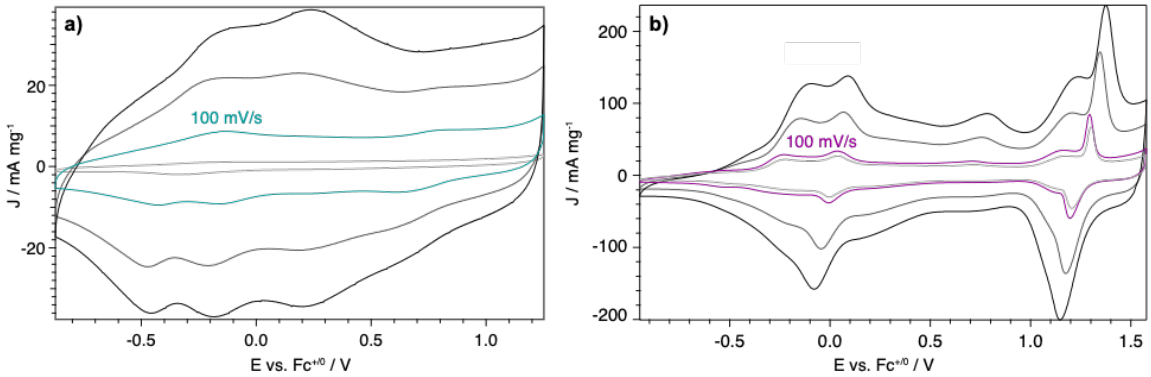

Figure C.20. CV scans with varying scan rate on QCM electrodes in $TBAPF_6$ (a) and $TBABF_4$ (b). The lightest grey corresponds to 10 mV/s, followed by 100 mV/s, 300 mV/s, and finally 500 mV/s.

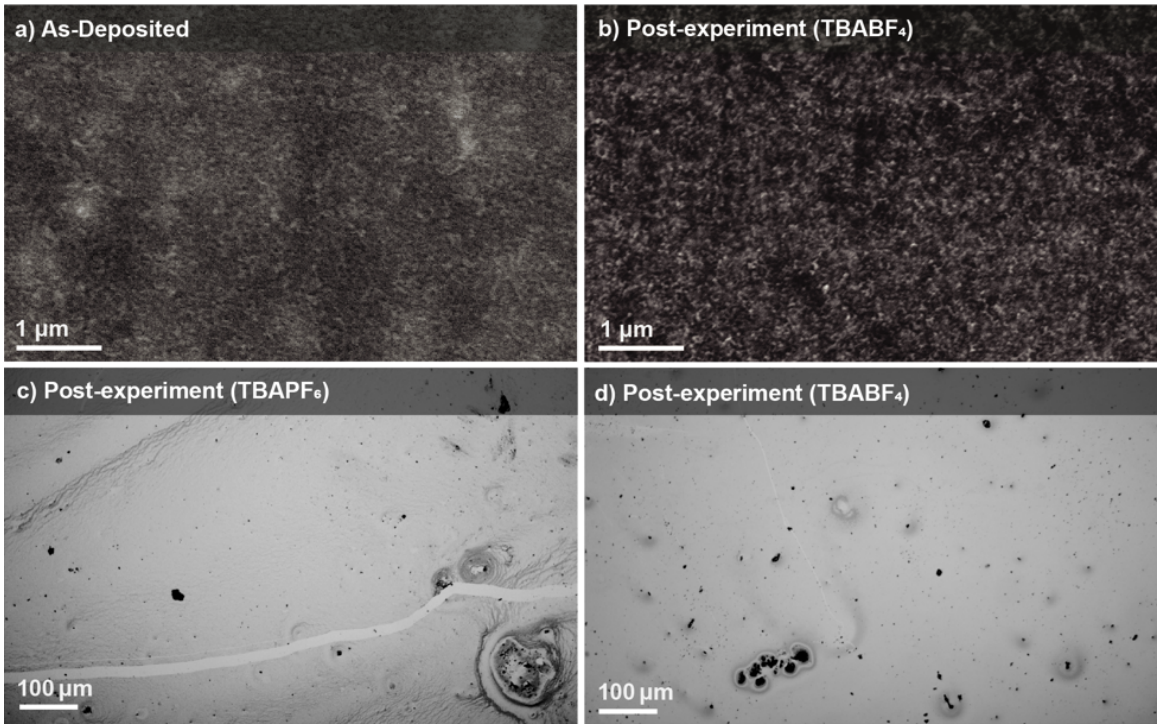

Figure C.21. Microscope images of films used in QCM experiments. a) SEM image of a film as-deposited. b) SEM image of a film used for CV scans in $TBABF_4$. This ex-situ analysis was not performed in the case of $TBAPF_6$ because the same electrode is cleaned and re-used. c) Optical microscope image of a film after running CVs in $TBAPF_6$. A few scratches and drying defects are visible. D) Optical microscope image of a film used to run CVs in $TBABF_4$. A small scratch and similar drying defects are visible.

Table C.7. Values of electrons and ions determined from QCM experiments at 100 mV/s. The mass of the MOF was calculated using the Sauerbrey relation from the change in frequency of the dry, bare QCM and the QCM after spin-coating and the crystal was allowed to dry fully. Moles of electrons was determined by integrating the CV curves. Moles of anions was calculated from change in frequency over a cycle, using first the Saurbrey relationship, then the molecular weight of the unsolvated anions.

	$TBAPF_6$	$TBABF_4$
Mass $Fe(TA)_2$ deposited / cm^2	5.50 µg	4.41 µg
Moles $Fe(TA)_2$ / cm^2	$2.86\ 10^{-8}$	$2.30\ 10^{-8}$
Average frequency change / cycle	22 Hz	46.8 Hz
Mass change / cm^2	$3.89\ 10^{-7}$ µg	$8.27\ 10^{-7}$ µg
Moles anions / cm^2	$2.68\ 10^{-9}$	$9.52\ 10^{-9}$
Anions per Fe	0.09	0.4
Moles e^- (oxidation)	$8.26\ 10^{-9}$	$2.25\ 10^{-8}$
Moles e^- (reduction)	$7.20\ 10^{-9}$	$1.86\ 10^{-8}$
Moles e^- (average)	$7.73\ 10^{-9}$	$2.05\ 10^{-8}$

Table C.8. Raw data for conductivity measurements on $Fe(TA)_2$ thin films made in air. The films were allowed to sit in ambient aerobic conditions for over 1 week. Measurements were performed with a co-linear four point probe method.

Particle Size	Additives	Film Thickness μm	Conductivity S/cm
Bulk material	None	4.1	1.08×10^{-5}
130 ± 20 nm	None	5.5	4.84×10^{-5}
84 ± 30 nm	None	6.6	1.53×10^{-4}
84 ± 30 nm	5% carbon, 5% PVDF	4.1	6.30×10^{-4}

Table C.9. Raw data for conductivity measurements on $Fe(TA)_2$ thin films made in N_2. The films were allowed to sit in ambient aerobic conditions for 1 day, and measurements were collected once per day whenever possible. Measurements were performed with a Van der Pauw four point probe method. Two measurements are collected in different orientations (R1 and R2). F is a correction factor.

Measurement	Thickness μm	R1 A/V	R2 A/V	F	Conductivity S/cm
80 nm N_2	2.1	36231884058	10615711253	0.8865	5.06×10^{-8}
80 nm Air Day 1	2.1	211416490.5	492610837.4	0.94215	3.17×10^{-6}
80 nm Air Day 2	2.1	137174211.2	267379679.1	0.96306	5.39×10^{-6}
80 nm Air Day 3	2.1	182149362.5	85251491.9	0.95276	8.25×10^{-6}
80 nm Air Day 4	2.1	35211267.61	60606060.61	0.97518	2.25×10^{-5}
80 nm Air Day 7	2.1	28818443.8	13003901.17	0.9484	5.30×10^{-5}
Bulk N_2	8.6	15220700152	86206896552	0.79954	6.33×10^{-9}
Bulk Air Day 1	8.6	37313432.84	854700854.7	0.5691	1.01×10^{-6}
Bulk Air Day 2	8.6	41841004.18	552486187.8	0.6528	1.32×10^{-6}
Bulk Air Day 3	8.6	43668122.27	617283950.6	0.6417	1.21×10^{-6}
25 nm N_2	2.6	3623188406	363636363.6	0.6999	6.11×10^{-7}
25 nm Air Day 3	2.6	32268473.7	1298701.299	0.5577	9.10×10^{-5}

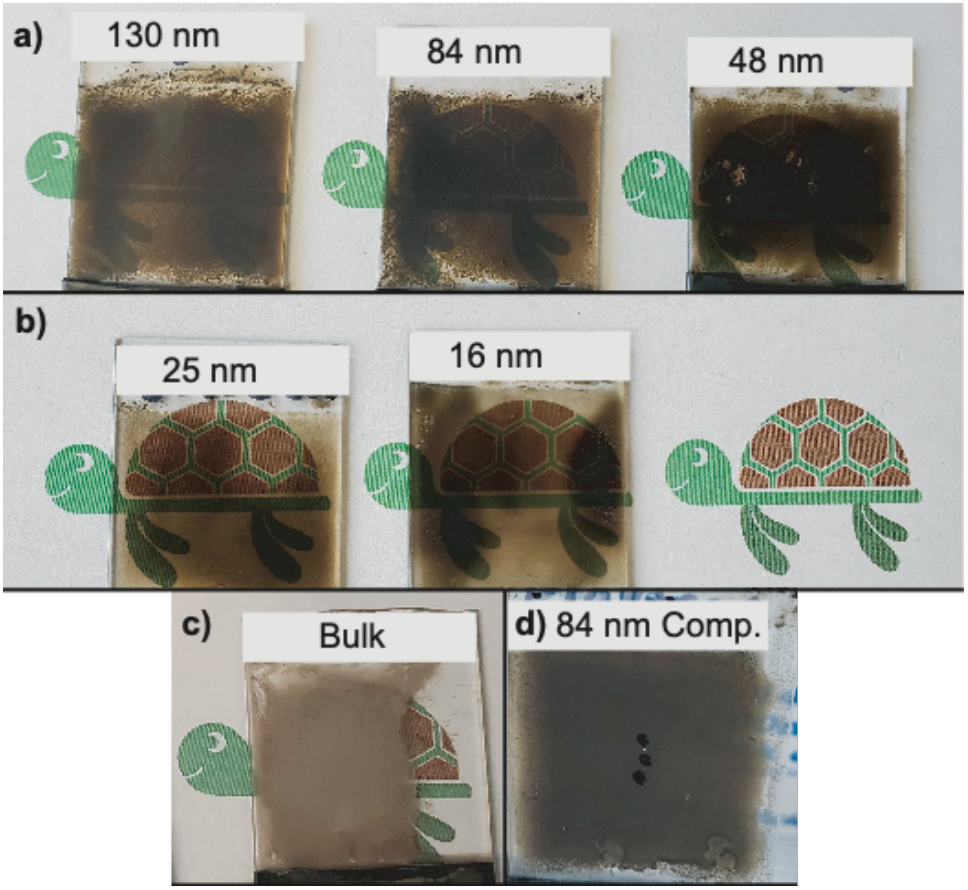

Figure C.22. Photos of $Fe(TA)_2$ thin films made in air. a) Films of the largest sizes of particles were created from 20 mg/mL dispersions. Such concentrated dispersions, when used for smaller particles, resulted in films that flaked easily off the glass b) For smaller particles, 10 mg/mL dispersions were used. c) The bulk film was fabricated from a 20 mg/ml dispersion. e) The composite film is comprised of 90% MOF, with 5% PVDF binder and 5% carbon black by weight. The black dots are sharpie marks, placed after a conductivity measurement, as a protective carbon cap for SEM-FIB cross-sectioning.

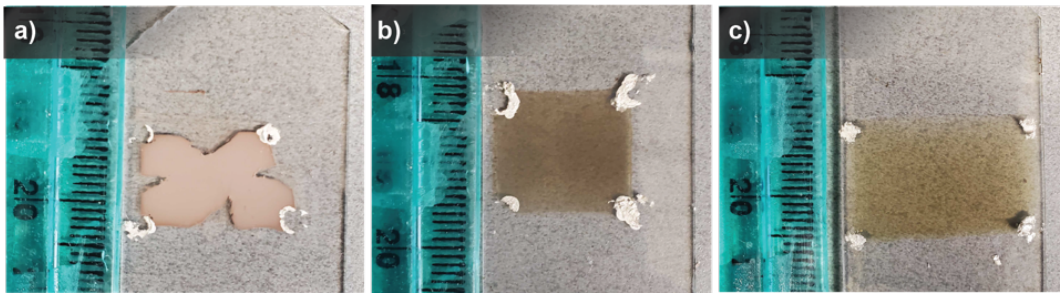

Figure C.23. Photos of $Fe(TA)_2$ thin films made in the glovebox, then brought out into air. a) Bulk film in a clover-like shape with silver contacts at the corners. b) 84-nm film in a square shape with silver contacts at the corners. c) 25-nm film in a rectangular shape with silver contacts at the corners.

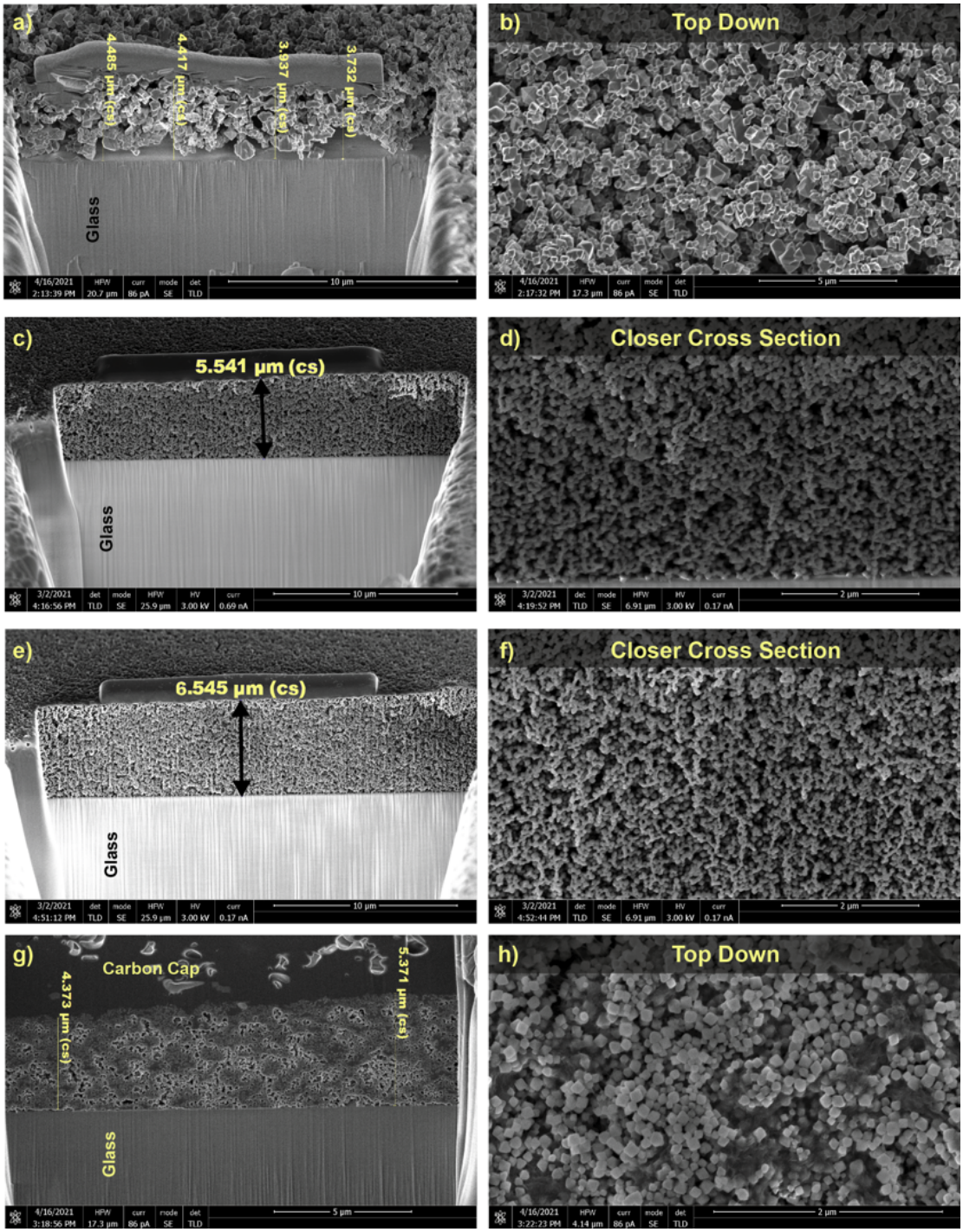

Figure C.24. SEM images of $Fe(TA)_2$ thin films of varying particle size made in air and used for in-air co-linear conductivity measurements. Cross section (CS, a) and surface (b) of the bulk material. Cross section (c) and close-up cross section (d) of 130-nm particles. Cross section (e) and close-up cross-section (f) of the 84-nm particle thin film. g) Cross section (g) and surface (h) of a composite film with 84-nm particles with 5% carbon black and 5% PVDF, with measurements.

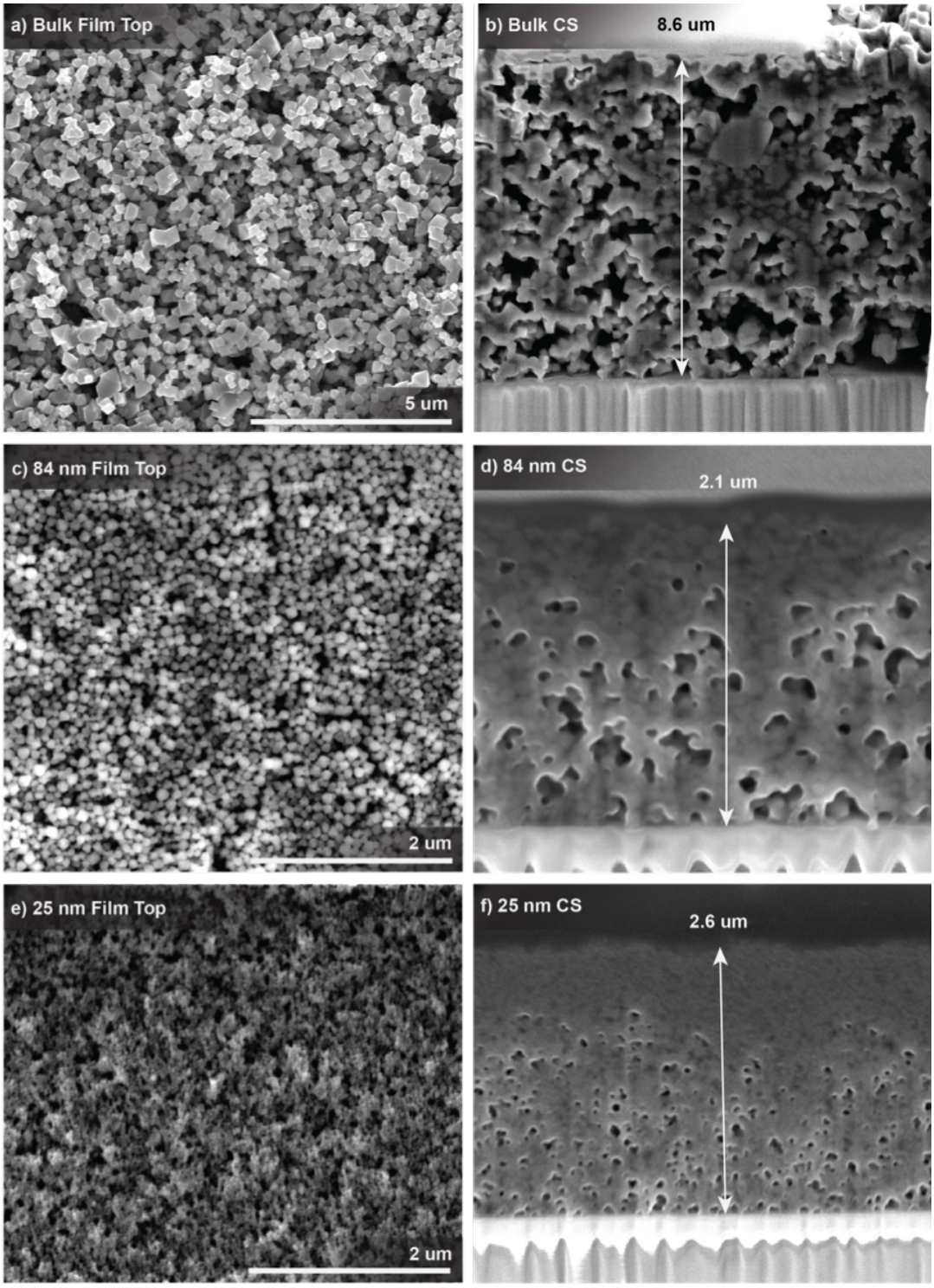

Figure C.25. SEM images of $Fe(TA)_2$ thin films of varying particle size made under N_2 and used for Van der Pauw conductivity measurements. a) Top of the bulk material. b) Cross-section (CS) of the bulk film. c) Top of the 84-nm particle film. d) Cross-section (CS) of the 84-nm particle film. e) Top of the 25-nm film. f) Cross-section (CS) of the 25-nm film.

APPENDIX D

SUPPLEMENTARY INFORMATION FOR CHAPTER 5

General Methods

Materials All commercial chemicals were used as received and handled in inert conditions unless stated otherwise. All solvents were collected from a solvent purification system and stored over 4A molecular sieves, and all liquid reagents were freeze-pump-thawed four cycles prior to use. N,N-dimethylformamide (DMF, ACS grade, Fisher Scientific), acetonitrile (MeCN, HPLC grade, Fisher Scientific), dichloromethane (DCM, ACS grade, Fisher Scientific), 1,2-difluorobenzene (98%, Sigma-Aldrich), tetrahydrofuran (THF, ACS grade, Fisher Scientific), iron (II) chloride (98%, anhydrous, Strem), 1-methylimidazole (99%, Sigma-Aldrich), 1,2,3-triazole (98%, TCI), tetrabutylammonium hexafluorophosphate (98%, TCI, recrystallized once from ethanol), tetrabutylammonium tetrafluoroborate (98%, ACROS, recrystallized once from ethanol), tetrabutylammonium perchlorate (99+%, Fisher Scientific), lithium tetrafluoroborate (98.0%, TCI), and tetramethylammonium tetrafluoroborate (98.0%, TCI).

Synthesis and Characterization of Iron Triazolate ($Fe(TA)_2$) Nanoparticles. Controlling the size of $Fe(TA)_2$ nanoparticles was achieved by adding different amounts of 1-methyl imidazole (1-mIm) to the synthesis. In detail, the solution of anhydrous iron(II) chloride in DMF (0.805 mmol, 0.0575 M, 14 mL) was first prepared, followed by adding 45.5 μL (0.709 equiv), 25 μL (0.436 equiv), and 14 μL (0.218 equiv) of 1-mIm for the synthesis of 16-nm, 25-nm, and 46-nm nanoparticles. It is noted that all equivalents are with respect to iron(II) chloride. Vials were further heated under 120 °C for 1.5 hours and then immediately centrifuged and washed twice with DMF.

PXRD Measurements and Analysis. PXRD data were collected in the air using BraggBrentano geometry with a step size of 0.02° in the range of 3.5-35° 2θ with a Bruker D2 Phaser. A variable detector opening was used to reduce air scattering at low angles. Patterns were matched to the low-spin $Fe(TA)_2$ cif file.

SEM Imaging for Size Analysis Imaging was performed using a Thermo Fisher Apreo 2 SEM instrument with 10.00 kV energy and 0.8 nA current. SEM samples were prepared by spin-coating the dispersion of $Fe(TA)_2$ nanoparticles in DMF onto silicon substrates. Particle sizing was performed in ImageJ.[(2)]

Atomic Force Microscopy (AFM) for $Fe(TA)_2$ Film Thickness Analysis A Bruker Dimension ICON with ScanAsyst was used for topographical AFM measurements. The SCANASYST-AIR probes were used to measure the $Fe(TA)_2$ film thickness on the quartz crystal electrode. Time-of-Flight Secondary Ion Mass Spectrometry (ToF-SIMS) Experiments. $Fe(TA)_2$ films on QCM electrodes were analyzed on a ToF-SIMS IV time-of-flight instrument manufactured by ION TOF GmbH, Münster, Germany. Mass spectra were collected using a beam of Bi^{3+} primary ions (bunched mode, 25 kV, 0.3 pA @ 10 kHz). The primary ion flux for each mass spectrum was less than 2.0 x 1012 ions/cm^2. An electron flood source was used for charge compensation. Spectra were acquired from three separate areas on a single sample. Data processing was done with SurfaceLab 6 software provided by the manufacturer.

Electrochemical Studies of $Fe(TA)_2$ Films All electrochemical data were collected using a Biologic SP200. For electrochemical quartz crystal microbalance (EQCM) experiments, the PT/Ti-coated 5 MHz AT-cut QCM working electrodes were cleaned using acidic piranha solution, then rinsed copiously with 18.2 MΩ nanopure water, followed by isopropyl alcohol, and lastly dried under N_2 pressure.

Different amounts of suspensions of $Fe(TA)_2$ nanoparticles in DMF were spin-coated onto the EQCM electrodes in the N_2 glovebox. The EQCM electrodes with $Fe(TA)_2$ films were further dried in the vacuum for 3 hours. A standard three-electrode electrochemical cell was set up with 0.1 M electrolytes (i.e., $TBABF_4$, $TBAPF_6$, $TBAClO_4$, $LiBF_4$, and $TMABF_4$) in acetonitrile (80 mL), the QCM as the working electrode, a platinum wire as the counter electrode, and a bare silver wire as a pseudo-reference electrode. Frequency data were collected simultaneously with CV scans using a SRS QCM200 apparatus. The frequency was converted to mass using the Sauerbrey equation below, in which f is the experimental change in frequency, Cf is the sensitivity factor (56.6 Hz cm^2 g^{-1} for 5 MHz AT-cut crystals), and m is the change in mass.

$$\Delta f = Cf\Delta m$$

Cyclic voltammogram (CV) of $Fe(TA)_2$ film was collected under N_2 condition at the rate of 10 mV/s. Titration experiments were conducted by adding certain amounts of either $TBAPF_6$ or $TBAClO_4$ into $TBABF_4$ / MeCN electrolyte without changing the solvent volume. Impedance data were recorded at potentials of either surface redox feature or ion-intercalation redox feature. An AC amplitude of 10mV was applied. The frequency was scanned from 4.5 kHz to 60 mHz with 6 points per decade. Most of the EIS data were fitted using Bio-Logic EC-Lab V11.33. For solvent-dependent electrochemical studies, CV was collected in different solvents with 0.1 M $TBABF_4$ as the supporting electrolyte in a standard three-electrode cell with a glassy carbon (GC) working electrode, a silver wire pseudo-reference electrode, and a platinum wire counter electrode. To prepare the working GC electrode, 16-nm $Fe(TA)_2$ nanoparticles were suspended in DMF at a concentration of 5mg/mL and then drop-casted (7 μL) onto the polished

GC surface. The electrode was further dried in the vacuum for 3 hours before electrochemical studies. In all CV experiments, potential is referenced to the $Fc^{0/+}$ couple which is determined by adding a small amount of ferrocene to the solution at the end of the experiment.

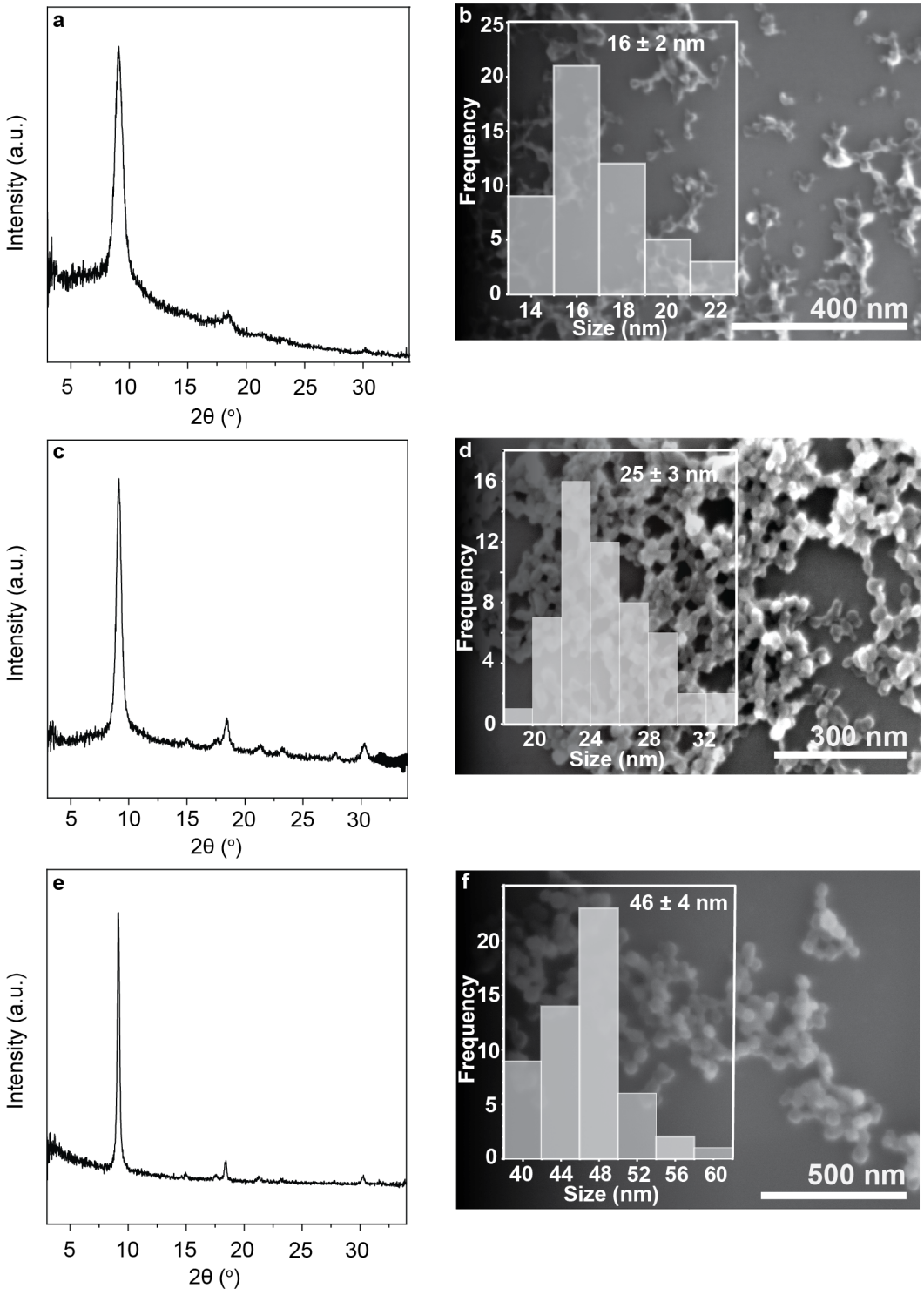

Figure D.1. Basic Characterization of $Fe(TA)_2$. PXRD pattern (a) and SEM image (b) of 16-nm particles. PXRD pattern (c) and SEM image (d) of 25-nm particles. PXRD pattern (e) and SEM image (f) of 16-nm particles.

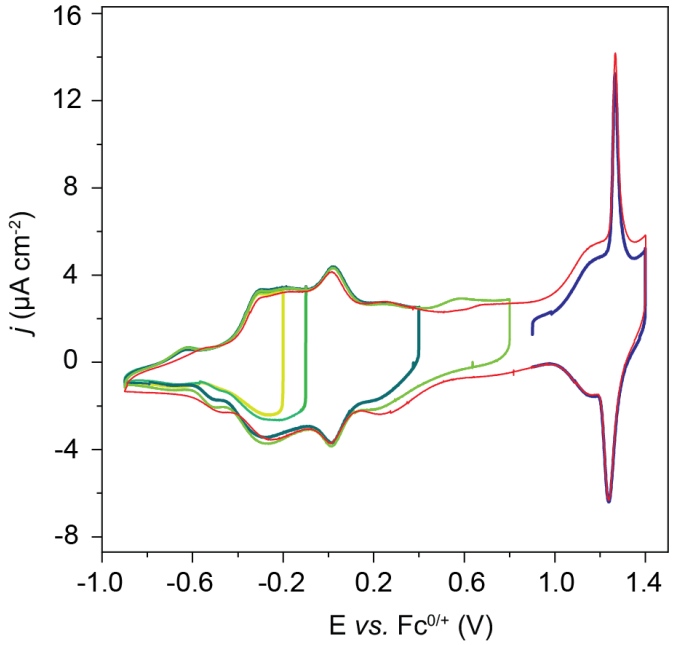

Figure D.2. CV traces starting and stopping at different voltages show that the 1.2 V feature is independent of other features in the CV.

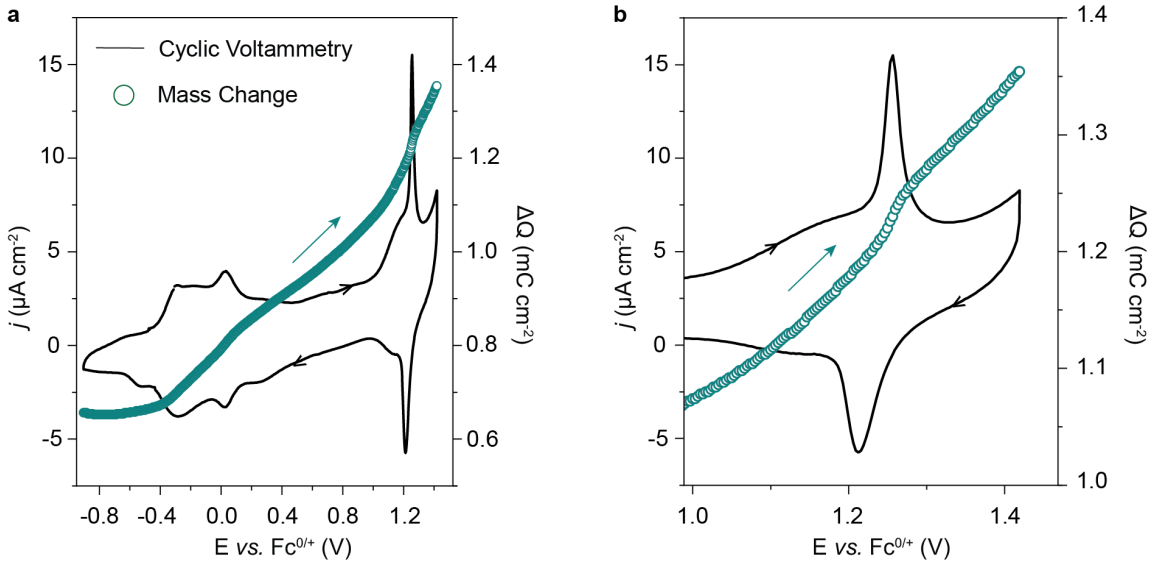

Figure D.3. Charge variation in $Fe(TA)_2$ films during CV measurements.(a) CV (black) and charge change (green) of $Fe(TA)_2$ film collected at a 10 mV/s scan rate. (b) CV (black) and charge change (green) of $Fe(TA)_2$ film focusing on the potential region of 1.2 V vs. $Fc^{0/+}$ redox feature. Scan direction is indicated by arrows and the charge change is only shown in the anodic CV direction. The loading amount of 16-nm $Fe(TA)_2$ nanoparticles on EQCM crystal is ca. 4.0 μg; this is the same sample depicted in Figure 5.2a

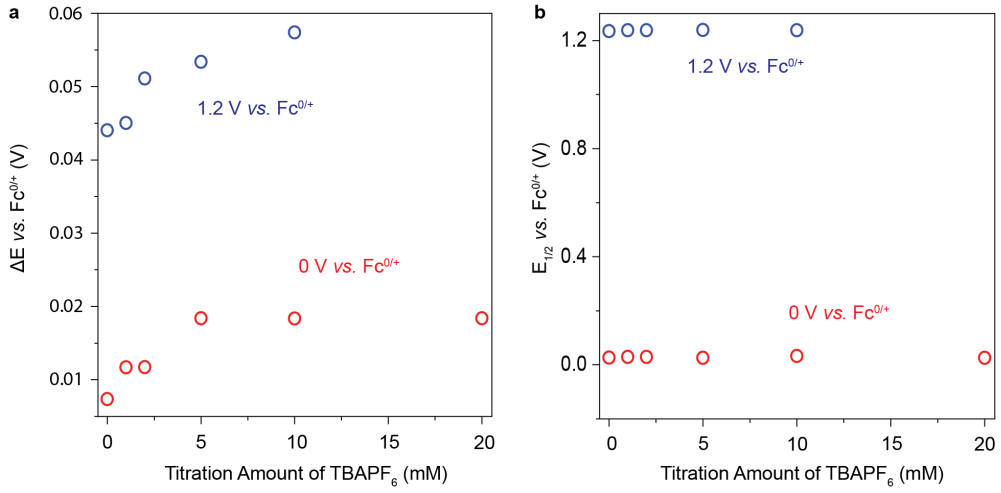

Figure D.4. Tracking the changes in ΔE and $E_{1/2}$ at the 0.0 V and 1.2 V feature during $TBABF_6$ electrolyte titration. (a) ΔE variation of redox features at 0 V and 1.2 V vs. $Fc^{0/+}$ of $Fe(TA)_2$ film when titrating different amount of $TBAPF_6$ into 0.1 M $TBABF_4$ electrolyte. (b) $E_{1/2}$ of redox features at 0 V and 1.2 V vs. $Fc^{0/+}$ for $Fe(TA)_2$ film when titrating different amount of $TBAPF_6$ into 0.1 M $TBABF_4$ electrolyte.

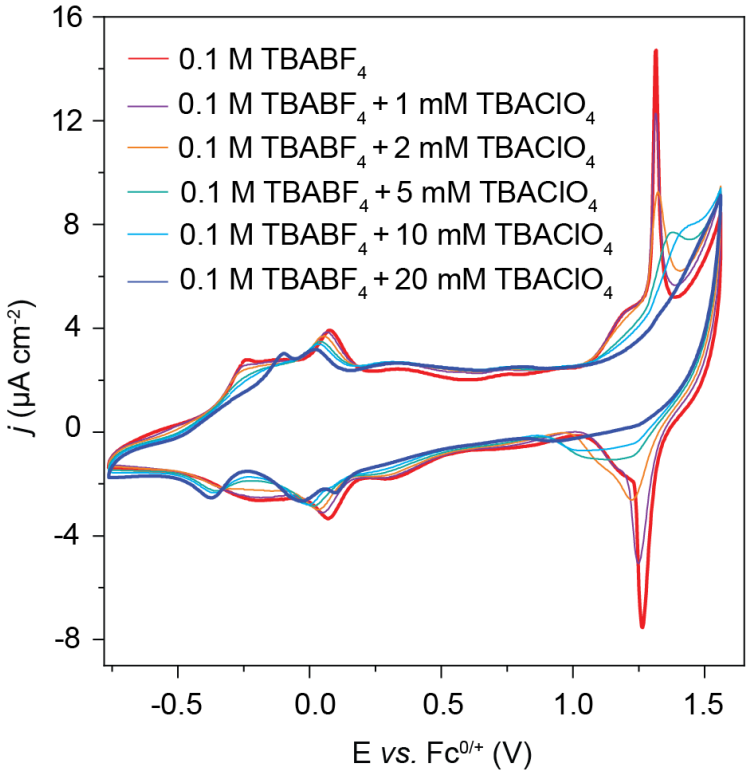

Figure D.5. CVs collected during a titration experiment where $TBACLO_4$ was added to the $TBABF_4$ electrolyte. CV results are collected at the scan rate of 10 mV/s

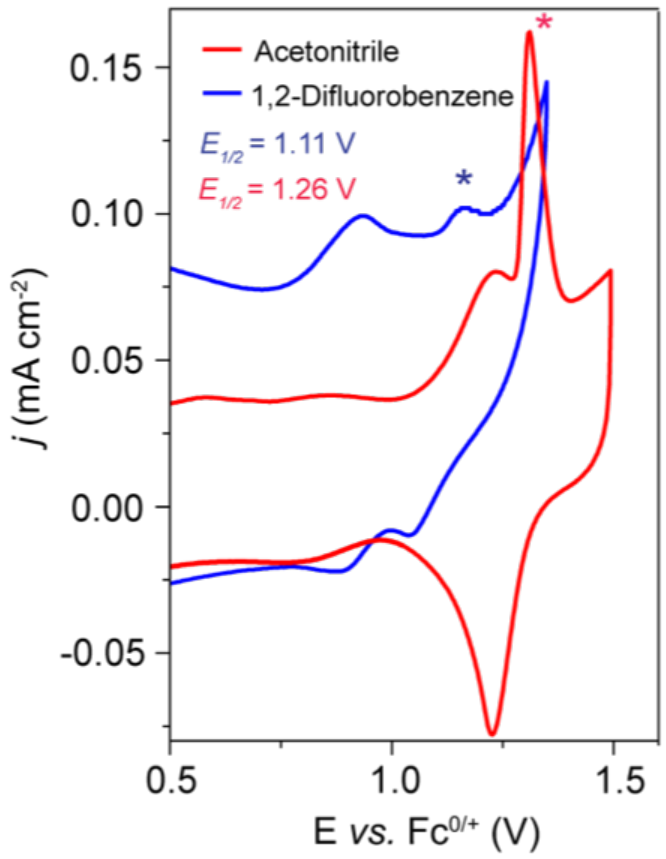

Figure D.6. CV measurements of $Fe(TA)_2$ films in acetonitrile (red) and 1,2-difluorobenzene (blue). The $E_{1/2}$ of BF_4^- intercalation redox feature is shifted from ca. 1.26 V in acetonitrile to 1.11 V in 1,2-difluorobenzene.

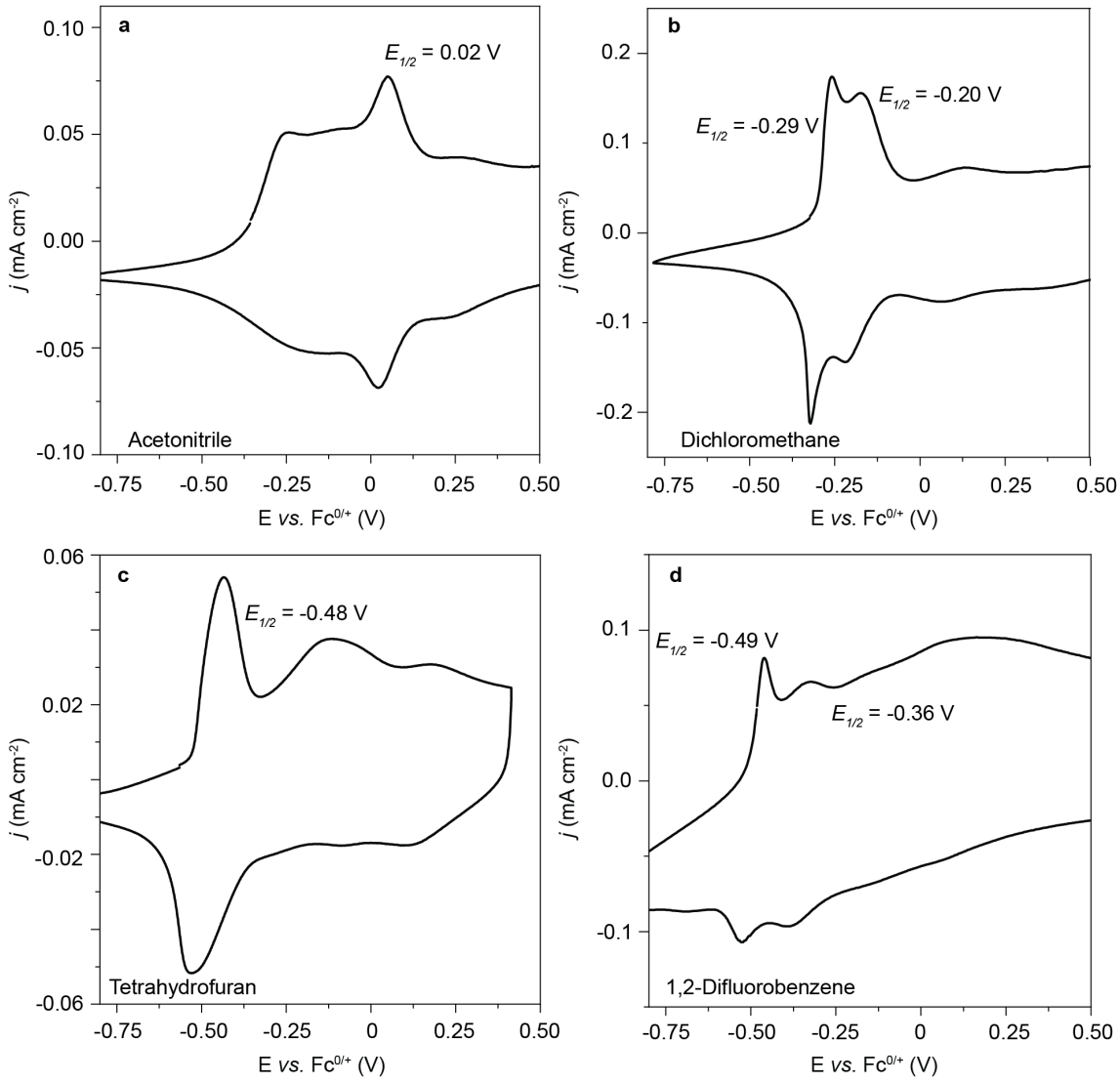

Figure D.7. CVs of $Fe(TA)_2$ particles in four different solvents. (a) CV of $Fe(TA)_2$ film in acetonitrile. (b) CV of $Fe(TA)_2$ film in dichloromethane. (c) CV of $Fe(TA)_2$ film in tetrahydrofuran. (d) CV of $Fe(TA)_2$ film in 1,2-difluorobenzene.

REFERENCES

1. Liu, B.; Vellingiri, K.; Jo, S.-H.; Kumar, P.; Ok, Y. S.; Kim, K.-H. Recent advances in controlled modification of the size and morphology of metal-organic frameworks. *Nano Res.* **2018**, *11*, 4441–4467.

2. Schindelin, J. et al. Fiji: An open-source platform for biological-image analysis. *Nature Methods* **2012**, *9*, 676–682.

3. Moosavi, S. M.; Nandy, A.; Jablonka, K. M.; Ongari, D.; Janet, J. P.; Boyd, P. G.; Lee, Y.; Smit, B.; Kulik, H. J. Understanding the diversity of the metal-organic framework ecosystem. *Nature Communications* **2020**, *11*, 4068.

4. Forgan, R. S. Modulated self-assembly of metal–organic frameworks. *Chem. Sci.* **2020**, *11*, 4546–4562.

5. Chang, M.; Wei, Y.; Liu, D.; Wang, J.-X.; Chen, J.-F. A General Strategy for Instantaneous and Continuous Synthesis of Ultrasmall Metal–Organic Framework Nanoparticles. *Angewandte Chemie International Edition* **2021**, *60*, 26390–26396.

6. Marshall, C. R.; Staudhammer, S. A.; Brozek, C. K. Size control over metal–organic framework porous nanocrystals. *Chem. Sci.* **2019**, *10*, 9396–9408.

7. Troyano, J.; Carné-Sánchez, A.; Avci, C.; Imaz, I.; Maspoch, D. Colloidal metal–organic framework particles: the pioneering case of ZIF-8. *Chem. Soc. Rev.* **2019**, *48*, 5534–5546.

8. Cravillon, J.; Münzer, S.; Lohmeier, S.-J.; Feldhoff, A.; Huber, K.; Wiebcke, M. Rapid Room-Temperature Synthesis and Characterization of Nanocrystals of a Prototypical Zeolitic Imidazolate Framework. *Chem. Mater.* **2009**, *21*, 1410–1412.

9. Cravillon, J.; Schröder, C. A.; Nayuk, R.; Gummel, J.; Huber, K.; Wiebcke, M. Fast Nucleation and Growth of ZIF-8 Nanocrystals Monitored by Time-Resolved In Situ Small-Angle and Wide-Angle X-Ray Scattering. *Angew. Chem. Int. Ed.* **2011**, *50*, 8067–8071.

10. Lim, I. H.; Schrader, W.; Schüth, F. Insights into the Molecular Assembly of Zeolitic Imidazolate Frameworks by ESI-MS. *Chem. Mater.* **2015**, *27*, 3088–3095.

11. Guo, H.; Zhu, Y.; Wang, S.; Su, S.; Zhou, L.; Zhang, H. Combining Coordination Modulation with Acid–Base Adjustment for the Control over Size of Metal–Organic Frameworks. *Chem. Mater.* **2012**, *24*, 444–450.

12. Umemura, A.; Diring, S.; Furukawa, S.; Uehara, H.; Tsuruoka, T.; Kitagawa, S. Morphology Design of Porous Coordination Polymer Crystals by Coordination Modulation. *J. Am. Chem. Soc.* **2011**, *133*, 15506–15513.

13. Day, R. W.; Bediako, D. K.; Rezaee, M.; Parent, L. R.; Skorupskii, G.; Arguilla, M. Q.; Hendon, C. H.; Stassen, I.; Gianneschi, N. C.; Kim, P.; Dincă, M. Single Crystals of Electrically Conductive Two-Dimensional Metal–Organic Frameworks: Structural and Electrical Transport Properties. *ACS Cent. Sci.* **2019**, *5*, 1959–1964.

14. Foster, M. E.; Sohlberg, K. Unraveling the semiconducting/metallic discrepancy in Ni3(HITP)2. *J. Phys. Chem. Lett.* **2018**, 11.

15. Hoppe, B.; Hindricks, K. D. J.; Warwas, D. P.; Schulze, H. A.; Mohmeyer, A.; Pinkvos, T. J.; Zailskas, S.; Krey, M. R.; Belke, C.; König, S.; Fröba, M.; Haug, R. J.; Behrens, P. Graphene-like metal–organic frameworks: morphology control, optimization of thin film electrical conductivity and fast sensing applications. *CrystEngComm* **2018**, *20*, 6458–6471.

16. Gittins, J. W.; Balhatchet, C. J.; Fairclough, S. M.; Forse, A. C. Enhancing the energy storage performances of metal–organic frameworks by controlling microstructure. **2022**, *13*, 9210–9219.

17. Mähringer, A.; Jakowetz, A. C.; Rotter, J. M.; Bohn, B. J.; Stolarczyk, J. K.; Feldmann, J.; Bein, T.; Medina, D. D. Oriented Thin Films of Electroactive Triphenylene Catecholate-Based Two-Dimensional Metal–Organic Frameworks. *ACS Nano* **2019**, *13*, 6711–6719.

18. Lahiri, N.; Lotfizadeh, N.; Tsuchikawa, R.; Deshpande, V. V.; Louie, J. Hexaaminobenzene as a building block for a Family of 2D Coordination Polymers. *J. Am. Chem. Soc.* **2017**, *139*, 19–22.

19. Gándara, F.; Uribe-Romo, F. J.; Britt, D. K.; Furukawa, H.; Lei, L.; Cheng, R.; Duan, X.; O'Keeffe, M.; Yaghi, O. M. Porous, Conductive Metal-Triazolates and Their Structural Elucidation by the Charge-Flipping Method. *Chem. Eur. J.* **2012**, *18*, 10595–10601.

20. Park, J. G.; Aubrey, M. L.; Oktawiec, J.; Chakarawet, K.; Darago, L. E.; Grandjean, F.; Long, G. J.; Long, J. R. Charge Delocalization and Bulk

Electronic Conductivity in the Mixed-Valence Metal–Organic Framework Fe(1,2,3-triazolate)$_2$(BF_4)$_x$. *J. Am. Chem. Soc.* **2018**, *140*, 8526–8534.

21. Grzywa, M.; Röß-Ohlenroth, R.; Muschielok, C.; Oberhofer, H.; Błachowski, A.; Żukrowski, J.; Vieweg, D.; von Nidda, H.-A. K.; Volkmer, D. Cooperative Large-Hysteresis Spin-Crossover Transition in the Iron(II) Triazolate [Fe(ta)$_2$] Metal–Organic Framework. *Inorg. Chem.* **2020**, *59*, 10501–10511.

22. Liu, L.; Corma, A. Metal Catalysts for Heterogeneous Catalysis: From Single Atoms to Nanoclusters and Nanoparticles. *Chem. Rev.* **2018**, *118*, 4981–5079.

23. Llordés, A.; Garcia, G.; Gazquez, J.; Milliron, D. J. Tunable near-infrared and visible-light transmittance in nanocrystal-in-glass composites. *Nature* **2013**, *500*, 323–326.

24. Schimpf, A. M.; Thakkar, N.; Gunthardt, C. E.; Masiello, D. J.; Gamelin, D. R. Charge-Tunable Quantum Plasmons in Colloidal Semiconductor Nanocrystals. *ACS Nano* **2014**, *8*, 1065–1072.

25. Kroupa, D. M.; Roh, J. Y.; Milstein, T. J.; Creutz, S. E.; Gamelin, D. R. Quantum-Cutting Ytterbium-Doped CsPb($Cl_{1-x}Br_x$)$_3$ Perovskite Thin Films with Photoluminescence Quantum Yields over 190%. *ACS Energy Lett.* **2018**, *3*, 2390–2395.

26. Sanehira, E. M.; Marshall, A. R.; Christians, J. A.; Harvey, S. P.; Ciesielski, P. N.; Wheeler, L. M.; Schulz, P.; Lin, L. Y.; Beard, M. C.; Luther, J. M. Enhanced mobility $CsPbI_3$ quantum dot arrays for record-efficiency, high-voltage photovoltaic cells. *Science Advances* **2017**, *3*.

27. Chakraborty, I.; Pradeep, T. Atomically Precise Clusters of Noble Metals: Emerging Link between Atoms and Nanoparticles. *Chem. Rev.* **2017**, *117*, 8208–8271.

28. Owen, J.; Brus, L. Chemical Synthesis and Luminescence Applications of Colloidal Semiconductor Quantum Dots. *J. Am. Chem. Soc.* **2017**, *139*, 10939–10943.

29. Hühn, J. et al. Selected Standard Protocols for the Synthesis, Phase Transfer, and Characterization of Inorganic Colloidal Nanoparticles. *Chem. Mater.* **2017**, *29*, 399–461.

30. Yin, Y.; Alivisatos, A. P. Colloidal nanocrystal synthesis and the organic–inorganic interface. *Nature* **2005**, *437*, 664–670.

31. Wuttke, S.; Braig, S.; Preiß, T.; Zimpel, A.; Sicklinger, J.; Bellomo, C.; Rädler, J. O.; Vollmar, A. M.; Bein, T. MOF nanoparticles coated by lipid bilayers and their uptake by cancer cells. *Chem. Commun.* **2015**, *51*, 15752–15755.

32. Wang, S.; Chen, Y.; Wang, S.; Li, P.; Mirkin, C. A.; Farha, O. K. DNA-Functionalized Metal–Organic Framework Nanoparticles for Intracellular Delivery of Proteins. *J. Am. Chem. Soc.* **2019**, *141*, 2215–2219.

33. Graf, M.; Moreno, N.; Kerl, K.; Bunzen, H. Metal–organic framework nanoparticles for arsenic trioxide drug delivery. *J. Mater. Chem.* **2018**, *6*, 6481–6489.

34. Rogge, S. M. J.; Bavykina, A.; Hajek, J.; Garcia, H.; Olivos-Suarez, A. I.; Sepúlveda-Escribano, A.; Vimont, A.; Clet, G.; Bazin, P.; Kapteijn, F.;

Daturi, M.; Ramos-Fernandez, E. V.; Llabrés i Xamena, F. X.; Van Speybroeck, V.; Gascon, J. Metal–organic and covalent organic frameworks as single-site catalysts. *Chem. Soc. Rev.* **2017**, *46*, 3134–3184.

35. Adil, K.; Belmabkhout, Y.; Pillai, R. S.; Cadiau, A.; Bhatt, P. M.; Assen, A. H.; Maurin, G.; Eddaoudi, M. Gas/vapour separation using ultra-microporous metal–organic frameworks: insights into the structure/separation relationship. *Chem. Soc. Rev.* **2017**, *46*, 3402–3430.

36. He, Y.; Zhou, W.; Qian, G.; Chen, B. Methane storage in metal–organic frameworks. *Chem. Soc. Rev.* **2014**, *43*, 5657–5678.

37. Yu, G.; Liu, Y.; Zou, X.; Zhao, N.; Rong, H.; Zhu, G. A nanosized metal–organic framework with small pores for kinetic xenon separation. *J. Mater. Chem. A* **2018**, *6*, 11797–11803.

38. Sakata, Y.; Furukawa, S.; Kondo, M.; Hirai, K.; Horike, N.; Takashima, Y.; Uehara, H.; Louvain, N.; Meilikhov, M.; Tsuruoka, T.; Isoda, S.; Kosaka, W.; Sakata, O.; Kitagawa, S. Shape-Memory Nanopores Induced in Coordination Frameworks by Crystal Downsizing. *Science* **2013**, *339*, 193–196.

39. Furukawa, H.; Cordova, K. E.; O'Keeffe, M.; Yaghi, O. M. The Chemistry and Applications of Metal-Organic Frameworks. *Science* **2013**, *341*, 1230444.

40. Freund, R.; Lächelt, U.; Gruber, T.; Rühle, B.; Wuttke, S. Multifunctional Efficiency: Extending the Concept of Atom Economy to Functional Nanomaterials. *ACS Nano* **2018-03-27**, *12*, 2094–2105.

41. Wang, J.; Wan, J.; Ma, Y.; Wang, Y.; Pu, M.; Guan, Z. Metal–organic frameworks MIL-88A with suitable synthesis conditions and optimal dosage

for effective catalytic degradation of Orange G through persulfate activation. *RSC Adv.* **2016**, *6*, 112502–112511.

42. Barros, B. S.; deLimaNeto, O. J.; deOliveiraFrós, A. C.; Kulesza, J. Metal-Organic Framework Nanocrystals. *ChemistrySelect* **2018**, *3*, 7459–7471.

43. Sindoro, M.; Yanai, N.; Jee, A.-Y.; Granick, S. Colloidal-Sized Metal–Organic Frameworks: Synthesis and Applications. *Acc. Chem. Res.* **2014**, *47*, 459–469.

44. Majewski, M. B.; Noh, H.; Islamoglu, T.; Farha, O. K. NanoMOFs: little crystallites for substantial applications. *J. Mater. Chem. A* **2018**, *6*, 7338–7350.

45. Hermes, S.; Witte, T.; Hikov, T.; Zacher, D.; Bahnmüller, S.; Langstein, G.; Huber, K.; Fischer, R. A. Trapping metal-organic framework nanocrystals: An in-situ time-resolved light scattering study on the crystal growth of MOF-5 in solution. *J. Am. Chem. Soc.* **2007**, *129*, 5324–5325.

46. Hirschle, P.; Preiß, T.; Auras, F.; Pick, A.; Völkner, J.; Valdepérez, D.; Witte, G.; Parak, W. J.; Rädler, J. O.; Wuttke, S. Exploration of MOF nanoparticle sizes using various physical characterization methods – is what you measure what you get? *CrystEngComm* **2016**, *18*, 4359–4368.

47. Patterson, J. P.; Abellan, P.; Denny, M. S.; Park, C.; Browning, N. D.; Cohen, S. M.; Evans, J. E.; Gianneschi, N. C. Observing the Growth of Metal–Organic Frameworks by *in Situ* Liquid Cell Transmission Electron Microscopy. *J. Am. Chem. Soc.* **2015**, *137*, 7322–7328.

48. Zhu, Y.; Ciston, J.; Zheng, B.; Miao, X.; Czarnik, C.; Pan, Y.; Sougrat, R.; Lai, Z.; Hsiung, C.-E.; Yao, K.; Pinnau, I.; Pan, M.; Han, Y. Unravelling

surface and interfacial structures of a metal–organic framework by transmission electron microscopy. *Nature Mater* **2017**, *16*, 532–536.

49. Khan, N. A.; Hasan, Z.; Jhung, S. H. Beyond pristine metal-organic frameworks: Preparation and application of nanostructured, nanosized, and analogous MOFs. *Coordination Chemistry Reviews* **2018**, *376*, 20–45.

50. Wang, S.; McGuirk, C. M.; D'Aquino, A.; Mason, J. A.; Mirkin, C. A. Metal-Organic Framework Nanoparticles. *Adv. Mater.* **2018**, *30*, 1800202.

51. Diring, S.; Furukawa, S.; Takashima, Y.; Tsuruoka, T.; Kitagawa, S. Controlled Multiscale Synthesis of Porous Coordination Polymer in Nano/Micro Regimes. *Chem. Mater.* **2010**, *22*, 4531–4538.

52. Wang, F.; Guo, H.; Chai, Y.; Li, Y.; Liu, C. The controlled regulation of morphology and size of HKUST-1 by "coordination modulation method". *Microporous and Mesoporous Materials* **2013**, *173*, 181–188.

53. Xin, C.; Zhan, H.; Huang, X.; Li, H.; Zhao, N.; Xiao, F.; Wei, W.; Sun, Y. Effect of various alkaline agents on the size and morphology of nano-sized HKUST-1 for CO_2 adsorption. *RSC Adv.* **2015**, *5*, 27901–27911.

54. Sun, W.; Zhai, X.; Zhao, L. Synthesis of ZIF-8 and ZIF-67 nanocrystals with well-controllable size distribution through reverse microemulsions. *Chemical Engineering Journal* **2016**, *289*, 59–64.

55. Ye, R.; Ni, M.; Xu, Y.; Chen, H.; Li, S. Synthesis of Zn-based metal–organic frameworks in ionic liquid microemulsions at room temperature. *RSC Adv.* **2018**, *8*, 26237–26242.

56. Qi, Y.; He, C.-T.; Lin, J.; Lin, S.; Liu, J.; Huang, J.; Xue, W.; Yu, G.; Chao, H.-Y.; Tong, Y.; Qiao, Z. Mild metal-organic-gel route for synthesis of stable sub-5-nm metal-organic framework nanocrystals. *Nano Res.* **2017**, *10*, 3621–3628.

57. Wang, J.; Fan, Y.; Tan, Y.; Zhao, X.; Zhang, Y.; Cheng, C.; Yang, M. Porphyrinic Metal–Organic Framework PCN-224 Nanoparticles for Near-Infrared-Induced Attenuation of Aggregation and Neurotoxicity of Alzheimer's Amyloid-β Peptide. *ACS Appl. Mater Interfaces* **2018**, *10*, 36615–36621.

58. LaMer, V. K.; Dinegar, R. H. Theory, Production and Mechanism of Formation of Monodispersed Hydrosols. *J. Am. Chem. Soc.* **1950**, *72*, 4847–4854.

59. Cravillon, J.; Nayuk, R.; Springer, S.; Feldhoff, A.; Huber, K.; Wiebcke, M. Controlling Zeolitic Imidazolate Framework Nano- and Microcrystal Formation: Insight into Crystal Growth by Time-Resolved In Situ Static Light Scattering. *Chem. Mater.* **2011**, *23*, 2130–2141.

60. Schäfer, P.; Kapteijn, F.; van der Veen, M. A.; Domke, K. F. Understanding the Inhibiting Effect of BTC on CuBTC Growth through Experiment and Modeling. *Crystal Growth & Design* **2017**, *17*, 5603–5607.

61. Van Vleet, M. J.; Weng, T.; Li, X.; Schmidt, J. In Situ, Time-Resolved, and Mechanistic Studies of Metal–Organic Framework Nucleation and Growth. *Chem. Rev.* **2018**, *118*, 3681–3721.

62. Liu, Y.-Y.; Decadt, R.; Bogaerts, T.; Hemelsoet, K.; Kaczmarek, A. M.; Poelman, D.; Waroquier, M.; Van Speybroeck, V.; Van Deun, R.; Van

Der Voort, P. Bipyridine-Based Nanosized Metal–Organic Framework with Tunable Luminescence by a Postmodification with Eu(III): An Experimental and Theoretical Study. *J. Phys. Chem. C* **2013**, *117*, 11302–11310.

63. Qi, Z.-P.; Yang, J.-M.; Kang, Y.-S.; Guo, F.; Sun, W.-Y. Facile water-stability evaluation of metal–organic frameworks and the property of selective removal of dyes from aqueous solution. *Dalton Trans.* **2016**, *45*, 8753–8759.

64. Guo, H.; Zhu, Y.; Wang, S.; Su, S.; Zhou, L.; Zhang, H. Combining coordination modulation with acid-base adjustment for the control over size of metal-organic frameworks. *Chem. Mater.* **2012**, *24*, 444–450.

65. Pang, M.; Cairns, A. J.; Liu, Y.; Belmabkhout, Y.; Zeng, H. C.; Eddaoudi, M. Synthesis and Integration of Fe-soc-MOF Cubes into Colloidosomes via a Single-Step Emulsion-Based Approach. *J. Am. Chem. Soc.* **2013**, *135*, 10234–10237.

66. Guo, C.; Zhang, Y.; Zhang, L.; Guo, Y.; Akram, N.; Wang, J. 2-Methylimidazole-Assisted Synthesis of Nanosized $Cu_3(BTC)_2$ for Controlling the Selectivity of the Catalytic Oxidation of Styrene. **2018**, *1*, 5289–5296.

67. Ranft, A.; Betzler, S. B.; Haase, F.; Lotsch, B. V. Additive-mediated size control of MOF nanoparticles. *CrystEngComm* **2013**, *15*, 9296–9300.

68. Li, D.; Wang, H.; Zhang, X.; Sun, H.; Dai, X.; Yang, Y.; Ran, L.; Li, X.; Ma, X.; Gao, D. Morphology Design of IRMOF - 3 Crystal by Coordination Modulation. *Cryst. Growth Des.* **2014**, *14*, 5856–5864.

69. Bunzen, H.; Grzywa, M.; Hambach, M.; Spirkl, S.; Volkmer, D. From Micro to Nano: A Toolbox for Tuning Crystal Size and Morphology of Benzotriazolate-Based Metal–Organic Frameworks. *Cryst. Growth Des.* **2016**, *16*, 3190–3197.

70. Amaro-gahete, J.; Klee, R.; Esquivel, D.; Ruiz, J. R.; Jiménez-sanchidrián, C.; Romero-salguero, F. J. Ultrasonics - Sonochemistry Fast ultrasound-assisted synthesis of highly crystalline MIL-88A particles and their application as ethylene adsorbents. *Ultrasonics - Sonochemistry* **2019**, *50*, 59–66.

71. Chalati, T.; Horcajada, P.; Couvreur, P.; Serre, C.; Ben Yahia, M.; Maurin, G.; Gref, R. Porous metal organic framework nanoparticles to address the challenges related to busulfan encapsulation. *Nanomedicine* **2011**, *6*, 1683–1695.

72. Cai, X.; Lin, J.; Pang, M. Facile Synthesis of Highly Uniform Fe-MIL-88B Particles. *Cryst. Growth Des.* **2016**, *16*, 3565–3568.

73. Pham, M.; Vuong, G.; Vu, A.; Do, T. Novel Route to Size-Controlled Fe–MIL-88B–NH_2 Metal–Organic Framework Nanocrystals. *Langmuir* **2011**, *27*, 15261–15267.

74. Liu, D.; Liu, Y.; Dai, F.; Zhao, J.; Yang, K.; Liu, C. Size- and morphology-controllable synthesis of MIL-96 (Al) by hydrolysis and coordination modulation of dual aluminium source and ligand systems. *Dalton Trans.* **2015**, *96*, 16421–16429.

75. Márquez, A. G.; Demessence, A.; Platero-prats, A. E.; Heurtaux, D.; Horcajada, P.; Serre, C.; Chang, J.; Férey, G.; De, A.; Boissière, C.; Grosso, D.; Sanchez, C. Green Microwave Synthesis of MIL-100 (Al, Cr, Fe)

Nanoparticles for Thin- Film Elaboration. *Eur. J. Inorg. Chem.* **2012**, *100*, 5165–5174.

76. Anand, R.; Borghi, F.; Manoli, F.; Manet, I.; Agostoni, V.; Reschiglian, P.; Gref, R.; Monti, S. Host–Guest Interactions in Fe(III)-Trimesate MOF Nanoparticles Loaded with Doxorubicin. *J. Phys. Chem. B* **2014**, *118*, 8532–8539.

77. Jiang, D.; Burrows, A. D.; Edler, K. J. Size-controlled synthesis of MIL-101(Cr) nanoparticles with enhanced selectivity for CO_2 over N_2. *CrystEngComm* **2011**, *13*, 6916.

78. Zhao, T.; Yang, L.; Feng, P.; Gruber, I.; Janiak, C.; Liu, Y. Facile synthesis of nano-sized MIL-101(Cr) with the addition of acetic acid. *Inorganica Chim. Acta* **2018**, *471*, 440–445.

79. Zhao, T.; Li, S.; Shen, L.; Wang, Y.; Yang, X. The sized controlled synthesis of MIL-101 (Cr) with enhanced CO2 adsorption property. *Inorg. Chem. Commun.* **2018**, *96*, 47–51.

80. Yang, L.; Zhao, T.; Boldog, I.; Janiak, C.; Yang, X.-Y.; Li, Q.; Zhou, Y.-J.; Xia, Y.; Lai, D.-W.; Liu, Y.-J. Benzoic acid as a selector–modulator in the synthesis of MIL-88B(Cr) and nano-MIL-101(Cr). *Dalton Trans.* **2019**, *48*, 989–996.

81. Guo, C.; Zhang, Y.; Guo, Y.; Zhang, Y.; Jide, W. A general and efficient approach for tuning the crystal morphology of classical MOFs. *Chem. Commun.* **2018**, *54*, 252–255.

82. Chi, W. S.; Roh, D. K.; Lee, C. S.; Kim, J. H. A shape- and morphology-controlled metal organic framework template for high-efficiency solid-state dye-sensitized solar cells. *J. Mater. Chem. A* **2015**, *3*, 21599–21608.

83. Vilela, S.; Salcedo-Abraira, P.; Colinet, I.; Salles, F.; de Koning, M.; Joosen, M.; Serre, C.; Horcajada, P. Nanometric MIL-125-NH_2 Metal–Organic Framework as a Potential Nerve Agent Antidote Carrier. *Nanomaterials* **2017**, *7*, 321.

84. Nayuk, R.; Zacher, D.; Schweins, R.; Wiktor, C.; Fischer, R. A.; Van Tendeloo, G.; Huber, K. Modulated formation of MOF-5 nanoparticles-A SANS analysis. *Journal of Physical Chemistry C* **2012**, *116*, 6127–6135.

85. Huang, L.; Wang, H.; Chen, J.; Wang, Z.; Sun, J.; Zhao, D.; Yan, Y. Synthesis, morphology control, and properties of porous metal–organic coordination polymers. *Microporous Mesoporous Mater.* **2003**, *58*, 105–114.

86. Wang, S.; Lv, Y.; Yao, Y.; Yu, H.; Lu, G. Modulated synthesis of monodisperse MOF-5 crystals with tunable sizes and shapes. *Inorg. Chem. Commun.* **2018**, *93*, 56–60.

87. Ma, M.; Zacher, D.; Zhang, X.; Fischer, R. A.; Metzler-Nolte, N. A Method for the Preparation of Highly Porous, Nanosized Crystals of Isoreticular MetalOrganic Frameworks. *Crystal Growth & Design* **2011**, *11*, 185–189.

88. Nesse, F. S.; Opitz, M.; Dietzel, P. D. C. Morphology control in modulated synthesis of metal-organic framework CPO-27. *Microporous Mesoporous Mater.* **2019**, *275*, 207–213.

89. Li, P.; Klet, R. C.; Moon, S.-y.; Wang, T. C.; Deria, P.; Peters, A. W.; Klahr, B. M.; Park, H.-j.; Al-juaid, S. S.; Hupp, J. T.; Farha, O. K. Synthesis of nanocrystals of Zr-based metal – organic frameworks with csq-net : significant. *Chem. Comm.* **2015**, *51*, 10925–10928.

90. Webber, T. E.; Liu, W.; Desai, S. P.; Lu, C. C.; Truhlar, D. G.; Penn, R. L. Role of a Modulator in the Synthesis of Phase-Pure NU-1000. *ACS Appl. Mater. Interfaces* **2017**, *9*, 39342–39346.

91. Wang, S.; Chen, Y.; Wang, S.; Li, P.; Mirkin, C. A.; Farha, O. K. DNA-Functionalized Metal–Organic Framework Nanoparticles for Intracellular Delivery of Proteins. *J. Am. Chem. Soc.* **2019**, *141*, 2215–2219.

92. Park, J.; Jiang, Q.; Feng, D.; Mao, L.; Zhou, H. Size-Controlled Synthesis of Porphyrinic Metal Organic Framework and Functionalization for Targeted Photodynamic Therapy. *J. Am. Chem. Soc.* **2016**, *138*, 3518–3525.

93. Morris, W.; Wang, S.; Cho, D.; Auyeung, E.; Li, P.; Farha, O. K.; Mirkin, C. A. Role of modulators in controlling the colloidal stability and polydispersity of the UiO-66 metal-organic framework. *ACS Appl. Mater. Interfaces* **2017**, *9*, 33413–33418.

94. Schaate, A.; Roy, P.; Godt, A.; Lippke, J.; Waltz, F.; Wiebcke, M.; Behrens, P. Modulated Synthesis of Zr-Based Metal-Organic Frameworks: From Nano to Single Crystals. *Chem. Eur. J.* **2011**, *17*, 6643–6651.

95. Li, Y. S.; Bux, H.; Feldhoff, A.; Li, G. N.; Yang, W. S.; Caro, J. Controllable synthesis of metal-organic frameworks: From MOF nanorods to oriented MOF membranes. *Adv. Mater.* **2010**, *22*, 3322–3326.

96. Springer, S.; Satalov, A.; Lippke, J.; Wiebcke, M. Nanocrystals and nanomaterials of isoreticular zeolitic imidazolate frameworks. *Microporous and Mesoporous Materials* **2015-11**, *216*, 161–170.

97. Rojas, S.; Carmona, F. J.; Maldonado, C. R.; Horcajada, P.; Hidalgo, T.; Serre, C.; Navarro, J. A.; Barea, E. Nanoscaled zinc pyrazolate metal-organic frameworks as drug-delivery systems. *Inorg. Chem.* **2016**, *55*, 2650–2663.

98. Haque, E.; Jhung, S. H. Synthesis of isostructural metal–organic frameworks, CPO-27s, with ultrasound, microwave, and conventional heating: Effect of synthesis methods and metal ions. *Chemical Engineering Journal* **2011**, *173*, 866–872.

99. Surblé, S.; Millange, F.; Serre, C.; Férey, G.; Walton, R. I. An EXAFS study of the formation of a nanoporous metal–organic framework: evidence for the retention of secondary building units during synthesis. *Chem. Commun.* **2006**, 1518.

100. Thi Thanh Chau, V.; Thi MinhThanh, H.; Dinh Du, P.; Thanh Tam Toan, T.; Ngoc Tuyen, T.; Xuan Mau, T.; Quang Khieu, D. Metal-Organic Framework-101 (MIL-101): Synthesis, Kinetics, Thermodynamics, and Equilibrium Isotherms of Remazol Deep Black RGB Adsorption. *Journal of Chemistry* **2018**, *2018*, 1–14.

101. Jiang, D.; Burrows, A. D.; Edler, K. J. Size-controlled synthesis of MIL-101(Cr) nanoparticles with enhanced selectivity for CO2 over N2. *CrystEngComm* **2011**, *13*, 6916.

102. Trickett, C. A.; Gagnon, K. J.; Lee, S.; Gándara, F.; Bürgi, H.-B.; Yaghi, O. M. Definitive Molecular Level Characterization of Defects in UiO-66 Crystals. *Angew. Chem. Int. Ed.* **2015**, *54*, 11162–11167.

103. Park, J.; Jiang, Q.; Feng, D.; Mao, L.; Zhou, H.-C. Size-Controlled Synthesis of Porphyrinic Metal–Organic Framework and Functionalization for Targeted Photodynamic Therapy. *J. Am. Chem. Soc.* **2016**, *138*, 3518–3525.

104. Pham, M.-H.; Vuong, G.-T.; Vu, A.-T.; Do, T.-O. Novel Route to Size-Controlled Fe–MIL-88B–NH_2 Metal–Organic Framework Nanocrystals. *Langmuir* **2011**, *27*, 15261–15267.

105. Morris, W.; Wang, S.; Cho, D.; Auyeung, E.; Li, P.; Farha, O. K.; Mirkin, C. A. Role of Modulators in Controlling the Colloidal Stability and Polydispersity of the UiO-66 Metal–Organic Framework. *ACS Appl. Mater. Interfaces* **2017**, *9*, 33413–33418.

106. Cai, X.; Lin, J.; Pang, M. Facile Synthesis of Highly Uniform Fe-MIL-88B Particles. *Crystal Growth & Design* **2016**, *16*, 3565–3568.

107. Zhao, T.; Yang, L.; Feng, P.; Gruber, I.; Janiak, C.; Liu, Y. Facile synthesis of nano-sized MIL-101(Cr) with the addition of acetic acid. *Inorganica Chimica Acta* **2018**, *471*, 440–445.

108. Suresh, M.; David Raju, B.; Rama Rao, K. S.; Raveendranath Reddy, K.; Kantam, M. L.; Srinivasu, P. Metal organic framework MIL-101(Cr) for dehydration reactions. *J Chem Sci* **2014**, *126*, 527–532.

109. Seoane, B.; Dikhtiarenko, A.; Mayoral, A.; Tellez, C.; Coronas, J.; Kapteijn, F.; Gascon, J. Metal organic framework synthesis in the presence

of surfactants: towards hierarchical MOFs? *CrystEngComm* **2015**, *17*, 1693–1700.

110. García Márquez, A.; Demessence, A.; Platero-Prats, A. E.; Heurtaux, D.; Horcajada, P.; Serre, C.; Chang, J.-S.; Férey, G.; de la Peña-O'Shea, V. A.; Boissière, C.; Grosso, D.; Sanchez, C. Green Microwave Synthesis of MIL-100(Al, Cr, Fe) Nanoparticles for Thin-Film Elaboration. *Eur. J. Inorg. Chem.* **2012**, *2012*, 5165–5174.

111. Lee, Y.-R.; Jang, M.-S.; Cho, H.-Y.; Kwon, H.-J.; Kim, S.; Ahn, W.-S. ZIF-8: A comparison of synthesis methods. *Chemical Engineering Journal* **2015**, *271*, 276–280.

112. Decker, G. E.; Stillman, Z.; Attia, L.; Fromen, C. A.; Bloch, E. D. Controlling Size, Defectiveness, and Fluorescence in Nanoparticle UiO-66 through Water and Ligand Modulation. *Chem. Mater.* **2019**, *31*, 4831–4839.

113. Zareba, J. K.; Nyk, M.; Samoć, M. Co/ZIF-8 Heterometallic Nanoparticles: Control of Nanocrystal Size and Properties by a Mixed-Metal Approach. *Crystal Growth & Design* **2016**, *16*, 6419–6425.

114. Schejn, A.; Aboulaich, A.; Balan, L.; Falk, V.; Lalevée, J.; Medjahdi, G.; Aranda, L.; Mozet, K.; Schneider, R. Cu^{2+} -doped zeolitic imidazolate frameworks (ZIF-8): efficient and stable catalysts for cycloadditions and condensation reactions. *Catal. Sci. Technol.* **2015**, *5*, 1829–1839.

115. Cao, J.; Yang, Z.-h.; Xiong, W.-p.; Zhou, Y.-y.; Peng, Y.-r.; Li, X.; Zhou, C.-y.; Xu, R.; Zhang, Y.-r. One-step synthesis of Co-doped UiO-66 nanoparticle

with enhanced removal efficiency of tetracycline: Simultaneous adsorption and photocatalysis. *Chemical Engineering Journal* **2018**, *353*, 126–137.

116. Hu, S.; Liu, M.; Guo, X.; Li, K.; Han, Y.; Song, C.; Zhang, G. Effects of Monocarboxylic Acid Additives on Synthesizing Metal–Organic Framework NH_2 -MIL-125 with Controllable Size and Morphology. *Crystal Growth & Design* **2017**, *17*, 6586–6595.

117. Yang, L.; Zhao, T.; Boldog, I.; Janiak, C.; Yang, X.-Y.; Li, Q.; Zhou, Y.-J.; Xia, Y.; Lai, D.-W.; Liu, Y.-J. Benzoic acid as a selector–modulator in the synthesis of MIL-88B(Cr) and nano-MIL-101(Cr). *Dalton Trans.* **2019**, *48*, 989–996.

118. Furukawa, H.; Gándara, F.; Zhang, Y.-B.; Jiang, J.; Queen, W. L.; Hudson, M. R.; Yaghi, O. M. Water Adsorption in Porous Metal–Organic Frameworks and Related Materials. *J. Am. Chem. Soc.* **2014**, *136*, 4369–4381.

119. Zhao, Y.; Zhang, Q.; Li, Y.; Zhang, R.; Lu, G. Large-Scale Synthesis of Monodisperse UiO-66 Crystals with Tunable Sizes and Missing Linker Defects via Acid/Base Co-Modulation. *ACS Appl. Mater. Interfaces* **2017**, *9*, 15079–15085.

120. Hu, Z.; Castano, I.; Wang, S.; Wang, Y.; Peng, Y.; Qian, Y.; Chi, C.; Wang, X.; Zhao, D. Modulator Effects on the Water-Based Synthesis of Zr/Hf Metal–Organic Frameworks: Quantitative Relationship Studies between Modulator, Synthetic Condition, and Performance. *Crystal Growth & Design* **2016**, *16*, 2295–2301.

121. Burton, A. W.; Ong, K.; Rea, T.; Chan, I. Y. On the estimation of average crystallite size of zeolites from the Scherrer equation: A critical evaluation of its application to zeolites with one-dimensional pore systems. *Microporous and Mesoporous Materials* **2009**, *117*, 75–90.

122. Uemura, T.; Ohba, M.; Kitagawa, S. Size and Surface Effects of Prussian Blue Nanoparticles Protected by Organic Polymers. *Inorg. Chem.* **2004-11**, *43*, 7339–7345.

123. Stetefeld, J.; McKenna, S. A.; Patel, T. R. Dynamic light scattering: a practical guide and applications in biomedical sciences. *Biophys Rev* **2016-12**, *8*, 409–427.

124. Mandø, M.; Yin, C.; Sørensen, H.; Rosendahl, L. On the modelling of motion of non-spherical particles in two-phase flow. *Powder Technology* **2007**, 15.

125. Abade, G. C.; Cichocki, B.; Ekiel-Jeżewska, M. L.; Nägele, G.; Wajnryb, E. High-frequency viscosity and generalized Stokes–Einstein relations in dense suspensions of porous particles. *J. Phys.: Condens. Matter* **2010**, *22*, 322101.

126. Chen, Z. H.; Kim, C.; Zeng, X.-b.; Hwang, S. H.; Jang, J.; Ungar, G. Characterizing Size and Porosity of Hollow Nanoparticles: SAXS, SANS, TEM, DLS, and Adsorption Isotherms Compared. *Langmuir* **2012**, *28*, 15350–15361.

127. Bellido, E.; Guillevic, M.; Hidalgo, T.; Santander-Ortega, M. J.; Serre, C.; Horcajada, P. Understanding the Colloidal Stability of the Mesoporous MIL-100(Fe) Nanoparticles in Physiological Media. *Langmuir* **2014**, *30*, 5911–5920.

128. Li, T.; Senesi, A. J.; Lee, B. Small Angle X-ray Scattering for Nanoparticle Research. *Chem. Rev.* **2016**, *116*, 11128–11180.

129. Lin, R.; Villacorta Hernandez, B.; Ge, L.; Zhu, Z. Metal organic framework based mixed matrix membranes: an overview on filler/polymer interfaces. *J. Mater. Chem. A* **2018**, *6*, 293–312.

130. Xiang, L.; Sheng, L.; Wang, C.; Zhang, L.; Pan, Y.; Li, Y. Amino-Functionalized ZIF-7 Nanocrystals: Improved Intrinsic Separation Ability and Interfacial Compatibility in Mixed-Matrix Membranes for CO_2/CH_4 Separation. *Adv. Mater.* **2017**, *29*, 1606999.

131. Della Rocca, J.; Liu, D.; Lin, W. Nanoscale Metal–Organic Frameworks for Biomedical Imaging and Drug Delivery. *Acc. Chem. Res.* **2011**, *44*, 957–968.

132. Ettlinger, R.; Sönksen, M.; Graf, M.; Moreno, N.; Denysenko, D.; Volkmer, D.; Kerl, K.; Bunzen, H. Metal–organic framework nanoparticles for arsenic trioxide drug delivery. *J. Mater. Chem. B* **2018**, *6*, 6481–6489.

133. Ghorbanloo, M.; Safarifard, V.; Morsali, A. Heterogeneous catalysis with a coordination modulation synthesized MOF: morphology-dependent catalytic activity. *New J. Chem.* **2017**, *41*, 3957–3965.

134. LaMer, V. K.; Dinegar, R. H. Theory, Production and Mechanism of Formation of Monodispersed Hydrosols. *J. Am. Chem. Soc.* **1950**, *72*, 4847–4854.

135. Watzky, M. A.; Finke, R. G. Transition Metal Nanocluster Formation Kinetic and Mechanistic Studies. A New Mechanism When Hydrogen Is the

Reductant: Slow, Continuous Nucleation and Fast Autocatalytic Surface Growth. *J. Am. Chem. Soc.* **1997**, *119*, 10382–10400.

136. Lazzari, S.; Abolhasani, M.; Jensen, K. F. Modeling of the formation kinetics and size distribution evolution of II–VI quantum dots. *React. Chem. Eng.* **2017**, *2*, 567–576.

137. Griffin, S.; Briuglia, M.; ter Horst, J.; Forgan, R. S. Assessing Crystallisation Kinetics of Zr Metal-Organic Frameworks through Turbidity Measurements to Inform Rapid Microwave-Assisted Synthesis. *Chem. Eur. J.* **2020**,

138. Haouas, M.; Volkringer, C.; Loiseau, T.; Férey, G.; Taulelle, F. In Situ NMR, Ex Situ XRD and SEM Study of the Hydrothermal Crystallization of Nanoporous Aluminum Trimesates MIL-96, MIL-100, and MIL-110. *Chem. Mater.* **2012**, *24*, 2462–2471.

139. Hu, S.; Liu, M.; Guo, X.; Li, K.; Han, Y.; Song, C.; Zhang, G. Effects of monocarboxylic acid additives on synthesizing metal-organic framework NH2-MIL-125 with controllable size and morphology. *Cryst. Growth. Des.* **2017**, *17*, 6586–6595.

140. Fishtik, I.; Nagypál, I.; Gutman, I. Response reactions: a way to explain the unusual behaviour of multiple equilibrium systems. *J. Chem. Soc., Faraday Trans.* **1995**, *91*, 259–267.

141. Smith, W.; Missen, R. *Reaction Equilibrium Analysis: Theory and Algorithms*; Wiley, 1982.

142. Avci, C.; Ariñez-Soriano, J.; Carné-Sánchez, A.; Guillerm, V.; Carbonell, C.; Imaz, I.; Maspoch, D. Post-Synthetic Anisotropic Wet-Chemical Etching of

Colloidal Sodalite ZIF Crystals. *Angew. Chem. Int. Ed.* **2015-11-23**, *54*, 14417–14421.

143. Li, L.; Sun, F.; Jia, J.; Borjigin, T.; Zhu, G. Growth of large single MOF crystals and effective separation of organic dyes. *CrystEngComm* **2013**, *15*, 4094.

144. Sanil, E. S.; Cho, K.-H.; Lee, S.-K.; Lee, U.-H.; Ryu, S. G.; Lee, H. W.; Chang, J.-S.; Hwang, Y. K. Size and morphological control of a metal–organic framework Cu-BTC by variation of solvent and modulator. *J Porous Mater* **2015**, *22*, 171–178.

145. Shan, B.; James, J. B.; Armstrong, M. R.; Close, E. C.; Letham, P. A.; Nikkhah, K.; Lin, Y. S.; Mu, B. Influences of Deprotonation and Modulation on Nucleation and Growth of UiO-66: Intergrowth and Orientation. *J. Phys. Chem. C* **2018**, *122*, 2200–2206.

146. Chiu, C.-C.; Shieh, F.-K.; Tsai, H.-H. G. Ligand Exchange in the Synthesis of Metal–Organic Frameworks Occurs Through Acid-Catalyzed Associative Substitution. *Inorg. Chem.* **2019**, *58*, 14457–14466.

147. Qian, J.; Sun, F.; Qin, L. Hydrothermal synthesis of zeolitic imidazolate framework-67 (ZIF-67) nanocrystals. *Materials Letters* **2012-09**, *82*, 220–223.

148. Saha, S.; Springer, S.; Schweinefuß, M. E.; Pontoni, D.; Wiebcke, M.; Huber, K. Insight into Fast Nucleation and Growth of Zeolitic Imidazolate Framework-71 by In Situ Time-Resolved Light and X-ray Scattering Experiments. *Crystal Growth & Design* **2016**, *16*, 2002–2010.

149. Tu, M.; Wiktor, C.; Rösler, C.; Fischer, R. A. Rapid room temperature syntheses of zeolitic-imidazolate framework (ZIF) nanocrystals. *Chem. Commun.* **2014**, *50*, 13258–13260.

150. Webber, T. E.; Desai, S. P.; Combs, R. L.; Bingham, S.; Lu, C. C.; Penn, R. L. Size Control of the MOF NU-1000 through Manipulation of the Modulator/Linker Competition. *Crystal Growth & Design* **2020**, 2965–2972.

151. Bosch, M.; Yuan, S.; Zhou, H.-C. In *The Chemistry of Metal-Organic Frameworks: Synthesis, Characterization, and Applications*; Kaskel, S., Ed.; Wiley-VCH Verlag GmbH & Co. KGaA, 2016; pp 137–170.

152. Wang, X.-G.; Cheng, Q.; Yu, Y.; Zhang, X.-Z. Controlled Nucleation and Controlled Growth for Size Predicable Synthesis of Nanoscale Metal-Organic Frameworks (MOFs): A General and Scalable Approach. *Angew. Chem. Int. Ed.* **2018**, *57*, 7836–7840.

153. Yeung, H. H.; Sapnik, A. F.; Massingberd-Mundy, F.; Gaultois, M. W.; Wu, Y.; Fraser, D. A. X.; Henke, S.; Pallach, R.; Heidenreich, N.; Magdysyuk, O. V.; Vo, N. T.; Goodwin, A. L. Control of Metal–Organic Framework Crystallization by Metastable Intermediate Pre-equilibrium Species. *Angew. Chem. Int. Ed.* **2019**, *58*, 566–571.

154. Lai, Y.-C.; Kung, C.-W.; Su, C.-H.; Ho, K.-C.; Liao, Y.-C.; Tsai, D.-H. Metal–Organic Framework Colloids: Disassembly and Deaggregation. *Langmuir* **2016**, *32*, 6123–6129.

155. Morris, W.; Wang, S.; Cho, D.; Auyeung, E.; Li, P.; Farha, O. K.; Mirkin, C. A. Role of Modulators in Controlling the Colloidal Stability and

Polydispersity of the UiO-66 Metal–Organic Framework. *ACS Appl. Mater. Interfaces* **2017**, *9*, 33413–33418.

156. Flory, P. J. Fundamental Principles of Condensation Polymerization. *Chem. Rev.* **1946**, *39*, 137–197.

157. Hong, M.; Teng, H. H. Implications of solution chemistry effects: Direction-specific restraints on the step kinetics of calcite growth. *Geochimica et Cosmochimica Acta* **2014**, *141*, 228–239.

158. Wang, Y.; Li, L.; Liang, H.; Xing, Y.; Yan, L.; Dai, P.; Gu, X.; Zhao, G.; Zhao, X. Superstructure of a Metal–Organic Framework Derived from Microdroplet Flow Reaction: An Intermediate State of Crystallization by Particle Attachment. *ACS Nano* **2019**, *13*, 2901–2912.

159. Shoaee, M.; Anderson, M.; Attfield, M. Crystal Growth of the Nanoporous Metal-Organic Framework HKUST-1 Revealed by In Situ Atomic Force Microscopy. *Angew. Chem. Int. Ed.* **2008**, *47*, 8525–8528.

160. Hellevang, H.; Haile, B. G.; Miri, R. A Statistical Approach To Explain the Solution Stoichiometry Effect on Crystal Growth Rates. *Crystal Growth & Design* **2016**, *16*, 1337–1348.

161. Feynman, C.; Gottlieb, M.; Leighton, R. *The Feynman Lectures of Physics*; California Institute of Technology, 1963.

162. Kim, T.-H.; Cho, K.-S.; Lee, E. K.; Lee, S. J.; Chae, J.; Kim, J. W.; Kim, D. H.; Kwon, J.-Y.; Amaratunga, G.; Lee, S. Y.; Choi, B. L.; Kuk, Y.; Kim, J. M.; Kim, K. Full-colour quantum dot displays fabricated by transfer printing. *Nature Photon* **2011**, *5*, 176–182.

163. Cai, X.; Xie, Z.; Li, D.; Kassymova, M.; Zang, S.-Q.; Jiang, H.-L. Nano-sized metal-organic frameworks: Synthesis and applications. *Coordination Chemistry Reviews* **2020**, *417*, 213366.

164. Gao, R.; Zhang, G.; Ru, X.; Xu, C.; Li, M.; Lin, R.; Wang, Z. Morphology control of metal-organic frameworks by Co-competitive coordination strategy for low-temperature selective catalytic reduction of NO with NH3. *Journal of Solid State Chemistry* **2021**, *297*, 122031.

165. Bonnett, B. L.; Smith, E. D.; De La Garza, M.; Cai, M.; Haag, J. V.; Serrano, J. M.; Cornell, H. D.; Gibbons, B.; Martin, S. M.; Morris, A. J. PCN-222 Metal–Organic Framework Nanoparticles with Tunable Pore Size for Nanocomposite Reverse Osmosis Membranes. *ACS Appl. Mater. Interfaces* **2020**, *12*, 15765–15773.

166. Mandal, T. N.; Karmakar, A.; Sharma, S.; Ghosh, S. K. Metal-Organic Frameworks (MOFs) as Functional Supramolecular Architectures for Anion Recognition and Sensing. *Chem. Rec.* **2018**, *18*, 154–164.

167. Qian, Q.; Asinger, P. A.; Lee, M. J.; Han, G.; Mizrahi Rodriguez, K.; Lin, S.; Benedetti, F. M.; Wu, A. X.; Chi, W. S.; Smith, Z. P. MOF-Based Membranes for Gas Separations. *Chem. Rev.* **2020**, acs.chemrev.0c00119.

168. Maka, V. K.; Mukhopadhyay, A.; Jindal, S.; Moorthy, J. N. Redox-Reversible 2D Metal–Organic Framework Nanosheets (MONs) Based on the Hydroquinone/Quinone Couple. *Chem. Eur. J.* **2019**, *25*, 3835–3842.

169. D'Alessandro, D. M. Exploiting redox activity in metal–organic frameworks: concepts, trends and perspectives. *Chem. Commun.* **2016**, *52*, 8957–8971.

170. Cravillon, J.; Schröder, C. A.; Bux, H.; Rothkirch, A.; Caro, J.; Wiebcke, M. Formate modulated solvothermal synthesis of ZIF-8 investigated using time-resolved in situ X-ray diffraction and scanning electron microscopy. *CrystEngComm* **2012**, *14*, 492–498.

171. Guo, C.; Zhang, Y.; Guo, Y.; Zhang, L.; Zhang, Y.; Wang, J. A general and efficient approach for tuning the crystal morphology of classical MOFs. *Chem. Commun.* **2018**, *54*, 252–255.

172. Manuel, D.; Mayoral, A.; Isabel, D.; Sa, M. Nanoscaled M - MOF-74 Materials Prepared at Room Temperature. *Cryst. Growth Des.* **2014**, *14*, 2479–2487.

173. Xu, X. Controllable synthesis of ultra-small metal-organic framework nanocrystals composed of copper(II) carboxylates. *Nanoscale* **2016**, *8*, 16725–16732.

174. Zheng, W.; Hao, X.; Zhao, L.; Sun, W. Controllable Preparation of Nanoscale Metal-Organic Frameworks by Ionic Liquid Microemulsions. *Ind. Eng. Chem. Res.* **2017**, *56*, 5899–5905.

175. Shimpi, J. R.; Sidhaye, D. S.; Prasad, B. L. V. Digestive Ripening: A Fine Chemical Machining Process on the Nanoscale. *Langmuir* **2017**, *33*, 9491–9507.

176. Van Vleet, M. J.; Weng, T.; Li, X.; Schmidt, J. In Situ, Time-Resolved, and Mechanistic Studies of Metal–Organic Framework Nucleation and Growth. *Chemical Reviews* **2018**, *118*, 3681–3721.

177. Pan, Y.; Liu, Y.; Zeng, G.; Zhao, L.; Lai, Z. Rapid synthesis of zeolitic imidazolate framework-8 (ZIF-8) nanocrystals in an aqueous system. *Chem. Commun.* **2011**, *47*, 2071.

178. Cheng, C.; Zhang, R.; Wang, J.; Zhang, Y.; Wen, C.; Tan, Y.; Yang, M. An ultrasensitive and selective fluorescent nanosensor based on porphyrinic metal–organic framework nanoparticles for Cu^{2+} detection. *Analyst* **2020**, *145*, 797–804.

179. Razavi, S. A. A.; Masoomi, M. Y.; Morsali, A. Stimuli-Responsive Metal–Organic Framework (MOF) with Chemo-Switchable Properties for Colorimetric Detection of $CHCl_3$. *Chemistry – A European Journal* **2017**, *23*, 12559–12564.

180. Wang, J.; Fan, Y.; Lee, H.-w.; Yi, C.; Cheng, C.; Zhao, X.; Yang, M. Ultrasmall Metal–Organic Framework Zn-MOF-74 Nanodots: Size-Controlled Synthesis and Application for Highly Selective Colorimetric Sensing of Iron(III) in Aqueous Solution. *ACS Appl. Nano Mater.* **2018**, *1*, 3747–3753.

181. Sun, L.; Hendon, C. H.; Park, S. S.; Tulchinsky, Y.; Wan, R.; Wang, F.; Walsh, A.; Dincă, M. Is iron unique in promoting electrical conductivity in MOFs? *Chem. Sci.* **2017**, *8*, 4450–4457.

182. Norris, D. J.; Bawendi, M. G. Measurement and assignment of the size-dependent optical spectrum in CdSe quantum dots. *Phys. Rev. B* **1996**, *53*, 16338–16346.

183. Siddiqui, S. A.; Domanov, O.; Schafler, E.; Vejpravova, J.; Shiozawa, H. Synthesis and size-dependent spin crossover of coordination polymer $[Fe(Htrz)_2(trz)](BF_4)$. *J. Mater. Chem. C* **2021**, *9*, 1077–1084.

184. Hauser, A.; Guetlich, P.; Spiering, H. High-spin / low-spin relaxation kinetics and cooperative effects in the hexakis(1-propyltetrazole)iron bis(tetrafluoroborate) and $[Zn_1 - xFe_x(ptz)_6](BF_4)_2$ (ptz = 1-propyltetrazole) spin-crossover systems. **1986**, *25*, 4245–4248.

185. Hauser, A. Intersystem crossing in the $[Fe(ptz)_6](BF_4)_2$ spin crossover system (ptz=1-propyltetrazole). *The Journal of Chemical Physics* **1991**, *94*, 2741–2748.

186. Rajh, T.; Chen, L. X.; Lukas, K.; Liu, T.; Thurnauer, M. C.; Tiede, D. M. Surface Restructuring of Nanoparticles: An Efficient Route for LigandMetal Oxide Crosstalk. *J. Phys. Chem. B* **2002**, *106*, 10543–10552.

187. Dai, Q.; Wang, Y.; Li, X.; Zhang, Y.; Pellegrino, D. J.; Zhao, M.; Zou, B.; Seo, J.; Wang, Y.; Yu, W. W. Size-Dependent Composition and Molar Extinction Coefficient of PbSe Semiconductor Nanocrystals. *ACS Nano* **2009**, *3*, 1518–1524.

188. Liu, X.; Atwater, M.; Wang, J.; Huo, Q. Extinction coefficient of gold nanoparticles with different sizes and different capping ligands. *Colloids and Surfaces B: Biointerfaces* **2007**, *58*, 3–7.

189. Moreels, I.; Lambert, K.; De Muynck, D.; Vanhaecke, F.; Poelman, D.; Martins, J. C.; Allan, G.; Hens, Z. Composition and Size-Dependent Extinction Coefficient of Colloidal PbSe Quantum Dots. **2007**, *19*, 6101–6106.

190. Zhang, Y.; Wang, X.; Ma, M.; Fu, D.; Gu, N.; Lu, Z.; Xu, J.; Xu, L.; Chen, K. Size dependence of second-order optical nonlinearity of CdS nanoparticles studied by hyper-Rayleigh scattering. *Journal of Colloid and Interface Science* **2003**, *266*, 377–381.

191. Mayerhofer, T. G.; Hofer, S.; Popp, J. Deviations from Beer's law on the microscale – nonadditivity of absorption cross sections. *Phys Chem Chem Phys* **2019**, *21*, 9793–9801.

192. Kornyshev, A. A.; Spohr, E.; Vorotyntsev, M. A. In *Encyclopedia of Electrochemistry*; Bard, A. J., Ed.; Wiley-VCH, 2007; p PAGES.

193. Reviakine, I.; Johannsmann, D.; Richter, R. P. Hearing What You Cannot See and Visualizing What You Hear: Interpreting Quartz Crystal Microbalance Data from Solvated Interfaces. *Anal. Chem.* **2011**, *83*, 8838–8848.

194. Celis-Salazar, P. J.; Cai, M.; Cucinell, C. A.; Ahrenholtz, S. R.; Epley, C. C.; Usov, P. M.; Morris, A. J. Independent Quantification of Electron and Ion Diffusion in Metallocene-Doped Metal–Organic Frameworks Thin Films. *J. Am. Chem. Soc.* **2019**, *141*, 11947–11953.

195. Huang, Z.; Xie, N.; Zhang, M.; Xu, B. Nonpyrolyzed FeN Coordination-Based Iron Triazolate Framework: An Efficient and Stable Electrocatalyst for Oxygen Reduction Reaction. *ChemSusChem* **2019**, *12*, 200–207.

196. Okada, K.; Sawai, S.; Ikigaki, K.; Tokudome, Y.; Falcaro, P.; Takahashi, M. Electrochemical sensing and catalysis using $Cu_3(BTC)_2$ coating electrodes from $Cu(OH)_2$ films. *CrystEngComm* **2017**, *19*, 4194–4200.

197. Kobayashi, H.; Tokita, Y. Modeling of hole transport across grain boundaries in organic semiconductors for mesoscale simulations. **2015**, *8*, 051602.

198. Vladimirov, I.; Kühn, M.; Geßner, T.; May, F.; Weitz, R. T. Energy barriers at grain boundaries dominate charge carrier transport in an electron-conductive organic semiconductor. *Sci Rep* **2018**, *8*, 14868.

199. Horowitz, G.; Hajlaoui, M. E. Mobility in Polycrystalline Oligothiophene Field-Effect Transistors Dependent on Grain Size. *Advanced Materials* **2000**, *12*, 1046–1050.

200. Chmiola, J.; Yushin, G.; Gogotsi, Y.; Portet, C.; Simon, P.; Taberna, P. L. Anomalous Increase in Carbon Capacitance at Pore Sizes Less Than 1 Nanometer. 2006.

201. Boyd, S.; Ganeshan, K.; Tsai, W.-Y.; Wu, T.; Saeed, S.; Jiang, D.-e.; Balke, N.; van Duin, A. C. T.; Augustyn, V. Effects of interlayer confinement and hydration on capacitive charge storage in birnessite. **2021**, *20*, 1689–1694.

202. Cai, M.; Loague, Q.; Morris, A. J. Design Rules for Efficient Charge Transfer in Metal–Organic Framework Films: The Pore Size Effect. *J. Phys. Chem. Lett.* **2020-02-06**, *11*, 702–709.

203. Castner, A. T.; Su, H.; Svensson Grape, E.; Inge, A. K.; Johnson, B. A.; Ahlquist, M. S. G.; Ott, S. Microscopic Insights into Cation-Coupled Electron Hopping Transport in a Metal–Organic Framework. **2022**, *144*, 5910–5920.

204. Marshall, C. R.; Dvorak, J. P.; Twight, L. P.; Chen, L.; Kadota, K.; Andreeva, A. B.; Overland, A. E.; Ericson, T.; Cozzolino, A. F.; Brozek, C. K.

Size-Dependent Properties of Solution-Processable Conductive MOF Nanocrystals. **2022**, *144*, 5784–5794.

205. Saji, T.; Yamada, T.; Aoyagui, S. Electron-transfer rate constants for redox systems of Fe(III)/Fe(II) complexes with 2,2-bipyridine and/or cyanide ion as measured by the galvanostatic double pulse method. **1975**, *61*, 147–153.

206. Bondarenko, A. S.; Stephens, I. E. L.; Hansen, H. A.; Pérez-Alonso, F. J.; Tripkovic, V.; Johansson, T. P.; Rossmeisl, J.; Nørskov, J. K.; Chorkendorff, I. The Pt(111)/Electrolyte Interface under Oxygen Reduction Reaction Conditions: An Electrochemical Impedance Spectroscopy Study. **2011**, *27*, 2058–2066.

207. Patwardhan, S.; Schatz, G. C. Theoretical Investigation of Charge Transfer in Metal Organic Frameworks for Electrochemical Device Applications. *119*, 24238–24247.

208. Sheberla, D.; Bachman, J. C.; Elias, J. S.; Sun, C.-J.; Shao-Horn, Y.; Dincă, M. Conductive MOF electrodes for stable supercapacitors with high areal capacitance. *Nature Mater* **2017-02**, *16*, 220–224.

209. Mendecki, L.; Mirica, K. A. Conductive Metal–Organic Frameworks as Ion-to-Electron Transducers in Potentiometric Sensors. *ACS Appl. Mater. Interfaces* **2018-06-06**, *10*, 19248–19257.

210. Qi, Y.; He, C.-T.; Lin, J.; Lin, S.; Liu, J.; Huang, J.; Xue, W.; Yu, G.; Chao, H.-Y.; Tong, Y.; Qiao, Z. Mild metal-organic-gel route for synthesis of stable sub-5-nm metal-organic framework nanocrystals. *Nano Research* **2017**, *10*, 3621–3628.

211. Wang, X. G.; Cheng, Q.; Yu, Y.; Zhang, X. Z. Controlled Nucleation and Controlled Growth for Size Predicable Synthesis of Nanoscale Metal–Organic Frameworks (MOFs): A General and Scalable Approach. *Angew. Chem. Int. Ed.* **2018**, *57*, 7836–7840.

212. Bachman, J. E.; Smith, Z. P.; Li, T.; Xu, T.; Long, J. R. Enhanced ethylene separation and plasticization resistance in polymer membranes incorporating metal-organic framework nanocrystals. *Nat. Mater.* **2016**, *15*, 845–849.

213. Abánades Lázaro, I.; Haddad, S.; Rodrigo-Muñoz, J. M.; Orellana-Tavra, C.; Del Pozo, V.; Fairen-Jimenez, D.; Forgan, R. S. Mechanistic Investigation into the Selective Anticancer Cytotoxicity and Immune System Response of Surface-Functionalized, Dichloroacetate-Loaded, UiO-66 Nanoparticles. *ACS Appl. Mater. Interfaces* **2018**, *10*, 5255–5268.

214. Chalati, T.; Horcajada, P.; Gref, R.; Couvreur, P.; Serre, C. Optimisation of the synthesis of MOF nanoparticles made of flexible porous iron fumerate MIL-88A. *J. Mater. Chem.* **2011**, *21*, 2220–2227.

215. Grall, R.; Hidalgo, T.; Delic, J.; Garcia-Marquez, A.; Chevillard, S.; Horcajada, P. In vitro biocompatibility of mesoporous metal (III; Fe, Al, Cr) trimesate MOF nanocarriers. *J. Mater. Chem. B* **2015**, *3*, 8279–8292.

216. Saouma, C. T.; Richard, S.; Smolders, S.; Delley, M. F.; Ameloot, R.; Vermoortele, F.; De Vos, D. E.; Mayer, J. M. Bulk-to-Surface Proton-Coupled Electron Transfer Reactivity of the Metal-Organic Framework MIL-125. *J. Am. Chem. Soc.* **2018**, *140*, 16184–16189.

217. Harvey, S. P.; Hupp, J. T.; Farha, O. K. Nanosizing a Metal Organic Framework Enzyme Carrier for Accelerating Nerve Agent Hydrolysis. *ACS Nano* **2016**, *10*, 9174–9182.

218. Schaate, A.; Roy, P.; Godt, A.; Lippke, J.; Waltz, F.; Wiebcke, M.; Behrens, P. Modulated Synthesis of Zr-Based Metal–Organic Frameworks: From Nano to Single Crystals. *Chem. Eur. J.* **2011**, *17*, 6643–6651.

219. Cravillon, J.; Nayuk, R.; Springer, S.; Feldhoff, A.; Huber, K.; Wiebcke, M. Controlling zeolitic imidazolate framework nano- and microcrystal formation: Insight into crystal growth by time-resolved in situ static light scattering. *Chem. Mater.* **2011**, *23*, 2130–2141.

220. Lim, I. H.; Schrader, W.; Schüth, F. Insights into the molecular assembly of zeolitic imidazolate frameworks by ESI-MS. *Chem. Mater.* **2015**, *27*, 3088–3095.

221. Chouhan, A.; Pilet, G.; Daniele, S.; Pandey, A. Shape Controllable Preparation of Submicronic Cadmium Tetrazole-Based Metal–Organic Frameworks via Solvothermal or Microwave-Assisted Methods and Their Photocatalytic Studies. *Chinese J. Chem.* **2017**, *35*, 209–216.

222. Enríquez, J.; Manquian, C.; Chi-Duran, I.; Herrera, F.; Singh, D. P. Controlled Growth of the Noncentrosymmetric Zn(3-ptz)$_2$ and Zn(OH)(3-ptz) Metal-Organic Frameworks. *ACS Omega* **2019**, *4*, 7411–7419.

223. Liu, Y.-y.; Decadt, R.; Bogaerts, T.; Hemelsoet, K.; Kaczmarek, A. M.; Poelman, D.; Waroquier, M.; Speybroeck, V. V.; Deun, R. V.; Voort, P. V. D. Bipyridine-Based Nanosized Metal Organic Framework with Tunable

Luminescence by a Postmodification with Eu (III): An Experimental and Theoretical Study. *J. Phys. Chem. C* **2013**, *117*, 11302–11310.

224. Qi, Z.; Yang, J.; Kang, Y.; Guo, F.; Sun, W. Facile water-stability evaluation of metal–organic frameworks and the property of selective removal of dyes from aqueous solution. *Dalton Trans.* **2016**, *45*, 8753–8759.

225. Klein, N.; Senkovska, I.; Baburin, I. A.; Grünker, R.; Stoeck, U.; Schlichtenmayer, M.; Streppel, B.; Mueller, U.; Leoni, S.; Hirscher, M.; Kaskel, S. Route to a family of robust, non-interpenetrated metal-organic frameworks with pto-like topology. *Chem. Eur. J.* **2011**, *17*, 13007–13016.

226. Zhou, Q.; Yang, F.; Xin, B.; Zeng, G.; Zhou, X.; Liu, K.; Ma, D.; Li, G.; Shi, Z.; Feng, S. Reversible switching of slow magnetic relaxation in a classic lanthanide metal-organic framework system. *Chem. Commun.* **2013**, *49*, 8244–8246.

227. Cai, X.; Liu, B.; Pang, M.; Lin, J. Interfacially synthesized Fe-soc-MOF nanoparticles combined with ICG for photothermal/photodynamic therapy. *Dalton Trans.* **2018**, *47*, 16329–16336.

228. Cai, X.; Xie, Z.; Pang, M.; Lin, J. Controllable Synthesis of Highly Uniform Nanosized HKUST-1 Crystals by Liquid–Solid–Solution Method. *Cryst. Growth Des.* **2019**, *19*, 556–561.

229. Xiang, S.; Zhou, W.; Gallegos, J. M.; Liu, Y.; Chen, B. Exceptionally high acetylene uptake in a microporous metal-organic framework with open metal sites. *J. Am. Chem. Soc.* **2009**, *131*, 12415–12419.

230. Wang, F.; Guo, H.; Chai, Y.; Li, Y.; Liu, C. The controlled regulation of morphology and size of HKUST-1 by "coordination modulation method". *Microporous Mesoporous Mater.* **2013**, *173*, 181–188.

231. Zhuang, J. L.; Ceglarek, D.; Pethuraj, S.; Terfort, A. Rapid room-temperature synthesis of metal-organic framework HKUST-1 crystals in bulk and as oriented and patterned thin films. *Adv. Funct. Mater.* **2011**, *21*, 1442–1447.

232. Diring, S.; Furukawa, S.; Takashima, Y.; Tsuruoka, T.; Kitagawa, S. Controlled multiscale synthesis of porous coordination polymer in nano/micro regimes. *Chem. Mater.* **2010**, *22*, 4531–4538.

233. Xin, C.; Zhan, H.; Huang, X.; Li, H.; Zhao, N.; Xiao, F.; Wei, W.; Sun, Y. Effect of various alkaline agents on the size and morphology of nano-sized HKUST-1 for CO_2 adsorption. *RSC Advances* **2015**, *5*, 27901–27911.

234. Abdelhameed, R. M.; Carlos, L. D.; Silva, A. M.; Rocha, J. Near-infrared emitters based on post-synthetic modified Ln^{3+}-IRMOF-3. *Chem. Commun.* **2013**, *49*, 5019–5021.

235. Biswas, S.; Grzywa, M.; Nayek, H. P.; Dehnen, S.; Senkovska, I.; Kaskel, S.; Volkmer, D. A cubic coordination framework constructed from benzobistriazolate ligands and zinc ions having selective gas sorption properties. *Dalton Trans.* **2009**, *9226*, 6487–6495.

236. Denysenko, D.; Grzywa, M.; Tonigold, M.; Streppel, B.; Krkljus, I.; Hirscher, M.; Mugnaioli, E.; Kolb, U.; Hanss, J.; Volkmer, D. Elucidating gating effects for hydrogen sorption in MFU-4-type triazolate-based metal-

organic frameworks featuring different pore sizes. *Chem. Eur. J.* **2011**, *17*, 1837–1848.

237. Volkringer, C.; Popov, D.; Loiseau, T.; Férey, G.; Burghammer, M.; Riekel, C.; Haouas, M.; Taulelle, F. Synthesis, single-crystal X-ray microdiffraction, and NMR characterizations of the giant pore metal-organic framework aluminum trimesate MIL-100. *Chem. Mater.* **2009**, *21*, 5695–5697.

238. Qiu, M.; Chen, C.; Li, W. Rapid controllable synthesis of Al-MIL-96 and its adsorption of nitrogenous VOCs. *Catalysis Today* **2015**, *258*, 132–138.

239. Férey, G.; Serre, C.; Mellot-Draznieks, C.; Millange, F.; Surblé, S.; Dutour, J.; Margiolaki, I. A hybrid solid with giant pores prepared by a combination of targeted chemistry, simulation, and powder diffraction. *Angew. Chem. Int. Ed.* **2004**, *43*, 6296–6301.

240. Seo, Y. K.; Yoon, J. W.; Lee, J. S.; Lee, U. H.; Hwang, Y. K.; Jun, C. H.; Horcajada, P.; Serre, C.; Chang, J. S. Large scale fluorine-free synthesis of hierarchically porous iron(III) trimesate MIL-100(Fe) with a zeolite MTN topology. *Microporous Mesoporous Mater.* **2012**, *157*, 137–145.

241. Suresh, M.; David Raju, B.; Rama Rao, K. S.; Raveendranath Reddy, K.; Kantam, M. L.; Srinvasu, P. Metal organic framework MIL-101(Cr) for dehydration reactions. *J. of Chem. Sci.* **2014**, *126*, 527–532.

242. Yang, L.; Zhao, T.; Boldog, I.; Janiak, C.; Yang, X.; Li, Q.; Zhou, Y.; Xia, Y.; Lai, D.; Liu, Y. Benzoic acid as a selector–modulator in the synthesis of MIL-88B(Cr) and nano-MIL-101(Cr). *Dalton Trans.* **2019**, *48*, 989–996.

243. Wang, J.; Wan, J.; Ma, Y.; Wang, Y.; Pu, M.; Guan, Z. Metal-organic frameworks MIL-88A with suitable synthesis conditions and optimal dosage for effective catalytic degradation of Orange G through persulfate activation. *RSC Advances* **2016**, *6*, 112502–112511.

244. Shih, Y. H.; Lo, S. H.; Yang, N. S.; Singco, B.; Cheng, Y. J.; Wu, C. Y.; Chang, I. H.; Huang, H. Y.; Lin, C. H. Trypsin-immobilized metal-organic framework as a biocatalyst in proteomics analysis. *ChemPlusChem* **2012**, *77*, 982–986.

245. Ma, M.; Bétard, A.; Weber, I.; Al-Hokbany, N. S.; Fischer, R. A.; Metzler-Nolte, N. Iron-based metal-organic frameworks MIL-88B and NH_2-MIL-88B: High quality microwave synthesis and solvent-induced lattice "breathing". *Cryst. Growth. Des.* **2013**, *13*, 2286–2291.

246. Kim, S.; Kim, J.; Kim, H.; Cho, H.; Ahn, W. Adsorption / catalytic properties of MIL-125 and NH_2-MIL-125. *Catalysis Today* **2013**, *204*, 85–93.

247. Liu, Y.; Zhao, X. Impact of moderative ligand hydrolysis on morphology evolution and the morphology-dependent breathing effect performance of MIL-53(Al). *CrystEngComm* **2018**, *20*, 2102–2111.

248. Xiao, Y.; Han, T.; Xiao, G.; Ying, Y.; Huang, H.; Yang, Q.; Liu, D.; Zhong, C. Highly selective adsorption and separation of aniline/phenol from aqueous solutions by microporous MIL-53(Al): A combined experimental and computational study. *Langmuir* **2014**, *30*, 12229–12235.

249. Han, S.; Lah, M. S. Simple and Efficient Regeneration of MOF-5 and HKUST-1 via Acid-Base Treatment. *Cryst. Growth. Des.* **2015**, *15*, 5568–5572.

250. Choi, J. S.; Son, W. J.; Kim, J.; Ahn, W. S. Metal-organic framework MOF-5 prepared by microwave heating: Factors to be considered. *Microporous Mesoporous Mater.* **2008**, *116*, 727–731.

251. Burgaz, E.; Erciyes, A.; Andac, M.; Andac, O. Synthesis and characterization of nano-sized metal organic framework-5 (MOF-5) by using consecutive combination of ultrasound and microwave irradiation methods. *Inorganica Chim. Acta* **2019**, *485*, 118–124.

252. Ma, M.; Zacher, D.; Zhang, X.; Fischer, R. A.; Metzler-Nolte, N. A Method for the Preparation of Highly Porous, Nanosized Crystals of Isoreticular MetalOrganic Frameworks. *Cryst. Growth Des.* **2011**, *11*, 185–189.

253. Huang, L.; Wang, H.; Chen, J.; Wang, Z.; Sun, J.; Zhao, D.; Yan, Y. Synthesis, morphology control, and properties of porous metal–organic coordination polymers. *Microporous Mesoporous Mater.* **2003**, *58*, 105–114.

254. Islamoglu, T.; Otake, K. I.; Li, P.; Buru, C. T.; Peters, A. W.; Akpinar, I.; Garibay, S. J.; Farha, O. K. Revisiting the structural homogeneity of NU-1000, a Zr-based metal-organic framework. *CrystEngComm* **2018**, *20*, 5913–5918.

255. Pankajakshan, A.; Sinha, M.; Ojha, A. A.; Mandal, S. Water-Stable Nanoscale Zirconium-Based Metal–Organic Frameworks for the Effective Removal of Glyphosate from Aqueous Media. *ACS Omega* **2018**, *3*, 7832–7839.

256. Zhang, G. Y.; Zhuang, Y. H.; Shan, D.; Su, G. F.; Cosnier, S.; Zhang, X. J. Zirconium-based porphyrinic metal-organic framework (PCN-222):

Enhanced photoelectrochemical response and its application for label-free phosphoprotein detection. *Anal. Chem.* **2016**, *88*, 11207–11212.

257. Decker, G. E.; Stillman, Z.; Attia, L.; Fromen, C. A.; Bloch, E. D. Controlling Size, Defectiveness, and Fluorescence in Nanoparticle UiO-66 through Water and Ligand Modulation. *Chem. Mater.* **2019**, *31*, 4831–4839.

258. Cavka, J. H.; Jakobsen, S.; Olsbye, U.; Guillou, N.; Lamberti, C.; Bordiga, S.; Lillerud, K. P. A New Zirconium Inorganic Building Brick Forming Metal Organic Frameworks with Exceptional Stability. *J. Am. Chem. Soc.* **2008**, *130*, 13850–13851.

259. Zhao, Y.; Zhang, Q.; Li, Y.; Zhang, R.; Lu, G. Large-Scale Synthesis of Monodisperse UiO-66 Crystals with Tunable Sizes and Missing Linker Defects via Acid/Base Co-Modulation. *ACS Appl. Mater. Interfaces* **2017**, *9*, 15079–15085.

260. Lozano, L. A.; Faroldi, B. M. C. Efficient solvothermal synthesis of highly porous UiO-66 nanocrystals in dimethylformamide-free media. *J. Mater. Sci.* **2018**, 1862–1873.

261. Han, Y.; Liu, M.; Li, K.; Sun, Q.; Song, C.; Zhang, G.; Zhang, Z.; Guo, X. Cu_2O Mediated Synthesis of MetalOrganic Framework UiO-66 in Nanometer Scale. *Cryst. Growth Des.* **2017**, *17*, 685–692.

262. Cao, J.; Yang, Z.; Xiong, W.; Zhou, Y.; Peng, Y.; Li, X. One-step synthesis of Co-doped UiO-66 nanoparticle with enhanced removal efficiency of tetracycline: Simultaneous adsorption and photocatalysis. *Chem. Eng. J.* **2018**, *353*, 126–137.

263. Park, T. H.; Cychosz, K. A.; Wong-Foy, A. G.; Dailly, A.; Matzger, A. J. Gas and liquid phase adsorption in isostructural Cu_3[biaryltricarboxylate]$_2$ microporous coordination polymers. *Chem. Commun.* **2011**, *47*, 1452–1454.

264. Lan, X.; Huang, N.; Wang, J.; Wang, T. A general and facile strategy for precisely controlling the crystal size of monodispersed metal-organic frameworks: Via separating the nucleation and growth. *Chem. Commun.* **2018**, *54*, 584–587.

265. Zaręba, J. K.; Nyk, M.; Samoć, M. Co/ZIF-8 Heterometallic Nanoparticles: Control of Nanocrystal Size and Properties by a Mixed-Metal Approach. *Cryst. Growth Des.* **2016**, *16*, 6419–6425.

266. Tu, M.; Wiktor, C.; Ro, C.; Fischer, R. A. Rapid room temperature syntheses of zeolitic-imidazolate framework (ZIF) nanocrystals. *Chem. Commun.* **2014**, *50*, 13258–13260.

267. Orsi, A.; Price, D. J.; Kahr, J.; Pillai, R. S.; Sneddon, S.; Cao, S.; Benoit, V.; Łozińska, M. M.; Cordes, D. B.; Slawin, A. M.; Llewellyn, P. L.; Casely, I.; Ashbrook, S. E.; Maurin, G.; Wright, P. A. Porous zinc and cobalt 2-nitroimidazolate frameworks with six-membered ring windows and a layered cobalt 2-nitroimidazolate polymorph. *CrystEngComm* **2017**, *19*, 1377–1388.

268. Zhao, P.; Lampronti, G. I.; Lloyd, G. O.; Wharmby, M. T.; Facq, S.; Cheetham, A. K.; Redfern, S. A. Phase transitions in zeolitic imidazolate framework 7: The importance of framework flexibility and guest-induced instability. *Chem. Mater.* **2014**, *26*, 1767–1769.

269. Lively, R. P.; Dose, M. E.; Thompson, J. A.; McCool, B. A.; Chance, R. R.; Koros, W. J. Ethanol and water adsorption in methanol-derived ZIF-71. *Chem. Commun.* **2011**, *47*, 8667–8669.

270. Cravillon, J.; Münzer, S.; Lohmeier, S.; Feldhoff, A.; Huber, K. Rapid Room-Temperature Synthesis and Characterization of Nanocrystals of a Prototypical Zeolitic Imidazolate Framework- Supporting Information. *Chem. Mater.* **2009**, *21*, 1–21.

271. Park, K. S.; Ni, Z.; Cote, A. P.; Choi, J. Y.; Huang, R.; Uribe-Romo, F. J.; Chae, H. K.; O'Keeffe, M.; Yaghi, O. M. ZIFs - first synthesis. *P. Natl. Acad. Sci.* **2006**, *103*, 10186–10191.

272. Colombo, V.; Montoro, C.; Maspero, A.; Palmisano, G.; Masciocchi, N.; Galli, S.; Barea, E.; Navarro, J. A. Tuning the adsorption properties of isoreticular pyrazolate-based metal-organic frameworks through ligand modification. *J. Am. Chem. Soc.* **2012**, *134*, 12830–12843.

273. He, T.; Xu, X.; Ni, B.; Wang, H.; Long, Y.; Hu, W.; Wang, X. Fast and scalable synthesis of uniform zirconium-, hafnium-based metal–organic framework nanocrystals. *Nanoscale* **2017**, 19209–19215.

274. Wang, F.; Guo, H.; Chai, Y.; Li, Y.; Liu, C. The controlled regulation of morphology and size of HKUST-1 by "coordination modulation method". *Microporous Mesoporous Mater.* **2013**, *173*, 181–188.

275. Bagherzadeh, E.; Zebarjad, S. M.; Hosseini, H. R. M. Morphology modification of the iron fumarate MIL-88A metal–organic framework using

formic acid and acetic acid as modulators. *Eur. J. Inorg. Chem.* **2018**, *2018*, 1909–1915.

276. Bellido, E.; Hidalgo, T.; Lozano, M. V.; Guillevic, M.; Simón-Vázquez, R.; Santander-Ortega, M. J.; González-Fernández, Á.; Serre, C.; Alonso, M. J.; Horcajada, P. Heparin-Engineered Mesoporous Iron Metal-Organic Framework Nanoparticles: Toward Stealth Drug Nanocarriers. *Adv. Healthc. Mater.* **2015**, *4*, 1246–1257.

277. Xiang, L.; Sheng, L.; Wang, C.; Zhang, L.; Pan, Y.; Li, Y. Amino-Functionalized ZIF-7 Nanocrystals: Improved Intrinsic Separation Ability and Interfacial Compatibility in Mixed-Matrix Membranes for CO_2/CH_4 Separation. *Adv. Mater.* **2017**, *29*, 1–8.

278. Xing, T.; Lou, Y.; Bao, Q.; Chen, J. Surfactant-assisted synthesis of ZIF-8 nanocrystals in aqueous solution via microwave irradiation. *CrystEngComm* **2014**, *16*, 8994–9000.

279. Springer, S.; Satalov, A.; Lippke, J.; Wiebcke, M. Nanocrystals and nanomaterials of isoreticular zeolitic imidazolate frameworks. *Microporous Mesoporous Mater.* **2015**, *216*, 161–170.

280. Toby, B. H.; Von Dreele, R. B. GSAS-II: the genesis of a modern open-source all purpose crystallography software package. *46*, 544–549, _eprint: https://onlinelibrary.wiley.com/doi/pdf/10.1107/S0021889813003531.

281. Vazquez-Molina, D. A.; Mohammad-Pour, G. S.; Lee, C.; Logan, M. W.; Duan, X.; Harper, J. K.; Uribe-Romo, F. J. Mechanically Shaped Two-

Dimensional Covalent Organic Frameworks Reveal Crystallographic Alignment and Fast Li-Ion Conductivity. *138*, 9767–9770.